UNIVERSITÉ DE STRASBOURG

ÉCOLE DOCTORALE de Physique Chimie

[UMR 7550]

THÈSE présentée par :

Carole FAURE

soutenue le : **29 Septembre 2014**

pour obtenir le grade de : **Docteur de l'université de Strasbourg**

Discipline/ Spécialité : Astrophysique

Simulation des effets des bras spiraux sur la dynamique stellaire dans la Voie Lactée

THÈSE dirigée par :
[Dr FAMAEY Benoit] Observatoire Astronomique de Strasbourg

RAPPORTEURS :
[Dr ROBIN Annie] Observatoire de Besançon
[Dr RUSSEIL Delphine] Laboratoire d'Astrophysique de Marseille

EXAMINATEUR :
[Pr BOILY Christian] Observatoire Astronomique de Strasbourg

AUTRES MEMBRES DU JURY :
[Dr SIEBERT Arnaud] Invité, Observatoire Astronomique de Strasbourg

Remerciements

Je voudrais tout d'abord remercier grandement mon directeur de thèse, Benoît FAMAEY, pour toute son aide. Je suis ravie d'avoir travaillé en sa compagnie car, outre son appui scientifique, il a toujours été là pour me soutenir et me guider au cours de l'élaboration de cette thèse. Je remercie Arnaud SIEBERT, co-directeur de cette thèse, pour sa présence et son aide précieuses et indispensables tout au long de ces trois années de recherche, pour son expertise informatique, ses excellents conseils et pour tout le temps qu'il m'a accordé durant ces trois années.
Je souhaite remercier Hervé WOZNIAK, directeur de l'Observatoire Astronomique de Strasbourg, de l'honneur qu'il m'a fait en me permettant de réaliser ces travaux dans son établissement et bien plus, puisque j'ai pu avoir la chance d'enseigner ainsi que de promouvoir l'astrophysique auprès de jeunes et de moins jeunes. Pour cela, je tiens aussi à saluer les personnes avec qui j'ai été amenées à collaborer.

Je remercie les membres du jury, Mme Annie ROBIN, directeur de Recherche de l'Institut UTINAM et Mme Delphine RUSSEIL, maître de conférences à l'université d'Aix-Marseille, d'avoir accepté de juger mes travaux en qualité de rapporteurs. Je remercie sincèrement Christian BOILY, professeur de l'Université de Strasbourg, d'avoir accepté d'examiner mes études.

Comme une thèse est aussi une longue et complexe aventure, je n'oublierai pas toutes les personnes qui ont participé à la rendre plus agréable. L'observatoire offre un cadre de travail formidable où des gens chaleureux sont nombreux autour d'une tasse de café ou de nos "travaux communs de chercheur de début d'après-midi" consistant à trouver des lettres à écrire dans des cases.
Je remercie mes supers collègues doctorants de leur amitié et bonne humeur, Fred et John, qui m'ont fait une petite place dans leur bureau et m'ont guidé pendant 2 ans tant dans le domaine astronomique que gastronomique, Julien et Nico qui les ont remplacés et ont su égayé notre bureau avec une touche personnelle de verdure, Anaïs et ses nombreuses petites attentions, JB toujours prêt à donner n'importe quel coup de main, François, Ben, Maxime et Enmanuelle venant compléter la fine équipe.
Comment terminer ces remerciements sans évoquer le soutien indéfectible de ma famille pour qui, tout comme moi, ces trois années l'ont fortement grandi.

Table des matières

Chapitre

Liste des tableaux

Table

Table des figures

Figure

Chapitre 1

INTRODUCTION

1.1 Galaxies spirales : généralités

L'étude des galaxies est un sujet encore relativement jeune en astrophysique. Ce n'est qu'en 1926, que Hubble (1926a) découvrit la première galaxie en dehors de notre Voie Lactée. Cela, 75 années après que Rosse (1850) eut mis en évidence la structure spirale de M51, la galaxie du tourbillon. Elle avait été classée à l'époque comme la première "nébuleuse spirale" et l'on pensait, à tort, qu'elle appartenait à notre Galaxie. Les observations de ces objets depuis cette découverte ont mis en évidence trois types de galaxies. Hubble a alors établi une classification, appelée classification de Hubble, selon l'apparence morphologique des galaxies : les elliptiques (E) qui sont des concentrations sphéroïdales, les spirales (S) en forme de disque aplati et les irrégulières (Irr) qui n'ont pas de structure clairement définie. Les Irr ont pu subir une formation très récente, avoir une masse trop faible ou encore une trop forte activité de leur noyau.

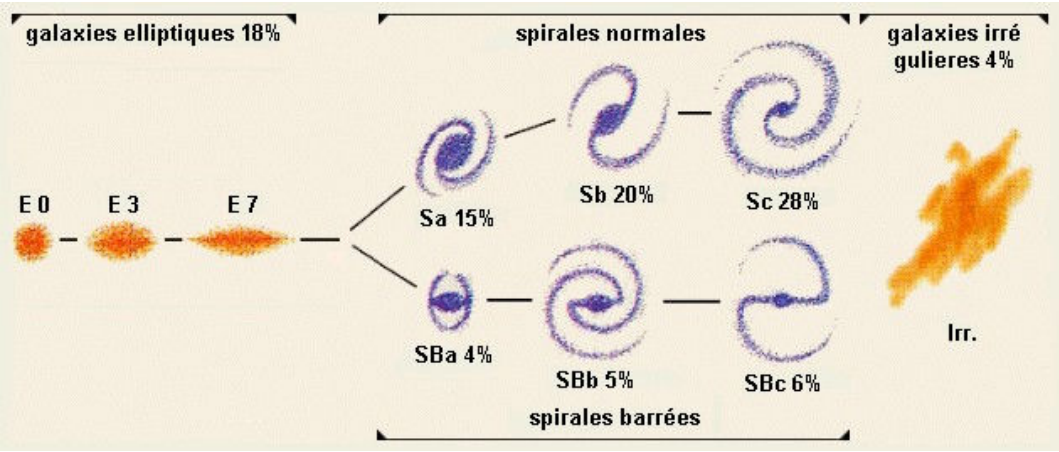

FIGURE 1.1 – Classification morphologique des galaxies selon Hubble. Crédit : sciences-physiques.ac-dijon.fr

Les galaxies elliptiques n'ont pas de structure particulière. Elles ont seulement la forme

d'une ellipsoïde de révolution notées de E0, pour les plus sphériques, à E7 pour les plus allongées. Les galaxies plus allongées que E7 possèdent un disque et sont appelées galaxies lenticulaires S0.
Les galaxies spirales sont classées par Hubble (1926b) en fonction de leur aspect en différents types selon la présence ou non d'une barre (SB ou SAB si la barre est faible) et le degré d'enroulement des bras de la spirale (de Sa à Sc ou de SBa à SBc avec la lettre 'a' pour les spirales les plus enroulées). La Fig. 1.1 présente cette classification.
Plus tard, Baade (1944) a introduit la notion de population stellaire en étudiant les diagrammes de Hertzprung-Russell du noyau de la galaxie d'Andromède et de deux de ses compagnons elliptiques. Il en tire deux populations différentes : les étoiles de la population I sont des étoiles riches en métaux et appartenant au disque avec le gaz interstellaire. Les étoiles de la population II sont plus vieilles et moins riches en métaux se trouvant dans les parties centrales de la galaxie et dans le halo galactique. Elles peuplent également les amas globulaires.
Vaucouleurs (1959) n'étant pas satisfait de la classification de Hubble car incomplète en proposa une révision pour que la classification prenne en compte d'autres caractéristiques qui jouent aussi un rôle important. Il rajoute les classes Sd et SBd ainsi que les galaxies spirales magellaniques (Sm), des galaxies ne possédant qu'un bras et qui tiennent leur nom du grand Nuage de Magellan, pour faire le pont entre les galaxies spirales et irrégulières (Im). Il prend en compte les galaxies spirales qui possèdent un anneau autour du noyau à la naissance des bras qu'il note "S(r)". Celles qui n'en ont pas sont les "S(s)" et la transition (rs). L'anneau peut aussi être extérieur dans le cas où les bras se rejoignent et est noté R. Il introduit aussi la notation SA pour parler des galaxies non barrées en opposition aux galaxies SB et y ajoute la classe intermédiaire SAB pour les galaxies faiblement barrées.
Les galaxies spirales, auxquelles nous nous intéresserons à travers l'étude de la Voie Lactée, sont les plus représentées dans l'univers local. Elles se distinguent par leur structure aplatie dite "à disque" possédant éventuellement plusieurs bras lumineux qui s'enroulent en spirale autour du centre. Ces galaxies présentent essentiellement deux composantes visibles. Un bulbe central, potentiellement barré, et un disque galactique plat dont l'épaisseur est très inférieure à son diamètre. Ce sont les galaxies qui contiennent le plus de gaz, de poussières et d'étoiles jeunes. Les étoiles les plus brillantes et massives décrivent la structure spirale. Les bras spiraux sont en réalité des zones de sur-densité, lieu de naissance d'une grande partie des étoiles de diverses masses. Le nombre de bras varie selon la longueur d'onde à laquelle on les regarde : habituellement quatre ou plus dans le bleu, pour le gaz et les étoiles jeunes, mais deux en général dans l'infrarouge proche, pour les étoiles plus vieilles. Il se peut aussi qu'il n'y ait pas de bras du tout. Une troisième composante des galaxies spirales, le halo, se manifeste par son action gravitationnelle mais n'émet que très peu de lumière visible. Les galaxies à disques sont en rotation autour de leur axe central suivant une courbe de rotation. Celle-ci ne peut-être expliquée sans la présence d'une masse bien supérieure à celle que l'on observe dans les composantes visibles : c'est l'origine du postulat de la matière noire. C'est donc dans le halo que se trouve la plus grande partie de la masse d'une galaxie spirale, répartie dans une vaste sphère beaucoup plus étendue que le disque visible.
Ainsi, ces galaxies sont caractérisées par une grande diversité de populations, d'âges et de vitesses des étoiles qui les composent et qui permettent de retracer leur formation.

Les bras spiraux sont connus pour jouer un rôle important dans l'évolution dynamique et chimique des disques galactiques. Lieu reconnu de formation d'étoiles, on sait maintenant qu'ils participent par exemple à la migration des étoiles et à la redistribution du moment angulaire dans le disque (Sellwood & Binney 2002; Quillen & Minchev 2005). Malgré des décennies de recherches, de nombreux points restent cependant à éclaircir. Vu leurs importances, il est donc nécessaire d'en apprendre plus à leurs sujets pour comprendre l'évolution des galaxies.

La mise en place et l'agencement des différentes composantes de ces systèmes stellaires devraient idéalement être comprises dans un contexte cosmologique. Dans ce dernier, l'influence respective des phénomènes extérieurs (tels que l'accrétion de galaxies satellites, les vents galactiques) et de phénomènes internes liés à l'évolution séculaire des galaxies, ainsi que leurs interactions, sont encore mal connus. Les bras spiraux peuvent eux-mêmes être engendrés par des perturbations externes. Mieux les comprendre est donc essentiel à cette entreprise de compréhension de la formation et de l'évolution des galaxies.
Or, aujourd'hui, on ne sait par exemple toujours pas si ils sont de nature transitoire ou stationnaire et l'ensemble de leurs effets dynamiques, notamment hors du plan des galaxies n'est pas bien établi. Pour essayer de mieux comprendre tout cela, on peut étudier en détail la Voie Lactée, notre Galaxie qui est une galaxie spirale normale.

1.2 Description de la Galaxie

La Voie Lactée ou la Galaxie (G), nommée d'après la bande lumineuse traversant le ciel nocturne, est une galaxie spirale de type SBb/c. Elle fait partie du Groupe Local, un ensemble d'une quarantaine de galaxies qui s'étend sur environ $1.5.10^6$ kpc dont elle est, après la galaxie d'Andromède (M31), la galaxie la plus massive. Sa masse totale est actuellement estimée à $1.5.10^{12}$ $M_\odot$et environ 10^{11} étoiles la composent. La figure 1.2 présente, à droite, une vue de son disque avec sa barre et, à gauche ses bras spiraux. À droite, la Voie Lactée est schématisée avec un bulbe d'un rayon d'environ 3 kpc. Les disques mince et épais s'étendent jusqu'à 20 kpc de rayon. Le halo sphérique va jusqu'à des rayons supérieurs à 30 kpc. Enfin, les amas globulaires, qui sont des ensembles d'étoiles gravitationnellement liées peuplent l'ensemble de la Galaxie. La courbe de rotation (fig 1.3), qui devrait décroître en fonction de la distance, montre que la quasi-totalité de sa masse réside dans le halo (environ 90%). Mais de nombreux éléments composant la Voie Lactée reste encore mal connus.
Ce ne fut qu'à partir des années 1930 que l'on a pu montrer que la Voie Lactée faisait elle aussi partie des galaxies spirales et que cette bande lumineuse n'était en réalité qu'une partie de bras visible. Encore plus récemment, en 2005, les observations du télescope spatial Spitzer, confirmant les observations de COBE, ont apporté des indices validant le fait que notre Galaxie est une spirale barrée (de type SBc). Elle ne posséderait cependant que deux bras dominants au lieu de quatre. La Voie Lactée, comme dans la majorité des galaxies spirales, a des bras *trailing*. C'est à dire que les extrémités de ses bras pointent dans la direction opposée à la rotation contrairement aux bras *leading* qui pointent dans la direction de la rotation.

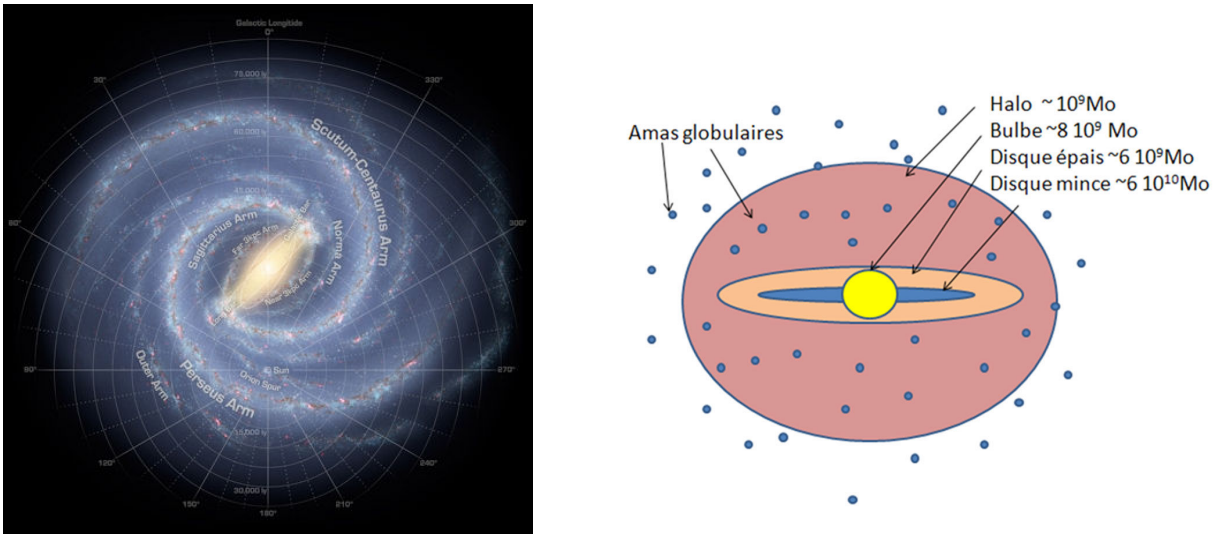

FIGURE 1.2 – À gauche : Vue d'artiste du modèle de la Voie Lactée à 2 bras à partir du relevé effectué par Spitzer, credit : Churchwell et al. (2009). À droite : Schéma des différentes composantes de la Voie Lactée, crédit : Françoise Combes

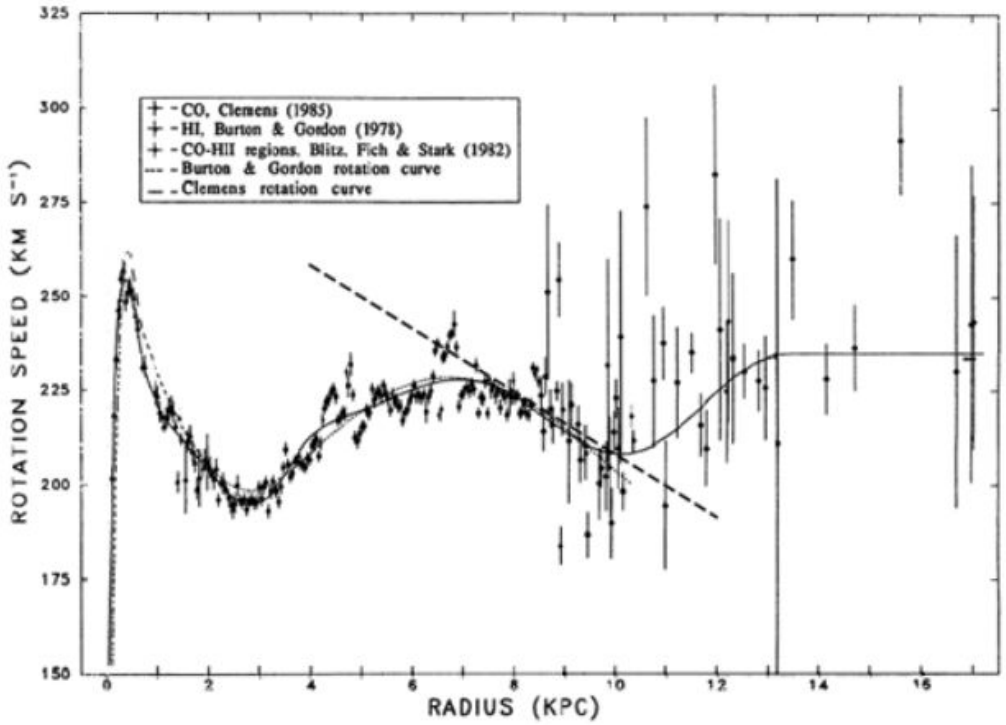

FIGURE 1.3 – Comparaison des courbes de rotations de la Voie Lactée obtenues avec différents traceurs, crédit : Combes (1991)

1.2.1 Le Bulbe

Le bulbe central de la Voie Lactée se particularise par une forme sphéroïdale. Il est relativement peu massif avec environ 10^{10} $M_\odot$. Son rayon effectif r_e d'environ $0,7$ kpc dans

l'infra-rouge a été mesuré par comptage d'étoiles avec le relevé IRAS, confirmé ensuite par la mission COBE. À cette occasion, l'universalité du profil de Vaucouleurs a été vérifié, à savoir, que la brillance de surface est une fonction du rayon. L'étude du bulbe est rendue difficile par une forte absorption due aux poussières dans la majorité des bandes (Schultheis et al. 2014). Le bulbe est peuplé majoritairement par des étoiles vieilles (plus de 7 milliards d'années) et peu riches en métaux (en moyenne, avec toutefois un gradient de métallicité : les étoiles au centre pouvant avoir une métallicité de l'ordre du Soleil voir Gonzalez et al. (2013); Martinez-Valpuesta & Gerhard (2013)) qui se sont formées lorsque le Voie Lactée était jeune. Grâce aux abondances chimiques, il a été mis en évidence deux autres populations distinctes d'étoiles. Une d'âge intermédiaire et une dernière très jeune (moins de 200 millions d'années) moins riche en métaux, conséquences d'accrétions récentes. La zone centrale du bulbe présente une forte densité d'étoiles et de poussières d'une masse de $2,6.10^6$ $M_\odot$, où les dispersions de vitesses sont plus élevées (Schödel et al. 2002). La barre au centre de notre galaxie joue un rôle important dans la géométrie et la composition du bulbe. En effet, les étoiles entrant en résonance avec la barre acquièrent une amplitude par rapport au plan plus élevée. Ce phénomène aurait tendance à donner au bulbe une forme de cacahuète (Wegg & Gerhard 2013).

1.2.2 Le disque mince et épais

Il a été mis en évidence que le disque galactique d'un rayon de 15 à 20 kpc est constitué d'un disque mince dont la masse stellaire domine et d'un second disque plus épais (Gilmore & Reid 1983). L'échelle de hauteur de ce disque épais est d'environ de 1 kpc (Gilmore et al. 2004), en comparaison avec les quelques centaines de parsec du disque mince (200-300 pc), et sa luminosité est estimée à 10% de celle du disque mince (Recio-Blanco et al. 2014). D'après Bensby et al. (2011), la longueur d'échelle du disque épais serait plus courte que celle du disque mince ($L_{thick} = 2.0$ kpc, $L_{thin} = 3.8$ kpc) mais ces valeurs sont encore discutées. Récemment, Robin et al. (2014) ont trouvé des échelles plus courte en hauteur (de 800 à 340 pc) pour des longueurs de 3.2 à 2 kpc. La masse de ces deux disques s'élèverait autour de 5.10^{10} $M_\odot$, mais dépend des échelles choisies.

Comparées aux étoiles du halo, celles des disques mince et épais possèdent des vitesses de rotation globalement plus élevées, de l'ordre de 220 km.s^{-1} pour les étoiles du voisinage solaire.
À cause notamment de la différence de hauteur mais aussi de l'âge (Seabroke & Gilmore 2007), la dispersion en vitesse verticale du disque épais est plus forte (~ 40 km.s^{-1}) que celle du disque mince (~ 20 km.s^{-1}). Les deux disques se distinguent également par la nature des étoiles qui les peuplent. Celles du disque mince sont riches en métaux ($-0.5 < [Fe/H]_{thin} < 0.5$) et couvrent un panel d'âge allant jusqu'à 10 milliards d'années. Les étoiles les plus jeunes se trouvent dans les bras spiraux. La métallicité des étoiles du disque épais est plus faible ($-2 < [Fe/H]_{thick} < -0.3$) pour une population âgée de plus de 10-12 milliards d'années voire 9 milliards d'années (Haywood et al. 2013). De plus, en comparant les métallicités des deux disques avec leurs teneurs en éléments α, il est possible de les différencier nettement (Fig. 1.4). En effet, il y a environ 10 milliards d'années, la fraction de gaz était plus élevée

qu'aujourd'hui ce qui a rendu la formation d'étoiles par effondrement gravitationnel plus rapide.

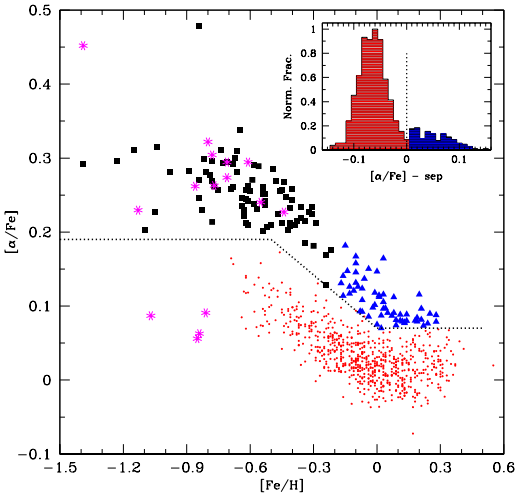

FIGURE 1.4 – Répartition chimique des étoiles de la Voie Lactée. Étoiles magentas : étoiles du halo ; ligne noire : séparation entre le disque mince et le disque épais ; carrés noirs : étoiles du disque épais ; points rouges : étoiles du disque mince ; triangle bleus : étoiles à forte métallicité et abondance en éléments α. Coin en haut à droite : histogramme de la séparation en éléments α, crédit : Adibekyan et al. (2013)

1.2.3 Le milieu interstellaire

Le milieu interstellaire (MIS) est composé d'une diversité de gaz et de poussières. Les surdensités du MIS sont le siège de la formation stellaire. Le CO, traceur du H_2 (environ 1.10^9 $M_\odot$), et les poussières se situent essentiellement dans un disque d'environ 7 kpc. Mais ils se concentrent majoritairement dans le disque galactique. Le HI (environ 4.10^9 $M_\odot$), observé en radio (21 cm), est une composante beaucoup plus étendue allant jusqu'à des distances de 25 kpc. À ces échelles, la répartition du HI suit la forme de la Voie Lactée. Le disque de gaz est en effet déformé (warp) (López-Corredoira et al. 2002; Levine et al. 2005; Reylé et al. 2009). Les effets dynamiques engendrant cette déformation ne sont pas entièrement compris. En effet, les influences du milieu intergalactique et celles de la dynamique interne à la galaxie créées des dégénérescences.
Certains nuages d'hydrogène se retrouvent également à haute altitude avec des vitesses radiales, le plus souvent positives, très élevées. Ces nuages ont été éjectés par des explosions de supernovae. Ils sont par la suite susceptibles de retomber sur le disque galactique. Ce phénomène est appelé fontaine galactique (Corbelli & Salpeter 1988). Ils peuvent également provenir d'accrétion par la Voie Lactée du milieu intergalactique (Marinacci et al. 2010). Enfin, la galaxie est entourée par un halo de gaz très chaud se trouvant jusqu'à environ 70 kpc du centre. Cette couronne est détectable en UV par raies d'absorptions sur des sources

extragalactiques. Ce gaz est très peu dense et ne s'effondre pas à cause de sa température élevée.

1.2.4 Le halo galactique

Le halo galactique se distingue lui aussi par la présence de deux composantes : le halo lumineux, un sphéroïde de 50 kpc de rayon entourant la Galaxie, et le halo sombre qui englobe l'ensemble d'un rayon de 200 kpc, allant jusqu'à celui de M31.
Le halo stellaire est un élément mineur de la Galaxie (environ 5.10^8 $M_\odot$). Ses étoiles, qui pour la plupart sont regroupées dans les amas globulaires, sont pauvres en métaux $-3 < [Fe/H]_{halo} < -1$ (Ryan et al. 1996) voir très pauvres, jusqu'à -5 (Christlieb et al. 2002). Ce qui en fait des étoiles probablement très vieilles (de 12 à 14 milliards d'années).
Carollo et al. (2010) sur un échantillon d'étoiles du SDSS a identifié deux composantes : le halo interne, dont la vitesse moyenne de rotation serait de 7 km.s^{-1} et la métallicité de -1.6, et le halo externe où la vitesse moyenne de rotation est de -80 km.s^{-1} avec une métallicité de -2.2.
Le halo lumineux se serait formé principalement par accrétion de petites galaxies ou bien, comme cela semble être le cas pour le halo interne, par dissipation au début de la formation de la Galaxie (Zolotov et al. 2009).
(À noter que la métallicité a fortement augmenté entre le moment où le halo stellaire s'est formé et la formation du disque épais.)
En ce qui concerne le halo de matière noire, il n'est révélé que par la courbe de rotation trop plate de la Voie Lactée. Les étoiles ont une vitesse trop élevées à grand rayon si on ne considère que le disque et le gaz. Il est massif, entre 90% et 97% de la masse totale de la Galaxie mais n'est observé qu'indirectement au niveau des effets sur le mouvement des étoiles et du gaz, l'interaction gravitationnelle semblant être l'unique interaction possible avec la matière composant cette matière noire.

1.2.5 Distribution de masse

Il existe différents modèles de masse de la Voie Lactée permettant de modéliser la partie axisymétrique du potentiel gravitationnel. L'un des plus célèbre est le modèle de Besançon (Robin et al. 2003) qui apporte une description auto-cohérente du potentiel de la Galaxie et des populations stellaires basé sur le dénombrement d'étoiles et sur la courbe de rotation. Ce modèle propose un ensemble de loi de densité pour le bulbe, le halo stellaire, le milieu interstellaire, les disques minces et épais et le halo de matière noire.
Dans cette thèse, nous utiliserons le modèle I du Binney & Tremaine (2008) décrit ci-dessous.

Modèle I du Binney & Tremaine (2008)

La partie axisymétrique du potentiel galactique considérée dans cette thèse est tirée du Modèle I de Binney & Tremaine (2008). Elle se compose des lois de densité d'un bulbe central, de disques stellaires (mince et épais), du milieu interstellaire (disque de gaz) et d'un halo de matière noire dont les principaux paramètres sont résumés par commodité dans la Table 1. Ce potentiel permet de reproduire un grand nombre de contraintes observationnelles comme la courbe de rotation et la force de rappel verticale du disque.

Le bulbe galactique central a une densité définie par une loi de puissance tronquée de forme

$$\rho_b(R,z) = \rho_{b0} \times \left(\frac{\sqrt{R^2 + (z/q_b)^2}}{a_b} \right)^{-\alpha_b} \exp\left(-\frac{R^2 + (z/q_b)^2}{r_b^2} \right) \tag{1.1}$$

où R définit le rayon Galactocentrique dans le plan médian, z la hauteur au-dessus du plan, ρ_{b0} la densité centrale, r_b le rayon de troncature et q_b l'aplatissement. La masse totale du bulbe est de $M_b = 5.18 \times 10^9 \mathrm{M}_\odot$.

Le disque stellaire est une somme de deux profils exponentiels (correspondant aux disques mince et épais) :

$$\rho_d(R,z) = \Sigma_{d0} \times \left(\sum_{i=1}^{i=2} \frac{\alpha_{d,i}}{2z_{d,i}} \exp\left(-\frac{|z|}{z_{d,i}} \right) \right) \exp\left(-\frac{R}{R_d} \right) \tag{1.2}$$

où Σ_{d0} est la densité de surface centrale, $\alpha_{d,1}$ et $\alpha_{d,2}$ les contributions relatives des disques mince et épais, $z_{d,1}$ et $z_{d,2}$ leurs hauteurs d'échelle respectives, et R_d la longueur d'échelle. La masse totale du disque est de $M_d = 5.13 \times 10^{10} \mathrm{M}_\odot$. Le potentiel du disque inclut également une contribution du milieu interstellaire de la forme

$$\rho_g(R,z) = \frac{\Sigma_g}{2z_g} \times \exp\left(-\frac{R}{R_g} - \frac{R_m}{R} - \frac{|z|}{z_g} \right) \tag{1.3}$$

où R_m est le rayon de troncature dans lequel se trouve le trou proche de la région du bulbe, R_g est la longueur d'échelle, z_g la hauteur d'échelle et Σ_g est tel qu'il contribue à 25% de la densité de surface du disque au rayon Galactocentrique du Soleil.

Enfin, le halo sombre est représenté par un modèle aplati en loi de puissance deux avec un aplatissement q_h, de la forme suivante

$$\rho_h(R,z) = \rho_{h0} \times \left(\frac{\sqrt{R^2 + (z/q_h)^2}}{a_h} \right)^{-\alpha_h} \times \left(1 + \frac{\sqrt{R^2 + (z/q_h)^2}}{a_h} \right)^{\alpha_h - \beta_h} \tag{1.4}$$

La courbe de rotation correspondant au potentiel axisymétrique est présentée Fig. 1.5. Pour des rayons inférieurs à 11 kpc, la courbe de rotation totale (trait noir) est principalement influencée par le disque (trait bleu en tiret) et au-dessus par le halo (trait rouge en pointillé).

1.3 Dynamique stellaire

La modélisation de la dynamique stellaire repose sur deux équations : celle de Poisson et celle de Boltzmann sans collision. L'équation de Poisson est une correction de l'équation de Laplace au second degré pour le potentiel. Elle a été un impact essentiel dans les domaines de l'électricité et du magnétisme ainsi qu'en astronomie sur le mouvement des corps célestes. L'équation de Boltzmann a été développée en 1872 et touche à la cinétique des gaz pour

TABLE 1.1 – Paramètres du modèle de potentiel axisymétrique (Binney & Tremaine 2008)

Paramètre	Potentiel axisymétrique
$M_b(\mathrm{M}_\odot)$	5.18×10^9
$M_d(\mathrm{M}_\odot)$	5.13×10^{10}
$M_{h,<100\ \mathrm{kpc}}(\mathrm{M}_\odot)$	$6. \times 10^{11}$
$\rho_{b0}(\mathrm{M}_\odot\,\mathrm{pc}^{-3})$	0.427
$a_\mathrm{b}(\ \mathrm{kpc})$	1.
$r_b(\ \mathrm{kpc})$	1.9
α_b	1.8
q_b	0.6
$\Sigma_{d0} + \Sigma_g(\mathrm{M}_\odot\,\mathrm{pc}^{-2})$	1905.
$R_d(\ \mathrm{kpc})$	2.
$R_g(\ \mathrm{kpc})$	4.
$R_m(\ \mathrm{kpc})$	4.
$\alpha_{d,1}$	14/15
$\alpha_{d,2}$	1/15
$z_{d,1}(\ \mathrm{kpc})$	0.3
$z_{d,2}(\ \mathrm{kpc})$	1.
$z_g(\ \mathrm{kpc})$	0.08
$\rho_{h0}(\mathrm{M}_\odot\,\mathrm{pc}^{-3})$	0.711
$a_h(\ \mathrm{kpc})$	3.83
α_h	$-2.$
β_h	2.96
q_h	0.8

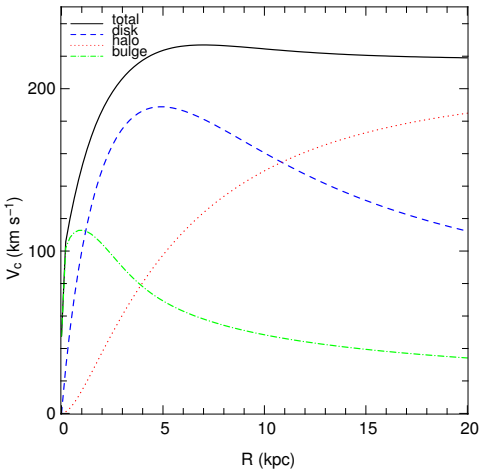

FIGURE 1.5 – Courbe de rotation correspondant au potentiel axisymétrique du modèle I

laquelle on cherche à expliquer le comportement des gaz à partir du mouvement de leurs particules. Elle a été introduite dans le domaine de l'astrophysique par Jeans en 1915. Les équations de Jeans en dérivent et permettent de décrire le mouvement d'un ensemble d'étoiles dans un potentiel. Ces équations sont similaires à celles d'Euler pour les fluides.

1.3.1 Équation de Poisson

La force gravitationnelle est une force conservative (le travail produit par cette force est indépendant du chemin suivi par son point d'action). Une des propriétés de ce type de force est qu'il existe un champ scalaire, le potentiel gravitationnel $\Phi(\overrightarrow{x}, t)$, tel que $\overrightarrow{F} = -\overrightarrow{\nabla}\Phi$. De plus, en dérivant la loi de gravitation de Newton, on peut relier le potentiel à sa source, la densité de masse ρ par l'équation de Poisson

$$\Delta\Phi(x,t) = 4\pi G\rho(x,t). \tag{1.5}$$

En coordonnées cylindriques, elle s'écrit

$$\frac{\partial^2\Phi}{\partial R^2} + \frac{1}{R}\frac{\partial\Phi}{\partial R} + \frac{1}{R^2}\frac{\partial^2\Phi}{\partial\theta^2} + \frac{\partial^2\Phi}{\partial z^2} = 4\pi G\rho(R,\theta,z,t). \tag{1.6}$$

1.3.2 Équation de Boltzmann sans collision

À chaque instant t, l'état d'un système non collisionnel tel que la Galaxie est donné par sa fonction de distribution $f(\overrightarrow{x}, \overrightarrow{v}, t)$. C'est une fonction complexe à 7 coordonnées. On a une équation sans collision car le temps de relaxation est long. Dans la limite fluide, avec un grand nombre d'étoiles, l'évolution de la fonction de distribution se fait de façon continue, c'est à dire qu'elle suit une équation de continuité. Sa dérivée temporelle totale est donc nulle :

$$\frac{\mathrm{d}f}{\mathrm{d}t} = 0. \tag{1.7}$$

En développant cette équation, on obtient

$$\frac{\partial f}{\partial t} + \sum_{i=1}^{3}\left(\frac{\partial x_i}{\partial t}\cdot\frac{\partial f}{\partial x_i} + \frac{\partial v_i}{\partial t}\cdot\frac{\partial f}{\partial v_i}\right) = 0. \tag{1.8}$$

La somme des variations de la densité de probabilité et des flux aux bords du système est nulle. Et en se servant des équations du mouvement

$$\begin{aligned} \tfrac{d\overrightarrow{x}}{dt} &= \overrightarrow{v}\,, \\ \tfrac{d\overrightarrow{v}}{dt} &= -\overrightarrow{\nabla}\Phi\,, \end{aligned} \tag{1.9}$$

l'équation de Boltzmann non collisionnelle peut donc s'écrire

$$\frac{\partial f}{\partial t} + \overrightarrow{v}\,.\,\overrightarrow{\nabla} f - \overrightarrow{\nabla}\Phi\,.\,\frac{\partial f}{\partial\overrightarrow{v}} = 0\,. \tag{1.10}$$

Cette équation combinée avec l'équation de Poisson permet de décrire la dynamique d'un système stellaire auto gravitant non collisionnel.

1.3.3 Équation d'Euler

L'équation d'Euler qui décrit le milieu interstellaire dérive du principe fondamental de la dynamique appliqué à une particule fluide non visqueuse subissant les forces de pression et la force du potentiel gravitationnel $\Phi(x,t)$.
Soit V un volume fermé de surface S. La masse de fluide du volume est $m(t) = \int_V \rho(x,t) d^3x$ et le champ des vitesses est $\overrightarrow{v}(\overrightarrow{x},t)$ donc d'après la deuxième loi de Newton,

$$m\frac{d\overrightarrow{v}}{dt} = -\int_S p d^2\overrightarrow{S} + m\overrightarrow{\nabla}\Phi. \tag{1.11}$$

On peut associer aux forces de pression, de densité surfacique $\overrightarrow{f_s} = p\overrightarrow{u_n}$ ($\overrightarrow{u_n}$ étant le vecteur unitaire entrant normal à la surface S), une densité volumique de force $\overrightarrow{f_v} = -\overrightarrow{\nabla}p$.
De plus,

$$\frac{\mathrm{d}\overrightarrow{v}}{\mathrm{d}t} = \frac{\partial\overrightarrow{v}}{\partial t} + \left(\overrightarrow{v}\,.\,\overrightarrow{\nabla}\right)\overrightarrow{v}\,. \tag{1.12}$$

Ainsi, l'équation d'Euler peut simplement s'exprimer par

$$\frac{\partial\overrightarrow{v}}{\partial t} + \left(\overrightarrow{v}\,.\,\overrightarrow{\nabla}\right)\overrightarrow{v} = -\frac{1}{\rho}\overrightarrow{\nabla}p - \overrightarrow{\nabla}\Phi. \tag{1.13}$$

Cette équation combinée avec l'équation de Poisson permet de décrire la dynamique d'un système fluide.
En première approximation, on peut considérer un fluide froid, de pression négligeable ($p \approx 0$), pour décrire le milieu interstellaire, pour étudier de façon qualitative la réponse d'un fluide froid à une perturbation spirale (voir 1.5.1.1 pour le cas à 2 dimensions, et le toy model du chapitre 3 pour le cas à 3 dimensions).

1.3.4 Équation de Jeans

Les moments de l'équation de Boltzmann sans collision permettent quant à eux d'arriver à des équations d'Euler mais pour un "fluide" stellaire. Si on intègre la forme scalaire de l'équation de Boltzmann sur toutes les vitesses,

$$\int \frac{\partial f}{\partial t} d^3\overrightarrow{v} + \int v_i \frac{\partial f}{\partial x_i} d^3\overrightarrow{v} - \frac{\partial\Phi}{\partial x_i}\int \frac{\partial f}{\partial v_i} d^3\overrightarrow{v} = 0\,, \tag{1.14}$$

on peut arriver à une équation de continuité. En prenant en compte que $\frac{\partial}{\partial t}$ et $\frac{\partial}{\partial x_i}$ ne dépendent pas des v_i, ils peuvent être sortis de l'intégrale et on introduit la densité spatiale $\nu(x)$ et la vitesse moyenne $\overrightarrow{v}(x)$ des étoiles telles que

$$\nu(x) = \int f d^3\overrightarrow{v} \text{ et } \overline{v_i} \equiv \frac{1}{\nu}\int f v_i d^3\overrightarrow{v}\,. \tag{1.15}$$

L'équation devient alors :

$$\frac{\partial\nu}{\partial t} + \frac{\partial\nu\overline{v_i}}{\partial x_i} = 0\,. \tag{1.16}$$

C'est l'équation de continuité pour une densité spatiale d'étoiles.

Si on multiplie l'équation par v_j et on intègre sur toutes les vitesses, on obtient

$$\frac{\partial}{\partial t}\int f v_j d^3\overrightarrow{v} + \int v_i v_j \frac{\partial f}{\partial x_i} d^3\overrightarrow{v} - \frac{\partial \Phi}{\partial x_i}\int v_j \frac{\partial f}{\partial v_i} d^3\overrightarrow{v} = 0\,. \tag{1.17}$$

En utilisant le théorème de la divergence pour le dernier terme de gauche

$$\int v_j \frac{\partial f}{\partial v_i} d^3\overrightarrow{v} = -\int \frac{\partial v_j}{\partial v_i} f d^3\overrightarrow{v} = -\delta_{ij}\nu \tag{1.18}$$

car :

$$\frac{\partial v_j f}{\partial v_i} = v_j \frac{\partial f}{\partial v_i} + \frac{\partial v_j}{\partial v_i} f\,. \tag{1.19}$$

Ce terme disparaît car pour des vitesses suffisamment larges $f(\overrightarrow{x}, \overrightarrow{v}, t) = 0$
Ainsi l'équation (1.17) devient

$$\frac{\partial(\nu\overline{v}_j)}{\partial t} + \frac{\partial(\nu\overline{v_i v_j})}{\partial x_i} + \nu\frac{\partial \Phi}{\partial x_j} = 0\,, \tag{1.20}$$

où

$$\overline{v_i v_j} \equiv \frac{1}{\nu}\int v_i v_j f d^3\overrightarrow{v}\,. \tag{1.21}$$

C'est l'équation de conservation du moment.
On peut soustraire leur vitesse moyenne à ces vitesses : $v_i - \overline{v_i} = w_i$ où $\overline{w_i} \equiv 0$. Ainsi

$$\sigma_{ij}^2 \equiv \overline{w_i w_j} = \overline{(v_i - \overline{v_i})(v_j - \overline{v_j})} = \overline{v_i v_j} - \overline{v}_i \overline{v}_j\,. \tag{1.22}$$

Le tenseur σ^2 est appelé l'ellipsoïde des vitesses en x.
En injectant l'équation (1.22) dans (1.20), on obtient

$$\nu\frac{\partial \overline{v}_j}{\partial t} + \nu\overline{v_i}\frac{\partial \overline{v}_j}{\partial x_i} = -\nu\frac{\partial \Phi}{\partial x_j} - \frac{\partial(\nu\sigma_{ij}^2)}{\partial x_i} \tag{1.23}$$

Le terme $-\nu\sigma_{ij}^2$ décrit la "pression" anisotropique. Cette équation est analogue à l'équation d'Euler d'un fluide mais avec cette pression anisotrope.
Ces équations sont appelées les équations de Jeans et elles relient les densités d'étoiles à la position, à la vitesse, à la dispersion des vitesses et au potentiel gravitationnel. Elles sont donc au "fluide" stellaire ce que l'équation d'Euler est au milieu interstellaire.

1.3.5 Intégrale du mouvement et théorème de Jeans

Des solutions simples de l'équation de Boltzmann sans collision peuvent être écrites si la dépendance de la fonction de distribution des coordonnées de l'espace des phases ne se

fait qu'au travers d'intégrales du mouvement.
Une fonction $I(\overrightarrow{x}, \overrightarrow{v})$ est appelée intégrale du mouvement si et seulement si,

$$\frac{d}{dt} I(\overrightarrow{x}(t), \overrightarrow{v}(t)) = 0\,. \tag{1.24}$$

En développant,

$$\frac{dI}{dt} = \frac{\partial I}{\partial \overrightarrow{x}} \cdot \frac{\partial \overrightarrow{x}}{\partial t} + \frac{\partial I}{\partial \overrightarrow{v}} \cdot \frac{\partial \overrightarrow{v}}{\partial t} = \overrightarrow{\nabla} I \,.\, \overrightarrow{v} - \frac{\partial I}{\partial \overrightarrow{v}} \,.\, \overrightarrow{\nabla}\Phi = 0\,. \tag{1.25}$$

On reconnait l'équation de Boltzmann dans le cas où I représente une solution indépendante du temps.

Soit $f(I_1, I_2, ..., I_n)$ une fonction de distribution générée par n intégrales du mouvement. Ainsi, la dérivée temporelle totale de f s'écrit

$$\frac{df}{dt} = \sum_{i=1}^{n} \frac{\partial f}{\partial I_i} \cdot \frac{dI_i}{dt} = 0 \tag{1.26}$$

car comme vu précédemment la dérivée temporelle totale d'une intégrale du mouvement est nulle. On en déduit donc que f est elle aussi une intégrale du mouvement et ainsi, elle aussi, une solution de l'équation de Boltzmann non-collisionnelle.

Théorème (de Jeans)**.** *Toute fonction de distribution, solution stationnaire de l'équation de Boltzmann sans collision, dépend de ses coordonnées d'espace de phase seulement à travers des intégrales du mouvement. Et toute fonction des intégrales de mouvement est une solution stationnaire de l'équation de Boltzmann sans collision.*

Cela revient à dire que la densité dans l'espace des phases se conserve le long de son orbite.

1.3.6 Orbites dans un potentiel axisymétrique : Approximation épicyclique

Dans un potentiel axisymétrique, le mouvement des étoiles en trois dimensions peut être réduit au mouvement de ces étoiles dans leur plan méridional subissant le potentiel effectif $\Phi_{eff}(R, z)$.
Les équations du mouvement sont

$$\begin{aligned} \ddot{R} &= -\tfrac{\partial \Phi_{eff}}{\partial R}\,, \\ \ddot{z} &= -\tfrac{\partial \Phi_{eff}}{\partial z}\,, \end{aligned} \tag{1.27}$$

avec

$$\Phi_{eff} \equiv \Phi(R, z) + \frac{L_z^2}{2R^2}\,. \tag{1.28}$$

Φ_{eff} atteint son minimum lorsque ses dérivées s'annulent, soit

$$\begin{aligned} \tfrac{\partial \Phi_{eff}}{\partial z} = 0 \quad &\Leftrightarrow \quad z = 0\,, \\ \tfrac{\partial \Phi_{eff}}{\partial R} = \tfrac{\partial \Phi}{\partial R} - \tfrac{L_z^2}{R^3} = 0 \quad &\Leftrightarrow \quad \left(\tfrac{\partial \Phi}{\partial R}\right)_{(R_g,0)} = \tfrac{L_z^2}{R_g^3} = R_g \dot{\phi}^2\,. \end{aligned} \tag{1.29}$$

Le mouvement décrit est alors une orbite circulaire dans le plan $z = 0$, de rayon R_g, de vitesse angulaire ϕ et de moment angulaire L_z.
La plupart des orbites des étoiles dans les galaxies spirales sont très proches de l'orbite circulaire. En faisant le changement de variable $x \equiv R - R_g$ et en approximant le potentiel, on peut écrire

$$\Phi_{eff} \approx \frac{1}{2}\left(\frac{\partial^2 \Phi_{eff}}{\partial R^2}\right)_{(R_g,0)} x^2 + \frac{1}{2}\left(\frac{\partial^2 \Phi_{eff}}{\partial z^2}\right)_{(R_g,0)} z^2 \tag{1.30}$$

On définit la fréquence épicyclique par

$$\kappa^2(R_g) \equiv \left(\frac{\partial^2 \Phi_{eff}}{\partial R^2}\right)_{(R_g,0)} \tag{1.31}$$

et la fréquence verticale par

$$\nu^2(R_g) \equiv \left(\frac{\partial^2 \Phi_{eff}}{\partial z^2}\right)_{(R_g,0)} . \tag{1.32}$$

Ainsi,

$$\begin{aligned} \ddot{x} &= -\kappa^2 \, x \, , \\ \ddot{z} &= -\nu^2 \, z \, . \end{aligned} \tag{1.33}$$

Il s'agit d'équation du mouvement de deux oscillateurs harmoniques non couplés, l'un à la fréquence κ, l'autre à la fréquence ν. Les étoiles effectuent des boucles autour de la position qu'elles occuperaient si leurs orbites étaient strictement circulaires. Les épicycles sont des ellipses possédant des boucles, dont l'excentricité est liée aux valeurs de κ. Les étoiles tournent dans le sens direct sur le cercle, et dans le sens rétrograde sur l'épicycle. Pendant ce temps, elles effectuent aussi un mouvement périodique de part et d'autre du plan de la galaxie lié à ν, voir Fig. 1.6.

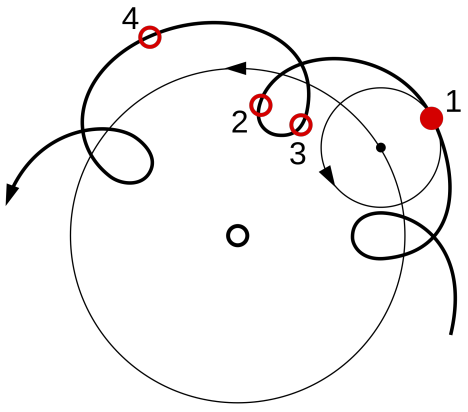

FIGURE 1.6 – Représentation d'une orbite épicyclique. Crédit : MLWattas

La fréquence circulaire est

$$\Omega^2(R) = \frac{1}{R}\left(\frac{\partial\Phi}{\partial R}\right)_{(R,0)} = \frac{L_z^2}{R^4}\,. \tag{1.34}$$

En utilisant l'expression de Φ_{eff}, on peut écrire κ en fonction de Ω,

$$\kappa^2 = \left(\frac{\partial^2\Phi}{\partial R^2}\right)_{(R_g,0)} + \frac{3L_z^2}{Rg^4} = \left(R\frac{\partial\Omega^2}{\partial R} + 4\Omega^2\right)_{(R_g,0)}\,, \tag{1.35}$$

avec en général $\Omega \leq \kappa \leq 2\Omega$. L'inégalité de gauche s'adopte lorsqu'on s'éloigne du centre de la galaxie, Ω déclinant avec le rayon. L'inégalité de droite s'applique lorsqu'on est près du centre, Ω y étant presque constant.
On peut tirer les énergies des équations du mouvement des deux oscillateurs qui sont

$$E_R = \frac{1}{2}(\dot{x}^2 + \kappa^2 x^2) \;\text{ et }\; E_z = \frac{1}{2}(\dot{z}^2 + \nu^2 z^2)\,, \tag{1.36}$$

où E_R est l'énergie épicyclique et E_z l'énergie verticale.
Si l'orbite d'une étoile est presque circulaire alors E_R, E_z et L_z sont des intégrales du mouvement.

1.3.7 Fonctions de distribution pour un disque stellaire

Les fonctions de distribution dépendent de deux intégrales du mouvement, l'énergie dans le plan Er et le moment angulaire Lz, ce qui permet d'assurer qu'elles soient solutions de l'équation de Boltzmann sans collision.
On se servira de la fonction de distribution de Bienayme & Séchaud (1997) pour déterminer les conditions initiales à trois dimensions. Elle se base sur celle de Shu à deux dimensions (Shu 1969). Dans cette fonction, l'énergie verticale est prise comme troisième intégrale du mouvement mais elle ne l'est pas parfaitement

$$f(E_R, L_z, E_z) = \frac{\Omega\,\rho_d}{\sqrt{2}\kappa\pi^{\frac{3}{2}}\sigma_R^2\sigma_z}\exp\left(\frac{-(E_R - E_c)}{\sigma_R^2} - \frac{E_z}{\sigma_z^2}\right), \tag{1.37}$$

où la vitesse angulaire Ω, la fréquence épicyclique radiale κ et la densité du disque dans le plan ρ_d sont toutes fonctions de L_z, étant prises au rayon $R_c(L_z)$ d'une orbite circulaire de moment angulaire L_z. La longueur d'échelle du disque est considérée comme étant 2 kpc, comme pour le potentiel axisymétrique. L'énergie $E_c(L_z)$ est celle de l'orbite circulaire de moment angulaire L_z au rayon R_c. Enfin, les dispersions radiale et verticale σ_R^2 et σ_z^2 sont également fonction de L_z et s'expriment :

$$\sigma_R^2 = \sigma_{R_\odot}^2 \exp\left(\frac{2R_\odot - 2R_c}{R_{\sigma_R}}\right), \tag{1.38}$$

$$\sigma_z^2 = \sigma_{z_\odot}^2 \exp\left(\frac{2R_\odot - 2R_c}{R_{\sigma_z}}\right) \tag{1.39}$$

où $R_{\sigma_R}/R_d = R_{\sigma_z}/R_d = 5$ (Bienayme & Séchaud 1997). Les dispersions initiales de vitesses diminuent ainsi de façon exponentielle avec le rayon mais pour chaque rayon, elles sont isothermes en fonction de la hauteur.

1.4 Perturbations non-axisymétriques : les bras spiraux et la barre centrale

Précédemment, nous avons supposé que la Galaxie est axisymétrique et stationnaire. Mais environ 5% de la masse totale de la Galaxie visible est non-axisymétrique : le bulbe possède une barre et le disque de la Voie Lactée possède des bras spiraux. De plus un phénomène de résonance modifiant la distribution de vitesse peut apparaître.

1.4.1 Les résonances

Un phénomène de résonance apparaît lorsqu'une des fréquences naturelles d'un système est égale à une des fréquences de forçage imposée par le perturbateur à ce système avec une vitesse de rotation spéciale que l'on appellera Ω_p.
Les résonances se produisent lorsque les boucles se referment sur elles-mêmes après un tour complet. Les étoiles vont repasser au même endroit par rapport au potentiel, ce qui va amplifier les effets de la perturbation.
On a vu précédemment que les fréquences naturelles de la Galaxie sont la fréquence épicyclique κ et la fréquence verticale ν. La fréquence de forçage d'une perturbation possédant une symétrie de rotation d'ordre m, un entier, s'écrit

$$\omega_p = m(\Omega - \Omega_p)\,, \tag{1.40}$$

avec $\Omega = \frac{v_c}{R}$, la vitesse angulaire des orbites de vitesse circulaire v_c de la Galaxie non perturbée.
Une symétrie d'ordre m signifie que la forme de la perturbation est invariante par rotation d'angle $2\pi/m$. Ainsi $m = 2$ modes pour la barre centrale et $m = 2$ ou $m = 4$ modes (ou plus) pour les bras spiraux.
Il y a donc résonance lorsque :

$$\begin{array}{ll} \omega_p(R) = 0 & \text{(Corotation)} \\ \omega_p(R) = \pm\kappa(R) & \text{(résonances radiales)} \\ \omega_p(R) = \pm\nu(R) & \text{(résonances verticales)} \end{array} \tag{1.41}$$

Dans la zone de résonance par corotation, on a $\Omega = \Omega_p$: la vitesse des étoiles est égale à la vitesse de la perturbation et dans le référentiel tournant, l'étoile ne tourne pas mais parcourt uniquement une épicycle.
Avant et après la corotation (CR), il existe deux zones où les orbites des étoiles sont fermées et périodiques. En effet, il y a un rapport rationnel entre la fréquence de rotation et la fréquence épicyclique. C'est à dire que les étoiles tournent plus ou moins rapidement que la perturbation mais sur des trajectoires qui comportent un nombre entier de boucles. Le rapport le plus fréquent à l'intérieur de la corotation est : $\Omega - \Omega_p = \kappa/2$. Cette zone s'appelle la *résonance de Lindblad interne* (ILR) tandis qu'à l'extérieur de la corotation, la résonance se produit lorsque $\Omega - \Omega_p = -\kappa/2$. C'est la *résonance externe de Lindblad* (OLR). Si le rapport est de 1/4, les résonances radiales associées sont appelées *ultra-harmoniques* (IUHR et OUHR). Les plus communes sont la résonance interne et la résonance externe de Lindblad. Connaissant la courbe de rotation (v_c et donc Ω) et la fréquence de rotation de la

perturbation (Ω_p), on peut retrouver les rayons auxquels les résonances apparaissent. Il se peut aussi qu'il y ait plusieurs ILR (ou aucune) selon la forme du potentiel.

Les résonances sont importantes car les orbites des galaxies changent au passage de ces zones. Les ondes de densité à l'origine des bras spiraux ne peuvent se développer qu'entre les ILR et OLR. Elles sont absorbées au passage d'une ILR ce qui empêche leur propagation par le centre de la galaxie. La barre ne s'étend pas plus loin que la CR et sa vitesse de rotation est probablement proche de la vitesse angulaire à la CR. On s'attend à des anneaux d'étoiles aux CR et OLR. Le gaz est poussé de chaque côté du ILR ce qui conduit à des anneaux de gaz ainsi qu'à de la formation d'étoiles.
S'il n'y a pas d'ILR, les ondes d'une spirale *trailing* peuvent traverser la région centrale et émerger comme des ondes *leading* de l'autre coté. Un effet d'amplification de la structure spirale aura ensuite lieu par *amplification du swing* car la rotation différentielle change graduellement les ondes *leading* en ondes *trailing*. Les mouvements épicycles dépendant de la forme des bras, ils sont amplifiés et la structure spirale est fortement amplifiée.

1.4.2 La barre

Comme évoqué dans la partie 1.2.1, le bulbe de la Galaxie est divisé en deux populations : un bulbe vieux axisymétrique (Sevenster 1999) et la barre centrale qui est une composante non-axisymétrique. Si son existence était soupçonnée dès les années 70 par l'étude des régions HI (Peters (1975) pour le modèle et Cohen & Few (1976) pour les observations), la véritable confirmation n'est venue qu'au cours des années 90 avec la multiplication des indices observationnels indépendants, que ce soit en infra-rouge proche (Blitz & Spergel 1991), en distribution spatiale des sources (Nakada et al. 1991) ou en émission CO (Binney et al. 1991).
La barre est vue de face, et a donc une taille angulaire minimale. De plus, elle est relativement petite, ce qui l'a rendu plus difficile à séparer du bulbe.
Elle joue un rôle important en concentrant la matière qui donnera naissance à de nouvelles générations d'étoiles. La présence d'un grand nombre d'étoiles jeunes dans la partie centrale et dans l'extrémité de la barre des galaxies spirales barrées s'explique par leurs orbites circulaires au centre et elliptiques au niveau de la barre.
Une barre stellaire a un effet important sur l'évolution d'une galaxie. Elle accélère la concentration du gaz du milieu interstellaire dans les régions centrales, provoquent des régions de chocs et modifie la distribution des étoiles et de la masse.
Le processus de formation de la barre est incertain, probablement du à une instabilité du disque de la Voie Lactée. Elle tourne comme s'il s'agissait d'un solide mais dès que 5% de la masse de la galaxie est concentrée dans le bulbe, la barre se détruit puis elle peut se reformer ultérieurement.

Dans cette thèse, nous nous concentrerons sur les bras spiraux et ne considérerons pas les effets de la barre centrale.

1.4.3 Les bras spiraux

Dans les années 30, Lindblad fut le premier à émettre l'hypothèse que les bras spiraux résultaient de l'interaction entre les orbites des étoiles et les forces gravitationnelles du disque. Cependant nous ne connaissons toujours pas clairement ni leurs mécanismes ni leurs origines ni leurs durées de vie.
Deux scénarios se démarquent sans expliquer la création : Lin & Shu (1964) ont proposé l'existence de bras spiraux à longue durée de vie (plusieurs milliards d'années) par des ondes de densité dont les modes quasi-stationnaires du disque sont étudiés de façon analytique dans l'approximation *tight-winding* (où l'angle d'enroulement de la spiral est faible) tandis que d'autres, à partir des résultats de simulations N-corps, suggèrent que les bras sont transitoires (Goldreich & Lynden-Bell (1965); Sellwood & Carlberg (1984) voir cependant D'Onghia et al. (2013) et Sellwood & Carlberg (2014)). Ni les bras spiraux à longues durées, ni les transitoires ne semblent se démarquer.

En ce qui concerne la Voie Lactée, la situation n'est guère meilleure. La structure des bras étant toujours incertaine. Lorsque nous prenons en compte le gaz, on observe une structure spirale possédant quatre bras principaux alors que le disque stellaire, via le comptage d'un grand nombre d'étoiles observées par les données Spitzer (de même type que notre Soleil) montre une structure à deux bras. Il n'y a donc que peu d'étoiles dans deux de ces quatre bras. Récemment, plusieurs radiotélescopes observant des étoiles massives (et donc plus jeune et à plus courte durée de vie) ont révélé une distribution à quatre bras spiraux qui laisse supposer une formation de la structure avec quatre bras puis une "accumulation" dans les deux bras spiraux révélés par Spitzer. De plus, on ne connait que vaguement la position et les propriétés de la structure spirale de la Voie Lactée (distance à laquelle les bras débutent, leurs phases, leurs vitesses de rotation, leurs enroulements) et encore moins l'âge des bras.

Par simplification, dans les modèles actuels, la Voie Lactée est généralement décrite comme une superposition de composantes axisymétriques (symétriques autour d'un axe perpendiculaire au disque et passant par son centre). Néanmoins, grâce aux relevés spectroscopiques récents, qui sont de plus en plus précis et profonds, nous avons maintenant accès à l'ensemble des informations de l'espace des phases (positions et vitesses). On y remarque des effets de perturbations non-axisymétriques non négligeables au voisinage solaire comme par exemple l'existence de groupes mobiles (association d'étoiles ayant le même mouvement mais qui ne sont pas en interaction gravitationnelle entre elles). Ces derniers peuvent nous renseigner sur la position exacte des résonances et donc sur la perturbation spirale (Antoja et al. 2008; Minchev et al. 2009) si les résonances sont à l'origine de ces groupes mobiles. Or les trois principaux groupes mobiles à faible vitesse du voisinage solaire (Hyades, Pléiades, Sirius) montrent des âges et des abondances très différents (Famaey et al. 2008; Pompéia et al. 2011), signe probable d'une origine dynamique. Plusieurs études pouvant reproduire la position en vitesse du groupe mobile des Hyades ont été proposées utilisant aussi bien des bras quasi-stationnaires (Quillen & Minchev 2005; Antoja et al. 2011) que transitoires (De Simone et al. 2004), avec ou sans les résonances dues à une barre centrale (Antoja et al. 2009).
On notera que les modèles avec les bras spiraux quasi-stationnaires reproduisent en plus

la position du groupe mouvant de Sirius ainsi que d'autres et place la résonance ultra-harmonique interne de la spirale (il y a 4 oscillations radiales pour une orbite dans le repère de la spirale en ce point) à proximité du Soleil. Dans le cas transitoire, seulement les Hyades peuvent être reproduites et la résonance est différente.

Comme autres effets de la perturbation spirale, les observations sur des galaxies externes ont montré que les bras spiraux peuvent aussi être à l'origine de mouvements non-axisymétriques globaux. Alors que les anciennes données indiquaient que les constantes de Oort dans le référentiel local de repos (référentiel suivant le mouvement moyen des étoiles de la Voie Lactée au voisinage du Soleil) étaient compatibles avec le modèle axisymétrique (K et C égaux à 0), Olling & Dehnen (2003) ont trouvé que C=-10 $km.s^{-1}$ kpc^{-1}, ce qui n'était pas attendu. Plus récemment, avec les données du relevé de vitesses radiales stellaires RAVE (pour Radial Velocity Experiment), Siebert et al. (2011a) ont mis en évidence un gradient au niveau de la moyenne des vitesses radiales Galactocentrique (C+K= -4 $km.s^{-1}$ kpc^{-1}) des étoiles du disque au voisinage solaire. Ce sont ces effets sur les mouvements globaux que je vais étudier plus en détail dans cette thèse.

Nous avons vu précédemment qu'il y avait une controverse sur le nombre de bras dominant de notre Galaxie.
La Voie Lactée possèderait 4 bras : ceux de Persée, de la Règle et du Cygne, du Centaure (ou écu-Croix), et Sagittaire-Carène. Le Soleil se situe à proximité du bras local d'Orion qui n'est pas un bras principal, mais un agglomérat d'étoiles et de gaz entre les bras du Sagittaire et de Persée bien qu'il soit probablement plus étendu qu'il ne l'est supposé actuellement.
En 1958, une première méthode pour déterminer la structure de la Galaxie se base sur l'étude de la densité de l'hydrogène neutre (HI) dans le plan de la galaxie, sachant que cette densité augmente dans les bras spiraux. En utilisant les premiers radiotélescopes dans les années 1950, Oort et al. (1958) sont parvenus à cartographier de façon incomplète la Voie Lactée et ont mis en évidence des sections de bras spiraux.
Par la suite, une autre étude consistant à tracer les régions géantes HII, présentes habituellement dans les bras spiraux, a conclu à l'existence de quatre bras spiraux et leurs positions (Georgelin & Georgelin 1976). Un peu plus tard, c'est une nouvelle carte de la densité de surface perturbée de l'hydrogène neutre du disque externe de la Voie Lactée qui a reconfirmé la présence de 4 bras spiraux logarithmiques (Levine et al. 2006). La figure 1.7 montre le contour de la densité de surface divisé par la densité de surface médiane. C'est un marqueur de la force des perturbations. On s'aperçoit que la structure spirale de la Voie Lactée s'étend jusqu'à une vingtaine de kiloparsec du centre Galactique.
Néanmoins, en 2008, les données de Spitzer ont permis de compter 110 millions d'étoiles de la Voie Lactée et d'évaluer sa densité à partir de son image prise par la tranche. Le décompte des étoiles révèle un saut dans la densité au niveau de la région du bras du Centaure mais cela n'est pas le cas dans les régions où doivent se trouver deux autres bras spiraux importants, celui de la Règle et celui du Sagittaire. Quant à celui de Persée, il n'est pas visible sur les images de Spitzer, car situé en grande partie de l'autre côté du bulbe galactique. Il semble donc bien que notre Galaxie ne possède que deux bras spiraux importants, comme c'est souvent le cas pour les galaxies spirales barrées observées dans l'Univers. Il s'agit des

bras de Persée et du Centaure alors que ceux du Sagittaire et de la Règle ne seraient que des bras mineurs (fig.1.2 à gauche).
Récemment, Urquhart et al. (2014), en utilisant plusieurs radiotélescopes pour observer individuellement environ 1650 étoiles massives dans la galaxie, les ont retrouvé parmi les quatre bras spiraux. Les différences dans les observations viennent du fait que Spitzer a détecté des étoiles beaucoup plus froides avec une plus faible masse, des étoiles comme notre Soleil. En fait, pour les travaux d'Urquhart et al. (2014), comme il s'agit d'étoiles massives, plus jeunes, on s'attend bien à ce qu'elles suivent le gaz. Du point de vue du potentiel gravitationnel, une structure à deux bras reste donc d'actualité.

1.5 Dynamique des bras spiraux

La première tentative d'explication des bras spiraux consistait à dire que la forme spirale était due à la rotation différentielle de la galaxie. Ainsi, les parties internes tournaient plus vite que les parties externes et la structure spirale apparaissait avec le temps. Mais dans ce cas, les bras auraient fini par s'enrouler sur eux-mêmes tout en s'étirant. Ils auraient rempli toute la Galaxie en un temps de l'ordre du milliard d'années, ce qui est incompatible avec les observations ("Winding problem").
La théorie des ondes de densité est suggérée par Lindblad (années 1940). La structure spirale est dessinée par une onde qui tourne dans la galaxie tout en conservant sa forme. Cette onde se propage à une vitesse angulaire constante et est différente de celle de la matière qui est en rotation différentielle. L'onde se fait rattraper dans les régions centrales de la galaxie mais elle dépasse la matière dans les régions plus éloignées. Au niveau de l'onde, la matière s'y trouve un peu plus comprimée, ce qui provoque une légère surdensité d'où son nom : *onde de densité*.
Lorsque des nuages de gaz traversent l'onde, la compression peut les amener à s'effondrer sur eux-même pour donner naissance à des étoiles chaudes. Ainsi, ces étoiles brillantes matérialisent l'onde spirale après son passage dans le bras et avant de s'éteindre quelques millions d'années plus tard.

Les orbites d'étoiles sont légèrement elliptiques. Si elles sont alignées, on peut créer une forme de barre. Si maintenant on tourne leur grand axe R d'un angle $\theta = -\alpha \log R +$ constant, les orbites se resserrent à certains endroits pour former des régions plus denses en forme de spirale à deux bras dans lesquelles les étoiles resteront plus longtemps du fait de la trajectoire tangentielle au bras avant d'en ressortir. Lindblad avait remarqué que pour une ellipse, le taux de précession des orbites $(\Omega - \kappa/2)$ restait constant en fonction du rayon. D'où une prédominance des galaxies spirales à 2 bras.

1.5.1 Ondes de densité spirales quasi-statiques

La théorie des ondes de densité, développée par Lin & Shu (1964), affirme que la structure spirale est due à une onde de densité spirale quasi-statique avec une vitesse de rotation

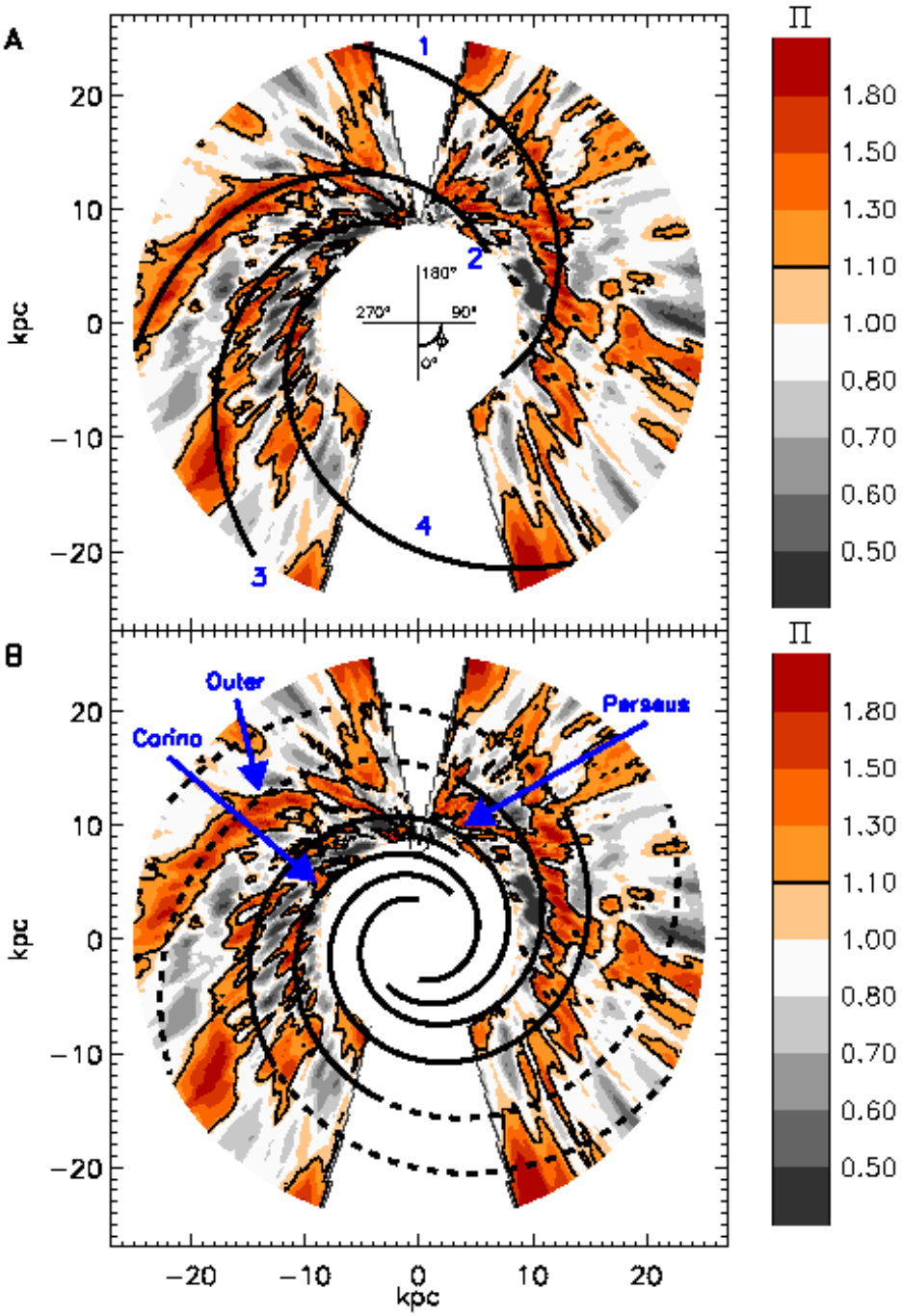

FIGURE 1.7 – 2 modèles de spirale à quatre bras en surimpression de la structure des bras HI externes. En haut : les bras logarithmiques sont choisis pour suivre les surdensités. En bas : le modèle de spirale est symétrique, les lignes pointées représentent le moment où le modèle diverge des observations. Le Soleil est à l'intersection des deux pans de carte en (0,8.5), le centre Galactique en (0,0), crédit : Levine et al. (2006)

constante, une onde qui se maintient dans un état d'équilibre sur plusieurs rotations.
L'existence des bras spiraux est donc expliquée mais le phénomène qui donne naissance aux ondes de densité ainsi que la façon dont elles sont entretenues alors qu'elles devraient avoir tendance à se dissiper au bout de quelques millions d'années n'est pas expliquée. Cette théorie, bien qu'elle soit très critiquée, reste néanmoins centrale car elle permet de nombreuses prédictions en accord avec les observations.
L'un des points noirs des ondes de densité spirales quasi-statiques est le théorème d'anti-spirale qui veut que : si la solution stationnaire d'un ensemble d'équations réversibles dans le temps a la forme d'une spirale *trailing* alors, il doit y avoir une solution identique à la forme d'une spirale *leading* (Lynden-Bell & Ostriker 1967). Or, comme il a été dit plus haut, les galaxies spirales sont majoritairement *trailing* . Par conséquent, soit ces ondes de densité ne sont pas stationnaires (mais récentes ou régénérées), soit elles ne sont pas réversibles dans le temps (mais dissipées ou absorbées).
Le scénario serait que le disque stellaire soit instable et qu'une forme spirale dominée par le mode le plus instable se développe. Ainsi, le choc du gaz interstellaire débute, amortissant l'onde de densité dans les étoiles qui atteint une amplitude stable, en équilibre avec la croissance des bras. Le mode le plus instable dessinerait une spirale très marquée.

1.5.1.1 le cas d'un fluide froid

Dans le but de trouver la réponse du disque galactique à une perturbation du potentiel, on commence sans utiliser l'approximation *tight-winding WKBJ* (ou approximation BKW en français pour Brillouin Kramers Wentzel). Dans cette approximation, on suppose que les ondes sont très enroulées tel que $|kR| \gg 1$ où $k = df(R)/dR$ est le nombre d'ondes ($k > 0$ pour le cas *trailing* et $k < 0$ pour le cas *leading*. Les quantités qui décrivent le mouvement fluide s'écrivent sous la forme

$$X(R, \theta, t) \sim X_0 + X_1(R) \exp[i(m\theta + \int kdR - \omega t)] \tag{1.42}$$

avec $\omega(t)$ la fréquence de l'onde.

Les étapes suivies pour trouver cette réponse suivent celles de Binney & Tremaine (2008). On néglige l'épaisseur du disque (z=0) mais aussi, on considère que **la pression est nulle**. L'équation d'Euler, eq 1.13, s'écrit en coordonnées cylindriques

$$\frac{\partial v_R}{\partial t} + v_R \frac{\partial v_R}{\partial R} + \frac{v_\theta}{R}\frac{\partial v_R}{\partial \theta} - \frac{v_\theta^2}{R} = -\frac{\partial \Phi}{\partial R}, \tag{1.43}$$

$$\frac{\partial v_\theta}{\partial t} + v_R \frac{\partial v_\theta}{\partial R} + \frac{v_\theta}{R}\frac{\partial v_\theta}{\partial \theta} + \frac{v_\theta v_R}{R} = -\frac{1}{R}\frac{\partial \Phi}{\partial \theta}. \tag{1.44}$$

Du fait que la composante non-axisymétrique soit faible, on peut linéariser le potentiel et les vitesses perturbées sous la forme $X(R, \theta, t) = X_0 + \epsilon X_1$ avec $\epsilon \ll 1$, $v_{R_0} = 0$ et $\partial \Phi_0 / \partial \theta = 0$, l'indice "0" désigne les quantités non perturbées.
La partie non perturbée de l'équation d'Euler s'écrit donc

$$\frac{v_{\theta_0}^2}{R} = \frac{\partial \Phi_0}{\partial R}. \tag{1.45}$$

L'accélération centripète est égale à la force gravitationnelle et

$$v_{\theta_0} \simeq \sqrt{R\frac{\partial \Phi_0}{\partial R}} = R\Omega(R). \tag{1.46}$$

Regardons à présent les termes au premier ordre en ϵ,

$$\frac{\partial v_{R_1}}{\partial t} + \Omega\frac{\partial v_{R_1}}{\partial \theta} - 2\Omega v_{\theta_1} = -\frac{\partial \Phi_1}{\partial R}, \tag{1.47}$$

$$\frac{\partial v_{\theta_1}}{\partial t} + v_{R_1}\left[\frac{d(\Omega R)}{dR} + \Omega\right] + \Omega\frac{\partial v_{\theta_1}}{\partial \theta} = -\frac{1}{R}\frac{\partial \Phi_1}{\partial \theta}. \tag{1.48}$$

La somme entre crochet est la constante d'Oort B multipliée par un facteur -2. En se servant de l'équation 1.35 pour l'expression de la fréquence épicyclique, on a

$$\kappa^2 = -4B\Omega \tag{1.49}$$

Les solutions de telles équations sont de la forme

$$X_1 = Re\left\{X_a(R)\exp[i(m\theta - \omega t)\right\}, \tag{1.50}$$

avec m un entier positif. En substituant ces solutions aux équations, on obtient

$$v_{R_a}(R) = \frac{i}{\Delta}\left[(\omega - m\Omega)\frac{d\Phi_a}{dR} - \frac{2m\Omega\Phi_a}{R}\right], \tag{1.51}$$

$$v_{\theta_a}(R) = -\frac{1}{\Delta}\left[-\left(\frac{\kappa^2}{2\Omega} + \Omega\right)\frac{d\Phi_a}{dR} + \frac{m(\omega - m\Omega)\Phi_a}{R}\right] \tag{1.52}$$

avec $\Delta \equiv \kappa^2 - (\omega - m\Omega)^2$.
Toutes ces équations dépendent du rayon et si ω est un entier, il existe un rayon où $\Delta = 0$ et v_{R_1} et v_{θ_1} divergent. En effet, en introduisant l'expression du *pattern speed* vu précédemment, $\Omega_p = \omega/m$, on voit que cela arrive lorsque

$$\Omega_p = \Omega \pm \frac{\kappa}{m} \tag{1.53}$$

soit lorsque l'on est dans une situation de résonance.
Si ce potentiel peut s'écrire localement comme

$$\Phi_a(R) = F(R)\exp\left[if(R)\right] = F(R)\exp\left[i\int_R kdR\right]. \tag{1.54}$$

alors, $d\Phi_a/dR = ik\Phi_a$ domine Φ_a/R dans l'approximation WKBJ ainsi

$$v_{R_a} = -\frac{m(\Omega - \Omega_p)}{\Delta}k\Phi_a \tag{1.55}$$

et

$$v_{\theta_a} = \frac{i\kappa^2}{\Omega\Delta} k\Phi_a. \tag{1.56}$$

v_{R_a} et v_{θ_a} sont du même ordre.
Ces solutions représentent des ondes dont leur structure se déplace périodiquement. Il peut y avoir des superpositions d'ondes avec des valeurs différentes pour m mais Lin & Shu (1964) affirme qu'il y a une préférence pour des valeurs de m faibles.

Je suivrai dans mon travail un raisonnement similaire basé sur les équations d'Euler linéarisées mais cette fois en 3 dimensions.

Pour savoir si le disque est stable à ces perturbations, si on considère que la perturbation du potentiel et la densité surfacique sont reliées par l'équation de Poisson, on obtient une relation de dispersion qui relie le nombre d'onde à la fréquence. La relation de dispersion des perturbations pour un disque plat, dans le cadre du WKBJ, s'écrit

$$(\omega - m\Omega)^2 = v_s^2 k^2 + \kappa^2 - 2\pi \mathrm{G}\Sigma_0 |k| \,, \tag{1.57}$$

avec Σ_0 la densité surfacique et v_s la vitesse du son du fluide ($v_s = 0$ pour un disque froid). Elles dépendent du rayon Galactocentrique R de même que Ω et κ.
On voit, en regardant le membre de droite que l'on peut obtenir des valeurs négatives pour $(\omega - m\Omega)^2$. Si $(\omega - m\Omega)^2$ est positif alors le disque est stable mais dans le cas négatif, l'amplitude de la perturbation est exponentielle (de la forme $\exp(\pm|\omega - m\Omega|t)$) et le disque est instable.
Dans le cas de perturbations axisymétrique, on a $m = 0$ alors

$$\omega^2 = v_s^2 k^2 + \kappa^2 - 2\pi \mathrm{G}\Sigma_0 |k| \,, \tag{1.58}$$

et le disque est instable si $\omega^2 < 0$. La limite de stabilité est donc

$$v_s^2 k^2 - 2\pi \mathrm{G}\Sigma_0 |k| + \kappa^2 = 0 \,, \tag{1.59}$$

c'est une équation du second degré. Le disque fluide est stable s'il n'y a pas de solution. Elle admet 2 racines qui sont

$$X_{1,2} = \frac{\pi \mathrm{G}\Sigma}{v_s^2} \left[1 \pm \sqrt{1 - \left(\frac{v_s \kappa}{\pi \mathrm{G}\Sigma} \right)^2} \right]. \tag{1.60}$$

Elle n'a pas de solution si $1 - Q^2$ est négatif, où

$$Q \equiv \frac{\kappa v_s}{\pi \mathrm{G}\Sigma_0} \tag{1.61}$$

est le critère de Toomre. Le disque est donc stable si $Q > 1$.

1.5.1.2 le cas stellaire

Si l'on considère un disque stellaire froid, on devrait en principe retrouver une expression pour la vitesse radiale moyenne des étoiles similaire à la vitesse radiale d'un disque fluide sans pression puisque les deux disques sont équivalents. Pour une dispersion non-nulle par-contre, dans le cas stellaire, les équations de la mécanique des fluides ne peuvent pas être utilisées pour décrire le disque puisque notre système est supposé sans collision. Or pour un disque de fluide, la pression va augmenter lorsque la longueur d'onde diminue. Ce qui n'est pas le cas pour un disque stellaire pour lequel les fréquences de perturbations ne peuvent pas dépasser la valeur de la fréquence épicyclique.
Mais il est possible de se servir d'un **facteur de réduction** $\mathcal{F} \leq 1$ pour abaisser la réponse du disque à une perturbation en-dessous de celle d'un disque froid via l'équation de Boltzmann linéarisée. S'il n'y a pas de dispersion de vitesse, $\mathcal{F} = 1$ et si la dispersion devient grande, $\mathcal{F}$ tend vers 0, le champ de vitesse du disque ne subit pas la perturbation spirale. La vitesse moyenne s'écrit alors

$$\overline{v}_{R_a} = -\frac{m(\Omega - \Omega_p)}{\Delta} k \Phi_a \mathcal{F} \tag{1.62}$$

De façon analogue que pour le disque fluide, on peut trouver une relation de dispersion mais en utilisant cette fois-ci l'équation de Jeans,

$$(\omega - m\Omega)^2 = \kappa^2 - 2\pi \mathrm{G}\Sigma_0 |k| \mathcal{F}(\frac{\omega - m\Omega}{\kappa}, \frac{\sigma_R^2 k^2}{\kappa^2}) \,, \tag{1.63}$$

avec

$$\mathcal{F}(s, \chi) \equiv \frac{2}{\chi}(1 - s^2) e^{-\chi} \sum_{n=1}^{\infty} \frac{I_{\mathrm{n}}(\chi)}{1 - s^2/n^2} \,, \tag{1.64}$$

σ_R la dispersion des vitesses radiales et I_n une fonction de Bessel.
Le critère de Toomre est

$$Q \equiv \frac{\kappa \sigma_R}{3.36 G \Sigma_0} \,. \tag{1.65}$$

1.5.2 Les bras spiraux : un phénomène transitoire ?

Toomre (1969) a aussi montré des limitations dues au fait que les spirales étroitement enroulées subissent de la dispersion et sont absorbées au niveau des résonances de Lindblad (Lynden-Bell & Kalnajs 1972). Il faut ajouter à cela que toutes les simulations dépendantes du temps n'ont pas réussi à prouver l'existence des ondes de densité stationnaires sans l'aide de perturbations extérieures ni d'une barre.
Toomre (1981) propose sa théorie de *swing amplification* où les ondes spirales sont transitoires et provoquées par des interactions de marrée ou par des barres.
Sellwood & Carlberg (1984) ont soutenu que dans les simulations N-corps, les bras spiraux disparaissaient au bout d'un certain temps car ils chauffaient le disque qui devenait par la suite plus stable contre les perturbations non-axisymétriques. Cependant, l'accrétion de gaz et la dissipation prolongeraient l'activité de la spirale indéfiniment. La nature des spirales reste néanmoins inexpliquée.

Fujii et al. (2011) ont mis en cause le nombre insuffisant de particules des anciennes simulations pour expliquer le fait que la structure spirale disparaisse aussi rapidement. En effet, les bras spiraux de leurs simulations à N-corps en 3 dimensions et à haute résolution ont duré jusqu'à 10 Gyr, le chauffage du disque étant moins important que ce que l'on pensait jusqu'alors.
D'Onghia et al. (2013) ont montré qu'il y a un équilibre entre un cisaillement qui détruit certaines parties de la spirale et les régions de surdensité où la spirale se reforme naturellement.
La structure des bras disparaît puis réapparait en se déplaçant à peu près à la vitesse circulaire dans un cycle apparemment auto-entretenu. Ce qui implique que les étoiles qui décrivent une orbite pratiquement circulaire sont proches de la corotation du mode spiral dominant pour chaque rayon. Le mécanisme de dispersion à la corotation de Sellwood & Binney (2002) serait donc favorisé.
Sellwood & Carlberg (2014) ont toutefois montré récemment que les deux approches (ondes stationnaires et transitoires) n'étaient peut-être pas si contradictoires puisque les bras spiraux transitoires à très courte durée de vie résulteraient en fait de la superposition de plusieurs modes quasi-stationnaires de fréquences différentes, survivant chacun au moins pendant 5 à 10 rotations au niveau de leur rayon de corotation. La structure spirale récurrente et transitoire des simulations ne serait donc que le résultat de la co-existence de plusieurs ondes de densité quasi-stationnaires au sein d'une même galaxie.

1.5.3 Mes recherches et plan de la thèse

J'ai tout d'abord commencé par utiliser les données RAVE pour faire une étude des variations du champ de vitesses du disque en fonction de l'échantillonnage, notamment en terme d'âge et de métallicité des populations stellaires. J'ai montré que les différents groupes ne subissaient pas les mêmes effets. Le fait que les étoiles plus âgées et moins métalliques ont un gradient de vitesse radiale plus important est un indice de plus qui laisse supposer que les bras spiraux ont une influence sur le disque et peuvent le perturber.
Puis Siebert et al. (2012), dans une recherche à laquelle je suis associée, ont montré qu'à partir d'une analyse du champ des vitesses dans un modèle analytique à deux dimensions, les bras spiraux pouvaient reproduire les observations que l'on a pu voir avec le relevé spectroscopique RAVE. L'étude suppose que le gradient est causé uniquement par les bras spiraux et utilise le modèle des ondes de densité de Lin & Shu. Ce travail nous a permis de définir un meilleur modèle pour les paramètres de la spirale. Cependant, il n'a été fait qu'en 2 dimensions, pour des étoiles se trouvant dans le disque. Or, de plus en plus d'indices montrent que l'on trouve aussi des effets dus à des perturbations non-axisymétriques en dehors du plan galactique.
Nous avons donc dû aller plus loin et passer à la troisième dimension pour vérifier si les bras spiraux peuvent aussi être à l'origine de ces mouvements verticaux et non uniquement causés par l'interaction de galaxies satellites ou de sous-halos, comme il était supposé jusqu'à présent.
Mon but a donc été de construire un modèle réaliste de la Voie Lactée en 3 dimensions auquel j'ai ajouté une perturbation pour voir si les résultats obtenus concordaient avec les observations. J'ai été amenée à écrire deux programmes : le premier permettant de définir

les conditions initiales de N particules tests représentant une population d'étoiles du disque mince, le second de les intégrer dans le potentiel de mon modèle.
J'ai montré que les bras spiraux pouvaient avoir un rôle dans les effets que nous observons, tant au niveau des vitesses radiales que verticales. Nous avons constaté des ensembles de *source point* et de *sink point* selon l'endroit où l'on se trouvait par rapport à la spirale ainsi qu'à la corotation. On a ensuite retrouvé ces résultats en linéarisant les équations d'Euler dans un *toy-model*.
Cette thèse présente mes recherches. Après cette longue introduction, je présenterai, dans un second chapitre, le champ de vitesse des étoiles du disque tel qu'il a été observé avec le récent relevé spectroscopique RAVE, un relevé que je présenterai en détail. Des mouvements stellaires moyens non nuls dans les directions radiales et verticales ont été clairement mis en évidence avec ce relevé. Le reste de ma thèse, dans un troisième chapitre, sera consacré à l'hypothèse que les mouvements observés pourraient être causés par les bras spiraux puis j'introduirai les simulations développées au cours de cette thèse et discuterai des résultats obtenus.

Chapitre 2

Le projet RAVE

2.1 Un petit historique du projet

RAVE est un relevé spectroscopique dont le but est de mesurer les vitesses radiales d'étoiles de la Voie Lactée afin de tester le modèle de formation hiérarchique des galaxies. C'est un relevé spectroscopique utilisant les capacités de multiplexage des instruments de type MOS (Multi Object Spectrograph) combinés aux capacités grand champ des télescopes de Schmidt.

RAVE a été lancé en 2002, les premières observations ayant eu lieu le 11 avril 2003. Le relevé utilise l'instrument 6dF monté sur le télescope UKST de 1.2m (UK Schmidt Telescope) de l'AAO (Anglo-Australian Observatory aujourd'hui Australian Astronomical Observatory) situé à Siding-springs en Australie (fig. 2.1). Ce télescope possède un très grand champ de 5.7 degrés de diamètre (à comparer à des champs de quelques minutes d'arcs pour les grands télescopes comme le VLT) ce qui permet de sonder une fraction significative du ciel austral de façon efficace. Sans cette capacité grand champ, le temps de pose étant fixé en fonction de la magnitude des étoiles et du rapport signal-sur-bruit désiré, il serait impossible d'observer une surface d'environ un hémisphère ($\sim$20,000 degrés carrés) sur l'échelle de temps du projet, 10 ans.

Cette capacité grand champ est combinée au multiplexage de l'instrument. En effet, si en spectroscopie traditionnelle les étoiles sont observées les unes après les autres, dans le cas de RAVE et des autres projets de grands relevés spectroscopiques dont l'objectif est d'observer plusieurs centaines de milliers d'étoiles voire des millions, l'utilisation d'instruments classiques étant impossible. En effet si l'on considère un temps de pose moyen d'une heure (overhead pour le pointage du télescope compris), un relevé de 100,000 étoiles demanderait environ 35 ans pour être réalisé. C'est pourquoi RAVE utilise un instrument multiplexé, le 6DF et son positionneur de fibre. Cet instrument permet d'obtenir jusqu'à 150 spectres en une seule pose (fig 2.2) et réduit donc considérablement le temps nécessaire pour effectuer le relevé. RAVE dispose de 3 plaques, avec chacune un réseau de 150 fibres et boutons. Pendant qu'une observation se déroule sur le ciel (une plaque montée dans le plan focal), la plaque suivante est préparée à l'aide du robot positionneur de fibres (panel de droite dans la figure 2.2). 3 plaques sont nécessaires pour une bonne opération du télescope, la plaque ayant le moins de fibres en bon état étant généralement mise en réparation. Sur l'ensemble

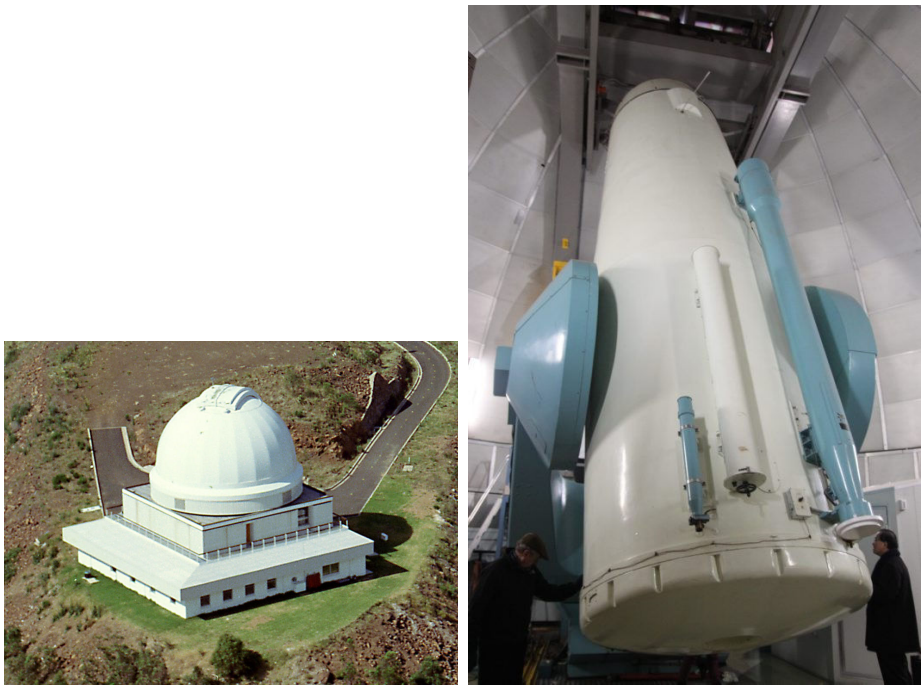

FIGURE 2.1 – A gauche : vue de la coupole du télescope UKST situé à Siding Spring, Australie. A droite : le télescope UKST de 1.2m, les plaques de fibres sont montées à la main dans le plan focal par le dessous du télescope.

du relevé, RAVE a disposé en moyenne de 100 fibres exploitables par plaque.

A l'origine, le projet RAVE avait pour ambition de mesurer les vitesses radiales pour 50 millions d'étoiles de la Voie Lactée et ce dans les deux hémisphères avec une précision meilleure que 5 km.s^{-1} . Sur la période de 10 ans prévue pour le relevé, cela nécessitait la construction de nouveaux instruments et RAVE était notamment censé disposer d'un nouveau système de type Echidna avec 4,000 fibres à positionnement rapide (quelques minutes à comparer à 1 heure nécessaire pour préparer une plaque 6dF) ainsi que de moyens similaires dans l'hémisphère nord. Néanmoins, pour des raisons extérieures au projet ces mises à niveau n'ont pas pu être réalisées et RAVE a utilisé l'instrumentation 6dF existante durant toute sa phase observationnelle.

Le projet RAVE a connu plusieurs phases que je vais décrire dans la suite, mais avant d'aborder la partie relevé, je vais décrire plus précisement le contenu et les specificités des observations.

2.1.1 Sondage de la Voie Lactée : le point de vue de RAVE

Comme nous l'avons vu plus précédemment, RAVE est un relevé spectroscopique d'étoiles de la Voie Lactée. La partie du spectre observée par RAVE est une bande d'environ 400 Angstroems autour du triplet du Calcium, de 841 à 880 nm. Les étoiles sont choisies en fonction de leur magnitude dans la bande I_c qui est la bande photométrique qui correspond à ce domaine de longueur d'onde.

La région du triplet du Calcium a la propriété de contenir trois raies très fortes (les raies du triplet) qui sont détectables même à très faible rapport signal sur bruit. C'est donc une région particulièrement adaptée aux mesures de vitesses radiales. C'est également le domaine de longueur d'onde sélectionné pour la mission *Gaia* de l'ESA qui vient de commencer ses observations scientifiques. Un exemple de spectres obtenu par RAVE est montré dans la Fig. 2.3.

Les étoiles RAVE sont sélectionnées dans l'intervalle de magnitude $9 < I_c < 13$ ce qui permet d'obtenir avec notre instrument et des temps de pose de l'ordre de 1 heure un rapport signal sur bruit d'environ 30 par pixel, suffisant pour des mesures précises de la vitesse radiale mais aussi des paramètres atmosphériques. Je reviendrai sur ce point plus en détail dans les sections suivantes. Dans cet intervalle de magnitude, RAVE sonde la Galaxie sur des distances allant de quelques parsecs jusqu'à plusieurs dizaines de kiloparsecs. Typiquement, pour une naine de type K0, RAVE les observe entre 50 et 250 pc alors qu'une géante de même type est située entre 700 pc et 3 kpc. On notera que les étoiles les plus lointaines du catalogue RAVE sont des LBV (luminous blue variable) du nuage de Magellan (Munari et al. 2009). Ainsi, RAVE permet de sonder une fraction importante du volume Galactique, principalement le voisinage solaire étendu et donc les régions de transition entre disques et disque/halo. Ce volume est complémentaire à celui étudié par le relevé SDSS-SEGUE qui, plus profond, est plus adapté à l'étude du halo Galactique.

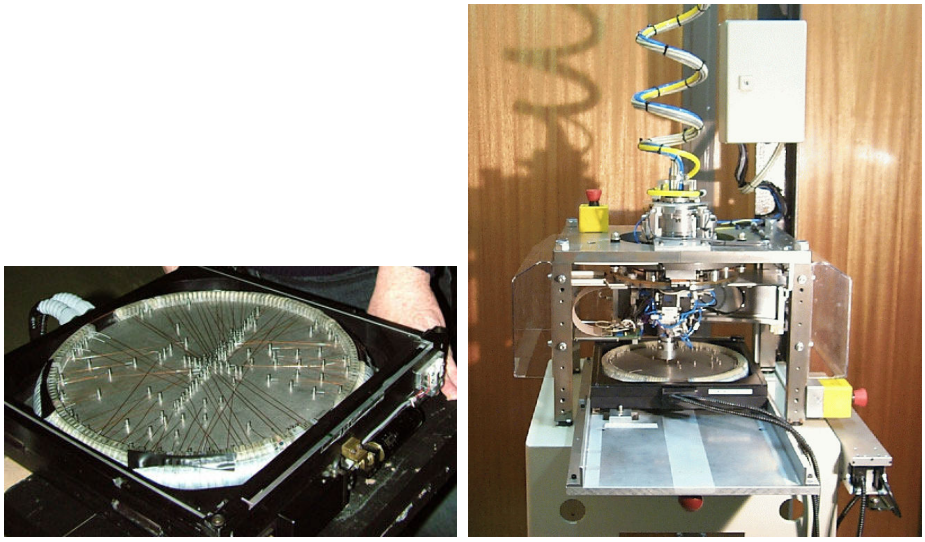

FIGURE 2.2 – A gauche : vue d'une plaque de fibres prête à être montée dans le plan focal du télescope. A droite : vue du robot positionneur de fibre. Lors d'une observation, pendant que l'intégration sur le ciel est en cours, le robot prépare la plaque suivante. Le projet RAVE dispose de 3 plaques pour palier aux temps morts dus à la réparation de fibres sur ces dernières.

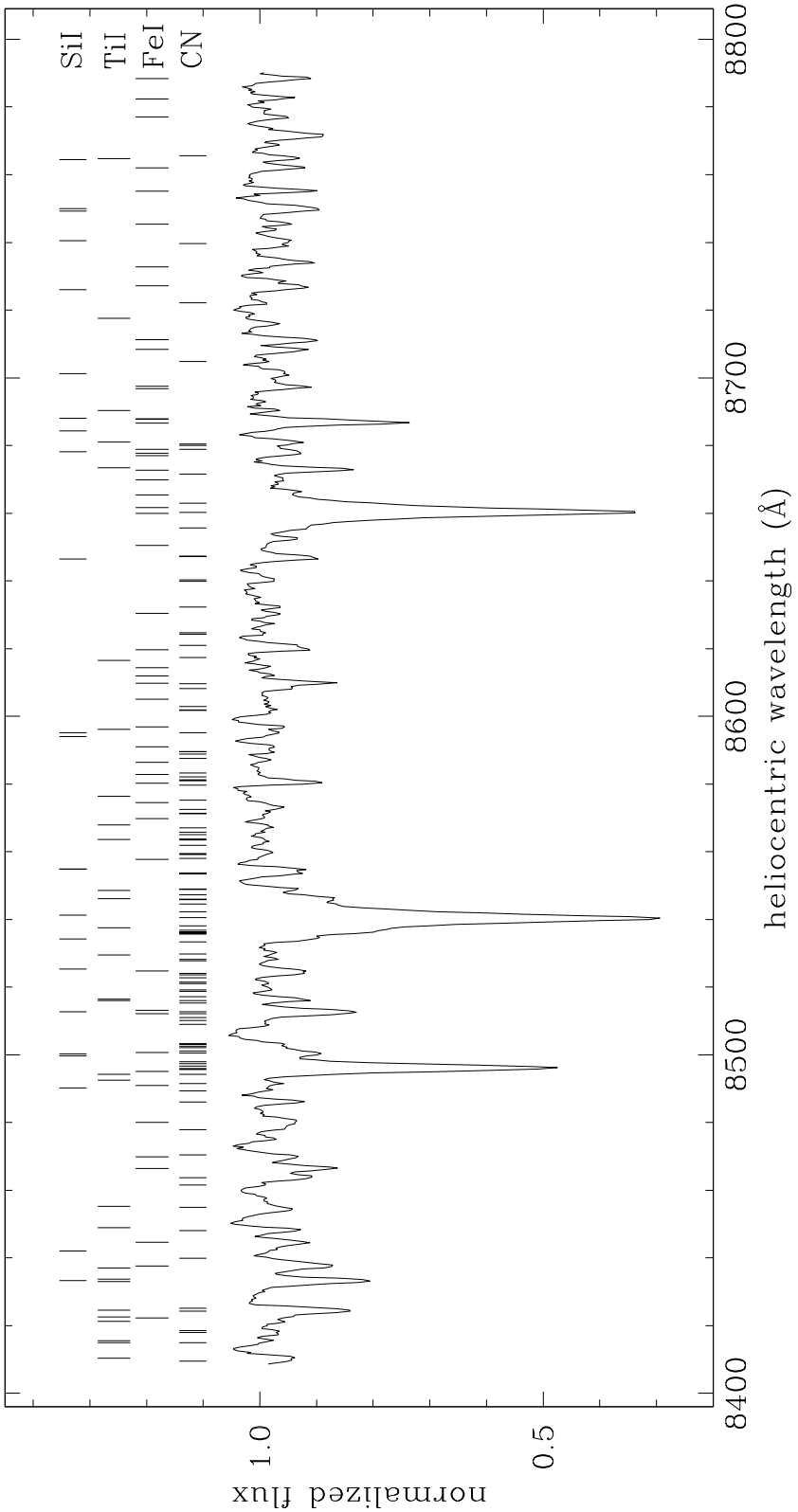

FIGURE 2.3 – Exemple de spectre obtenu par RAVE. Les trois raies proéminentes sont les raies du triplet du Calcium. Les positions des raies du fer, du silicium, du titane et de la molécule CN attendues dans ce domaine spectral sont également indiquées. D'autres raies, notamment d'éléments alpha sont aussi présentes dans les spectres RAVE. (crédit T. Zwitter)

En plus des mesures de vitesses radiales, le domaine de longueur d'onde de RAVE permet aussi des estimations de parametres atmosphériques comme la température effective, la gravité de surface ($\log g$) et la métallicité de l'étoile, [M/H] ou [Fe/H], cependant la "faible" résolution des spectres (R$\sim$ 7500) ne permet pas des mesures aussi précises que les analyses effectuées sur des spectres à plus haute résolution. Typiquement, pour une étude détaillée de la composition d'une étoile, une résolution de l'ordre de 20,000 est nécessaire. Néanmoins, les mesures obtenues par RAVE sont suffisantes pour effectuer la séparation naines/géantes ainsi que pour des analyses statistiques des catalogues associés. Ces mesures sont même suffisantes pour obtenir une estimation réaliste de la distance des étoiles (distances spectrophotométriques) si l'on adopte une méthode Bayésienne qui tient compte des erreurs (Burnett & Binney 2010; Binney et al. 2014). Comme nous le verrons par la suite, ces estimations de distance sont particulièrement utiles pour l'étude de la dynamique de la Voie Lactée car elles permettent l'étude de l'espace des phases au complet (les 6 dimensions) alors qu'en général nous ne disposons que de projections de ce dernier.

2.1.2 Le déroulement du relevé

Le projet RAVE s'est déroulé en deux phases quasiment distinctes. La première, le *pilot survey*, a été entrepris les trois premières années d'exploitation du télescope, la seconde, *le main survey*, a suivi et ce jusqu'à la fin de la phase observationnelle du relevé en 2013. Je vais détailler les différences entre ces deux phases dans la suite.

Le Pilot Survey 2003-2006

Le *pilot survey* est la phase préparatoire du projet RAVE. Elle s'est étendue sur 3 ans de mai 2003 à mars 2006 pour un total de 257 nuits d'observations (Siebert et al. 2011b). La surface sur le ciel couverte par cette phase est de 11,500 degrés carrés et le catalogue final contient plus de 83,000 spectres correspondants à plus de 77,000 étoiles (une fraction d'environ 10% est ré-observé à intervalles réguliers pour vérifier la calibration de l'instrument).

Cette phase nous a permis de développer les chaines de traitement de données adaptées aux besoins spécifiques de RAVE, l'instrument 6dF n'ayant pas été développé pour l'étude d'étoiles mais de galaxies. Cette phase s'est avérée nécessaire car le projet a dû essuyer *de nombreux plâtres* aux cours des premières années. Par exemple, la première année d'observation est contaminée par la présence de spectres du second ordre dus à l'absence de filtre bloquant la lumière bleue dans le chemin optique de l'instrument. Ce filtre n'est pas nécessaire pour la mesure de redshifts sur des spectres à basse résolution de galaxies, mais dans le cas de RAVE, avec des spectres à plus haute résolution sur un intervalle spectral restreint, cette absence génère des structures sur les spectres observés (la contamination du second ordre qui est la superposition au spectre observé du spectre à des longueurs d'ondes deux fois moindre). Cette contamination rend la mesure de la vitesse radiale moins précise et surtout empêche toute détermination fiable des paramètres atmosphériques. Ceci explique l'absence de ces derniers pour les spectres de la première année d'observation dans les catalogues RAVE.

Un autre effet qu'il a fallu apprendre à corriger est lié à la non-thermalisation de la chambre du spectrographe. Les variations de température influent sur le chemin optique suivi par la lumière et les supports des différents éléments étant sensibles à ces changements de température, elles finissent par modifier légèrement la calibration en longueur d'onde. À nouveau, ces effets sont négligeables pour l'observation de galaxies mais si l'on cherche à mesurer précisément la vitesse (à mieux que 5 $km.s^{-1}$ dans le cas de RAVE) ils ont une influence considérable. Les écarts dans la calibration en longueur d'onde peuvent atteindre 30 $km.s^{-1}$ en début ou en fin de nuit sur les bords de plaques même si l'écart pour une observation moyenne est plutôt de l'ordre de quelques $km.s^{-1}$. Ainsi une méthode a été mise au point pour corriger à postériori de ces effets. Au final, le point zéro de la vitesse radiale est contraint à 1, maximum 2 $km.s^{-1}$ pour l'ensemble du catalogue. Si ces deux exemples sont les plus marquants, d'autres effets plus mineurs ont aussi dû être pris en compte et ont conduit à des mises à jour régulières des chaînes de traitement des données.

Ensuite, il n'existait pas en 2003 de catalogue complet du ciel austral dans la bande I_c aux magnitudes sondées par RAVE. Le premier catalogue DENIS, qui était le seul disponible ne couvrait pas de manière homogène le ciel. Ainsi, pour le pilot survey, le catalogue d'entrée a été construit en se basant sur deux relevés optiques : Tycho-2(Høg et al. 2000) et le Super Cosmos Sky Survey (Hambly et al. 2001) qui est basé sur la numérisation de plaques photographiques. Le catalogue d'entrée final du projet pilote contient en tout 100,000 étoiles de l'hémisphère sud et est décrit dans le premier papier RAVE (Steinmetz et al. 2006).

La couverture finale du relevé pilote est donnée dans la figure 2.4. On notera également que les deux premières années d'observation se sont déroulées à un taux de 7 nuits par lunaison car le projet de relevé de galaxies 6dF n'était pas encore terminé. À partir de la fin 2005, RAVE a eu accès à l'intégralité du temps d'observation et a donc continué sur une base de 20 nuits par lunaison, le reste étant utilisé pour les mises à niveau du télescope et autres travaux de maintenance. Ceci explique qu'entre le DR2 et le DR3 (un an d'observation les sépare) le nombre d'objet observés a quasiment doublé.

Main Survey 2006-2013

Le relevé principal de RAVE était censé se reposer sur une nouvelle instrumentation (le système Echidna) ainsi que sur une contrepartie au nord du relevé effectué sur le UKST. Pour des raisons variées, ni la nouvelle instrumentation ni la contrepartie nord n'ont pu être réalisées. Il a donc été décidé de continuer le projet en conservant le même mode opérationnel (20 nuits par lunaison sur UKST avec 6dF) en améliorant autant que possible la qualité des spectres. Aussi, avec la fin du projet pilote, la quasi totalité du catalogue d'entrée a été observée. Un nouveau catalogue d'entrée était devenu nécessaire.

En 2005, la collaboration DENIS a publié le résultat de son relevé de l'hémisphère sud dans les bandes photométriques I_c, J et K. Ce catalogue couvre l'intervalle de magnitude de RAVE et a donc naturellement été choisi pour créer le nouveau catalogue d'entrée. Après sélection des objets répondant aux critères pour être observés par RAVE, à savoir

– $9 < I < 13$

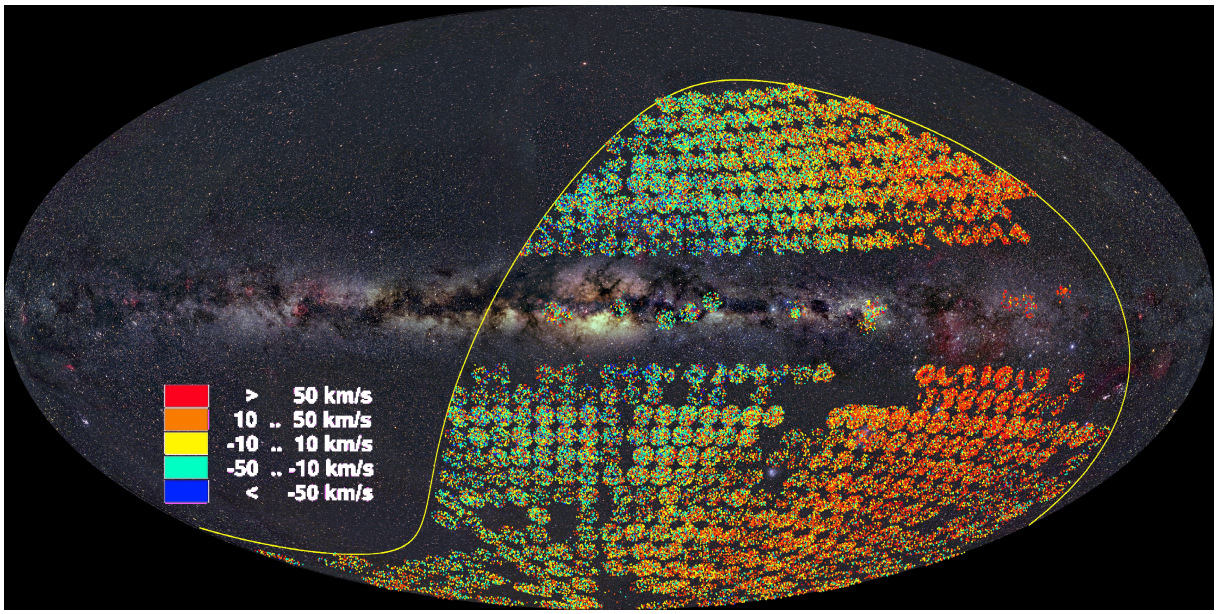

FIGURE 2.4 – Couverture finale du troisième catalogue RAVE sorti en 2011 (Siebert et al. 2011b). Chaque point correspond à un spectre observé par RAVE. Le code couleur est lié à la valeur de la vitesse radiale mesurée. Le gradient de vitesse observé est une signature du mouvement reflex du soleil le long de son orbite autour de la Galaxie. Image de fond : carte du ciel par A. Meusinger.

- $|b| > 25$
- pas de compagnon à moins de 4 arcsec
- pas d'étoile brillante à moins de 6 arcsec.

Le catalogue résultant contient 1 million d'étoiles et est la base du relevé principal de RAVE. Aussi, DENIS procure une vraie magnitude I, bien plus précise que la magnitude I construite à partir de données optiques pour le projet pilote (dans certains cas l'écart de magnitude dans la bande I de DENIS et du projet pilote peut atteindre plus d'une magnitude). Cette magnitude fiable nous a permis d'améliorer très nettement la stratégie d'observation en ne groupant sur une plaque que des étoiles de magnitude "similaire" afin de limiter le cross-talk entre les fibres et donc de diminuer le bruit résiduel sur les spectres des étoiles les moins brillantes. Le résultat de ce changement de stratégie est un bien meilleur rapport signal sur bruit des spectres RAVE et des spectres plus "propres". Ceci nous a permis d'obtenir des meilleures mesures de vitesses radiales ainsi que des paramètres atmosphériques.

Le catalogue complet de ce projet principal (DR4), auquel je suis associée a été rendu public début 2014, une version interne ayant été disponible pour les membres de la collaboration courant 2013. Ce catalogue contient l'ensemble des observations RAVE, y compris le projet pilote, et couvre la partie observable du ciel austral. La figure 2.5 montre la répartition des étoiles observées par RAVE et figurant dans le catalogue DR4 disponible soit sur le site de la collaboration soit au CDS via VizieR. On notera sur cette figure qu'en plus du nouveau catalogue d'entrée, certaines régions ont bénéficié d'amendements au catalogue original. Ceci est principalement dû au manque d'objets à observer dans les régions observables en hiver vers la fin du projet. Par exemple, des régions plus proches du plan ont été ajoutées loin du bulbe en ajoutant un critère en couleur pour favoriser les étoiles géantes.

Néanmoins, si les critères peuvent paraître compliqués, le catalogue RAVE est, en dehors de ces quelques régions spécifiques, libre de tout biais cinématique. En effet, chaque observation RAVE, en fait chaque plaque est un tirage aléatoire des étoiles du catalogue d'entrée (qui est complet) dans l'intervalle de magnitude séléctionné. Ceci est très important car cela va nous permettre d'utiliser ce catalogue pour l'étude de la dynamique du disque qui est la base de cette thèse.

2.2 Contenu du catalogue DR4

Au début de cette thèse nous nous sommes basés sur le catalogue DR3 présenté plus haut, le catalogue DR4 a rapidement été disponible pour la collaboration, d'abord sous forme de tables séparées puis sous forme de catalogue complet peu avant la publication du catalogue final. Je ne décrirai donc ici que le catalogue le plus récent. La différence principale avec les versions précedentes est une nouvelle détermination des paramètres atmosphériques bases sur les algorithme MATISSE et DEGAS (Recio-Blanco et al. 2006; Bijaoui et al. 2012, voir section suivante). En effet, les paramètres estimés par la chaine de traitement de RAVE nécessite une calibration de la métallicité afin de concorder avec les mesures effectuées à haute résolution. C'est également le cas des algorithmes cités plus hauts mais la relation de calibration est plus fine et donc engendre moins d'erreur résiduelle. Il a donc été choisi

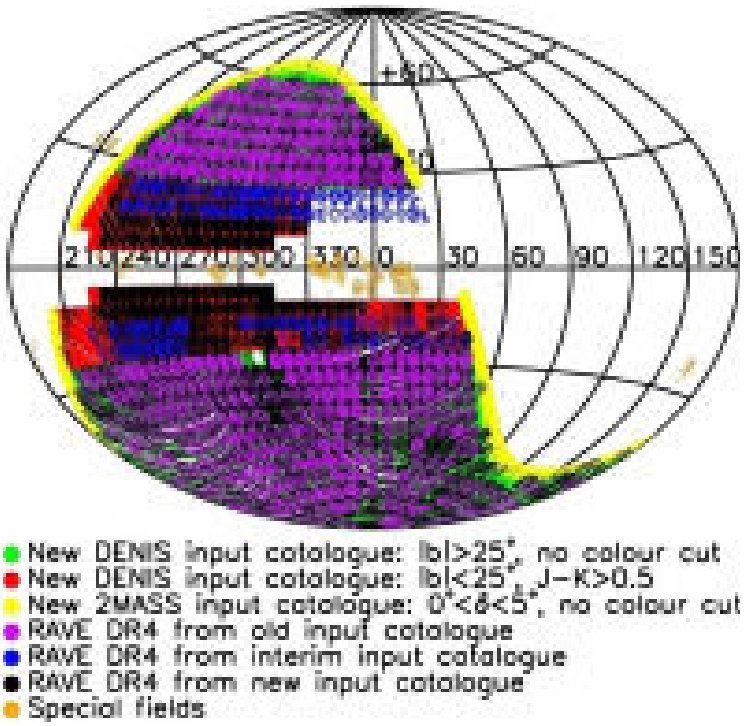

FIGURE 2.5 – Répartition des étoiles du DR4 de RAVE en coordonnées galactiques. Les différentes couleurs correspondent au catalogue d'entrée d'origine de l'étoile observée. Ce relevé couvre quasiment 20 000 degrés carrés et contient près de 500 000 mesures.

d'utiliser ces méthodes pour le projet RAVE. Ces nouveaux paramètres atmosphériques, plus précis, ont aussi pour conséquence de fournir des mesures de distance moins biaisées et donc nous permettent une analyse plus fine de l'espace des phases. Pour ce qui est des vitesses radiales, le traitement est resté inchangé même si on note une nette amélioration de la précision en fonction du temps (fig 29 de l'article présenté dans la section suivante). Cette amélioration qui permet d'obtenir une erreur interne inférieure à 1 $km.s^{-1}$ est entièrement dû aux améliorations dans la procedure d'observation (réduction du cross-talk, meilleur contrôle des écarts de température etc.).

Ainsi, le catalogue utilisé pour ce travail contient des mesures non seulement de vitesses radiales mais également de la température effective, de la gravité, de la métallicité, de la classification spectrale et d'abondances chimiques des étoiles et cela pour près d'un demi-million d'objets. A l'aide de ces mesures "originales", au sens qu'elles sont effectuées directement sur les spectres, une mesure de distance, d'âge et d'extinction est également fournie via la méthode bayésienne de Burnett & Binney (2010).

Pour les études de cinématique galactique, nous cherchons avant tout à reconstruire l'espace des phases. Pour cela, une mesure de la vitesse tangentielle est nécessaire. Cette information est fournie par les mesures de mouvements propres qui ne sont pas mesurés par RAVE. Néanmoins, des catalogues de mouvements propres couvrant le domaine d'observation de RAVE sont disponibles (magnitudes et position sur le ciel). Un travail d'identifications croisées a été effectué par la collaboration et le catalogue final contient les mesures de mouvements propres de Tycho-2, PPMXL (Roeser et al. 2010), et UCAC2 3 et 4 (Zacharias et al. 2004, 2010, 2013) pour les objets en commun. Ces identifications croisées sont basées uniquement sur la position. Une description complète du catalogue DR4 de RAVE est fournie dans la table 7 du papier présenté dans la section suivante.

Avec ces mesures de mouvements propres combinées aux mesures de RAVE (distances et vitesses radiales) il nous est alors possible d'obtenir l'information complète dans l'espace des phases des étoiles RAVE, et combinées aux mesures d'âge et de métallicité, d'étudier en détail la variation du champ de vitesse dans le disque. C'est l'objet de cette thèse qui va être développé dans les deux chapitres suivants.

2.3 Les résultats RAVE qui ont motivé nos recherches

Parmi les résultats les plus marquants que le relevé RAVE a permis de mettre à jour, il y a celui de Siebert et al. (2011a) dans lequel, en étudiant des étoiles à une distance de 2 kpc du Soleil (distances estimées par Zwitter et al. (2010)), ils ont trouvé un gradient de vitesse radiale dont l'origine suspectée serait celle d'une perturbation non-axisymétrique du disque (fig 2.6 en haut). Williams et al. (2013) ont eux aussi mis en évidence un gradient de vitesse verticale en travaillant sur les étoiles du *red clump*. Ils ont montré qu'un mouvement de compression avait lieu en dehors du cercle solaire et un mouvement d'expansion avait lieu juste avant de façon similaire à un *breating mode* (fig 2.6 en bas).

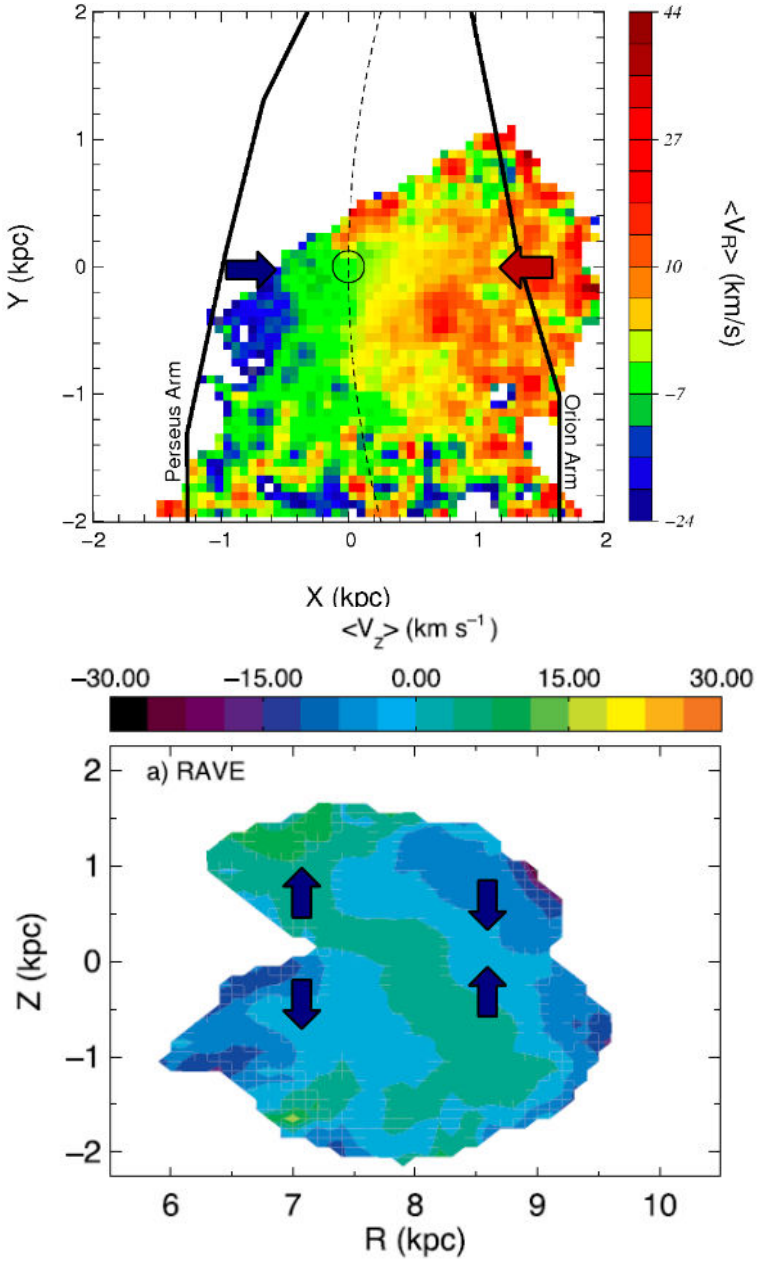

FIGURE 2.6 – Gradients de vitesse observés par le relevé RAVE. En haut, gradient en vitesse Galactocentrique radiale dans le plan Galactique. Le Soleil se situe au centre du cercle en (0,0) et le centre Galactique se trouve à 8 kpc en X positif, crédit : Siebert et al. (2011). En bas, gradient en vitesse Galactocentrique verticale dans le plan méridien, crédit : Williams (2013). Les flèches sont rajoutées pour souligner le mouvement des étoiles.

On s'est aussi aperçu en échantillonnant les données RAVE que certaines populations d'étoiles ne subissaient pas les mêmes gradients de vitesse. L'exemple le plus flagrant reste le

cas de la métallicité où les étoiles les plus riches (fig.2.7 en bleu à gauche) subissent un plus fort gradient alors que les étoiles les plus pauvres en métaux ont une vitesse radiale moyenne plus grande mais sont moins affectées. On retrouve le même comportement avec des groupes d'âges différents mais il est moins marqué. Les étoiles jeunes sont les plus affectées (fig.2.7 en bleu à droite), ce qui n'est pas si étonnant puisque les étoiles les plus jeunes sont souvent les plus riches en métaux (fig.2.7 en bas).
La différence de traitement entre les groupes d'étoiles partageant les mêmes caractéristiques semble être l'indice qu'un mécanisme interne (comme les bras spiraux) "trie" ces étoiles.
L'échantillon se compose d'étoiles normales ayant un spectre pour lesquelles leur ratio signal/bruit est mieux que 20 pixel^{-1}. Leur vitesse radiales héliocentrique ne dépassent pas 600 km.s^{-1} en absolu et 400 mas yr^{-1} pour leurs mouvements propres. Les erreurs sur leurs vitesses et mouvements propres sont inférieurs à 8 km.s^{-1} et 7 mas yr^{-1}.

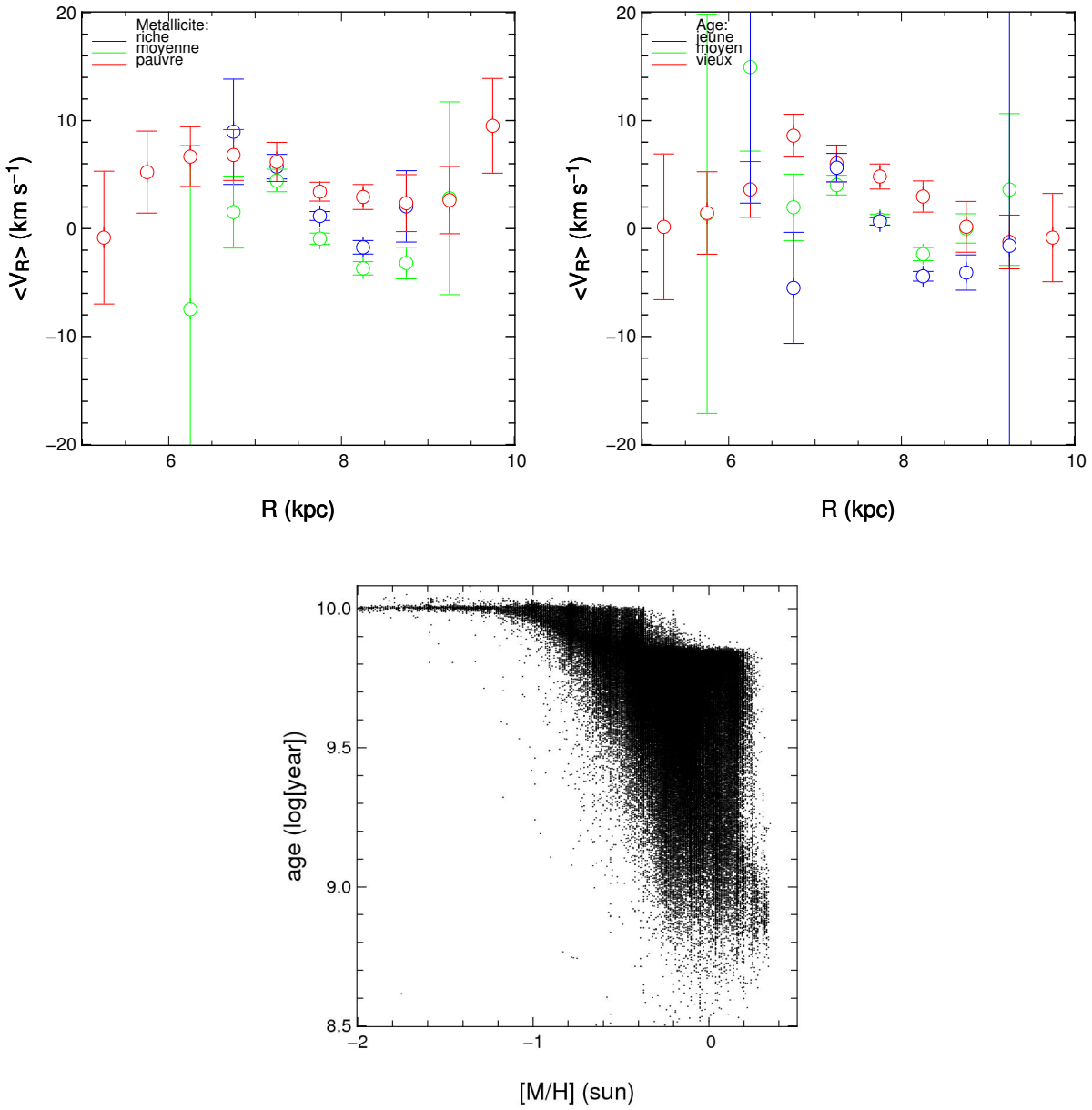

FIGURE 2.7 – Gradients de vitesses radiales galactocentriques en fonction du rayon. À gauche : pour la métallicité avec des intervalles de [-1,-0.6] (en rouge), [-0.25,-0.2] (en vert) et [0.1,0.25] (en bleu). À droite : pour des classes d'âges avec des intervalles de [8.75,9.25] (en bleu), [9.63,9.67] (en vert) et [9.9,10] (en rouge). En bas : diagramme âge - métallicité

Publication DR4

The Astronomical Journal, 146:134 (36pp), 2013 November doi:10.1088/0004-6256/146/5/134

THE RADIAL VELOCITY EXPERIMENT (RAVE): FOURTH DATA RELEASE

G. Kordopatis[1], G. Gilmore[1], M. Steinmetz[2], C. Boeche[3], G. M. Seabroke[4], A. Siebert[5], T. Zwitter[6,7], J. Binney[8], P. de Laverny[9], A. Recio-Blanco[9], M. E. K. Williams[2], T. Piffl[2], H. Enke[2], S. Roeser[3], A. Bijaoui[9], R. F. G. Wyse[10], K. Freeman[11], U. Munari[12], I. Carrillo[2], B. Anguiano[13,14], D. Burton[11,15], R. Campbell[16], C. J. P. Cass[15], K. Fiegert[15], M. Hartley[15], Q. A. Parker[13,14,17], W. Reid[14,17], A. Ritter[18], K. S. Russell[15], M. Stupar[15], F. G. Watson[15], O. Bienaymé[5], J. Bland-Hawthorn[19], O. Gerhard[20], B. K. Gibson[21], E. K. Grebel[3], A. Helmi[22], J. F. Navarro[23], C. Conrad[2], B. Famaey[5], C. Faure[5], A. Just[3], J. Kos[6], G. Matijevič[6], P. J. McMillan[8], I. Minchev[2], R. Scholz[2], S. Sharma[19], A. Siviero[2], E. Wylie de Boer[11], and M. Žerjal[6]

[1] Institute of Astronomy, University of Cambridge, Madingley Road, Cambridge, CB3 0HA, UK; gkordo@ast.cam.ac.uk
[2] Leibniz-Institut für Astrophysik Potsdam, An der Sternwarte 16, D-14482 Potsdam, Germany
[3] Astronomisches Rechen-Institut, Zentrum für Astronomie der Universität Heidelberg, Mönchhofstr. 12-14, D-69120 Heidelberg, Germany
[4] Mullard Space Science Laboratory, University College London, Holmbury St. Mary, Dorking, Surrey, RH5 6NT, UK
[5] Observatoire Astronomique de Strasbourg, Université de Strasbourg, CNRS, UMR 7550, 11 rue de l'Université, F-67000 Strasbourg, France
[6] Faculty of Mathematics and Physics, University of Ljubljana, Jadranska 19, 1000 Ljubljana, Slovenia
[7] Center of Excellence SPACE-SI, Askerceva cesta 12, 1000 Ljubljana, Slovenia
[8] Rudolf Peierls Centre for Theoretical Physics, Keble Road, Oxford, OX1 3NP, UK
[9] Laboratoire Lagrange, UMR 7293, Université de Nice Sophia Antipolis, CNRS, Observatoire de la Côte d'Azur, BP4229, F-06304 Nice, France
[10] Johns Hopkins University, 3400 North Charles Street, Baltimore, MD 21218, USA
[11] Research School of Astronomy and Astrophysics, Australian National University, Cotter Road, Weston, ACT 2611, Australia
[12] INAF National Institute of Astrophysics, Astronomical Institute of Padova, I-36012 Asiago (VI), Italy
[13] Australian Astronomical Observatory, P.O. Box 915, North Ryde, NSW 1670, Australia
[14] Department of Physics and Astronomy, Macquarie University, Sydney, NSW 2109, Australia
[15] Anglo-Australian Observatory, P.O. Box 296, Epping, NSW 1710, Australia
[16] Western Kentucky University, Bowling Green, KY 42101, USA
[17] Macquarie Research Centre for Astronomy, Astrophysics and Astrophotonics, Sydney, NSW 2109, Australia
[18] National Central University, 300 Zhongda Road, Zhongli City, Taoyuan County 325, Taiwan, Republic of China
[19] Sydney Institute for Astronomy, School of Physics A28, University of Sydney, NSW 2006, Australia
[20] Max-Planck-Institut fuer Ex. Physik, Giessenbachstrasse, D-85748 Garching b. Muenchen, Germany
[21] Jeremiah Horrocks Institute, University of Central Lancashire, Preston, PR1 2HE, UK
[22] Kapteyn Astronomical Institute, University of Groningen, P.O. Box 800, NL-9700 AV Groningen, The Netherlands
[23] Department of Physics and Astronomy, University of Victoria, Victoria, BC, Canada
Received 2013 July 11; accepted 2013 September 2; published 2013 October 17

ABSTRACT

We present the stellar atmospheric parameters (effective temperature, surface gravity, overall metallicity), radial velocities, individual abundances, and distances determined for 425,561 stars, which constitute the fourth public data release of the RAdial Velocity Experiment (RAVE). The stellar atmospheric parameters are computed using a new pipeline, based on the algorithms of MATISSE and DEGAS. The spectral degeneracies and the Two Micron All Sky Survey photometric information are now better taken into consideration, improving the parameter determination compared to the previous RAVE data releases. The individual abundances for six elements (magnesium, aluminum, silicon, titanium, iron, and nickel) are also given, based on a special-purpose pipeline that is also improved compared to that available for the RAVE DR3 and Chemical DR1 data releases. Together with photometric information and proper motions, these data can be retrieved from the RAVE collaboration Web site and the Vizier database.

Key words: catalogs – stars: abundances – stars: fundamental parameters – surveys – techniques: spectroscopic

Online-only material: color figures

1. INTRODUCTION

The assembly history of the Milky Way can be obtained by analyzing the positions, kinematics, ages, and chemical compositions of large statistical samples of Galactic stars (Freeman & Bland-Hawthorn 2002). In addition to the identification and characterization of hierarchical signatures (e.g., Helmi et al. 1999; Abadi et al. 2003; Sales et al. 2009), the precise measurement of the age–metallicity relation in the solar neighborhood, for a very large sample of stars, allows us to establish, among much else, the strength and the importance of radial migration in the Galaxy, perhaps a key ingredient for Galactic evolution (Sellwood & Binney 2002; van der Kruit & Freeman 2011).

Ideally, one would need stellar spectra and precise distances to achieve such a goal. Nevertheless, even in the case where parallaxes are not available, it is still possible to estimate statistically valuable ages and distances of the stars by measuring from their spectra their atmospheric parameters (effective temperature, $T_{\rm eff}$, surface gravity, $\log g$, overall metallicity, [M/H][24]) and projecting them afterward on theoretical stellar isochrones (Breddels et al. 2010; Zwitter et al. 2010; Burnett et al. 2011; Kordopatis et al. 2011b; Binney et al. 2013).

In the past decade, the advent of multi-fiber spectrographs, combined with large telescopes, has allowed the astronomical community to obtain such very large amounts of spectra in order to explore the evolution of our Galaxy. Until the release of the first substantial catalog of *Gaia* (estimated to be available in

[24] The stellar overall metallicity is defined as $[{\rm M/H}] = \log(N(M)/N(H))_{\star} - \log(N(M)/N(H))_{\odot}$, where N represents the number density and M all the elements heavier than He.

early 2017), the already current main large spectroscopic surveys of the Milky Way are the Sloan Extension for Galactic Understanding and Exploration (SEGUE), the RAdial Velocity Experiment (RAVE), the APO Galactic Evolution Experiment (APOGEE), the LAMOST Experiment for Galactic Understanding and Exploration (LEGUE), the GALactic Archaeology with HERMES (GALAH), and the Gaia–ESO Survey (GES).

RAVE[25] began observations in 2003, and since then it has released three data releases (hereafter DR): DR1 in 2006, DR2 in 2008, and DR3 in 2011 (Steinmetz et al. 2006; Zwitter et al. 2008; Siebert et al. 2011b). Furthermore, three catalogs with spectrophotometrically derived distances were published (Breddels et al. 2010; Zwitter et al. 2010; Burnett et al. 2011), and one catalog with abundances for the individual elements magnesium (Mg), aluminum (Al), silicon (Si), calcium (Ca), titanium (Ti), iron (Fe), and nickel (Ni; Boeche et al. 2011). RAVE is a magnitude-limited survey of stars randomly selected in the southern celestial hemisphere. The original design was to only observe stars in the interval $9 < I < 12$, but the actual selection function includes stars both brighter and fainter (see Section 2). The spectra are obtained from the 6dF facility on the 1.2 m Anglo-Australian Observatory's Schmidt telescope in Siding Spring, Australia, where three field plates with 150 robotically positioned fibers are used in turn. The effective resolution of RAVE is $R = \lambda/\Delta\lambda \sim 7500$, and the wavelength range coverage is around the infrared ionized Calcium triplet (IR Ca II, $\lambda\lambda$8410–8795), one of the widely used wavelength ranges for Galactic archaeology. Up to now, previous RAVE catalogs have released 83,072 radial velocities for 77,461 stars, and 41,672 sets of atmospheric parameters for 39,833 stars. These produced many valuable studies.

Seabroke et al. (2008) used the symmetry of the velocity distributions to rule out the presence of the Sagittarius stream or the Virgo overdensity in the solar neighborhood. Recently, RAVE data allowed Williams et al. (2011) to discover the Aquarius stream and Antoja et al. (2012) to identify additional moving groups in the Galactic disk, consistent with dynamical models of the effects of the bar and the spiral arms. Pasetto et al. (2012a, 2012b) used RAVE data in order to constrain the solar motion relative to the local standard of rest, the rotational lag of the thick disk component, and the components of the thin disk velocity ellipsoids in the solar neighborhood. Additionally, Siebert et al. (2011a, 2012) measured the mean galactocentric radial velocity (RV) of stars in the extended solar neighborhood and constrained the parameters of Milky Way spiral structure. Williams et al. (2013) identified differences in the velocity distribution between the north and the south of the Galactic plane with indications of a rarefaction-compression pattern, suggestive of wave-like behavior. Furthermore, Ruchti et al. (2011), Wilson et al. (2011), and Fulbright et al. (2010) studied the chemo-dynamical information of the thick disk and metal-poor stars of the Galaxy, whereas Matijevič et al. (2010, 2011) used RAVE to study single-lined and double-lined binary stars.

Here we present the new DR4 catalog, which includes 482,430 spectra. In order to obtain the atmospheric parameters, an updated version of the Kordopatis et al. (2011a) pipeline is used, which combines the DEGAS decision-tree method (*DEcision tree alGorithm for AStrophysics*; Bijaoui et al. 2012) and the MATISSE projection algorithm (*MATrix Inversion for Spectral SynthEsis*; Recio-Blanco et al. 2006) and takes into account, for the first time, the Two Micron All Sky Survey (2MASS) photometric information. This allows us to treat more efficiently the spectral degeneracies than the maximum a posteriori method used in the previous data releases, reducing parameter combinations that were found in astrophysically non-justified parts of the ($T_{\rm eff}$–log g) space.

Furthermore, this DR4 catalog takes advantage of a multitude of new calibration data sets that have been collected recently in order to obtain reliable metallicities. The calibration libraries consist of RAVE and RAVE-like spectra for which there are parameter determinations derived from high-resolution spectroscopy, as well as stars selected from open and globular clusters of well-known metallicities. In addition to the stellar atmospheric parameters published for the newly observed targets, these calibration spectra and the new pipeline have also been applied in order to re-estimate and re-calibrate the parameters from the previous data releases. Then, given the new effective temperatures, surface gravities, and metallicities, individual abundances are also computed for the entire data set, using an updated version of the Boeche et al. (2011) chemical pipeline. Finally, new distances are also inferred, using the methods presented in Zwitter et al. (2010) and Binney et al. (2013).

The paper is structured as follows: first, in Section 2 we present the new input catalog of RAVE, and in Section 3 we present the pipeline that is used in order to obtain the atmospheric parameters, by recalling the basic equations and the updates of the MATISSE and DEGAS algorithms that are in the core of this new parameterization pipeline. Then, in Section 4, we show which calibration data sets are used and discuss how the calibration relation is obtained. Section 5 presents the updates on the chemical pipeline that is used in order to measure the individual abundances. Based on the presented pipelines and the calibration relation that is established, we present in Section 6 the DR4 atmospheric parameter catalog, as well as a comparison with the previous DR3 parameters, in particular for the metallicities. Sections 7, 8, 9, and 10 present the DR4 catalog for the proper motions, the radial velocities, and the stellar distances, as well as a description of the AAVSO Photometric All-Sky Survey (APASS) photometry, which is recommended to be used as it becomes available. Finally, Section 11 provides a summary.

2. NEW RAVE INPUT CATALOGS

The RAVE wavelength window of 8410–8795 Å implies that an *I*-band selection of the targets is the most appropriate. However, when RAVE started observing in 2003 April, there was no southern sky *I*-band photometric survey spanning the RAVE magnitude range. Therefore, the original input catalog was constructed by deriving *I* magnitudes from Tycho-2 photometry and filling in Tycho-2's incompleteness at the faint end of the RAVE magnitude range with SuperCOSMOS photographic *I* magnitudes (see DR1 paper for more details). The DEep Near Infrared Survey of the Southern Sky (DENIS) DR2 was available in 2005 May (DENIS Consortium 2003), which included Gunn-*I* photometry at 0.82 nm, but did not have sufficient coverage (55% of the southern sky) to be used as the basis for a new RAVE input catalog. RAVE DR1, DR2, and DR3 were solely observed from the original input catalog. DR3 was the last release to be solely observed from the original input catalog, thereby concluding the pilot survey.

DENIS DR3 was available in 2005 September (DENIS Consortium 2005) and did have sufficient coverage (80% of the southern sky) to be used as the basis for a new RAVE

[25] http://www.rave-survey.org

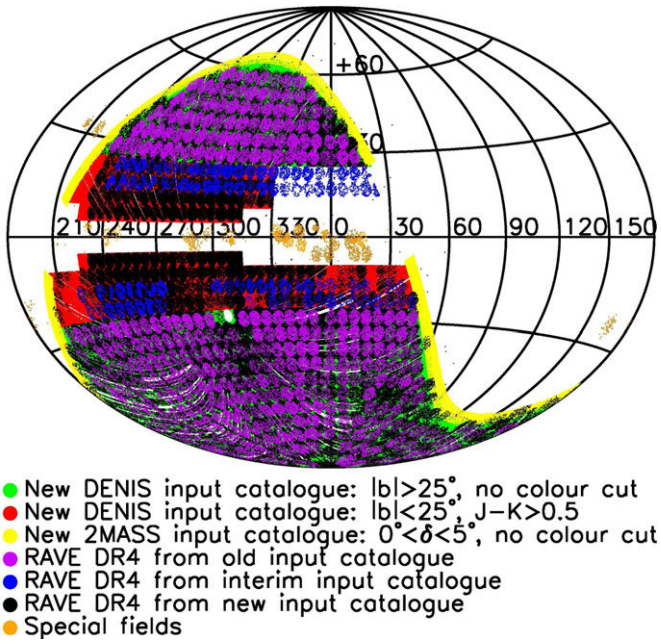

Figure 1. Aitoff projection of Galactic coordinates of the new input catalogs, color-coded into no color cut and color cut samples. Overlaid are the RAVE DR4 stars, color-coded according to their source input catalog. Their pattern is due to the 6dF field of view (5.°9). The original input catalog was observed with field center coordinates separated by 5.°7. The new input catalog was observed with field center coordinates separated by 5.°0.

(A color version of this figure is available in the online journal.)

input catalog. DENIS entries within the RAVE magnitude range ($9 < I < 12$ mag) were selected, including saturated entries (DENIS saturates at $I < 9.8$ mag—see later discussion). Entries with I magnitude error $= 1$ indicate a non-estimated error, so these entries were rejected. Then the remaining entries were cross-matched with 2MASS using a 1 arcsec box search. This search region was chosen because both DENIS and 2MASS were calibrated on the USNO-A2.0 catalog, which has an astrometric accuracy of 0.5 arcsec. The nearest DENIS DR3 catalog entry to a 2MASS star provided the I magnitude for that star (2MASS does not include I-band photometry). DENIS catalog entries not within a 1 arcsec search box of a 2MASS star were rejected.

At the edges of the DENIS CCD detector, both the astrometry and photometry become less accurate. For each different scan of DENIS strip overlap regions, the catalog reports every detection of a source. If a star in this region is imaged more than once, each detection is included in the catalog because, although the multiple detections have almost identical magnitudes and positions, they cannot be associated with the same source. Cross-matching DENIS with 2MASS not only removes these multiple detections from the new input catalog but also provides more accurate astrometry, leading to fiber placement better matching stellar positions on the sky, which results in higher signal-to-noise spectra. DENIS includes spurious sources due to charge bleeding and diffraction spikes, which do not have matches in 2MASS and so are removed from the new DENIS input catalog, increasing its efficiency.

Comparison of Figure 1 with Figure 17 of Siebert et al. (2011b) shows that, in addition to covering the sky area of the original RAVE input catalog, the new DENIS input catalog has the major new feature of extending to lower Galactic latitudes (b). The aim of the extension toward the Galactic anti-rotation direction ($225° < l < 315°$, $5° < |b| < 25°$) is to observe the outer Galactic disk. Distances probed at the faint magnitude limit ($I = 12$ mag) are expected to be up to ∼5 kpc for K-type giants (assuming $M_I = +1$ mag and no extinction). Therefore, at low Galactic latitudes in this direction, giants just reach the nominal "edge" of the stellar disk. Symmetric sampling about the Galactic plane will constrain the disk warp and flare. Distances probed at $I = 12$ mag are only up to ∼400 pc for G-type dwarfs (assuming $M_I = +4$ mag). Therefore, the most efficient way to observe the outer disk is to apply a color cut ($J - K > 0.5$ mag) in this region to avoid observing G-type dwarfs and preferentially observe K-type giants. The Besançon Galactic model (Robin et al. 2003) predicts that in the RAVE magnitude range at $J - K > 0.5$ mag 70% of stars are KM-type giants and 30% are KM-type dwarfs. Although DENIS includes J and K photometry, the color cut is performed using 2MASS J and K. This is because of the aforementioned edge effect on the DENIS CCDs and due to higher levels of sky image noise in DENIS than 2MASS. The noise comes from the thermal infrared background radiation emitted by the instrument itself. 2MASS optics avoid this by including a cold stop, which DENIS optics do not have.

After observing the new DENIS input catalog from 2006 to 2010, more targets closer to the Galactic plane were required to maintain RAVE's observing efficiency due to sky regions not always being observable from the UK Schmidt Telescope at different times of the year. The aim was still to target red giants by selecting $J - K > 0.5$ mag, thereby rejecting young foreground stars, which have weak Paschen lines that yield less accurate radial velocities. This selection works with reddening of $E(B-V) < 0.35$ mag. Therefore, to preserve a homogeneous selection function with this color cut, the new DENIS input catalog was extended closer to the Galactic plane in regions where $E(B-V) < 0.35$ mag. The northern Galactic hemisphere of the Galactic bulge has $E(B-V) > 0.35$ mag, and so $b < 25°$ at $l > 330°$ and $l < 30°$ is not included in the new extended DENIS input catalog. $10° < b < 25°$ at $l < 225°$ and at $315° < l < 330°$ has $E(B-V) < 0.35$ mag and so is included. In the southern hemisphere of the bulge, $-10° < b < -25°$ at $l < 225°$, $l > 315°$, and $l < 30°$ all have $E(B-V) < 0.35$ mag and so are included.

DR4 includes observations of the interim input catalog, which extended the original input catalog from $|b| < 25°$ to $|b| < 15°$ at all l. These observations were taken before the new DENIS input catalog was available, which is why they sample the northern bulge (blue dots in Figure 1) outside of the new extended DENIS input catalog color cut footprint (red dots in Figure 1). However, there are many observations of the interim input catalog (blue dots in Figure 1) within the color cut footprint. It is important to note that these do not include the color cut and so include all colors. These fields can be identified using the Galactic coordinates in Figure 1 and obsdate ⩽20060312. The special fields outside of the color cut footprint (orange dots in Figure 1) are specific science and calibration fields and do not include the color cut.

More bright targets north of the celestial equator ($\delta \leqslant 5°$) were required, again, to maintain RAVE's observing efficiency in bright time. DENIS's sky coverage is $\delta \leqslant 2°$. Therefore, to extend the input catalog to $\delta = 5°$ required DENIS I to be constructed from 2MASS J and K using

$$I_{\rm DENIS} = J_{\rm 2MASS} + 0.054 + 1.18(J_{\rm 2MASS} - K_{\rm 2MASS}), \quad (1)$$

where $\Delta_{\rm DENIS} = 0.15$ mag. This was done for 2MASS sources with $0° \leqslant \delta \leqslant 5°$ and $0^{\rm h} < \alpha < 6^{\rm h}$, $7^{\rm h}30 < \alpha < 17^{\rm h}$, and

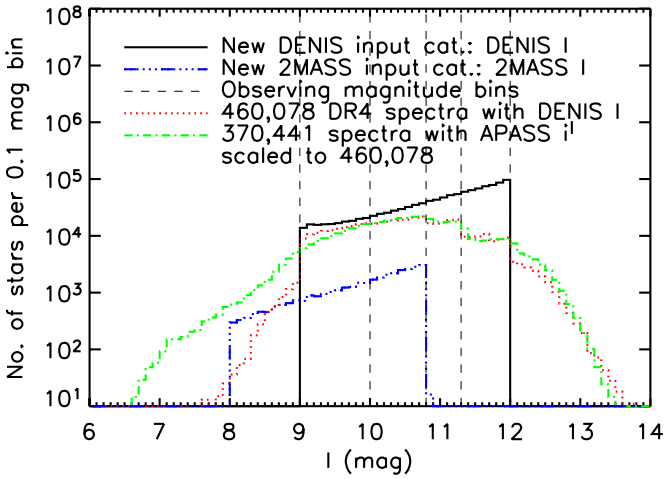

Figure 2. Histogram comparing the new input catalogs as a function of I magnitude and the selection functions of all the observed RAVE stars as a function of I magnitude and as a function of APASS i' magnitude, which is similar but not identical to DENIS I.

(A color version of this figure is available in the online journal.)

$19^h30 < \alpha < 24^h$ (yellow dots in Figure 1) to avoid the Galactic plane. The 2MASS input catalog spatially overlaps the DENIS input catalog by $\Delta\delta = 3°$ because DENIS's sky coverage is not complete. The long white areas within the colored regions in Figure 1 are one or more slots (12 arcmin in α by 30° in δ), where the observed DENIS strips filling these slots are missing from DENIS DR3. The small white areas within the colored regions are one or more missing DENIS images (12 arcmin × 12 arcmin). The white circular region within the colored regions is the southern equatorial pole, which is not observed by DENIS. The width of the missing DENIS strips and images is 3.5% of the 6dF field of view and so does not pose a fiber configuration problem. Its effect on RAVE's random selection of targets should be negligible. It is important to note that observations from the 2MASS input catalog at $|b| > 25°$ do not include the color cut and so include all colors. Figure 1 shows that there are only three DR4 fields that spatially overlap the DENIS input catalog color cut footprint and the 2MASS input catalog footprint and so have mixed selection functions.

Figure 2 compares the new input catalogs and the number of observed DR4 spectra as a function of I magnitude. It emphasizes that the observed DR4 spectra have not exhausted the new DENIS input catalog overall and so are not complete with respect to DENIS overall, although individual fields may be complete. Indeed, the new DENIS input catalog is only complete where DENIS has sky coverage. DR4's completeness with respect to 2MASS is shown in Figure 3. Figure 2 also shows that the 2MASS input catalog extends the bright limit of the survey to $I = 8$ mag. Each 6dF field setup only selects new input catalog targets from one of the following four magnitude bins: $9.0 < I < 10.0$ ($8.0 < I < 10.0$ for the new 2MASS input catalog), $10.0 < I < 10.8$, $10.8 < I < 11.3$, and $11.3 < I < 12$ mag, which are visible in Figure 2. This minimizes the magnitude range within any one 6dF field setup to be within a bin, meaning exposure times can be scaled more appropriately for all the targets in the same field. Each field

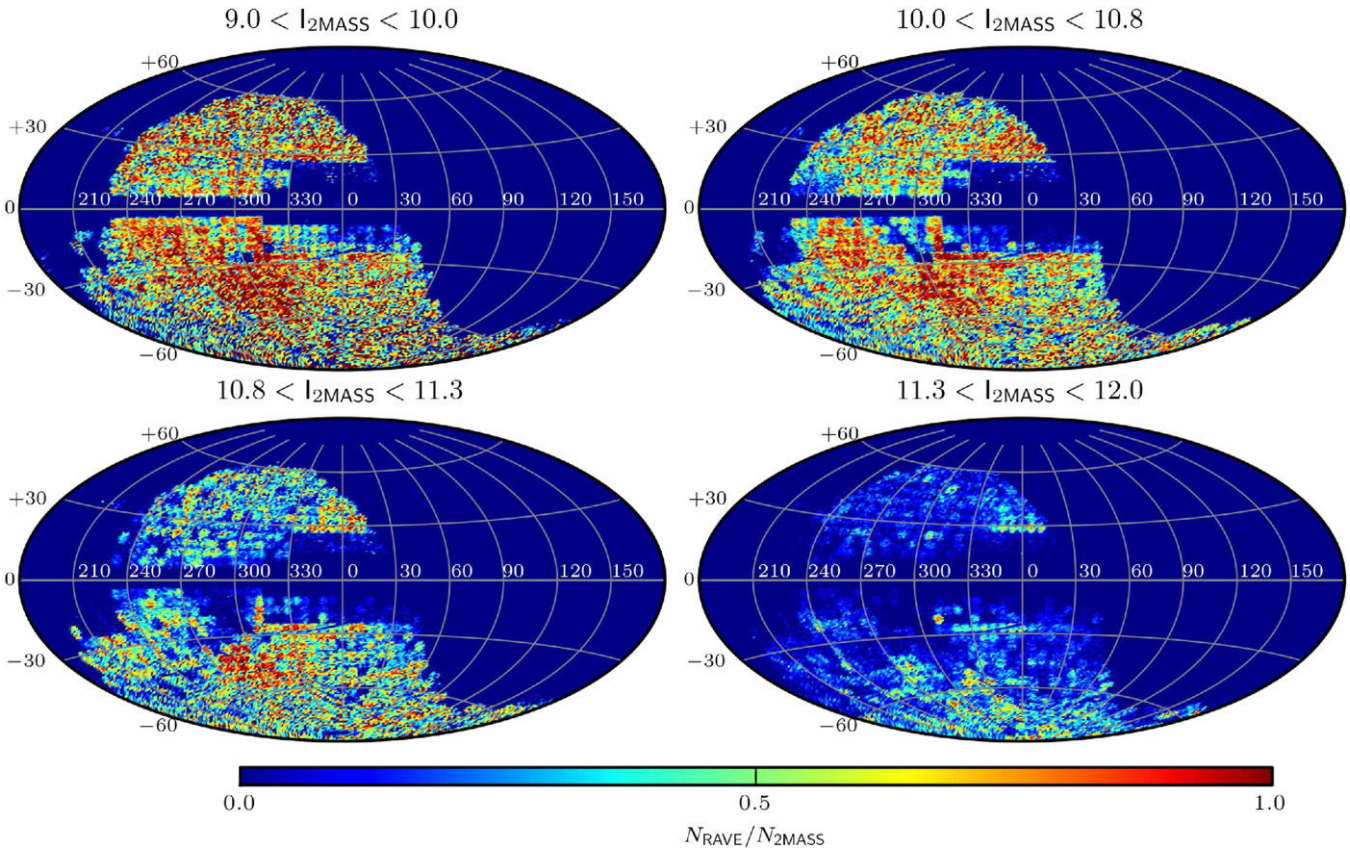

Figure 3. Aitoff projection of Galactic coordinates of the completeness of the stars in the I_{2MASS} band for which radial velocity measurements are available. Each panel shows a different magnitude bin. Gray-scale coding represents the ratio of RAVE observations to 2MASS stars. Only stars with errors in radial velocity less than 10 km s^{-1} are shown.

(A color version of this figure is available in the online journal.)

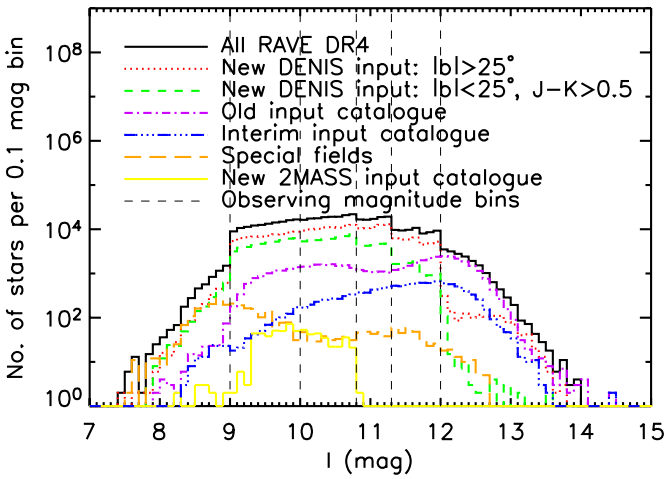

Figure 4. Histogram decomposing DR4 into its constituent input catalogs as a function of I magnitude. Note that this is either DENIS I or 2MASS constructed DENIS I and so is not reliable at $I < 9.8$ mag due to DENIS I saturation.

(A color version of this figure is available in the online journal.)

setup is a random selection of unobserved targets within these bins (apart from designed repeat observations). Any spectrum within a 6dF field setup can be adjacent to any other in the same setup on the CCD, but the bins limit the magnitude difference, which also minimizes fiber cross-talk.

Figure 2 compares the selection functions of the new input catalogs and the observed DR4 stars. The input catalogs have step functions at their bright and faint ends. However, the observed DR4 stars do not have step functions but extend to brighter and fainter than the input catalogs. Because DENIS saturates at $I < 9.8$ mag, the selection function of RAVE's new input catalog and observations need to be compared to an I-band survey that does not saturate in the RAVE magnitude range. The recent advent of the APASS (see Section 10) means that this can now be explored. Future data releases will be supplemented with APASS photometry. At the time of writing, APASS i' (internal release DR7) was available for 370,441 spectra and is plotted in Figure 2, scaled to the number of DR4 spectra. It shows that the distribution of APASS i' approximately agrees with the distribution of DENIS I at the faint end but extends to much brighter magnitudes at the bright end. This is because DENIS saturates at $I < 9.8$ mag, which means some sources are actually $I < 9$ mag.

The overall selection function of DR4 is more clearly seen in Figure 4. It has a complex shape due to the observing strategy and because DR4 includes all RAVE observations up to the end of 2012, which have been selected from four different RAVE input catalogs. Numerically, DR4 is dominated by stars selected from the new DENIS input catalog ($|b| > 25°$). This means the observing magnitude bins are visible in the DR4 selection function. It also means that overall the new input catalog observations have filled in the incompleteness of the old input catalog (mainly due to Tycho-2), thus reducing the presence of its subtle selection biases in DR4, compared to DR1, DR2, and DR3. Therefore, overall RAVE DR4 is more representative of the underlying Galactic stellar populations than previous DRs, with the exception of $|b| < 25°$, which deliberately targets giants with $J - K > 0.5$ mag. Nevertheless, on a field-by-field basis, Galactic science still requires care to account for the various selection biases introduced by the inhomogeneous photometry used to derive some of the input samples (detailed in the DR1 paper). Care is required if stars are selected from DR4 using their observation date as the selection function changes as a function of time: old and interim input catalog obsdate $\leqslant$20060312; new DENIS input catalog obsdate $>$ 20060312; new 2MASS input catalog obsdate $>$ 20120128. There may also be a stellar position bias because the 6dF fiber positioner software avoids putting targets too close to each other and also avoids crossing of fibers.

Figure 4 shows that the faint tail of the DR4 magnitude distribution is dominated by the old input catalog. This tail is fainter than the nominal selection of $I < 12$ mag due to SuperCOSMOS photographic I magnitudes being saturated. The twin peaks of the old input catalog are due to the merging of Tycho-2 and SuperCOSMOS. The interim input catalog also includes Tycho-2 and SuperCOSMOS but weights their relative numbers to achieve a single peak in its magnitude distribution. The special fields are identified by being away from the main data. However, there are many calibration and science stars within the main footprint of the survey and so are classed as stars observed from the new input catalog. These dominate the bright tail of the DR4 magnitude distribution in Figure 4 and also contribute to the faint tail. The old and interim input catalogs contribute to the bright tail because their bright magnitudes were constructed from Tycho-2 B_T and V_T.

To summarize, DR4 has no kinematic bias and no overall photometric bias. The notable exception is the color criterion ($J - K > 0.5$ mag) to deliberately target giants at $|b| < 25°$ (except where $\delta > 0°$). No other color cuts exist in the data. However, on a field-by-field basis, subtle selection biases may still be present.

3. THE NEW PIPELINE FOR THE STELLAR PARAMETERS

The wavelength region λλ8410–8795 is often used for Galactic archaeology purposes, as for instance with the multi-fiber spectrographs of ESO FLAMES-Giraffe at the LR8 and HR21 setups, and the *Gaia*–RVS. Indeed, it is a spectral region with relatively few telluric absorptions that exhibits many iron and α-element lines, in particular the prominent Ca II triplet (λ = 8498.02 Å, 8542.09 Å, 8662.14 Å). This feature is still visible at low signal-to-noise-ratio (S/N) and low metallicity, and as a consequence, it allows relatively easily to have RV measurements and metallicity estimations for any type of spectrum.

3.1. Spectral Degeneracies in the Infrared Ionized Calcium Triplet Wavelength Range

The recent work of Kordopatis et al. (2011a, hereafter K11) on spectra with a resolution $R \leqslant 10,000$ has shown that the Ca II wavelength range suffers from spectral degeneracies that, if not appreciated, can introduce serious biases in spectroscopic surveys that use automated parameterization pipelines. These degeneracies are mostly important for cool main-sequence stars and stars along the giant branch. On the one hand, the spectral signatures that are used to determine the surface gravities for the main-sequence stars are insensitive to small $\log g$ variations, hence reducing the accuracy of the measurement of that parameter. On the other hand, the spectra of stars along the giant branch can be identical for different sets of parameters. In this case, the degeneracy is due to the fact that the spectral signatures sensitive to variations of effective temperature, surface gravity, and metallicity are the same. The degeneracy works as follows: the spectrum corresponding

to a given $T_{\rm eff}$, $\log g$, and [M/H] is almost identical to a spectrum corresponding to a lower (higher) temperature, lower (higher) surface gravity, and lower (higher) metallicity.

Automated parameterization pipelines try to find the model template that minimizes the distance function, defined as the difference between the observation and a set of reference (model) spectra. In the case where not enough information is available in the data, the distance function can become non-convex, and secondary minima can appear, in which the parameterization algorithms can falsely converge. If these secondary minima are close in the parameter space, the resulting parameter estimation will have a large scatter around the true value, whereas if they are distant in the parameter space, the algorithms might converge randomly to one or the other according to where the noise is placed in the spectrum.

In K11 it has been shown that for low- and medium-resolution spectra around the IR Ca II, decision-tree methods manage to better find the absolute minimum of the distance function, compared to other algorithms, like the projection methods (e.g., principal component analysis) or the ones trying to solve an optimization problem (e.g., minimum χ^2), in particular when the S/N is low. For that reason, the pipeline presented in K11 iteratively renormalizes the spectra and obtains the atmospheric parameters using a combination of a decision-tree algorithm called DEGAS (Bijaoui et al. 2012) and a projection method called MATISSE (Recio-Blanco et al. 2006), which allows us to better interpolate between the grid points.

Both DEGAS and MATISSE have a learning phase based on a nominal library of synthetic spectra (i.e., the templates), described in Section 3.4. Here we describe briefly the pipeline and the two algorithms, but we refer the reader to Recio-Blanco et al. (2006), Bijaoui et al. (2012), and Kordopatis et al. (2011a) for further details.

3.2. DEGAS: An Oblique k-d Decision-tree Method for the Low-S/N Spectra, and for Re-normalizations

In the limit of the sampling precision of a learning grid (i.e., the parameter steps), parameter estimation is a pattern recognition problem. The grid of synthetic spectra can be treated as a known set of patterns among which the observed spectra should be identified. The DEGAS algorithm is an oblique 3D decision tree (in our case $T_{\rm eff}$, $\log g$, and [M/H]), for which the decisions result from the projection of the observations onto N node vectors noted $D_n(\lambda)$ ($n = 1, \ldots, N$). These node vectors are associated with a subset of spectra of the nominal library, in the sense that the result of the projection of an observed spectrum on that node will select half of the subset which most closely resembles the observation.

The recognition rules of DEGAS, at each node, are established during the learning phase as follows:

1. The mean vector $M(\lambda)$ of the flux values per pixel of all the reference spectra in the subset is computed.
2. For each reference spectrum $S_j(\lambda)$ associated with the node, the scalar product $c_j = \sum_\lambda S_j(\lambda) \cdot M(\lambda)$ is calculated. Let $\tilde{c}$ be the median value of c_j.
3. The reference spectra are bisected in two new subsets, T_1 and T_2, according to the following criteria:
   S_j belongs to the subset T_1 if $c_j \leqslant \tilde{c}$
   S_j belongs to the subset T_2 if $c_j > \tilde{c}$.
4. The difference vector $D(\lambda) = M_1(\lambda) - M_2(\lambda)$ is determined, where $M_1(\lambda)$ and $M_2(\lambda)$ are the mean vectors of the flux values of each subset.
5. If the correlation coefficient between $M(\lambda)$ and $D(\lambda)$ is too small (typically, smaller than 0.999), the initial subset of reference spectra is re-separated by the hyperplane defined by $D(\lambda)$, iterating until convergence (going back to step 2, replacing $M(\lambda)$ by $D(\lambda)$).

When the previous procedure has converged for a particular node n, the final adopted projection node vector $D_n(\lambda)$ is determined, which will display the features that allow the separation of the subset of learning spectra at that node. The final median value $\tilde{c_n}$ of $c_j = \sum_\lambda S_j(\lambda) \cdot D_n(\lambda)$ that will allow us to make the decisions is also set.

In this way, the recognition tree is built, having $\log_2(N)$ levels, where N is the number of spectra of the learning grid. At the lowest level nodes of the tree, only one training spectrum remains associated with each node. During the application phase, the target data $O_i(\lambda)$ pass through all the levels of the recognition tree, and a template is associated with it.

Of course, noise can induce misclassifications. The exploration of the branches, even if the decision threshold $\tilde{c_n}$ does not allow it, is accomplished thanks to an activation function on the directions of the tree. Let us consider

$$u_i = \frac{c_i - \tilde{c_n}}{\sigma_{c_i}}, \tag{2}$$

where $c_i = \sum_\lambda O_i(\lambda) \cdot D_n(\lambda)$, $\sigma_{c_i} = S_f \cdot \sqrt{\Sigma_\lambda D_n(\lambda)^2}$, and S_f is an arbitrary constant chosen in order to explore optimally the branches. If $u_i \leqslant -k$, we decide that the correct direction is 1. If $u_i \geqslant k$, the direction 2 is chosen. If $-k < u_i < k$, both directions are considered.

After the scanning of all the nodes, a subset of synthetic templates is selected, and their distances (in terms of the difference with the observed spectrum) are computed. Then, the parameters of the observed spectrum are determined by computing a weighted mean on the selected spectra, taking into account these distances, setting

$$W_i^n = \left(1 - \left[\sum_\lambda O_i(\lambda) - S_n(\lambda)\right]^2\right)^p. \tag{3}$$

The value p of the exponent is rather arbitrary. Following K11, where it was found that $p = 64$ gave the best results, the same value was adopted in what follows.

DEGAS has a key role in the pipeline used for the RAVE DR4 analyses. Because of its pattern recognition approach, it is exploring more efficiently the parameter space than other mathematical methods and, as a consequence, is less affected by secondary minima in the distance function. Hence, given a roughly normalized spectrum at the rest frame, DEGAS is used in order to achieve a good normalization for the data, using the synthetic spectrum corresponding to the intermediate solution found.

Once DEGAS has converged on a set of parameters, the new parameters are used to re-normalize the spectrum given the intermediate solution template. The re-normalization process might need several iterations until the shape of the continuum stays unchanged from one normalization to another. The number of needed iterations may vary from 3 to 10. In the case where the distance function has many secondary minima (low-S/N spectra and/or low-metallicity stars), the results of DEGAS at that stage are the most accurate among the other methods. Nevertheless, it has been shown in K11 that MATISSE manages to better

interpolate between the grid points when the astrophysical information is sufficient in the spectra. Thus, once the shape of the continuum has converged, the mean S/N per pixel is estimated in the same way as in Zwitter et al. (2008), and in the case of high-S/N spectra MATISSE is run to get more precise atmospheric parameters. The S/N threshold at which MATISSE is run has been established in K11 to be S/N = 30 pixel^{-1}.

3.3. MATISSE: A Projection Method for the High-S/N Regimes

The MATISSE algorithm is a local multi-linear regression method. It estimates a $\hat{\theta}_i$ stellar atmospheric parameter ($i \equiv T_{\rm eff}$, log g, [M/H]) by projecting the observed spectrum $O(\lambda)$ on a particular vector $B_\theta(\lambda)$ associated to a theoretical θ_i parameter, as follows:

$$\hat{\theta}_i = \sum_{\lambda} B_{\theta_i}(\lambda) \cdot O(\lambda). \quad (4)$$

These vectors, called $B_\theta(\lambda)$ functions hereafter, are computed during a learning phase. They relate, in a quantitative way, the pixel-to-pixel flux variations in a spectrum to a given variation of the θ_i parameter. In the case where the $B_\theta(\lambda)$ are orthogonal, the effects due to each parameter affect the spectrum in an independent way, and hence the atmospheric parameters are derived accurately. When this is not the case (as in most applications), possible degeneracies in the parameter space can occur, causing a correlation of the parameter errors.

The $B_\theta(\lambda)$ functions are computed within a given range of parameters, from an optimal multi-linear combination of theoretical, synthetic spectra $S(\lambda)$, as follows:

$$B_{\theta_i}(\lambda) = \sum_{j} \alpha_{ij} \cdot S_j(\lambda), \quad (5)$$

where the α_{ij} factor is the weight associated with each synthetic spectrum $S_j(\lambda)$, in order to retrieve the $\hat{\theta}_i$ parameter. The weights are computed during the learning phase by applying Equation (4) to a subset of synthetic spectra. Thus, combining Equations (4) and (5), one obtains

$$\Theta_i = C\alpha_i, \quad (6)$$

where $C = [c_{jj'}]$ is the correlation matrix and Θ_i the vector of the parameters θ_i for all the considered spectra. The weights α_{ij} are then obtained by inverting the correlation matrix C. As explained in K11, a direct inversion of C would take into account all the available spectral signatures, including the smallest ones. Nevertheless, in the case of noisy spectra some lines become insignificant and should hence be discarded from the analysis. In order to achieve that, we adopt here the same approach as in K11, which used the Landweber algorithm to iteratively invert C. By stopping the inversion procedure at different convergence values, smaller weights are then applied to the most insignificant lines, which allows the solution to be less affected by secondary minima in the distance function. Extensive analysis of the parameter space for spectra of different S/N values allowed adoption of a different set of $B_\theta(\lambda)$ functions for different S/N values and hence achieved enhanced accuracy in the parameter determination (see K11 for further details).

The convergence of the algorithm works as follows: if the projection of the observed spectrum on a set of $B_\theta(\lambda)$ gives results that are not within the parameter ranges for which these $B_\theta(\lambda)$ have been computed, then a new set of $B_\theta(\lambda)$ is used, centered on the previous solution. This step is repeated until the results stay within the parameter range of applicability of the projection vectors. In the case where the distance function is convex, less than five iterations are usually needed to reach the absolute minimum, but in some cases of degeneracy in the distance function, the algorithm might not converge (these spectra are then flagged and should not be used from the catalog; see Section 6.1).

As noted previously, MATISSE has the advantage of interpolating accurately between the learning grid points, achieving a good parameter estimation at the high-S/N regimes. Nevertheless, local projection methods such as MATISSE have, in general, two main disadvantages. The first consists in not exploring entirely the parameter space and hence being easily trapped in secondary minima of the distance function if there is a lot of noise in the spectrum. The second disadvantage is that it can extrapolate results outside the boundaries of the learning grid. These two undesired effects are attenuated with the parallel use of DEGAS. Indeed, as described in Section 3.2, DEGAS is first used to converge toward a sub-region of the parameter space. Then, for the lowest S/N spectra or when the derived MATISSE parameters are outside the grid's limits, the results of DEGAS are adopted, and MATISSE is not implemented.[26]

3.4. The Grid of Synthetic Spectra for the Learning Phase of the Pipeline

The very high resolution grid computed in K11 has been convolved with a Gaussian kernel, in order to obtain a new synthetic library at $R = 7500$,[27] with a constant wavelength step of 0.35 Å and covering the wavelength range of 8450.80–8746.55 Å. In addition, the cores of the Ca II lines have been removed from the synthetic spectra, corresponding to 1 pixel for the first Ca II line and 2 pixels for the other two lines. This removal is justified since the cores of the lines are formed in the upper stellar atmospheric layers where some modeling assumptions like the local thermodynamical equilibrium (LTE) or hydrostatic equilibrium might not be valid hypotheses anymore. The flux disagreement with real spectra for these pixels can induce the algorithms to converge to false minima, and hence the cores must be discarded (see K11 for further details).

We recall that the synthetic library has been computed using the one-dimensional, LTE and hydrostatic equilibrium MARCS model atmospheres (Gustafsson et al. 2008), in combination with the Turbospectrum code (Alvarez & Plez 1998). The atomic line list has been calibrated on high-S/N and high-resolution spectra of the Sun and Arcturus (Brault & Neckel 1987; Hinkle et al. 2003), assuming the solar abundances of Grevesse (2008), except for CNO, where we used the values of Asplund et al. (2005). The molecular line list includes ZrO, TiO, VO, CN, C2, CH, SiH, CaH, FeH, and MgH lines with their corresponding isotopic variations (kindly provided by B. Plez).

The reference grid spans effective temperatures from 4000 K to 8000 K with a constant step of 250 K and surface gravities from 0.0 dex to 5.0 dex with a constant step of 0.5 dex. In addition, the library spans with a constant step of 200 K effective temperatures from 3000 K to 4000 K and surface gravities from 0.0 dex to 5.5 dex. As far as the metallicities are concerned,

[26] The stars for which DEGAS parameters have been adopted after MATISSE has given parameters outside the grid boundaries are flagged as well, and should be used with caution.

[27] We note that the effective resolution of RAVE can in reality vary from $6500 < R < 8500$, the changes being a function of both time and position on the CCD. Nevertheless, simple tests, degrading the S^4N library (see Section 4.5) to $R \sim 6500$, 7500, and 8500 and then analysis as if the spectra were at $R \sim 7500$, show that the effect on the parameter estimation was of the second order. We hence did not take into account these resolution changes for DR4. However, future data releases will implement these second-order effects.

the number of grid models has increased compared to K11. Instead of having a variable metallicity step, ranging from 0.25 dex for the most metal-rich stars to 1 dex for the stars with [M/H] < -3 dex, the new grid has a constant metallicity step of 0.25 dex for all the metallicities ranging from [−5.0; +1.0] dex. These new spectra, whose atmospheric models did not exist in the MARCS database, have been linearly interpolated from the existing synthetic spectra.

One of the noticeable differences between previous data releases and DR4 is that, in this work, only three parameters are independent in the grid: the effective temperature, $T_{\rm eff}$, the logarithm of the surface gravity, $\log g$, and the overall metallicity, [M/H]. This restriction decreases the number of the secondary minima of the distance function, hence increasing the accuracy of the parameter derivation. It should be noted though that the microturbulent velocity (ξ) is not constant within the grid, but is changed in lock-step with the gravity of the stars. Dwarfs ($\log g \geqslant 3.5$ dex) have a microturbulent velocity of $\xi = 1$ km s^{-1}, whereas giants have $\xi = 2$ km s^{-1}. Abundances of the α-elements[28] are also changed systematically with metallicity, being scaled on the iron abundance, [Fe/H], following the standard α-enhancement found for the metal-poor stars of the Milky Way (thick disk and halo):

1. [α/Fe] = 0.0 dex for [Fe/H] $\geqslant$0.0 dex
2. [α/Fe] = $-0.4\times$[Fe/H] dex for $-1 \leqslant$[Fe/H]$\leqslant$ 0 dex
3. [α/Fe] = +0.4 dex for [Fe/H] $\leqslant -1.0$ dex.

In addition, spectra for which the parameter combinations did not correspond to realistic astrophysical stars have been removed from the learning grid and hence from the solution space as well. To minimize the importance of our astrophysical priors in the derived parameters, we removed only the templates with $\log g = 5$ dex and $T_{\rm eff} > 6250$ K, those with $T_{\rm eff} \leqslant 4250$ K and $4 \leqslant \log g \leqslant 3$ dex, as well as all stars with [M/H] $\leqslant -3$ dex, $T_{\rm eff} \leqslant 4000$ K, and $\log g \leqslant 4$ dex. These criteria correspond to excluding very young stars with extremely metal-poor abundances (age < 0.5 Gyr and [Fe/H] < -2.5 dex), as well as old stars that are extremely metal-rich (age > 14 Gyr and [Fe/H] > 0.75 dex). The final grid contains 3580 spectra of 839 pixels each.

Based on this grid, a subset of reference models can be selected, according to the additional information that is available for each data set to be treated. In the case of RAVE, the 2MASS photometric information that is available for the observed targets is used to exclude some parameter combinations from the solution space corresponding to derived temperature ranges which are grossly inconsistent with the photometric color. In practice, the RAVE spectra have been separated into four different color ranges. Then, according to their 2MASS $(J-K_s)$ color, a set of solutions has been imposed as soft photometric priors for every analyzed spectrum, defining:

1. $(J - K_s) > 0.75 \Rightarrow T_{\rm eff} < 4500$ K
2. $0.4 < (J - K_s) < 0.75 \Rightarrow 3750 < T_{\rm eff} < 6000$ K
3. $(J - K_s) < 0.4 \Rightarrow T_{\rm eff} > 5250$ K.

The few stars for which no 2MASS photometry was available (less than 2%) form a fourth category for which there is no prior on the solution space.

The above-mentioned effective temperature ranges have been determined by requesting a color–magnitude diagram of the Galaxy from the web interface[29] of the Padova database with the 2MASS photometric system. Then, for the above three color ranges we inferred the full range of effective temperatures of the simulated stars and increased these limits by ±500 K. We note that the effective temperature bins have been made deliberately large, because neither the photometric errors nor the extinction have been taken into account when separating the spectra into color bins.

3.5. Computation of the Internal Uncertainties

The total uncertainty of the pipeline for a given star is the quadratic sum of its internal and external errors. The internal uncertainties relate the capacity of an algorithm to treat spectral degeneracies and S/N, whereas external uncertainties concern the difference between the template synthetic spectra and the true stellar spectra (see Section 4.6).

Following K11, the internal uncertainties of the algorithm have been estimated by computing a set of spectra of realistic Galactic populations. Based on the Besançon Galactic model, a simulated catalog of stars toward three different Galactic directions (Galactic center, north Galactic pole, and intermediate Galactic latitudes) has been constructed, from which 10^4 stars have been randomly selected to be our realistic Galactic sample. In addition, in order to explore different metallicity regimes, each star has been replicated in the catalog, with its partner having reduced (by -0.75 dex) metallicity. The 2×10^4 synthetic spectra corresponding to these parameter combinations have been computed thanks to the interpolation capabilities of MATISSE, and four different values of white Gaussian noise were added to them (S/N = 100, 50, 20, 10 pixel^{-1}). Given these final 8×10^4 spectra, the pipeline was run in order to retrieve the associated errors.

In order to simulate the way the RAVE spectra are analyzed, the pipeline was run twice: once without any photometric prior (see Table 1), and once by imposing soft priors (see Table 2), based on their temperatures. These priors have been selected in order to be similar with the ones that are applied in the analysis of the RAVE spectra (see Section 3.4). The error values for different stellar types, presented in Tables 1 and 2, have been computed as the 70th percentile of the error distribution. Indicative atmospheric parameter uncertainties for typical thin disk dwarfs, thick disk dwarfs, and halo giants are also given in the last three lines of these tables. A comparison of the uncertainty values with or without photometric priors shows that when the spectral degeneracy is important, the applied soft priors improve significantly the associated uncertainties (see, for example, the hot, metal-poor dwarfs). In addition, it has been noticed, as expected, that the use of the soft photometric priors improves the 90th percentile of most of the stellar categories considered in these tables.

The way the internal errors are associated with a specific parameter estimation is as follows: once the pipeline has converged toward a set of parameters, the final S/N is computed as in Zwitter et al. (2008), utilizing the associated solution template. According to the S/N, the stellar type, the luminosity class, its metallicity, and the use or not of 2MASS photometric prior, the equivalent internal error estimations in Table 1 or Table 2 are adopted. We note that this approach does not optimally take into account the properties of the distance function and hence the degeneracies. Nevertheless, we find that

[28] The chemical species considered as α-elements are O, Ne, Mg, Si, S, Ar, Ca, and Ti.

[29] http://stev.oapd.inaf.it/cmd

Table 1
Internal Errors after Re-normalizations without Photometric Priors

S/N (pixel^{-1})	$T_{\rm eff}$ (K)				log g (dex)				[M/H] (dex)			
	100	50	20	10	100	50	20	10	100	50	20	10
K II–IV, [M/H]>-0.5 dex	72	76	117	201	0.12	0.13	0.20	0.48	0.08	0.08	0.10	0.23
K II–IV, $-1<$[M/H]<-0.5 dex	62	85	133	302	0.14	0.20	0.35	0.72	0.08	0.09	0.16	0.30
K II–IV, $-2<$[M/H]<-1 dex	75	96	178	330	0.20	0.30	0.57	0.97	0.09	0.11	0.19	0.33
K II–IV, [M/H]<-2 dex	78	105	184	382	0.31	0.40	0.76	1.26	0.09	0.10	0.20	0.37
G II–IV, [M/H]>-0.5 dex	78	111	233	402	0.09	0.20	0.40	0.69	0.07	0.09	0.15	0.35
G II–IV, $-1<$[M/H]<-0.5 dex	81	110	241	426	0.15	0.25	0.54	0.98	0.08	0.10	0.17	0.44
G II–IV, $-2<$[M/H]<-1 dex	98	164	282	472	0.25	0.46	0.74	1.08	0.10	0.13	0.23	0.43
G II–IV, [M/H]<-2 dex	187	248	375	553	0.37	0.61	0.99	1.07	0.17	0.26	0.49	0.60
F II–IV all [M/H]	79	73	138	140	0.14	0.13	0.14	0.15	0.09	0.09	0.10	0.27
K V, [M/H]>-0.5 dex	66	69	92	171	0.11	0.14	0.22	0.34	0.08	0.09	0.09	0.21
K V, $-1<$[M/H]$<-0.$	75	85	112	225	0.15	0.17	0.24	0.38	0.09	0.10	0.13	0.30
K V, $-2<$[M/H]<-1	83	98	173	328	0.16	0.19	0.25	0.51	0.09	0.11	0.14	0.35
K V, [M/H]<-2 dex	93	133	278	518	0.11	0.17	0.47	1.03	0.06	0.06	0.15	0.38
G V, [M/H]>-0.5 dex	67	98	209	344	0.10	0.16	0.33	0.51	0.09	0.10	0.14	0.30
G V, $-1<$[M/H]$<-0.$	87	147	246	426	0.14	0.22	0.36	0.55	0.09	0.12	0.21	0.38
G V, $-2<$[M/H]<-1	119	181	358	669	0.19	0.32	0.44	0.71	0.11	0.14	0.28	0.54
G V, [M/H]<-2 dex	279	435	690	843	0.44	0.54	0.72	1.06	0.26	0.38	0.61	0.80
F V, [M/H]>-0.5 dex	81	117	307	493	0.13	0.18	0.34	0.52	0.11	0.13	0.27	0.43
F V, $-1<$[M/H]$<-0.$	96	151	306	575	0.14	0.21	0.33	0.49	0.11	0.14	0.26	0.48
F V, $-2<$[M/H]<-1	155	257	563	999	0.21	0.30	0.40	0.69	0.13	0.19	0.43	0.83
F V, [M/H]<-2 dex	447	641	1046	1165	0.43	0.65	0.84	1.22	0.40	0.53	0.95	1.14
Thin disk dwarfs	66	89	199	344	0.09	0.14	0.32	0.50	0.09	0.10	0.13	0.29
Thick disk dwarfs	91	146	280	501	0.14	0.22	0.35	0.52	0.09	0.13	0.24	0.43
Halo giants	90	149	244	443	0.23	0.43	0.70	1.05	0.10	0.13	0.24	0.39

Notes. Luminosity classes I and II assume $\log g \leqslant 3.5$, luminosity class V assumes $\log g > 3.5$. Spectral types are defined by $T_{\rm eff}$ ranges as follows: $T_{\rm eff} < 5000$ K for K-type, $5000 \leqslant T_{\rm eff} < 6000$ K for G-type, and $T_{\rm eff} \geqslant 6000$ K for F-type stars.

Table 2
Internal Errors after Re-normalizations with Photometric Priors

S/N (pixel^{-1})	$T_{\rm eff}$ (K)				log g (dex)				[M/H] (dex)			
	100	50	20	10	100	50	20	10	100	50	20	10
K II–IV, [M/H]>-0.5 dex	71	76	112	180	0.12	0.14	0.24	0.50	0.08	0.08	0.11	0.21
K II–IV, $-1<$[M/H]<-0.5 dex	61	86	137	285	0.14	0.20	0.40	0.69	0.08	0.10	0.17	0.29
K II–IV, $-2<$[M/H]<-1 dex	75	96	173	312	0.20	0.31	0.59	1.02	0.09	0.11	0.21	0.34
K II–IV, [M/H]<-2 dex	75	101	213	399	0.27	0.35	0.79	0.98	0.10	0.10	0.18	0.32
G II–IV, [M/H]>-0.5 dex	78	104	237	332	0.09	0.21	0.48	0.49	0.07	0.09	0.18	0.26
G II–IV, $-1<$[M/H]<-0.5 dex	79	103	238	412	0.15	0.23	0.52	0.97	0.08	0.10	0.17	0.37
G II–IV, $-2<$[M/H]<-1 dex	90	158	283	412	0.21	0.45	0.78	1.05	0.11	0.12	0.23	0.33
G II–IV, [M/H]<-2 dex	203	265	378	479	0.33	0.61	0.91	1.14	0.15	0.25	0.49	0.54
F II–IV all [M/H]	79	83	93	138	0.14	0.13	0.14	0.26	0.09	0.09	0.09	0.31
K V, [M/H]>-0.5 dex	66	69	92	168	0.11	0.15	0.22	0.36	0.08	0.09	0.09	0.20
K V, $-1<$[M/H]<-0.5 dex	75	84	110	219	0.15	0.17	0.23	0.38	0.09	0.10	0.12	0.29
K V, $-2<$[M/H]<-1 dex	82	97	172	293	0.16	0.19	0.23	0.52	0.08	0.10	0.14	0.33
K V, [M/H]<-2 dex	92	144	240	480	0.11	0.17	0.46	0.54	0.07	0.07	0.17	0.39
G V, [M/H]>-0.5 dex	66	95	203	316	0.10	0.15	0.35	0.55	0.09	0.10	0.15	0.30
G V, $-1<$[M/H]<-0.5 dex	85	144	238	360	0.14	0.22	0.38	0.55	0.09	0.12	0.20	0.33
G V, $-2<$[M/H]<-1 dex	101	169	291	441	0.15	0.28	0.43	0.62	0.10	0.13	0.24	0.39
G V, [M/H]<-2 dex	220	317	393	480	0.35	0.46	0.53	0.80	0.21	0.30	0.39	0.50
F V, [M/H]>-0.5 dex	66	94	257	464	0.13	0.18	0.38	0.56	0.10	0.11	0.25	0.41
F V, $-1<$[M/H]<-0.5 dex	84	127	277	498	0.14	0.21	0.35	0.52	0.09	0.13	0.25	0.43
F V, $-2<$[M/H]<-1 dex	104	182	440	601	0.18	0.25	0.38	0.53	0.11	0.15	0.32	0.51
F V, [M/H]<-2 dex	331	503	617	678	0.32	0.51	0.54	0.66	0.33	0.48	0.54	0.69
Thin disk dwarfs	61	85	183	330	0.09	0.14	0.33	0.53	0.09	0.10	0.12	0.30
Thick disk dwarfs	84	133	256	406	0.14	0.21	0.38	0.54	0.09	0.12	0.22	0.37
Halo giants	83	143	258	399	0.21	0.41	0.74	1.04	0.10	0.12	0.24	0.38

in the case of spectral degeneracy, the associated errors are larger, being consistent with what is expected.

3.6. Description of the Observed Input Spectra

The extraction and reduction procedures applied to the observed spectra are as described in Steinmetz et al. (2006) and Zwitter et al. (2008). As far as the normalization and rest-frame corrections are concerned, we have used the results and the raw data coming from DR3, details of which can be found in Siebert et al. (2011b) and for which the general properties are summarized in Section 8. In addition, in order to be able to perform a pattern recognition and a pixel-to-pixel comparison with the spectra of the learning grid, the RAVE spectra have been interpolated at the wavelengths of the templates and the cores of the IR Ca II triplet lines have been removed (see Section 3.4).

Since the DR4 pipeline re-normalizes the observed spectra, initially erroneous or inaccurate continuum shapes do not influence the final parameter accuracy of DR4. One might worry about the accuracy of the RV of the stars and hence their rest-frame correction. Indeed, the radial velocities have been computed using cross-correlation with the solution template derived in DR3, whereas in the present work, the atmospheric parameters are recomputed, leading to different values. Nevertheless, the pipeline requires an RV precision only better than $\sim$7–10 km s^{-1} (see K11) in order not to be affected by Doppler shifts in the parameter estimation. This threshold is much higher than the accuracy of the radial velocities coming from the DR3, where 95% of the sample has errors of less than $\sim$4 km s^{-1} and 98% less than 7 km s^{-1} (Siebert et al. 2011b, and Section 8). Thus, we can assume that the spectra are indeed at the rest frame for the purpose of our analysis.

4. VALIDATION OF THE PARAMETERIZATION WITH EXTERNAL DATA SETS

Up to here in this paper, only the internal performances of the pipeline have been discussed. Nevertheless, any given pipeline based on a grid of synthetic spectra needs to be verified and calibrated on observed spectra with high S/N and well-determined parameters. The grid of synthetic spectra that has been used for this work has been computed with an atomic line list calibrated on the high-resolution and high-S/N spectra of the Sun and Arcturus of Brault & Neckel (1987) and Hinkle et al. (2003). However, these calibrations concern only two particular stars, and further investigation needs to be done in order to correct possible biases in the parameter's estimation. In order to calibrate the $T_{\rm eff}$, log g, and [M/H], instead of going through the process of calibrating all the lines for many reference stars, and improve the quality of the atmosphere modeling, one can also validate the pipeline's parameter results with reference parameter measurements from the literature.

This calibrating data set needs to cover as much as possible the parameter space investigated by the survey. Ideally the calibration of the parameters would be done using only RAVE spectra of suitable standards, but RAVE-like spectra, at the same resolution and (if possible) reduced in the same manner, can be sufficient in the case where not enough calibration spectra are available.

4.1. The Calibration Data Sets of Observed Spectra

First, the RAVE database has been explored to find spectra of stars that had atmospheric parameter determinations available from high-resolution spectroscopy. For that purpose, we made extensive use of the heterogeneous PASTEL catalog[30] to identify such targets, retrieving roughly 400 star candidates. Following Soubiran et al. (2010), we considered only the reference values coming from Fuhrmann (1998a, 1998b, 2004, 2008), Gratton et al. (1996, 2003), Hekker & Meléndez (2007), Luck & Heiter (2006, 2007), McWilliam (1990), Mishenina & Kovtyukh (2001), Mishenina et al. (2004, 2006, 2008), Ramírez et al. (2007), and Valenti & Fischer (2005). These studies, when considered by author, all include a large number of stars (at minimum 222 stars) and are all analyzed in a homogeneous way. This allows us to minimize the discrepancies between the sub-catalogs of PASTEL. When for a given star several measurements were available, the mean was computed and the dispersion of the parameters has been considered as the uncertainty on the reference values. We kept only those stars for which measurements were available for the three parameters from a single study, and for which the dispersions among the literature values were less than 100 K, 0.2 dex, and 0.1 dex for $T_{\rm eff}$, log g, and [M/H], respectively. In total, 169 stars were selected that way, mainly dwarfs of intermediate metallicity.

In order to investigate the pipeline's behavior in the low-metallicity regime for giant stars, we chose to use the parameters of 229 thick disk stars analyzed by Ruchti et al. (2011), as well as 163 stars observed by J. P. Fulbright et al. (in preparation). The targets of both of these data sets are drawn from RAVE, while the stellar parameters have been obtained from an equivalent-width (EW) analysis of high-resolution spectra. In addition, the very metal-poor giant star CD-38245 ([M/H] = $-$4.2 dex; Cayrel et al. 2004), which has been observed twice by RAVE, has been included in the list, in order to calibrate the results at the very metal-poor regime.

Metal-rich giant stars have been explored thanks to the CFLIB library (Valdes et al. 2004). The entire spectral library was downloaded from the Web site[31] of that project, excluding only spectra that did not include the wavelength range around the IR Ca II triplet. The final comparison catalog is the same as in K11, where once again we used the updated values that can be found in the PASTEL database and discarded the stars for which the dispersions in the literature values were greater than 100 K, 0.2 dex, and 0.1 dex for $T_{\rm eff}$, log g, and [M/H], respectively.

Finally, in order to have a more significant statistical sample at the high-metallicity regime, we used the 2.3 m telescope at the Siding Spring Observatory (SSO) to obtain spectra of stars belonging to open clusters. Although the data have not been obtained with the same instrument, the same reduction pipeline has been used as for the RAVE spectra. For calibration purposes, we have used 16 RAVE-like SSO spectra of giant stars belonging to the open cluster M67 and 12 RAVE-like SSO spectra of giants belonging to the open cluster IC 4651, with a few additional data sets used as testing sets (see Section 4.5). These targets were selected given their positions, colors, and radial velocities when available, prioritizing bright stars in order to have high-S/N spectra. For these stars, no individual atmospheric parameters were available, but their metallicity is expected to have a small dispersion around their mean open cluster metallicity value.

In total, 809 stars are used as calibrators, each having S/N $>$ 40 pixel^{-1}. The final number of spectra used from each data set is summarized in Table 3, and their reference and retrieved $T_{\rm eff}$–log g diagrams are plotted in Figure 5.

[30] http://pastel.obs.u-bordeaux1.fr/
[31] http://www.noao.edu/cflib/

Table 3
Calibration Data Sets with S/N > 40 pixel^{-1}

Data Set	Object	N Spectra	[Fe/H]	Reference for the Stellar Parameters
IC 4651	Open cluster	6	+0.10	Pasquini et al. (2004)
M67	Open cluster	16	+0.05	Pancino et al. (2010)
CFLIB	Dwarfs and giants	224	[−1.0, 0.0]	PASTEL database
CD-38245	$T_{\rm eff}$ = 4800 K, log g = 1.5	2	−4.2	Cayrel et al. (2004)
Ruchti et al. (2011)[a]	Giants and dwarfs	229	[−2.5; −0.5]	Ruchti et al. (2011)
Fulbright et al.	Giants	163	[−2.5; 0.0]	J. P. Fulbright et al. (in preparation)
RAVE spectra	Giants and dwarfs	169	[−1.5; 0.0]	PASTEL database

Note. [a] For the Ruchti et al. (2011) catalog we selected stars with [M/H] > −2.5 dex and log g <3 and stars with [M/H] < −0.8 dex and log g >3.

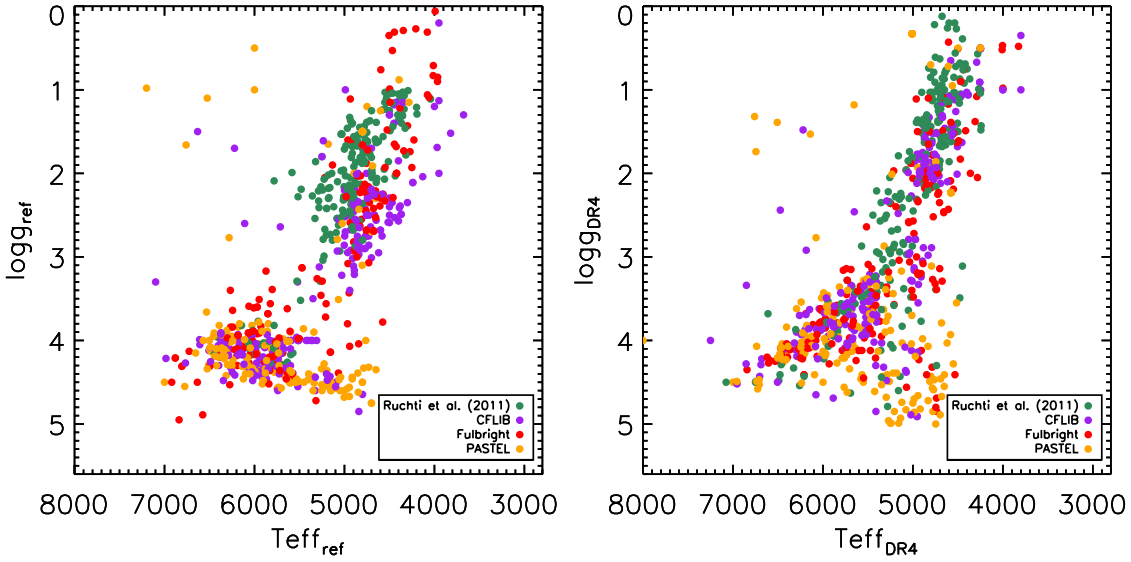

Figure 5. Surface gravity (log g) vs. effective temperature ($T_{\rm eff}$) diagram of the calibration data sets for which we have parameter estimations coming from high-resolution spectroscopy. On the left-hand side are represented the values found in the literature, whereas on the right-hand side are plotted the results obtained from the DR4 pipeline.

(A color version of this figure is available in the online journal.)

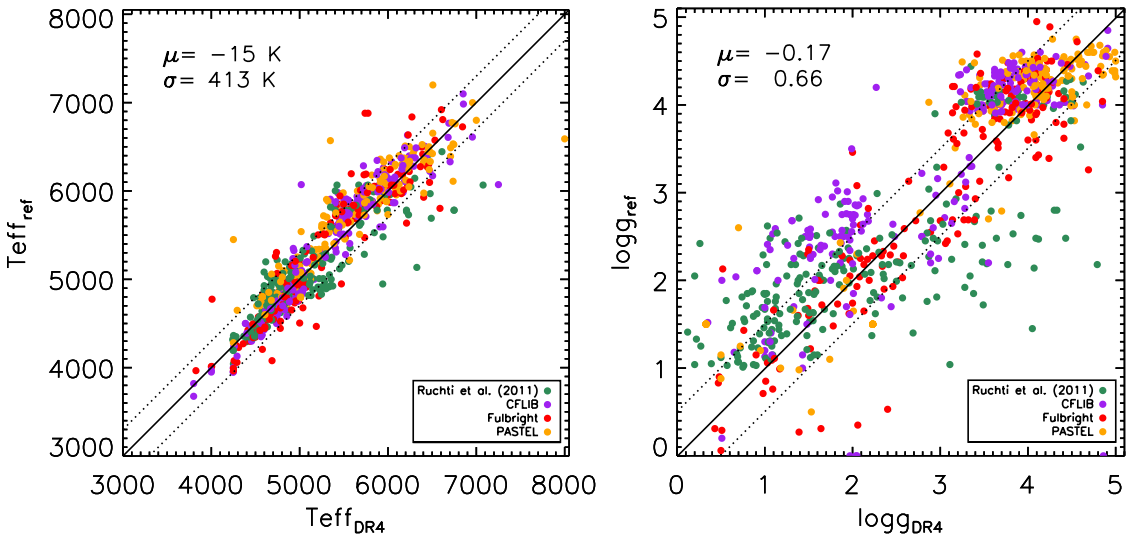

Figure 6. Comparison of the reference values found in the literature and the derived effective temperatures (left panel) and surface gravities (right panel). Color-coding for each data set is the same as in Figure 5. Dotted diagonal lines represent offsets from unity of ±300 K and ±0.5 dex for $T_{\rm eff}$ and log g, respectively. The mean offsets (μ) and the dispersions (σ) are indicated in the upper left corner of each plot.

(A color version of this figure is available in the online journal.)

4.2. Validation of the Effective Temperatures and Surface Gravities

Figures 5 and 6 show the comparison between the reference values found in the literature and those found with the present pipeline for all the data sets except those for open cluster members (where no reference values were available). As far as the effective temperature is concerned, good agreement is found, with a mean offset of 15 K and a dispersion of roughly 400 K.

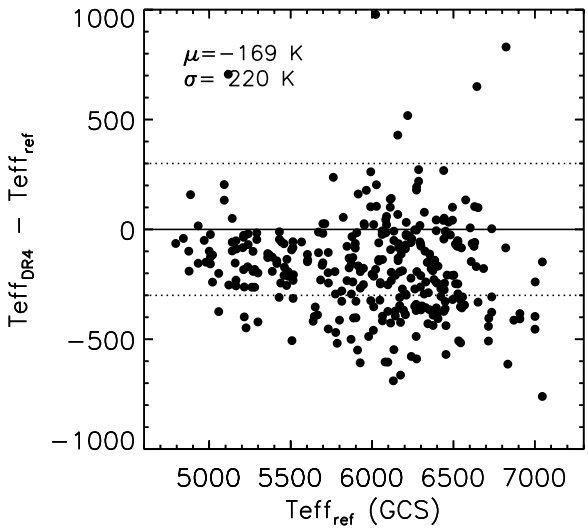

Figure 7. Comparison of the effective temperatures found by the DR4 pipeline for RAVE spectra of stars that are part of the Geneva–Copenhagen Survey with the updated values of Casagrande et al. (2011). The constant offset of ∼170 K shows that DR4 is not on the same effective temperature scale.

On the other hand, the agreement is less good for the surface gravity, with a rather big scatter for the giant stars. This effect is a manifestation of the previously cited spectral degeneracy that is present for the low- and intermediate-resolution spectra around the IR Ca II triplet. According to the stochastic position of the noise on the spectrum, a metal-rich turn-off star can be easily confused with a star on the sub-giant branch of lower metallicity. Unless precise photometric temperatures are known, this degeneracy cannot be lifted using medium-resolution spectra alone and is a true degeneracy. Nevertheless, as noted in the previous sections, the DR4 pipeline takes advantage of the 2MASS photometric information (see Section 3.4), hence partly reducing the effect of these degeneracies.

Discussion on the effective temperature scale. In order to verify the determination of the effective temperatures, we compared the DR4 values of RAVE spectra with S/N > 20 pixel^{-1} for 327 stars in common with the photometric effective temperatures from the Casagrande et al. (2010) calibration of the Geneva–Copenhagen Survey (GCS; Nordström et al. 2004). Figure 7 shows on one hand a small dispersion of the DR4 pipeline's effective temperatures when comparing with the values published by Casagrande et al. (2011) for the GCS, but on the other hand there is a constant underestimation of ∼170 K. Nevertheless, since the GCS covers only a limited range of the parameter space (only metal-rich dwarfs), and because any such offset is not seen with the other calibration data sets, it has been decided not to apply any correction to the RAVE $T_{\rm eff}$ scale. We note though that the user of the DR4 effective temperatures should be aware that in order to be in agreement with the Casagrande et al. (2010) effective temperature scale, for the type of stars analyzed by the GCS, an offset correction should be performed.

4.3. Overall Metallicity Calibration

In order to investigate the calibration needs for the metallicities, we used the iron abundances ([Fe/H]) from the literature. Indeed, we recall that the iron-peak and the α-element abundances of the synthetic spectra are scaled to the iron abundance. Since the metallicity measurement is dominated by the Ca II lines (which correspond to an α-element), in our case and for standard Galactic α-abundances (i.e., following the trend defined in Section 3.4) we have $[M/H]_{DR4} \approx [Fe/H]$. Nevertheless, for non-standard stars, the overall metallicity will not be equal to the iron abundance, and hence it has been decided to keep in what follows the notation [M/H] instead of [Fe/H]. In what follows, the nomenclature of the DR3 paper is adopted, denoting the raw metallicity estimation of the DR4 pipeline as [m/H] and the calibrated (final) metallicity as [M/H]. Comparison of the reference values and those derived by the DR4 pipeline is presented in the left panel of Figure 8.

The results of Figure 8 have been obtained with all the data sets of Table 3, assuming the metallicities given in the fourth column of that table. From the left panel of Figure 8 one can notice that there is an offset between the derived metallicities from the RAVE spectra and the reference iron abundances.

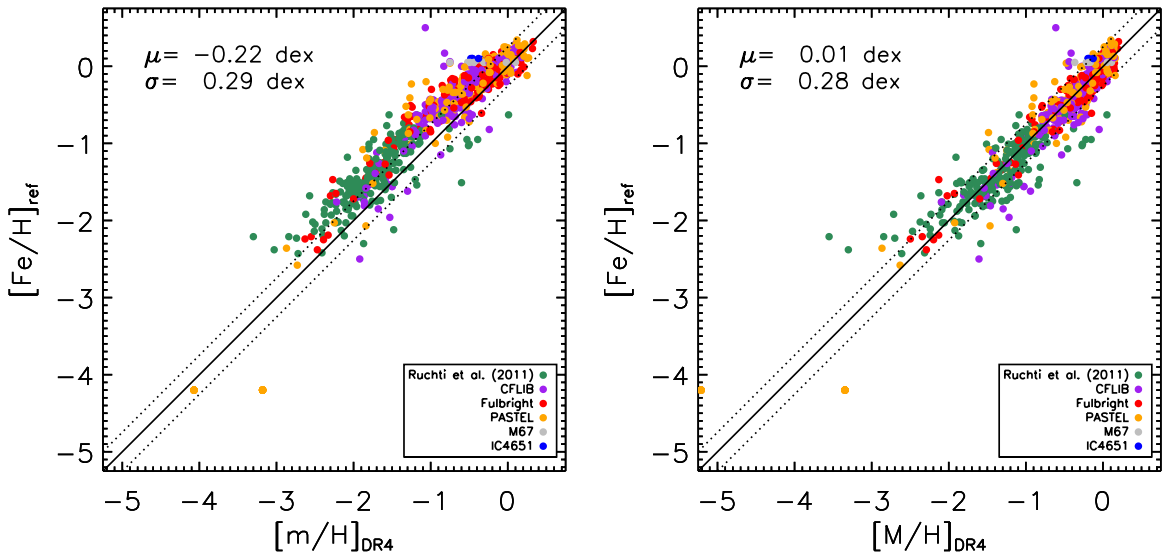

Figure 8. Comparison between the reference iron abundances found in the literature ($[Fe/H]_{ref}$) and the derived overall metallicities ($[m/H]_{DR4}$, left panel) and the calibrated overall metallicities ($[M/H]_{DR4}$, right panel), according to Equation (7). Color-coding for each data set is the same as in Figure 5. Dotted diagonal lines represent offsets from unity of ±0.25 dex.

(A color version of this figure is available in the online journal.)

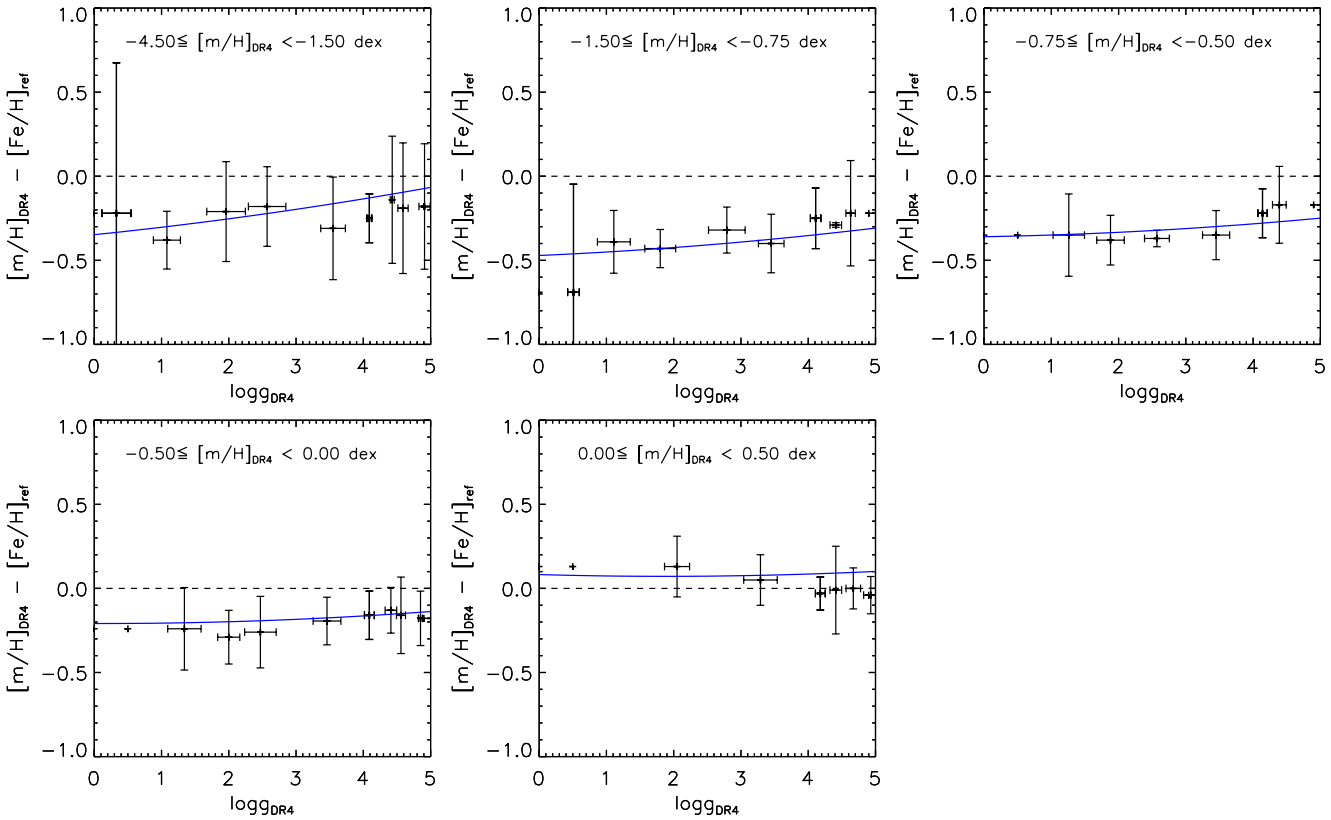

Figure 9. Trends in the metallicity determination for different gravity bins, at different metallicity ranges. The error bars correspond to the dispersion of log g and the error in metallicity inside each bin. The blue lines represent the polynomial that has been adopted in order to best describe the metallicity offsets. It corresponds to the polynomial of Equation (7) and has been computed for the mean metallicity of each subsample.

(A color version of this figure is available in the online journal.)

This bias is not the same for all metallicities, and it is more important for metal-poor stars than in the metal-rich regime. We investigated the correlations of the errors and found that the main parameters driving the bias are the surface gravity and the metallicity itself. Figure 9 illustrates the covariance of the residual errors on the metallicity with respect to the surface gravity, for different metallicity ranges. In this figure, each point and error bar represent the median and the dispersion of the metallicity error for the stars inside each gravity bin. This binning approach smooths the errors, minimizes the impact of outliers, and highlights the general trends of the biases. On one hand, the results of Figure 9 show for the lowest metallicities a rather constant underestimation of the metallicity by 0.2 dex. On the other hand, there are some clear trends in the more metal-rich regimes, where the giant stars exhibit higher offsets than the dwarfs. These trends are too strong to be explained by a variation of microturbulent velocity along the giant branch, where the expected offsets should be less than 0.1 dex (see, e.g., Kirby et al. 2009).

Using the binned points of Figure 9, the resulting fit of a quadratic surface for the errors in metallicity, taking into account the dependences on both the surface gravity and the metallicity, is

$$\begin{aligned}[\mathrm{m/H}] - [\mathrm{M/H}]_{\mathrm{ref}} = & -0.076 - 0.006 \times \log g + 0.003 \\ & \times \log^2 g - 0.021 \times [\mathrm{m/H}] \times \log g \\ & + 0.582 \times [\mathrm{m/H}] + 0.205 \times [\mathrm{m/H}]^2. \end{aligned} \quad (7)$$

Given this relation, the trend for the typical mean metallicity inside each box of Figure 9 has been plotted in blue. As expected, the fits are in good agreement with the offsets, hence assimilating the metallicity calibration relation to Equation (7). The right panel of Figure 8 shows the improvement that has been made on the metallicity determination thanks to the correction of Equation (7). We note, however, that due to the lack of reference stars with super-solar metallicities, our calibration is not optimal for [M/H] $>$ +0.1 dex. This limitation will be addressed in a future study.

A more detailed investigation of the residuals for different gravity regimes and with respect to the calibrated metallicity is shown in Figure 10, for the Ruchti, Fulbright, PASTEL, and CFLIB libraries. As expected, there is no bias for the calibrated metallicity (lower plots), nor for the other parameters, except for the surface gravity of the lowest gravity giant stars (see also Section 6.1). The self-consistency of the calibration is hence validated.

4.4. A Comment on RAVE DR1, DR2, and DR3 Parameters

Previous RAVE data releases used the Munari et al. (2005) grid of synthetic spectra and a penalized χ^2 algorithm in order to determine the effective temperatures, surface gravities, overall metallicities, and α-abundances. The stellar rotational velocities (V_{rot}) and the microturbulent velocities (ξ) were also left as free parameters, although without attributing any constraint on these values in the end.[32] Furthermore, the 2MASS photometric information was not used to help reduce spectral degeneracies, and the calibration data sets were not fully available.

[32] For DR3 the microturbulent parameter was fixed at $\xi = 2$ km s^{-1}.

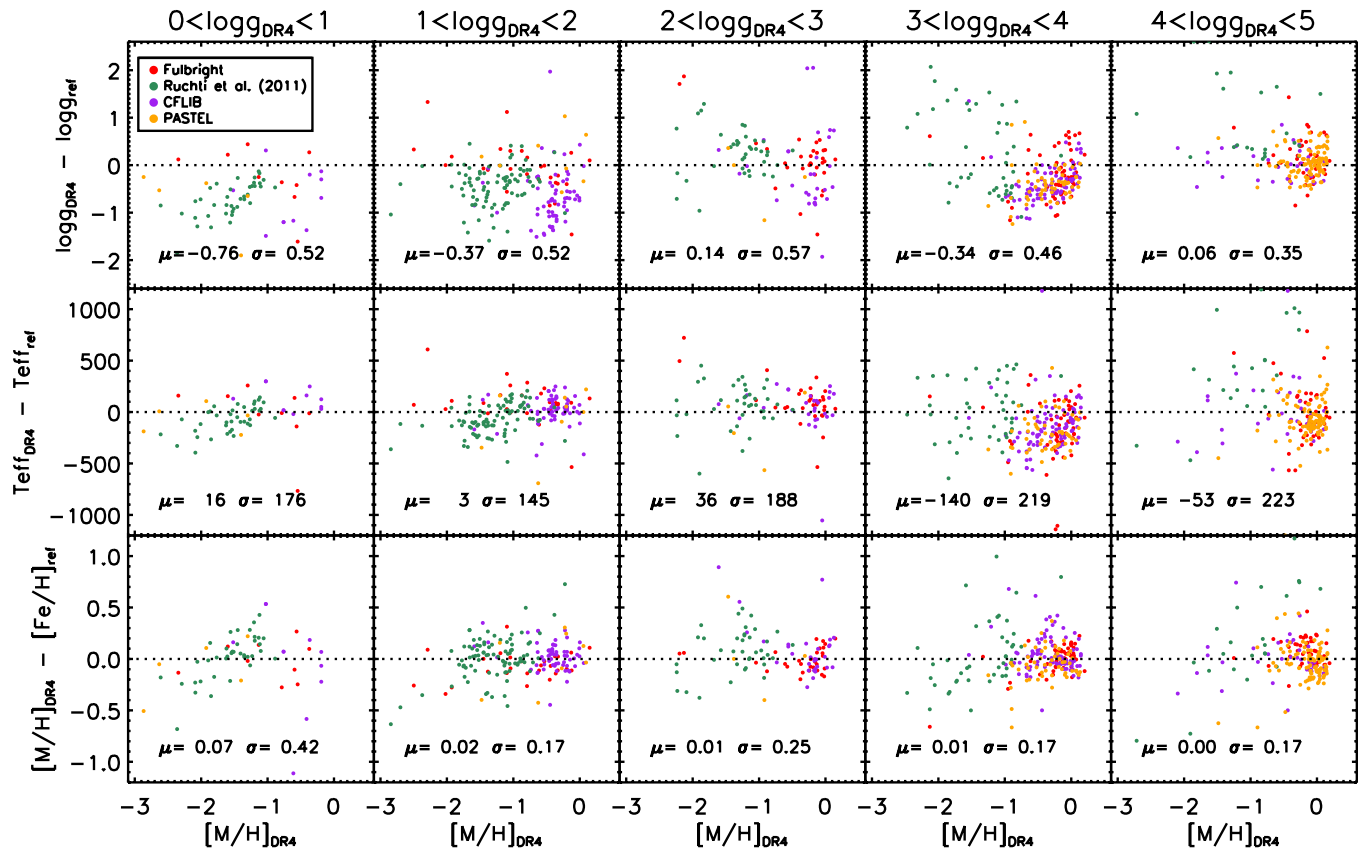

Figure 10. DR4 residual plots for RAVE (RAVE-PASTEL in yellow, Ruchti in green, and Fulbright in red) and RAVE-like spectra (CFLIB, in purple). The trends in the stellar parameter systematics are shown with respect to the calibrated metallicity, divided into different (DR4) log g bins of 1 dex. In each panel, the median offset and the dispersion is indicated.

(A color version of this figure is available in the online journal.)

The present DR4 pipeline reduces the parameter space to only the three free atmospheric parameters we are trying to measure. In addition to imposing a photometric effective temperature range, the new pipeline explores more efficiently the parameter space, thanks to the decision-tree algorithm. This makes the new results more robust and less susceptible to biases caused by spectral degeneracies.

Efficient exploration of the low-dimension parameter space is crucial for the accurate determination of the atmospheric parameters and calibration of the results. Indeed, tests done on the above-mentioned calibration data sets, using the DR3 pipeline output, showed that the metallicity biases could not be calibrated adequately, especially for the turn-off stars, where the degeneracy of the distance function is the most important (see Figure 11). As will be shown in Section 6.3, this led to biases and interdependences between the DR3 parameters and motivated the effort to develop the approach implemented here in DR4.

4.5. Sanity Check of the Metallicity Calibration on a Set of Observed Spectra

Our proposed metallicity calibration relation (see Equation (7)) has been further verified on spectra that are not part of the calibration process. For that purpose, we used the 327 RAVE spectra of the GCS stars described previously, 105 non-RAVE spectra from the S^4N library degraded to RAVE resolution (Allende Prieto et al. 2004), and 65 RAVE-like spectra of open and globular cluster stars obtained by the 2.3 m telescope at the SSO, listed in Table 4. We note though that the reference metallicity values that have been adopted for these test spectra are not as reliable as the calibration data sets. Indeed, except for the S^4N library, all the other data sets do not have individual spectroscopically measured metallicities. In addition, non-member stars might be included in the cluster data sets. Finally, the mean metallicity value has been considered for the stars belonging to the globular clusters, whereas dispersions up to few tenths of a dex (Gratton et al. 2004) can be expected in some cases.

The three plots of Figure 12 show the recovered $T_{\rm eff}$–log g diagram of the total considered sample (left), the log g versus residuals in [m/H] (middle), and versus residuals in calibrated [M/H] (right). Despite the relatively large dispersion due to the heterogeneous quality of the data sets, one can see that the bias is greatly reduced in all the samples, and for all gravities, providing a sanity validation check of the calibration relation established previously.

4.6. Computation of the Total Uncertainties of the Pipeline

The errors described in Section 3.5 concern only the internal accuracies of the method. To estimate the total uncertainties of the pipeline, one needs also to estimate the external errors.

We used all the spectra with S/N $\geqslant$ 50 pixel^{-1} of the previously described calibration data set to estimate the external uncertainties for different ranges of stellar parameters. Given the total number of spectra in the data set, we divided the sample into cool ($T_{\rm eff}$ $\leqslant$ 6000 K) and hot ($T_{\rm eff}$ $>$ 6000 K) dwarfs (log g $\geqslant$ 3.5 dex) and giants (log g $<$ 3.5 dex). Furthermore, we also divided into metal-rich ([M/H] $\geqslant$ −0.5 dex) and metal-poor ([M/H] $<$ −0.5 dex) regimes, except for the hot giants, for which not enough stars were available in the sample. The

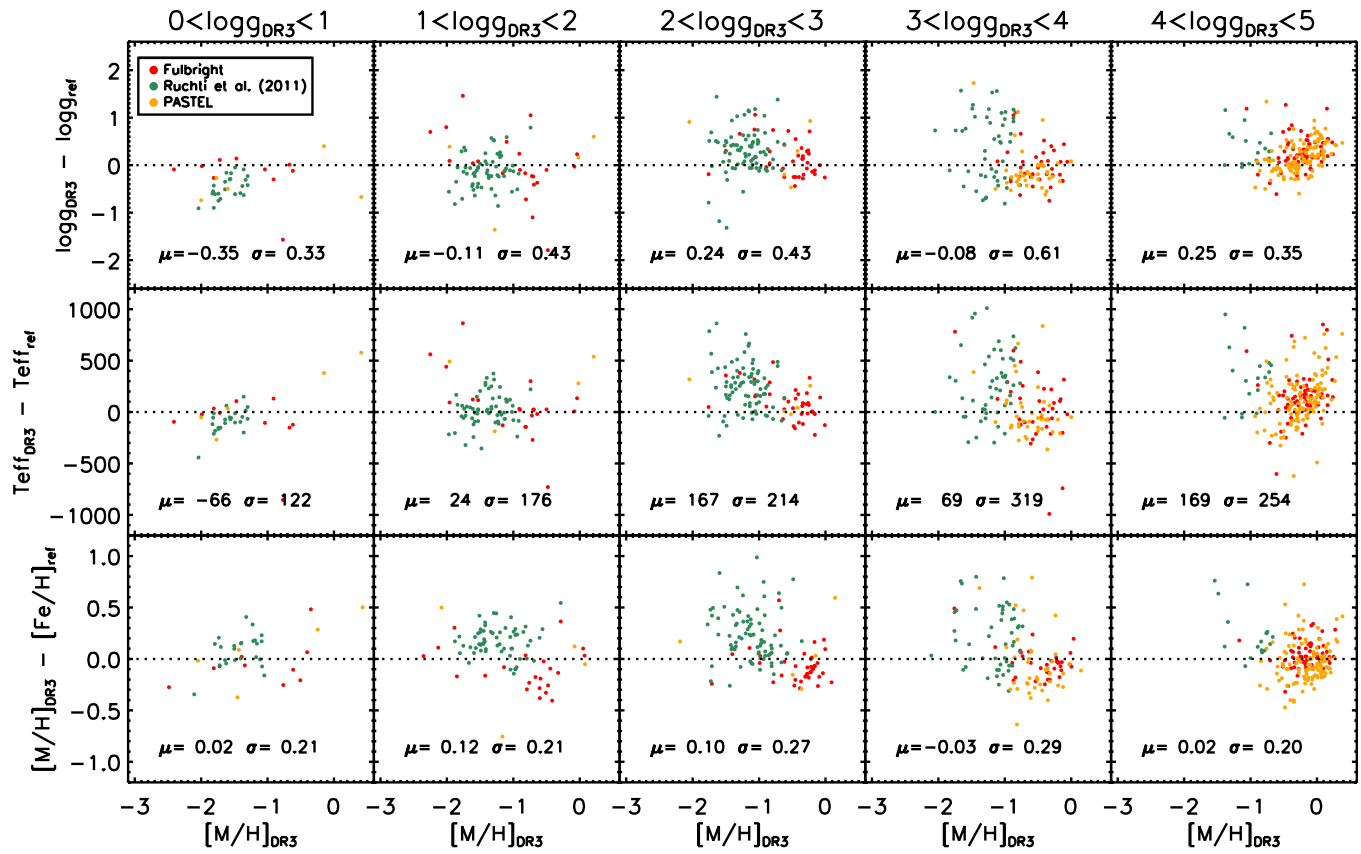

Figure 11. Same as Figure 10 but for the RAVE DR3 pipeline and without the CFLIB analysis. The calibrated metallicities correspond to those obtained using Equation (2) of Siebert et al. (2011b) with parameters $c_0 = 0.578$, $c_1 = 1.095$, $c_3 = 1.246$, $c_4 = -0.520$. The metallicity trends found for the turn-off stars are representative of the uncalibratable biases present in RAVE DR3.

(A color version of this figure is available in the online journal.)

Table 4
Post-calibration Verification Data Sets

Data Set	Type	N Stars	⟨[Fe/H]⟩	σ([Fe/H])	Reference
M5	Globular cluster	8	−1.28	0.11	Ramírez & Cohen (2003)
NGC 3680	Open cluster	7	−0.04	0.03	Pace et al. (2008)
IC4651	Open cluster	5	+0.10	0.05	Pasquini et al. (2004)
M67	Open cluster	10	+0.05	0.04	Pancino et al. (2010)
NGC 6752	Globular cluster	12	−1.42	0.10	Gratton et al. (2001)
NGC 2808	Globular cluster	10	−1.14	0.06	Carretta et al. (2004)
NGC 6397	Globular cluster	11	−2.10	0.05	Koch & McWilliam (2011)
Praesepe	Open cluster	35	+0.14	0.04	Mean literature value
GCS	MW dwarf stars	327	solar	...	Casagrande et al. (2011)
S^4N	MW dwarf stars	105	solar	...	Allende Prieto et al. (2004)

dispersion of the residual differences is presented in Table 5, together with the number of stars that have been considered in order to compute these uncertainties.

Using the values presented in Table 5, the total uncertainties of the pipeline parameter determinations are then estimated by adding in quadrature the external errors with the internal errors given in Tables 1 and 2.

5. COMPUTATION OF THE CHEMICAL ABUNDANCES

The atmospheric parameters inferred in the previous sections are used as an input in order to determine abundances of individual elements. For that purpose, we use an improved version of the RAVE chemical pipeline described in detail in Boeche et al. (2011, afterward B11). Below, we recall the general features of that pipeline and present the current improvements.

The chemical pipeline relies on an EW library that contains the expected EWs of the lines visible in the RAVE wavelength range (604 atomic and molecule lines). These EWs are computed for a grid of stellar parameter values covering the range [4000, 7000] K in $T_{\rm eff}$, [0.0, 5.0] dex in $\log g$, and [−2.5, +0.5] dex in [M/H] and five levels of abundances in the range [−0.4, +0.4] dex relative to the metallicity, in steps of 0.2 dex (adopting the solar abundances of Grevesse & Sauval 1998). The chemical pipeline constructs on-the-fly spectrum models by adopting the effective temperatures and surface gravities obtained by the DR4 pipeline (see Section 3). It then searches for the best-fitting model by minimizing the χ^2 between the models and the observations.

For a given normalized, RV-corrected, and wavelength-calibrated spectrum, the chemical pipeline determines the elemental abundances, following the steps described below:

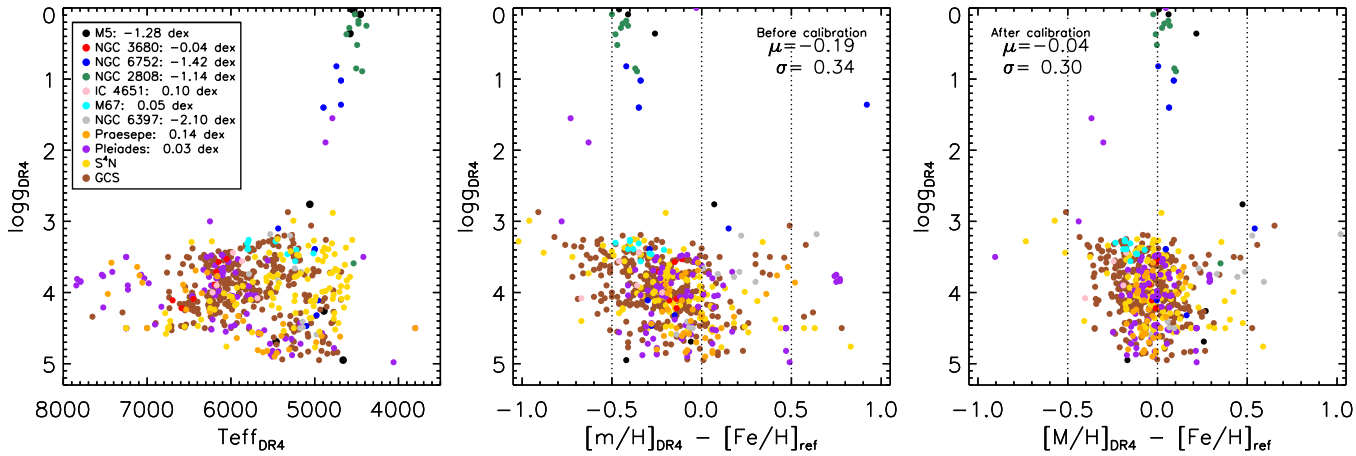

Figure 12. Post-calibration verification data sets of open and globular cluster stars, the Geneva–Copenhagen Survey, and the S^4N library. The plot on the right shows that the offsets are greatly improved once the log g dependent corrections in metallicity have been applied. The mean offsets (μ) and dispersions (σ) of the residuals are noted in the upper corner of each plot.

(A color version of this figure is available in the online journal.)

Table 5
Estimation of the External Uncertainties

Dwarfs				
Parameter Range	N	$\sigma(T_{\rm eff})$	$\sigma(\log g)$	σ([M/H])
$T_{\rm eff} > 6000$, [M/H] < -0.5	28	314	0.466	0.269
$T_{\rm eff} > 6000$, [M/H] $\geqslant -0.5$	104	173	0.276	0.119
$T_{\rm eff} \leqslant 6000$, [M/H] < -0.5	97	253	0.470	0.197
$T_{\rm eff} \leqslant 6000$, [M/H] $\geqslant -0.5$	138	145	0.384	0.111
Giants				
Parameter Range	N	$\sigma(T_{\rm eff})$	$\sigma(\log g)$	σ([M/H])
$T_{\rm eff} > 6000$	8	263	0.423	0.300
$T_{\rm eff} \leqslant 6000$, [M/H] < -0.5	273	191	0.725	0.217
$T_{\rm eff} \leqslant 6000$, [M/H] $\geqslant -0.5$	136	89	0.605	0.144

1. Upload the EWs for the lines at the estimated DR4 $T_{\rm eff}$, log g, [M/H], and for the five different abundance levels.
2. Keep only the lines that, at the given stellar parameters, have large enough EWs to be visible above the noise. Mathematically, the condition to satisfy is the following:

$$\mathrm{EW(m\AA)} > \frac{\sqrt{2\pi}\sigma_{\rm res}}{\mathrm{S/N}} \cdot 1000,$$

   where $\sigma_{\rm res} = 0.56$ Å is the standard deviation of the RAVE Gaussian line profile. In practice, any absorption line whose intensity is larger than 1σ of the noise fulfills this condition.
3. Fit the strong Ca II and H I lines and correct the continuum (see Section 5.3).
4. Construct the curve of growth (COG) of the lines by fitting a polynomial function through the five EW-abundance points.
5. Create the model by assuming a Voigt profile for each line and summing these profiles together (see Section 5.2).
6. Vary the chemical elemental abundances to obtain different models by changing the EWs of the lines according to their COG.
7. Finally, minimize the χ^2 between the models and the observed spectrum to find the best-matching model.

Further details on the line list and the way the EW library has been constructed can be found in B11. In the following subsections we describe the changes that have been brought to B11. These concern a better consideration of the opacity of neighboring lines, an implementation of a pseudo-Voigt profile to model the lines, and an improved continuum re-normalization.

5.1. Equivalent-width Corrections for the Opacity of the Neighboring Lines

The EW library is built using the driver *ewfind* of the spectrum synthesis code MOOG (Sneden 1973), which computes the EW of every line as if they were isolated. Nevertheless, line blends when not carefully taken into account can lead to abundance overestimations. In the case of lines instrumentally (but not physically) blended, the observed blend has a total EW that is the sum of the EWs of the two isolated lines, and thus no problem arises. However, when two lines are physically blended (i.e., not instrumentally), the quantity of radiation absorbed by one line is affected by the opacity of the neighboring line, and the total EW of the blend is smaller than the sum of the two isolated EWs. In this case the blend in the constructed model is too strong, leading to abundance overestimations. In order to avoid such overestimation, we corrected the EWs of the blended lines in the EW library with the following procedure:

1. Consider the line l_0 having EW_0, blended with some lines l_i with EW_i. Compute the ratio $\mathrm{EW}_r = \mathrm{EW}_0/\sum \mathrm{EW}_i$ with EW_0 and EW_i computed as if they were isolated.
2. Synthesize the blend composed by l_0 and all l_i, and measure the overall $\mathrm{EW}_{\rm tot}$.
3. Compute the corrected EW of the line l_0 as $\mathrm{EW}_0^{\rm corr} = \mathrm{EW}_r \cdot \mathrm{EW}_{\rm tot}$.

Two lines are considered blended if they are closer than 0.2 Å. In addition, we applied this correction to lines that are blended with one or more lines having EW > 10 mÅ. Lines with EWs smaller than 10 mÅ would affect the EW of the neighboring lines by less than 0.7%, which can be considered negligible. Although $\mathrm{EW}_0^{\rm corr}$ is only an approximation, the constructed blends with such corrected EWs match the synthesized blend better than 1% of the normalized flux. This correction replaces the previous one adopted in the B11 chemical pipeline.

5.2. Improved Line Profile

Most of the absorption lines in the RAVE wavelength range and resolution have an intrinsic width smaller than the RAVE instrumental profile. Therefore, their line profile is dominated by the instrumental one, which is Gaussian. Nevertheless, this is not the case for the strongest lines, where the broad wings extend beyond the instrumental profile. In that case, the line is better approximated by a Voigt profile.

Compared to B11, the new chemical pipeline drops the simplistic Gaussian assumption and now uses an improved line profile. Because of the difficulties of implementing a real Voigt profile, we use the approximation implemented by Bruce et al. (2000):

$$V(x) = \mathrm{EW} \cdot [rL(x) + (1 - r)G(x)], \quad (8)$$

where L and G are the Lorentzian and Gaussian functions, respectively, and EW is expressed in Å. The r parameter rules the linear combination between L and G, so that when $r = 0$, $V(x)$ is a pure Gaussian, and when $r = 1$, $V(x)$ is a pure Lorentzian. The FWHM of L and G is forced to be identical and varies as a function of the EW with the following relation:

$$\mathrm{FWHM} = \mathrm{FWHM}_{\mathrm{best}} + \mathrm{EW}/4, \quad (9)$$

where $\mathrm{FWHM}_{\mathrm{best}}$ is the best-matching FWHM found by the minimization routine during the best-matching model searching. Unlike Bruce et al. (2000), we make the parameter r dependent from the EW:

$$r = 0.5 \cdot \exp\left(\frac{-1}{(3\mathrm{EW})^2 + 0.001}\right) \quad (10)$$

so that for small EW the line profile is Gaussian and for large EW the line profile approximates a Voigt profile.

Kielkopf (1973) showed that the difference between the real and the pseudo-Voigt profile described by Equation (8) is always smaller than 1.2% for EW = 0.5 Å, which corresponds to an error smaller than 0.72% in EW (Bruce et al. 2000).

5.3. Improved Continuum Re-normalization

In order to remove some fringing effects that sometimes affect the initial input RAVE spectra (the same ones as used by the DR4 pipeline; see Section 3.6), the chemical pipeline has its own internal re-normalization algorithm. It can be summarized as follows (a more detailed discussion can be found in Section 2.5 and Figure 3 of B11):

1. A preliminary metallicity estimation is performed and the modeled metallic lines are subtracted from the observed spectrum.
2. The strong lines belonging to the Ca II and H I are fitted with a Lorentzian profile and subtracted from the observation.
3. The continuum profile is then defined by a box-car smoothing of the residuals obtained after the previous two steps.
4. The strong Ca II and H I lines are added to the continuum profile to obtain the new "continuum." The chemical pipeline does not measure the broad lines of the Ca II and H I, and their profiles are considered part of the continuum level. Therefore, by adding them to the classical continuum, they are excluded from the chemical analysis. It is by comparison with this level of "continuum" that the metallic lines are measured.

This re-normalization permits better continuum placement around the absorption lines for a better elemental abundance estimation. In particular, the new adopted Voigt profile (see Section 5.2) contributes to improve the continuum placement thanks to the superior fit of the line's wings, which can now be properly subtracted during the re-normalization procedure.

The present chemical pipeline applies the continuum placement like the chemical pipeline outlined in B11 (see their Section 2.5), with the difference that it is applied twice for spectra with S/N $\geqslant$ 40 pixel^{-1} and only once for S/N $<$ 40 pixel^{-1}. Indeed, thanks to the pseudo-Voigt profile, the continuum placement process becomes more stable at S/N $\geqslant$ 40 pixel^{-1}, and when applied iteratively the continuum estimation converges after two iterations. On the other hand, for S/N $<$ 40 pixel^{-1} the continuum estimation cannot converge to the right level. The noise spikes (mistaken as metallic lines by the code) lead to a too high continuum placement and, consequently, to a too high metallicity estimation. Thus, the re-normalization is applied only once for low-S/N spectra.

5.4. Precision and Accuracy of the RAVE Chemical Elemental Abundances

In order to evaluate the precision and accuracy of the new chemical pipeline, we ran tests on synthetic and real spectra with known chemical abundances and compared the results with the expected abundances. The samples of synthetic and real spectra used are the same as those employed in B11. This allows us to have a clear view of the achieved improvement between the two pipelines.

Unlike the work presented in B11, we present here the tests and results for only six elements (aluminum, magnesium, silicon, titanium, nickel, and iron). We rejected the calcium abundance as not being reliable (see Section 6.3.1).

5.4.1. Internal Errors: Tests on Synthetic Spectra

The tests have been performed on a sample of 1353 synthetic spectra. The values for the effective temperature and the surface gravity for these spectra have been taken from a mock sample of RAVE observations created using the Besançon model, whereas the adopted chemical abundances have been taken from the Soubiran & Girard (2005) catalog, whose star metallicities span from −1.5 dex to +0.4 dex (for further details on how the sample has been constructed, see B11). This ensures plausible stellar parameters and chemical abundance distributions of the synthetic spectra.

We evaluated the precision and accuracy of the results at S/N = 100, 40, 20 pixel^{-1}. In Figures 13 and 14 we report the detailed results.

Results at S/N = 100 pixel^{-1}. While the B11 chemical pipeline gave slightly underestimated abundances, the present one reduces or removes such underestimation for most of the elements at S/N = 100 pixel^{-1}. [Ni/H] is underestimated by ∼0.1 dex, whereas the [Ti/H] estimate is good for giants but should be rejected for dwarfs (for which Ti lines are too weak for a good estimation).

Results at S/N = 40 pixel^{-1}. All the elements have reliable abundances, except for [Si/H] and [Ti/H], which look overestimated by ∼+0.1 and ∼+0.2 dex, respectively.

Results at S/N = 20 pixel^{-1}. [Fe/H], [Si/H], and [Al/H] are reliable, with uncertainties of ∼0.15–0.20 dex. [Mg/H] and

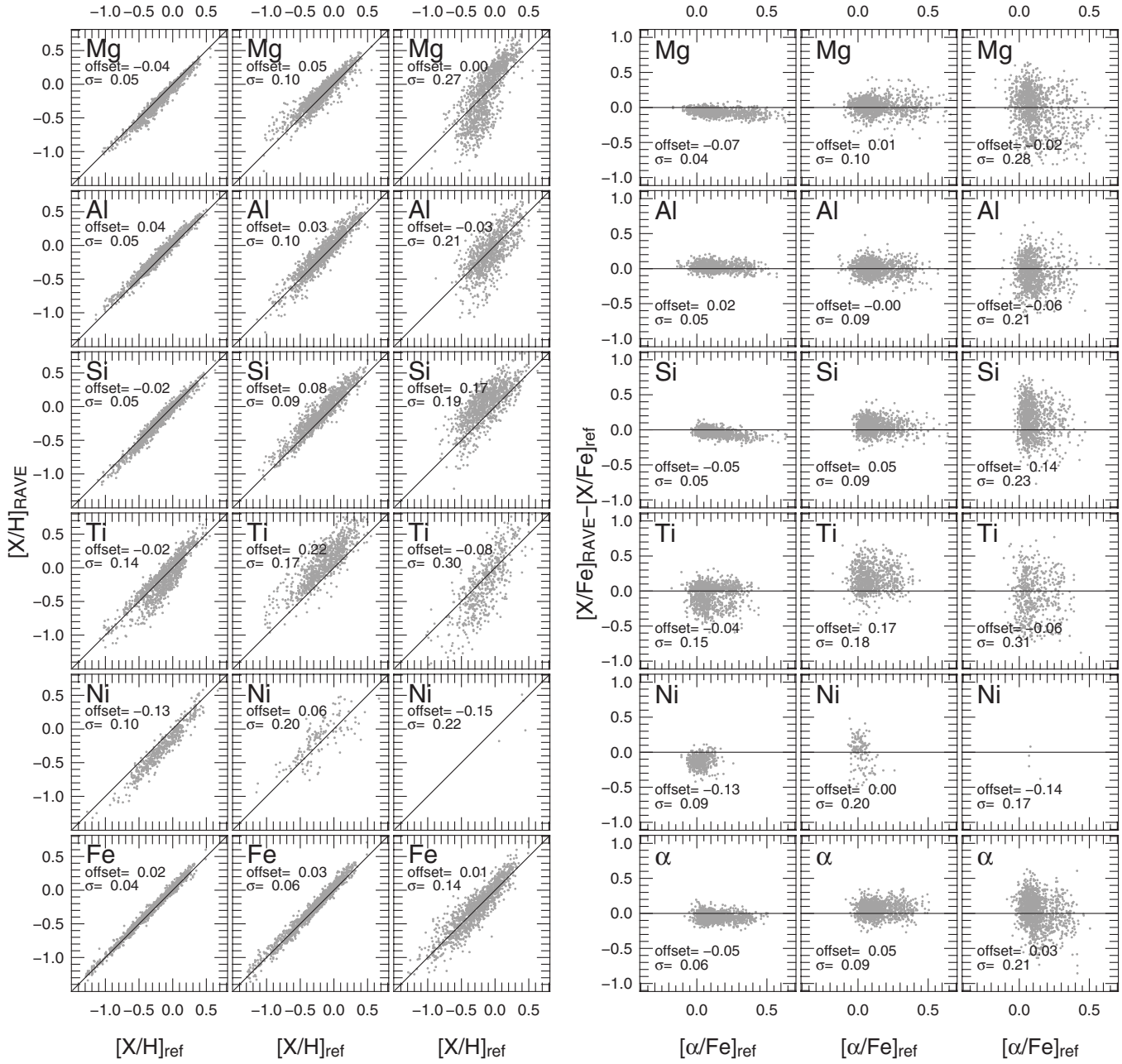

Figure 13. Left: expected elemental abundances [X/H] (*x*-axis) vs. measured elemental abundances (*y*-axis) for the sample of synthetic spectra at S/N = 100, 40, and 20 pixel^{-1} (for the left, middle, and right column, respectively) and assuming no errors in stellar parameters. Right: as in left panels but for the expected enhancement [X/Fe] (*x*-axis) and the residuals measured-minus-expected (*y*-axis). Offsets and standard deviations are reported in the panels. α-abundances are computed as in B11, i.e., the mean of Mg and Si abundances.

[Ti/H] show significant systematics, and [Ni/H] cannot be measured because its lines are too weak.

For Ni and Ti the selection effect due to the S/N is particularly evident. Moving to lower S/N, the number of spectra with Ti and Ni estimations decreases, because the lines of Ti (in dwarfs stars) and Ni are weak in the RAVE wavelength range and do not overcome the noise at low S/N. This selection bias is further discussed in Section 6.3.1.

In general, the new chemical pipeline suffers smaller systematics with respect to the old one. Underestimations are reduced, and abundances of important elements (Fe, Si, Al, and Mg) do not correlate with the effective temperature (see Figure 15) as they did with the previous pipeline. [Ti/H] appears reliable only for cool giants.

We further tested the robustness of our results by repeating the abundance measurements after adjusting randomly the initial $T_{\rm eff}$, $\log g$, and [M/H] by values normally distributed around their true values with $\sigma_{T_{\rm eff}} = 250$ K, $\sigma_{\log g} = 0.5$ dex, and $\sigma_{\rm [M/H]} = 0.2$ dex, respectively. The results are shown in Figure 14. The shifts in stellar parameters (representing the input errors) simply inflate the errors in abundances seen in the test without stellar parameters errors, without introducing any new systematics.

5.4.2. External Errors: Tests on Real Spectra

The overall uncertainties have been estimated by computing the elemental abundances of 98 RAVE spectra of dwarf stars from Soubiran & Girard (2005, hereafter SG05) and 233

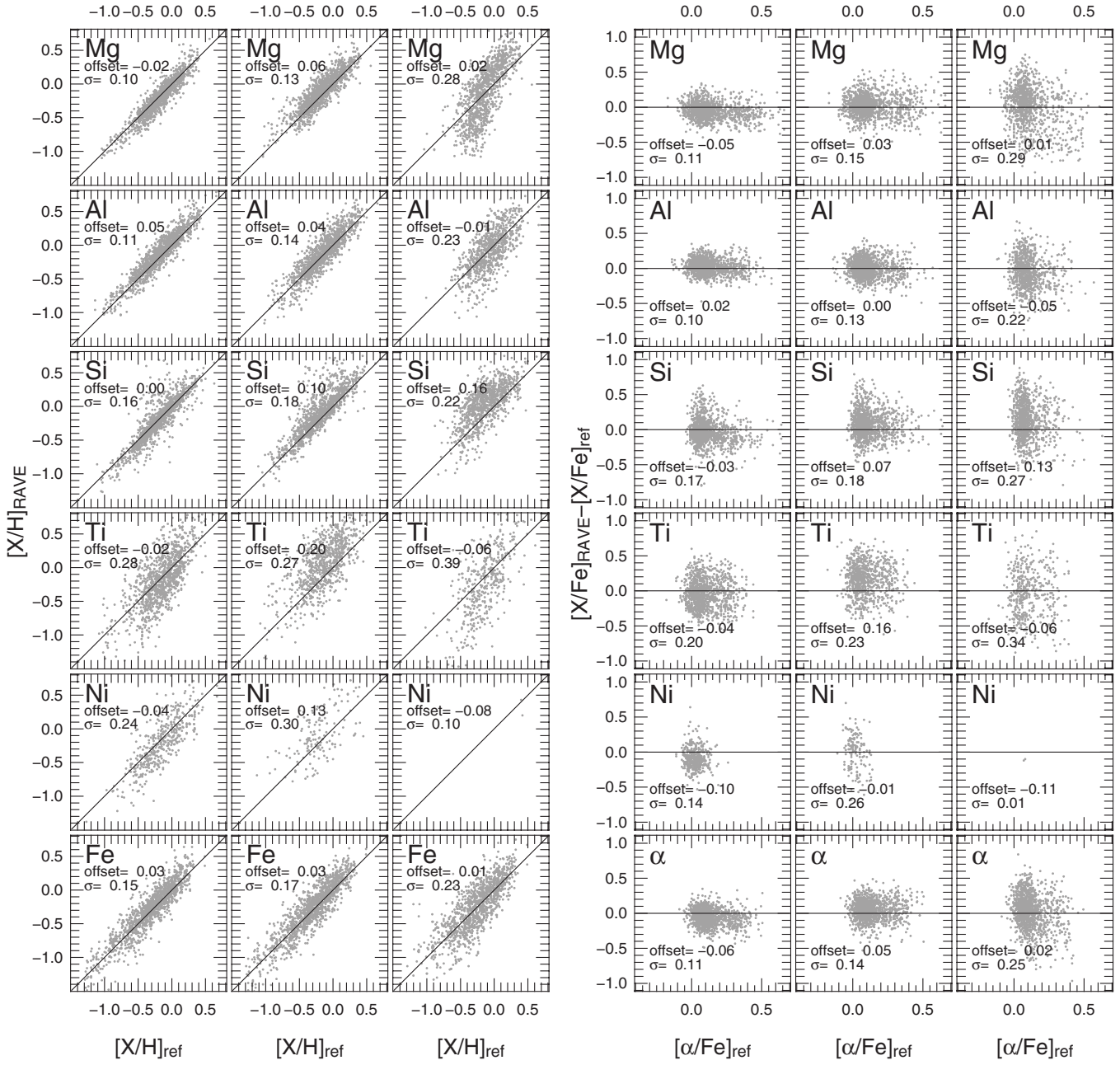

Figure 14. As in Figure 13 but with noisy stellar parameters to simulate the errors appropriate for the RAVE pipeline.

RAVE spectra of 203 giant stars from Ruchti et al. (2011, hereafter R11). Most of the SG05 stars have RAVE spectra with S/N > 100 pixel^{-1}, whereas the R11 stars have RAVE spectra with S/N ranging between 30 pixel^{-1} and 90 pixel^{-1}. Hence, the results are representative of the medium–high S/N regime. Figures 16 and 17 show the results obtained for the six elements in common with SG05 and the four in common with R11.

Adopting the RAVE DR4 stellar parameters, the RAVE chemical pipeline delivers slightly underestimated abundances for Mg, Al, and Ti (∼ −0.1 dex). There is a general improvement in precision for most of the elements with respect to the B11 pipeline (dispersions smaller than ∼0.05–0.07 dex for Mg, Ti, and Fe) with no visible systematic offsets. The estimated errors in abundance depend on the element and range from 0.17 dex for Mg, Al, and Ti to 0.3 dex for Ti and Ni. The error for Fe is estimated as 0.23 dex. We note that the errors reported here are conservative estimations of the RAVE abundance errors, because we are comparing our results with other more precise but still uncertain measurements, and we have not corrected the variance for the second contribution. For illustration, assuming an uncertainty in the reference abundances of 0.1 dex, our estimated RAVE errors decrease by 0.03–0.05 dex.

6. FOURTH PUBLIC DATA RELEASE: CATALOG PRESENTATION

The fourth public data release of the RAVE data (RAVE DR4) includes the observations obtained from the 2004 April 3 to the 2012 December 20. In total, 425,561 stars have been observed, collecting 482,430 spectra. The catalog is accessible online, and it contains also radial velocities, proper motions, photometric information, stellar morphological flags (coming from Matijevič et al. 2012), line-of-sight distances, ages, and

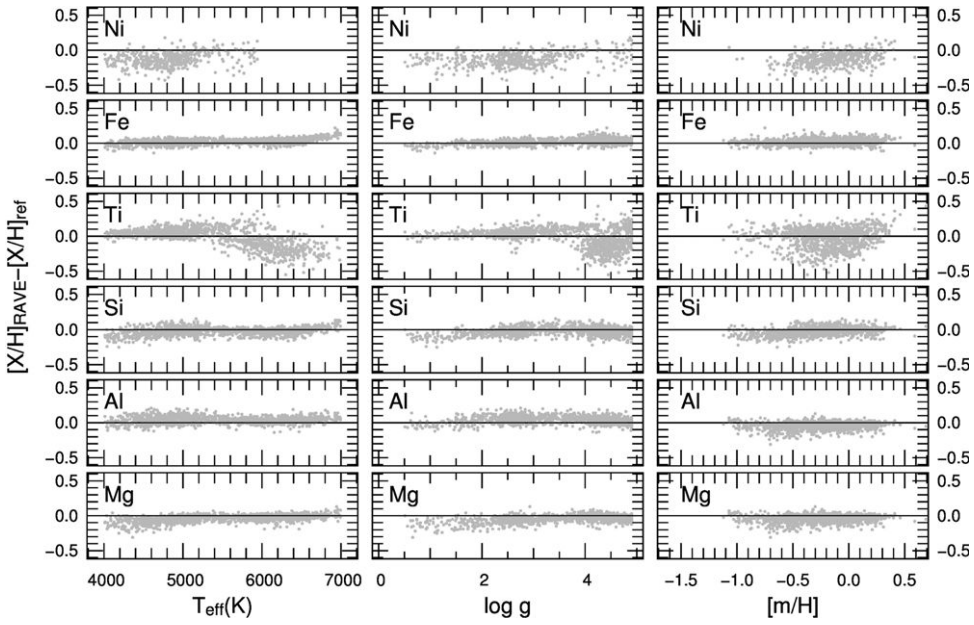

Figure 15. Correlation between the elemental abundance residuals and the stellar parameters at S/N = 100 pixel^{-1}.

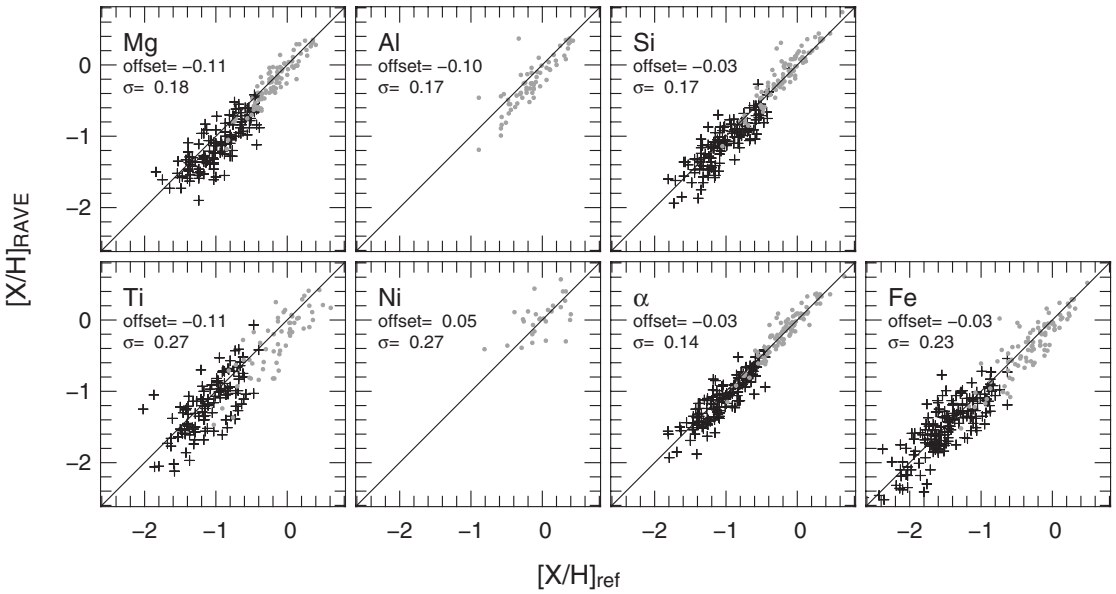

Figure 16. Comparison between the reference high-resolution elemental abundances (*x*-axis) and RAVE elemental abundances (*y*-axis) for the SG05 (98 dwarf stars, gray dots) and the R11 samples (233 spectra of 203 giant stars, black "+") measured by adopting the stellar parameters provided by the RAVE pipeline.

interstellar extinction for each star. In addition, the parameters obtained with the previous DR3 pipeline are also published, to assist readers of papers published based on those parameters, though we strongly recommend the use of the parameters obtained with the latest DR4 pipeline in all future analyses. The DR4 catalog can be queried or retrieved from the Vizier database at the Centre de Données Astronomiques de Strasbourg (CDS), as well as from the RAVE collaboration Web site (www.rave-survey.org).

The completeness of the published catalog for the radial velocities, atmospheric parameters, distances, and chemical abundances with respect to the I_{2MASS} catalog can be seen in Figure 18. In addition, Aitoff maps for the completeness of the catalog at four different magnitude bins as a function of the stellar positions on the sky are shown in Figure 3.

Below we discuss which criteria to apply in order to obtain a high-quality and reliable sample of stars from the catalog of the atmospheric parameters and the elemental abundances. Brief discussions about proper motions, radial velocities, distances, and the new APASS photometry are also included in what follows, but we refer the reader to Siebert et al. (2011b), Zwitter et al. (2010), and Binney et al. (2013) for full details.

6.1. Criteria for Reliable Sub-sample Selection Considering the Atmospheric Parameters

The following criteria need to be understood as the confidence limits for selection based on observational (S/N) and pipeline limitations (mainly the boundaries of the grid).

We selected all the stars that had S/N > 20 pixel^{-1}, had errors in the RV estimation of less than 8 km s^{-1} (measured by RAVE DR3; see Section 8), had derived $\log g >$ 0.5 dex, determined $T_{\rm eff} >$ 3800 K, and calibrated metallicity [M/H]> −5 dex (measured by the DR4 pipeline), and for which

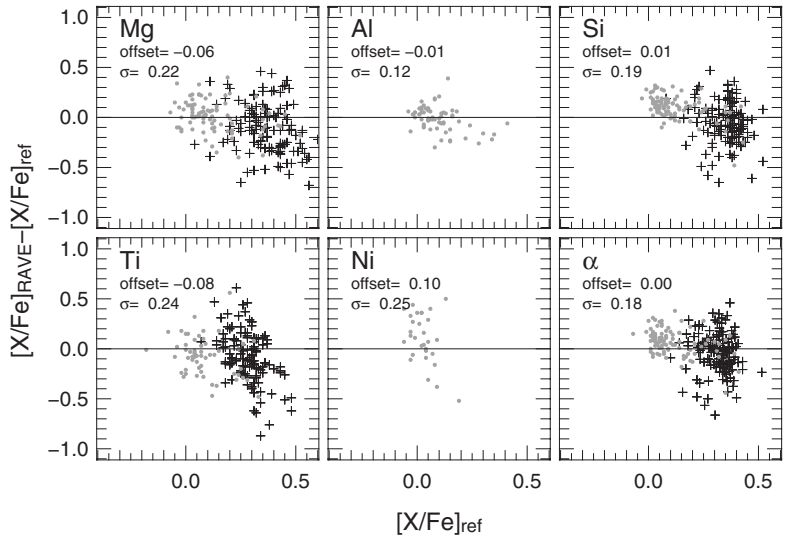

Figure 17. Comparison between expected relative elemental abundance (*x*-axis) and residual abundances RAVE-minus-reference (*y*-axis). Stellar parameters adopted and symbols are as in Figure 16.

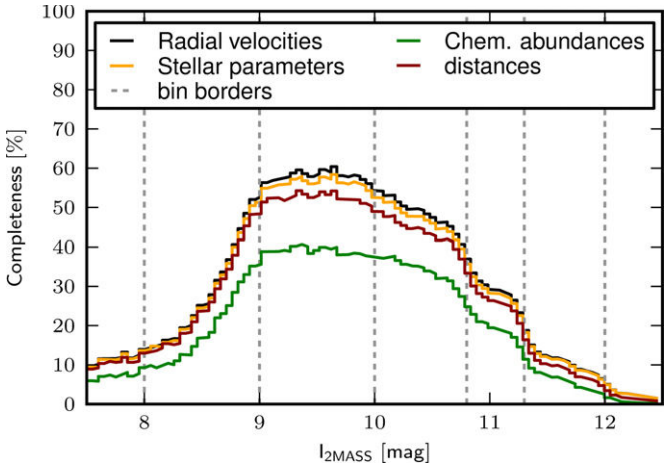

Figure 18. Fractional completeness of the RAVE DR4 sample with respect to the I_{2MASS} stars for the published radial velocities, stellar atmospheric parameters, chemical abundances, and line-of-sight distances.

(A color version of this figure is available in the online journal.)

the DR4 algorithm had converged toward a stable solution.[33] In total, roughly 19% ($\sim 8.7 \times 10^4$) of the spectra have been rejected after these quality criteria. We are working toward the next DR5 RAVE data release, with work that we hope will improve the parameters for at least some of these currently non-reliable stars.

The cut on the error on the RV ($\Delta V_{HRV} < 8$ km s^{-1}, 12,974 spectra) has been defined based on the results of Kordopatis et al. (2011a), where it has been shown that for Doppler shifts larger than approximately half a pixel, the results of the pipeline were seriously degraded. Nevertheless, a criterion based on the Tonry–Davis correlation coefficient (R) might be preferred in some cases, since some stars can have large errors but good R (due, for example, to strong hydrogen lines) and vice versa (small errors but $R < 5$).

The removal of the stars with gravities lower or equal to 0.5 dex (25,882 spectra), T_{eff} lower than 3800 K (20,143 spectra), and/or calibrated [M/H] lower than −5 dex (1282 spectra) has been decided because the results are considered both unrealistic (the synthetic spectra computed with the MARCS atmospheric models at such $\log g$ have not been carefully compared to real spectra) and less reliable (e.g., missing models in the reference grid). Finally, the cut on the convergence of the DR4 algorithm (14,454 spectra) is made in order to minimize cases badly affected by the spectral degeneracies. Indeed, these degeneracies can cause, in some cases, an impossibility for the algorithm to converge due to a negative gradient in the distance function between the spectrum and the templates. MATISSE can in some cases oscillate between two solutions (∼11% of the published sample). We decided to keep these solutions because, in general, they are close in the parameter space. Nevertheless, in case the user decides not to use them, we have flagged these stars in the *algo_conv* parameter, which is also published with this data release (see the Appendix).

An additional cut, based on the velocity width parameter of the spectral lines, V_{rot}, has been applied, since our algorithm cannot treat fast rotators. We discarded empirically stars at the high-velocity tail of the distribution ($V_{rot} > 100$ km s^{-1}, 11,735 in total). We recall that the estimation of the V_{rot} is made through the DR3 pipeline, as a free parameter, at the same moment as the first estimation of T_{eff}, $\log g$, and [M/H] is made. Nevertheless, the rather low resolving power of RAVE spectra (∼1.2 Å or 30 km s^{-1}) does not allow the determination of rotational velocities for slow rotators, which represent the vast majority of RAVE stars. Hence, this parameter is not published, but true fast rotators will be discussed in a separate paper.

Finally, we note that targets at low Galactic latitudes should also be treated with caution, since the possibly high interstellar extinctions in these directions are not taken into account in the photometric constraints imposed by the DR4 pipeline.

6.2. Criteria for Reliable Sub-sample Selection Considering the Chemical Abundances

From the whole RAVE internal data set, we measured chemical abundances only for spectra with the following features:

1. Effective temperature $4000 \leqslant T_{eff}$ (K)$\leqslant 7000$ K
2. S/N > 20 pixel^{-1}
3. Rotational velocity $V_{rot} < 50$ km s^{-1}.

[33] MATISSE iterates up to 10 times until the result of the projection of the spectrum on the projection functions $B_\theta(\lambda)$ is within the parameter range defined by the $B_\theta(\lambda)$ (see Recio-Blanco et al. 2006; Kordopatis et al. 2011a, and Section 3.3)

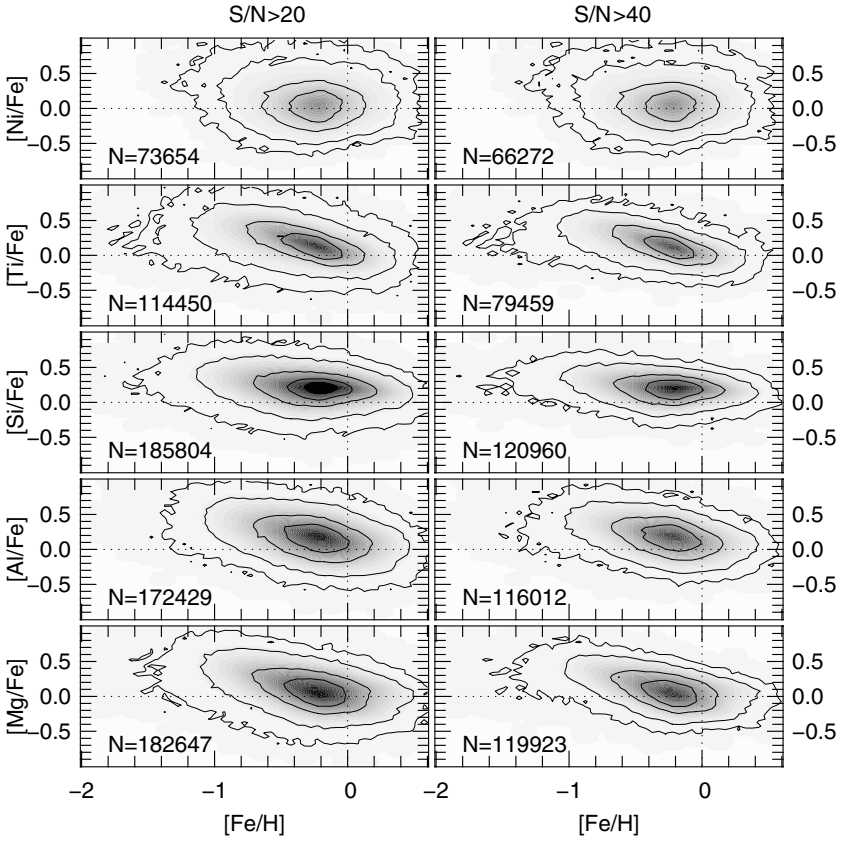

Figure 19. Distribution on the chemical plane of spectra after the application of the quality indicators reported in Section 6.2. The isocontours hold 34.0%, 68.0%, 95.0%, and 99.5% of the sample.

Such limitations are due to the following facts. First, the EW library (and the B11 line list on which it is based) is reliable only in this effective temperature range. In addition, the line measurement and stellar parameters are reliable only for S/N larger than 20 pixel^{-1}. Finally, the absorption lines can be reliably measured only if their FWHM does not significantly exceed the RAVE instrumental FWHM ($\sim$1.2 Å), which corresponds to a rotational velocity of 30 km s^{-1}. Such criteria leave 313,874 spectra selected from the RAVE database.

Besides the chemical abundances of this selected sample, we provide some extra statistical quantities and flags to be employed for further quality selection:

1. χ^2 *between best-matching model and observed spectrum*. The lower the values, the better the expected abundance precision. We suggest a user reject spectra with $\chi^2 > 2000$.
2. *The value frac*, which represents the fraction of the observed spectrum that satisfactorily matches the model. We suggest a user reject spectra with $frac < 0.7$ (see B11 for further details).
3. *Classification flags by Matijevič et al. (2012)*. We suggest a user select spectra classified as "normal" by Matijevic et al. in order to avoid peculiar objects on which the chemical pipeline fails.
4. $Algo\_Conv$ *value*. This value indicates if the DR4 pipeline has converged or if the stellar parameters were either outside the grid boundaries or MATISSE was oscillating between two values. The higher quality data have $Algo\_Conv = 0$.

The application of these quality flags is left to the user. The number of spectra that meet all such quality flags is 187,305. In Figure 19 we show the distribution of the chemical abundances, given the above-mentioned criteria, for S/N > 20 pixel^{-1} and S/N > 40 pixel^{-1}.

6.3. Results and Comparisons with DR3

A description of Galactic properties based on the published parameters of this catalog is beyond the scope of this paper. Nevertheless, as a sanity check, we explore in this section the general properties of the catalog, by analyzing the correlation of the parameters and the change of the metallicity properties according to the S/N, the effective temperature, or the surface gravity. By comparing the behaviors of the DR3 and the DR4 pipelines, we show that although the differences between the atmospheric parameters of the two methods are relatively subtle, DR4 better reproduces the expected behavior for different subpopulations of stars and thus is the method of choice for most Galaxy evolution studies.

Figure 20 compares the resulting $T_{\rm eff}$–log g diagrams of the DR4 and the DR3 pipelines as selected according to the criteria of Section 6.1. One can notice that besides the well-understood and described discretization due to the DEGAS algorithm, there are some additional subtle differences in the parameters of the two pipelines. In particular, hot dwarfs, as well as turn-off stars, have now smaller surface gravities and the main sequence is better defined. Finally, giants have slightly higher effective temperatures.

The DR4 and DR3[34] calibrated metallicity trends, as a function of the surface gravity and the effective temperatures, can be seen in Figure 21. As far as the $T_{\rm eff}$ dependencies

[34] Calibrated according to Equation (2) of Siebert et al. (2011b), with $c_0 = 0.578$, $c_1 = 1.095$, $c_3 = 1.246$, $c_4 = -0.520$.

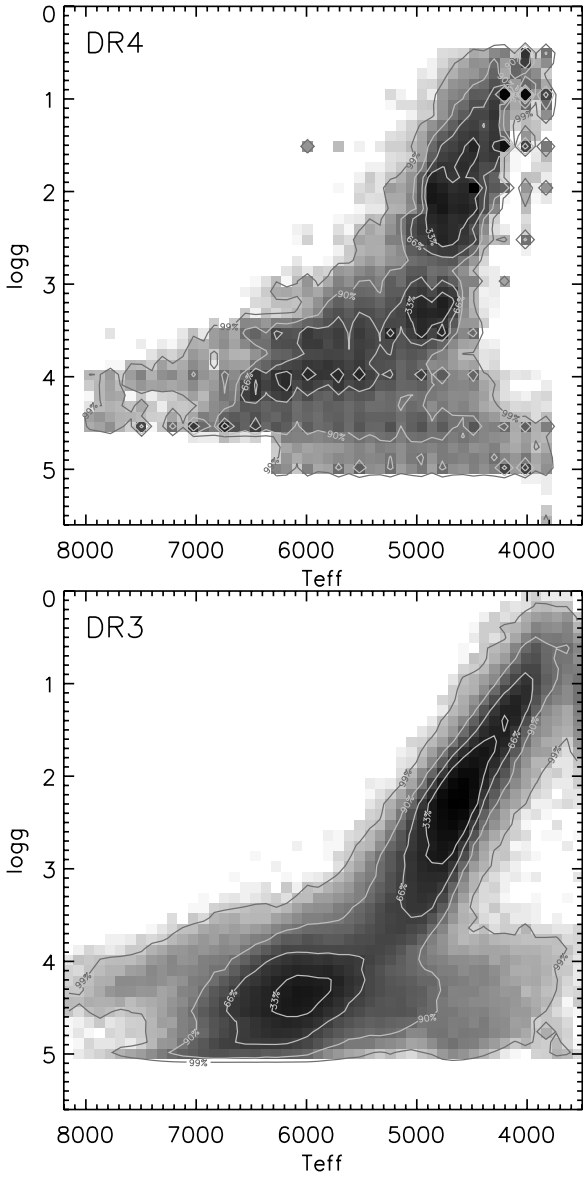

Figure 20. $T_{\rm eff}$–log g diagram for the selected RAVE stars (top: DR4 pipeline; bottom: DR3 pipeline), meeting our criteria defined in Section 6.1. In total the parameters of $\sim 4 \times 10^5$ spectra are represented in these diagrams. The contour lines contain 33%, 66%, 90%, and 99% of the total considered sample.

are concerned, one can notice that the metallicity distribution functions (MDFs) of the DR4 pipeline get broader when the effective temperature lowers. In particular, the DR4 pipeline finds that the hottest stars have a narrow metallicity distribution with a mean value at slightly super-solar values, as expected for the young stars in the solar neighborhood. This is not the case for the results of the DR3 pipeline, where metallicities as low as [M/H] ~ -0.5 dex are obtained. Furthermore, from the isocontours of the log g versus [M/H], we can see that despite the mild pixelization of the values, there are no trends of the metallicities as a function of the surface gravity for the dwarfs, as derived by the DR4 pipeline. This is not the case for the DR3 pipeline results, where a shift is noticed.

In order to investigate whether this shift is real and justified given our classical view of the Milky Way, we explored the stellar heliocentric radial velocities and the evolution of the MDFs for different surface gravity bins. Figure 22 shows the resulting histograms for the calibrated metallicities of the DR4 (in black solid lines) and the DR3 pipelines (red dashed lines). The RV dispersions of the selected stars have also been reported inside each box. For the lower panels, corresponding to the dwarf stars ($3.5 <$ log g < 5 dex), the RV dispersion stays constant. Considering that each Galactic population (thin disk, thick disk, and halo) is characterized by a different velocity dispersion, the constant $\sigma_{V_{\rm HRV}}$ that is found indicates that the same proportions of Galactic populations are probed for these gravity bins. As a result, the MDFs should not vary inside these bins. This is the case only for the DR4 MDFs, the DR3 ones shifting by 0.2 dex in this range of log g. As far as the sub-giant and giant stars are concerned, a good agreement is found between the DR3 and DR4 MDFs, with a shift toward lower metallicities with decreasing log g and at the same time an increase in the RV dispersion. This is in agreement with a change in the mixture of the probed Galactic populations as a function of the probed volume, passing from an old thin disk dominated population to the presence of more halo stars for the larger volume probed by the more luminous giant stars.

To show the correlations between the parameters, we select among the DR4 catalog those stars that are observed multiple times, and for which several independent spectra and derived parameter sets are available. In the panels we plot the differences between the several determinations of the measured $T_{\rm eff}$, log g, and calibrated metallicities. Figure 23 shows the results for the stars with S/N > 20 pixel^{-1}, for both DR4 and DR3 pipelines. From that figure one can see that the new DR4 pipeline is more robust than the DR3 one, since the bulk of the stellar parameters show a very small discrepancy between the repeated observations, as well as a negligible parameter correlation. This validates once more the robustness of our calibration relation of Equation (7). However, we note that correlations between the parameter estimations still exist for some stars. This is expected, due to the intrinsic spectral degeneracy: an underestimation of the $T_{\rm eff}$ leads to a similar underestimation of the log g and the [M/H].

The robustness of the DR4 pipeline in terms of better treatment of the spectral degeneracies can also be seen in Figure 24. The evolution of the mean metallicity as a function of the S/N (yellow points on Figure 24) shows no trends down to S/N $>$ 15 pixel^{-1}. Nevertheless, the cost for this better treatment is the pixelation of the results for the most metal-poor stars or the ones having low S/N. In particular, the pixelization effect can be clearly seen in Figure 24 below the threshold of S/N $= 30$ pixel^{-1}. Indeed, we recall that for all the observed spectra DEGAS is first used to find the nominal template spectrum of the learning grid in order to re-normalize the observed one. Then, on one hand, for the high-S/N regime, the MATISSE algorithm is used on these optimally re-normalized spectra in order to obtain the final parameters. On the other hand, for the low-S/N data ($<$30 pixel^{-1}) and at the boundaries of the learning grid, tests on synthetic spectra have shown that the projection method was giving less accurate results than the decision tree. Given these facts, Kordopatis et al. (2011a) showed that DEGAS is preferred over the projection approach of MATISSE for S/N < 30 pixel^{-1}, even if a pixelization of the parameters is introduced.

6.3.1. Chemical Abundance Reliability: Element by Element

Besides the quality indicators described in Section 6.2, the number of measured absorption lines for an element can be a good indicator of the reliability and precision of the abundance

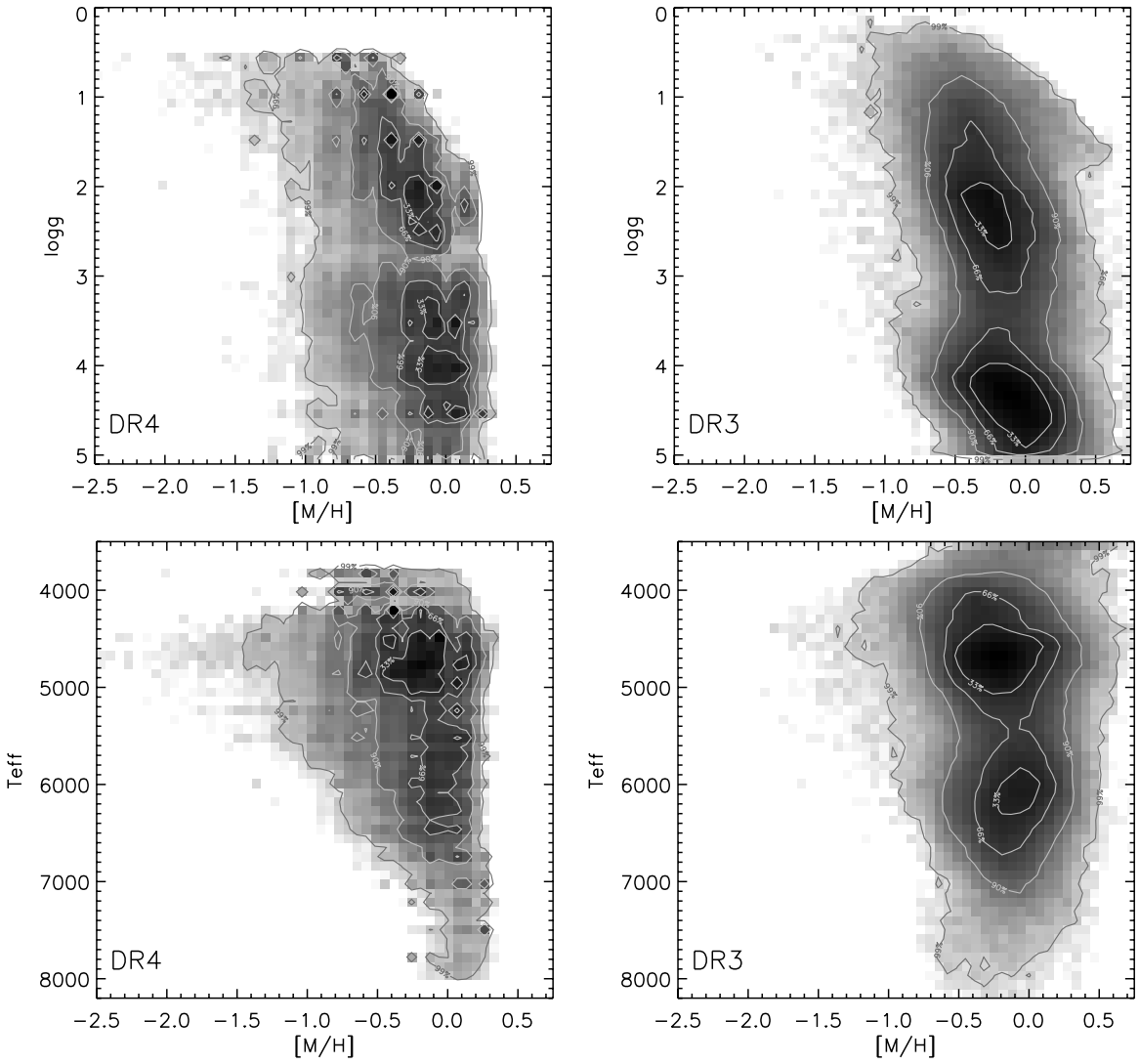

Figure 21. Surface gravity (log g, upper plots) and effective temperature ($T_{\rm eff}$, lower plots) vs. metallicity for all the selected RAVE stars, defined in Section 6.1. The contour lines contain 33%, 66%, 90%, and 99% of the total considered sample. The results for the DR4 pipeline are on the left-hand side, whereas the results from the DR3 pipeline are on the right-hand side. For both pipelines the mean metallicity slightly decreases for the lowest gravities, which is a signature of a different mixture in the probed Galactic populations. In addition, one can notice the log g and the $T_{\rm eff}$ trends that are present for the dwarfs analyzed with the DR3 pipeline.

estimation (as illustrated in Figure 25). We outline here a summary of the expected precision of the abundance element by element.

Magnesium yields reliable results on synthetic and real spectra with no significant correlation with stellar parameters. We expect errors $\sigma_{\rm Mg} \leqslant 0.15$ dex for S/N > 40 pixel^{-1} and $\sigma_{\rm Mg} \sim 0.25$ dex for $20 <$ S/N < 40 pixel^{-1}. Tests on synthetic spectra show that magnesium suffers a systematic error when measured at low S/N. Such an error has not been confirmed with real spectra.

Aluminum gives a reliable abundance although obtained with only two isolated lines. Abundance errors expected are $\sigma_{\rm Al} \leqslant 0.15$ dex for S/N > 40 pixel^{-1} and $\sigma_{\rm Al} \sim 0.25$ dex for $20 <$ S/N < 40 pixel^{-1}.

Silicon is among the most reliably determined elements. Abundance errors expected are $\sigma_{\rm Si} \leqslant 0.15$ dex for S/N $>$ 40 pixel^{-1} and $\sigma_{\rm Si} \sim 0.25$ dex for $20 <$ S/N < 40 pixel^{-1} with a small overestimation of $\sim$0.1 dex.

Titanium gives reliable estimates at high S/N for cool giants ($T_{\rm eff} < 5500$ K and log $g < 3$). We suggest rejecting Ti abundances for dwarf stars. Tests on synthetic and real spectra suggest an expected error of $\sigma_{\rm Ti} \leqslant 0.2$ dex for S/N > 40 pixel^{-1} and $\sigma_{\rm Ti} \sim 0.3$ dex for $20 <$ S/N < 40 pixel^{-1}.

Iron gives robust and precise abundances thanks to its large number of measurable lines at all stellar parameter values. Expected errors are $\sigma_{\rm Fe} \leqslant 0.1$ dex for S/N > 40 pixel^{-1} and $\sigma_{\rm Fe} \sim 0.2$ dex for $20 <$ S/N < 40 pixel^{-1}.

Nickel abundances have to be used with care because of the few lines that are measurable. From synthetic spectra we infer that Ni should be used for cool stars only ($T_{\rm eff} < 5000$ K) and high S/N. In this regime, the abundances are reliable (despite being underestimated by $\sim$0.1 dex) with an expected error of $\sigma_{\rm Ni} \sim 0.25$ dex. The mean abundance correlates with the number of measured lines (i.e., with S/N) as highlighted in Figure 25.

α-enhancement is the average of [Mg/Fe] and [Si/Fe], and it proved to be a robust estimation, particularly useful at low S/N, where the measurements are more uncertain. The expected error is $\sim$0.15 dex for S/N > 40 pixel^{-1} and $\sim$0.2 dex for $20 <$ S/N < 40 pixel^{-1}.

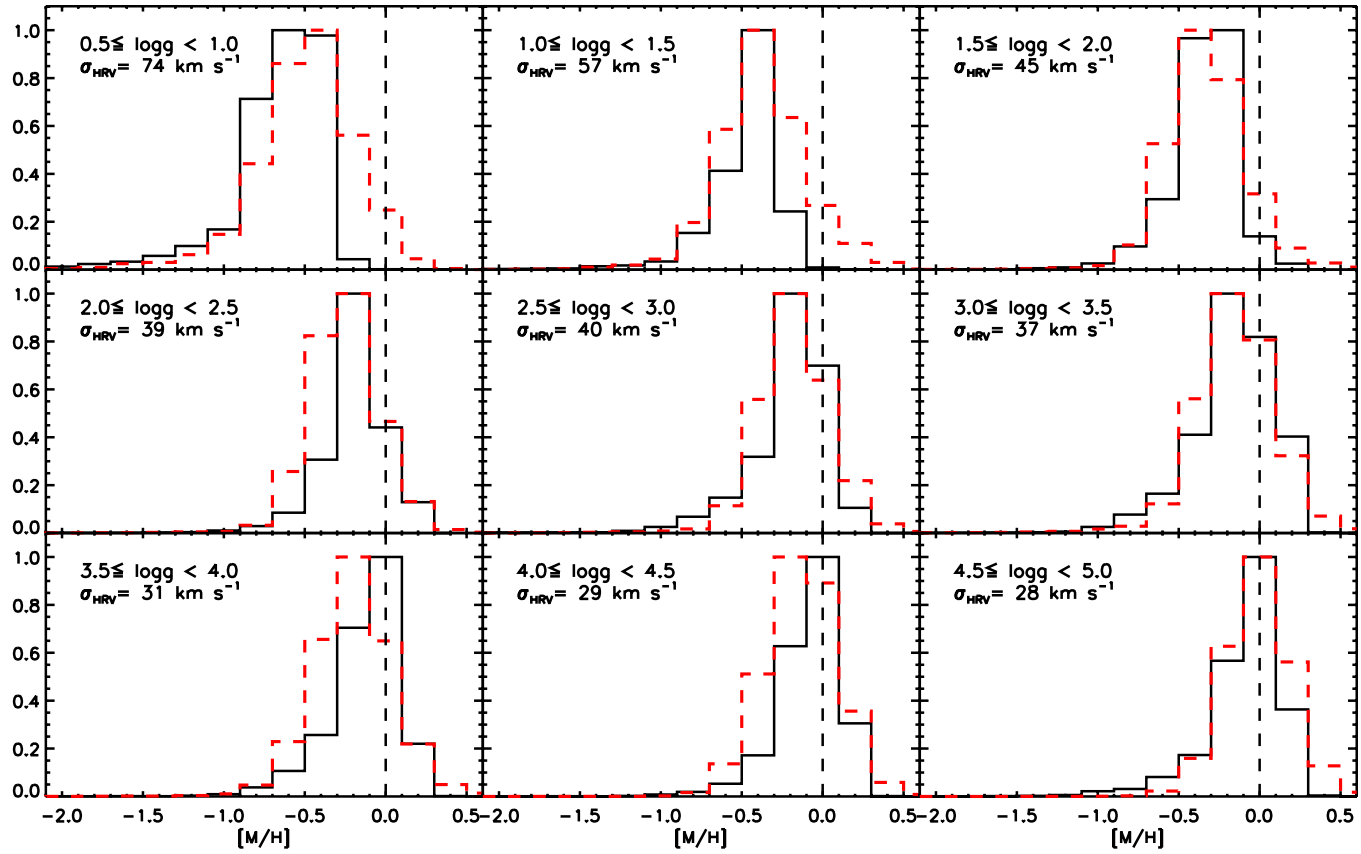

Figure 22. Calibrated metallicity distribution functions for different surface gravity (log g) bins. The peaks of the histograms have been normalized to unity. The mean radial velocity dispersion for the selected stars per surface gravity bin ($\sigma_{\rm HRV}$) is noted in the upper part of each box. RAVE DR4 results are plotted in black solid lines, RAVE DR3 ones in red dotted lines.

(A color version of this figure is available in the online journal.)

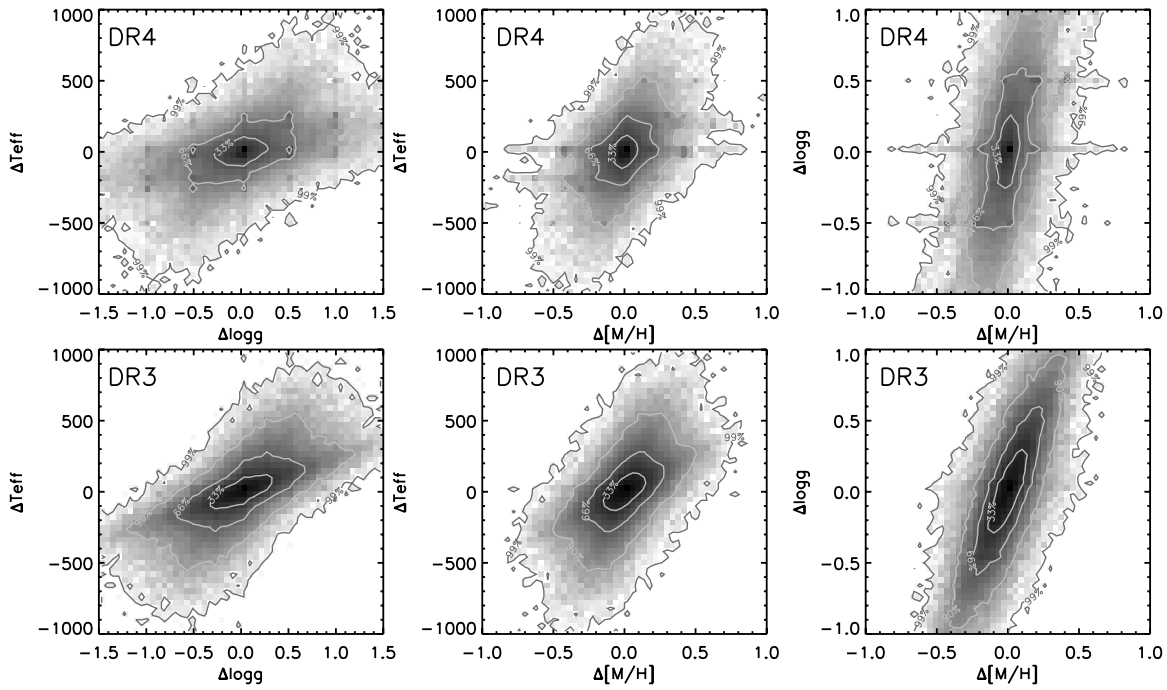

Figure 23. Correlations between the derived atmospheric parameters (top: DR4 pipeline; bottom: DR3 pipeline) for the stars that have been observed several times by RAVE. The isocontour levels contain 33%, 66%, 90%, and 99% of the total considered sample. See the text for an explanation.

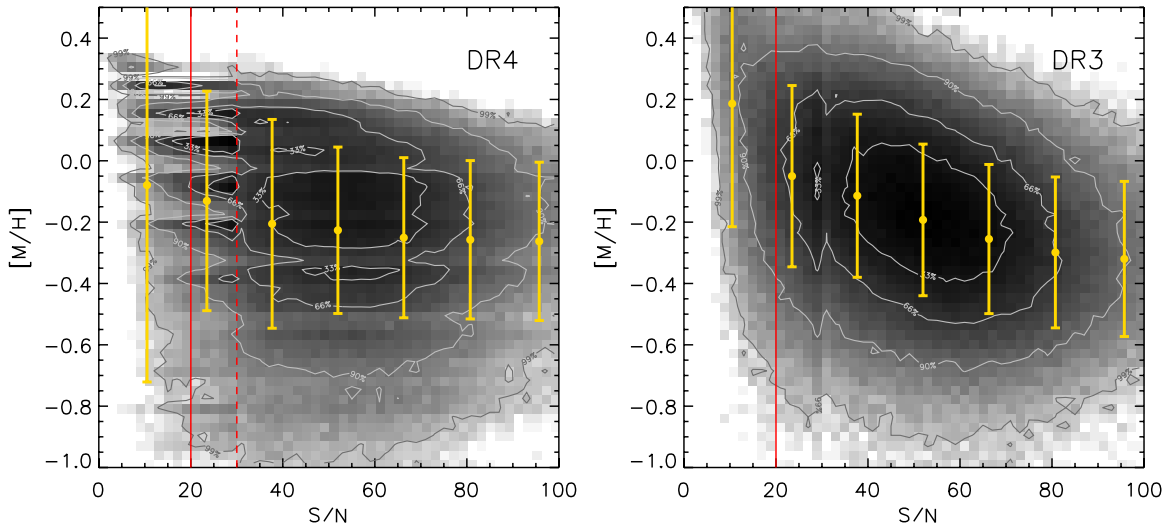

Figure 24. Calibrated [M/H] vs. S/N for the selected RAVE stars with the DR4 pipeline (left-hand side) and the DR3 one (right-hand side). One can notice the pixelization at low S/N (S/N $<$ 30 pixel^{-1}, red dashed line), due to the DEGAS algorithm. The yellow points are calculated as the mean measured metallicity in different S/N bins, and the error bars represent the metallicity dispersion inside each bin. One can notice that the DR4 results (left-hand side) are more stable to S/N changes, compared to the results of the DR3 (right-hand side). A red solid line is plotted at the S/N = 20 pixel^{-1} value, below which the parameters are not considered reliable.

(A color version of this figure is available in the online journal.)

Thanks to the improved line profile and the correction of the EW library for the opacity of the neighboring lines, the continuum re-normalization has improved. The new abundances are now less affected by systematic errors than the previous ones, and their correlations with $T_{\rm eff}$ are now negligible. On the other hand, the new continuum re-normalization reveals the scarcity of information for elements with weak and few visible lines like [Ca/H] (which has been dropped in this data release) and [Ti/H] on dwarf stars, which turns out to be not reliable. A slight correlation between abundances and S/N is present, as shown in Figure 26. Such correlation is negligible for giant stars, whereas for dwarf stars $[{\rm m/H}]_{\rm chem}$ (computed with the formula given by Salaris et al. 1993, see Section 3.4 of B11) increases by ∼0.1 dex from S/N = 80 pixel^{-1} to S/N = 40 pixel^{-1}. The different re-normalization procedure for the two S/N regimes generates the step in average metallicity seen at S/N = 40 pixel^{-1}.

The accuracy of the RAVE abundances depends on many variables, often inter-dependent in a non-linear way, which makes difficult the accuracy estimation of the individual abundances. Indeed, on one hand the abundance accuracy depends on the number of measured absorption lines. On the other hand, the number of measurable lines (i.e., strong enough to be identified in the noise) depends on S/N and on the stellar parameters. In Figure 25 the dispersion of the residuals between measured and expected abundances (for the sample of synthetic spectra) decreases as the number of measured lines increases. This number is a useful index of goodness of the abundance accuracy, although it must be considered together with S/N. In Figure 27 we illustrate the fraction of spectra having an abundance estimation (i.e., at least one absorption line measured) for different elements, and how this fraction decreases when S/N and/or metallicity decrease. This is a selection effect due to the measurement process, and it must be taken into account during data analysis and interpretation.

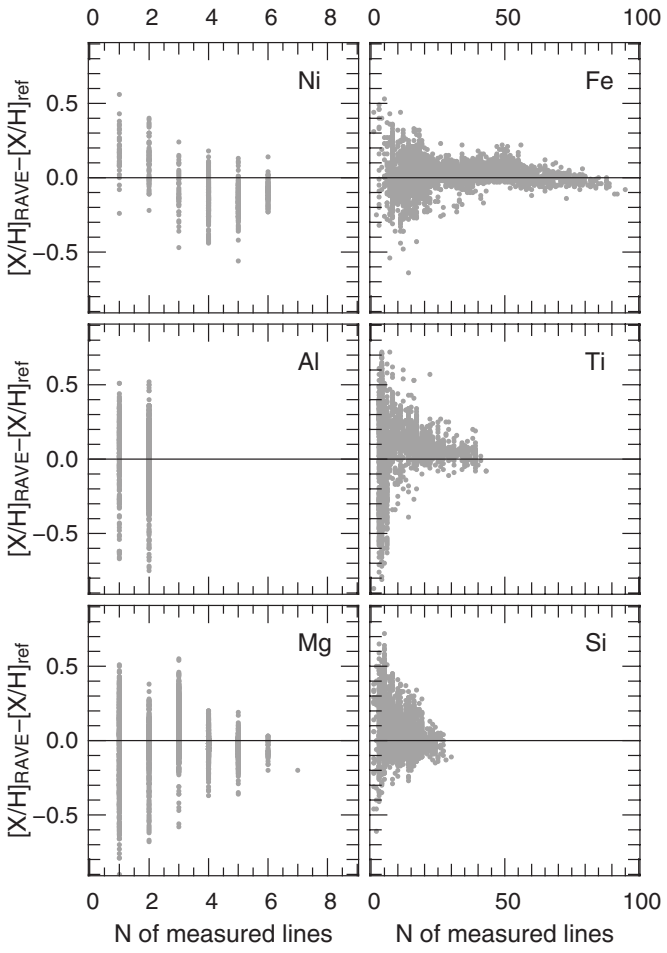

Figure 25. Residuals between measured and expected abundances (y-axis) as a function of the number of measured lines (x-axis) for each element in the test with synthetic spectra at S/N = 100, 40, 20 pixel^{-1}.

6.3.2. *Comparison between* [M/H] *and* $[{\rm m/H}]_{\rm chem}$

In order to measure the chemical abundances, the RAVE chemical pipeline uses on one hand the estimation of $T_{\rm eff}$ and $\log g$ of the RAVE pipeline, and on the other hand [M/H] is employed only as a first guess. This means that the metallicity

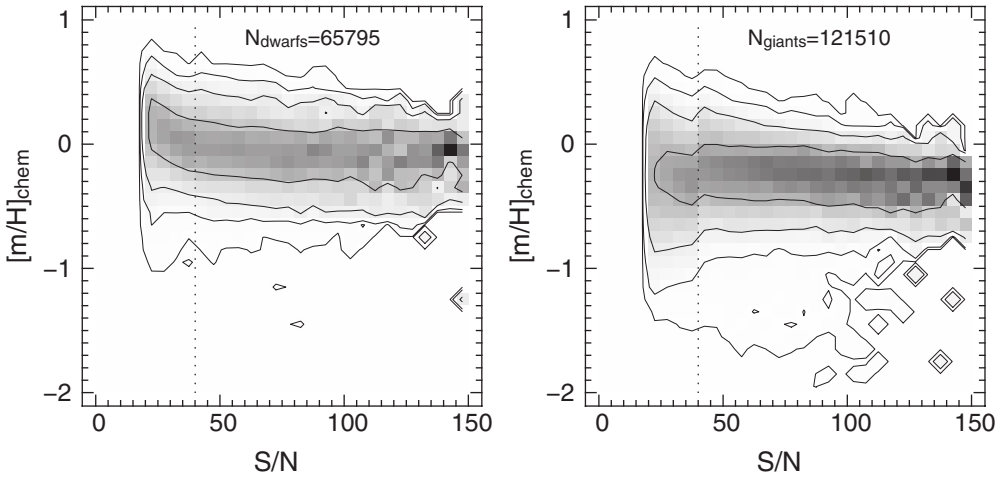

Figure 26. $[m/H]_{chem}$ distribution for dwarfs (left panel) and giants (right panel) as a function of S/N. In order to highlight the shape of the distribution at any S/N, the $[m/H]_{chem}$ distribution has been normalized for every S/N bin.

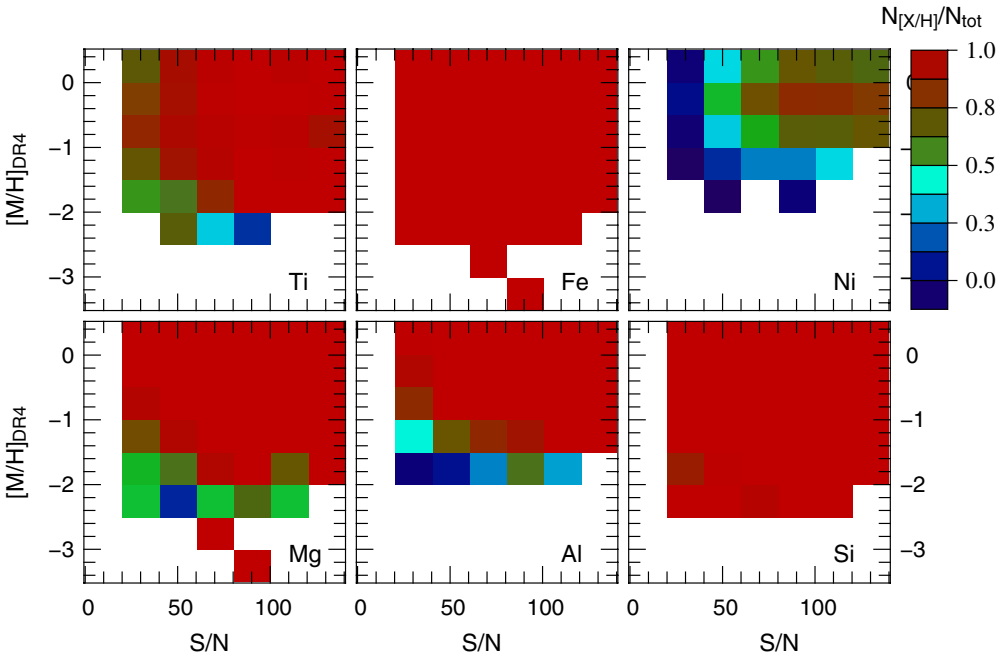

Figure 27. Colors of the bins represent the number of spectra having abundance estimation (N_X/N_{tot}) as a fraction of the total number of spectra as a function of metallicity and S/N. Each panel shows the distribution for the identified element.
(A color version of this figure is available in the online journal.)

$[m/H]_{chem}$ (computed as explained in Section 3.4 of B11) and any elemental abundance provided by the chemical pipeline are independent of [M/H]. It is, therefore, interesting to compare [M/H] with $[m/H]_{chem}$ as much as with [Fe/H], because the latter is the element of reference used to calibrate [M/H]. In Figure 28 the residuals between [M/H], $[m/H]_{chem}$, and [Fe/H] are shown as a function of T_{eff}, $\log g$, and [M/H] for spectra with S/N > 40 pixel^{-1}. In general, [M/H] appears to lie between [Fe/H] and $[m/H]_{chem}$, in the order $[Fe/H] \leqslant [M/H] \leqslant [m/H]_{chem}$. More specifically, there are some differences: for dwarf stars this difference is slightly larger (∼0.1 dex) than for giants (⩽0.05 dex). This can be due to the higher number of strong and narrow absorption lines available in giants with respect to hot dwarfs, which allows better measurements over the whole S/N range. In addition, the [Fe/H] deviation can be due to the α-enhanced stars, which do not follow the enhancement relation of the learning grid (see Section 3.4) and for which $[Fe/H] \neq [M/H]$. Indeed, roughly 25% of the stars with S/N > 40 pixel^{-1} deviate more than 1σ (0.15 dex) from the enhancements of the learning grid of Section 3.4.

7. PROPER MOTIONS

In DR3, the proper motions were sourced from the PPMX (Röser et al. 2008), Tycho-2 (Høg et al. 2000), SSS (Hambly et al. 2001), and UCAC2 (Zacharias et al. 2004) catalogs. As already described in DR2, the most precise available proper motion was chosen for each object. In DR4, we no longer follow this procedure but publish a set of available proper motions for each object and leave the selection to the user. The reason is the following: the proper-motion error bars published are of different origin; they may be calculated either from the scatter or from the weights of the individual positions. Hence, the proper motion with the smallest formal error is not necessarily

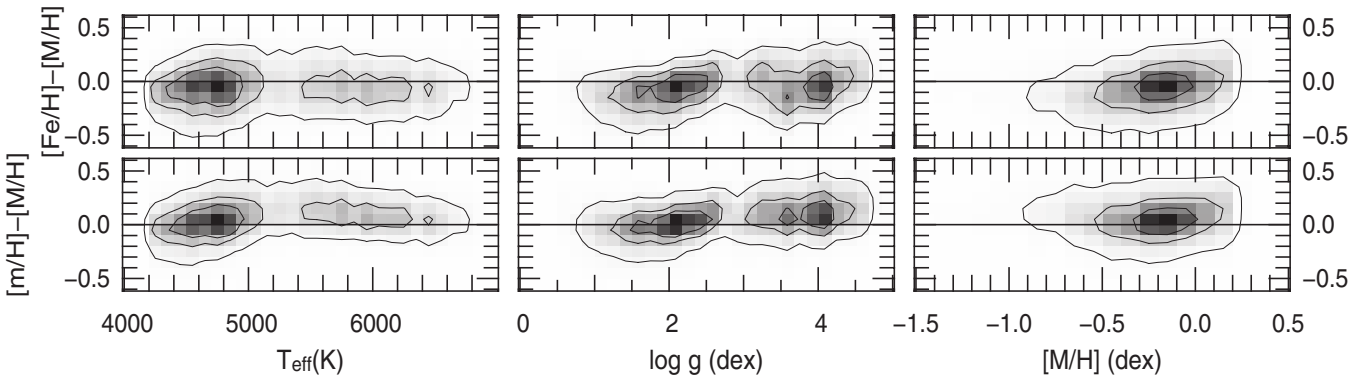

Figure 28. Residuals between the DR4 metallicity ([M/H]), the chemical pipeline metallicity ([m/H]), and the measured iron abundance ([Fe/H]) as a function of the effective temperature, surface gravity, and metallicity. The contour levels hold 34%, 68%, and 95% of the points, respectively.

the most accurate. So, the DR4 catalog lists proper motions from the following sources: Tycho-2, UCAC2, UCAC3, UCAC4 (Zacharias et al. 2010, 2013), PPMX, PPMXL (Roeser et al. 2010), and SPM4 (Girard et al. 2011).

8. RADIAL VELOCITIES

The radial velocities for this fourth data release are based on the RAVE pipeline described in Siebert et al. (2011b); therefore, only a brief reminder of the general features is given here.

The radial velocities are obtained using a standard cross-correlation algorithm in Fourier space on the continuum subtracted spectra. First, an estimate of the RV is obtained using a subset of 10 template spectra. This first estimate, with an accuracy better than 5 km s^{-1}, is used to put the spectrum in the zero velocity frame. A new template is constructed using the full template database using a penalized chi-square technique described in Zwitter et al. (2008). The new template is then used to derive the final, more precise RV. The internal error is obtained as the error on the determination of the maximum of the correlation function. This part is performed using the IRAF xcsao task.

The histogram distribution of the internal RV error is presented in Figure 29 (top panel). The different histograms contain data new to each data release as indicated in the top right corner. The bottom panel of Figure 29 is the associated cumulative distribution of internal RV error. The figure shows a clear improvement of the quality of the RV from DR1 toward DR4, with a jump in quality for data new to DR4. From DR2 to DR4,[35] while the mode of the distribution remains constant at ∼1 km s^{-1}, the tail at larger velocity errors is consistently reduced with a leap between DR3 and DR4. Indeed, while for DR3 68% of the data had internal errors better than 2 km s^{-1}, for DR4 the 68% limit goes down to 1.4 km s^{-1}. The source of this improvement is twofold. First, the DR4 data are based upon a new input catalog that uses DENIS *I*-band magnitude instead of a pseudo-*I* magnitude constructed from Tycho-2 B_T and V_T photometry for the bright part of the catalog and photographic *I* band from the SuperCosmos Sky Survey for the faint part. This more accurate photometry allows a better splitting of the bright and faint sub-samples, which have different exposure times. Second, at the telescope the S/N is now "monitored," and fields with insufficient S/N benefit from longer exposure times to ensure a minimal quality of the data. The combination

[35] DR1 data suffer from second-order contamination, which was corrected for DR2 data; hence, the radial velocity measurement is not as precise as for subsequent releases.

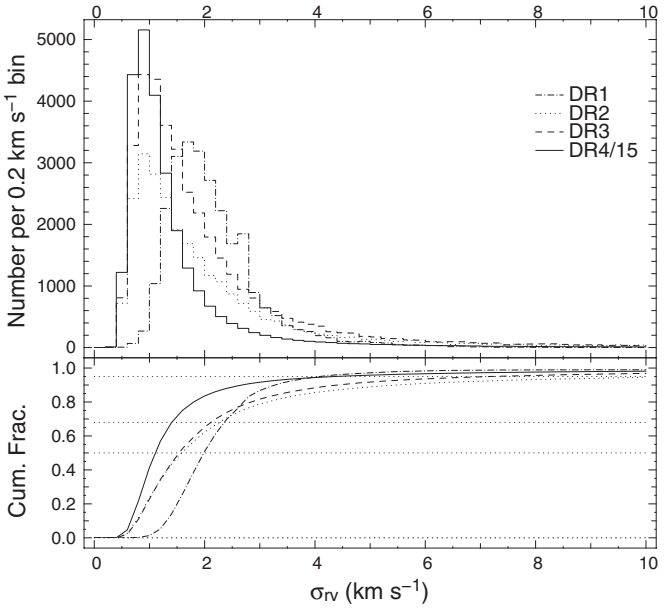

Figure 29. Top: histograms of the internal radial velocity error for data new to each data release. The bin size is 0.2 km s^{-1}. For DR4, the number of stars per bin is divided by 15 to compensate for the increase in sample size. Bottom: cumulative distributions. The dotted lines mark 50%, 68%, and 95% of the samples.

of these two points allows us to considerably reduce the tail of the RV error distribution.

8.1. Repeat Observations

To verify the quality of the RAVE data, a fraction of the survey time is devoted to multiple observations of RAVE targets with time intervals between observations ranging from a few hours to 4 yr. In the present release, 23,288 stars belong to this program, for a total of 61,457 measurements, some stars having been observed up to 13 times. The distribution of the number of observations per star is presented in the left panel of Figure 30. The distribution of the time interval Δt between re-observations is presented in Figure 30, right panel, where the Δt are binned using intervals of 1 day. As seen from this figure, the distribution is not random. A quasi-logarithmic spacing is used to sample optimally the possible orbital state of the spectroscopic binaries with an enhancement of the observations at specific intervals of 1 day, 2 weeks, 1, 2, 3, and 6 months, and 1, 2, 3, and 4 yr.

The comparison between the RV measurements for the different observations is given in Figure 31. In the top panel,

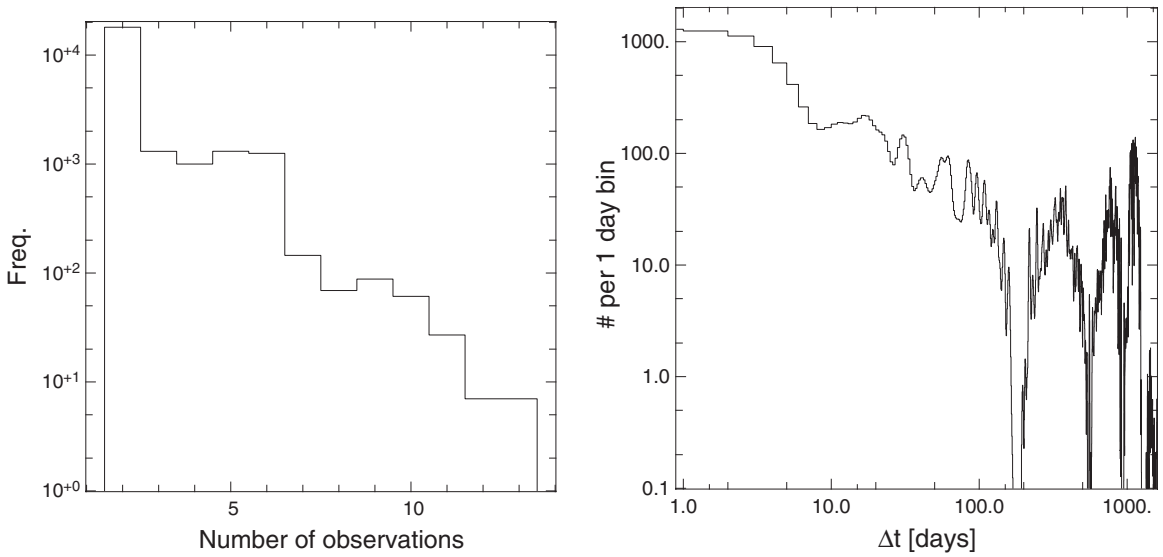

Figure 30. Left: histogram of the number of observations for stars observed more than once. Right: distribution of the time intervals between the first observation of a star and its re-observation.

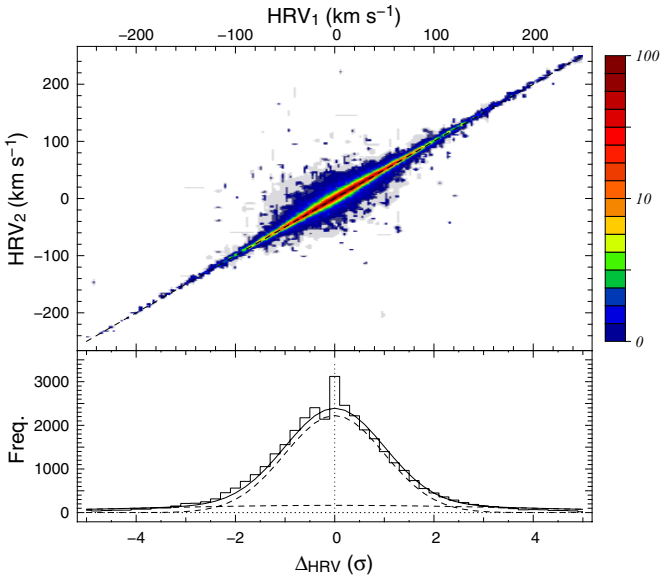

Figure 31. Top: comparison of the radial velocities measured for re-observed RAVE targets. For each star in this sample, the measurement with highest S/N is used as the reference point on the x-axis (HRV_1), while other measurements are along the y-axis (HRV_2). Along each axis the distribution is obtained by convolving the measurement with a Gaussian function whose dispersion is the associated internal error. The color-coding follows the resulting density on a logarithmic scale. The one-to-one relation is indicated by the dashed line. Bottom: histogram of the radial velocity differences normalized to the error. The plain black line is a fit to the histogram assuming that it is composed of two Gaussian populations (see the text). From this fit, the contribution to the histogram of spectroscopic binaries and problematic spectra is 23%.

(A color version of this figure is available in the online journal.)

the color coding follows the density per bin of 2 km s^{-1}. For each star, the velocity of the observation with the highest S/N is used as the reference velocity along the x-axis (HRV_1), while subsequent observations are along the y-axis (HRV_2). The measurements are convolved with a Gaussian function along each direction. The dispersion of the Gaussian is the internal error associated with the measurement along each axis. The general trend follows closely the one-to-one relation, showing no sign of any systematic effects.

Another way to look quantitatively at the RV difference is presented in the bottom panel of Figure 31, which shows the histogram of the RV difference normalized to the errors $\Delta_{HRV} = (HRV_1 - HRV_2)/(\sqrt{\sigma_1^2 + \sigma_2^2})$. If our measurements were perfect, this distribution should follow a Gaussian function of zero mean and unit dispersion. Binaries and problematic measurements contribute to the tail and can be assumed to follow a Gaussian function with a larger dispersion. In the case of our RAVE data, a sum of two Gaussians is used to fit the histogram, setting the dispersion of the first Gaussian function to one. Also, we remove the central bin from the fit. This central bin is mostly populated by repeat observations without delay in time. The best fit is shown as a continuous black line, the contribution of each Gaussian function being represented by a dashed line. Apart from the central bin, the fit provides an adequate representation of the observed histogram. The respective contributions of the two Gaussian functions are 77% for the standard population and 23% for the spectroscopic binaries/problematic observations. This fraction is in agreement with our finding for DR3 data (26%).

8.2. Zero-point Offset

As for the DR3 and previous releases, the RV solutions are corrected for potential zero-point offsets due to change in temperature in the spectrograph room. The procedure uses the available sky lines in the RAVE spectra to construct a smooth solution of the zero-point offset across the field plate. This procedure is fully described in Siebert et al. (2011b), and the relevant measurements for each fiber are given in the catalog. To verify the validity of our velocity zero-point solution, comparison to independent measurements is made. Our comparison sample comprises data from seven different sources: the GCS (Nordström et al. 2004) data and high-resolution echelle follow-up observations of RAVE targets at the ANU 2.3 m telescope, Asiago Observatory, Apache Point Observatory from Ruchti et al. (2011), and Observatoire de Haute Provence using the Elodie and Sophie instruments. In total, the sample of RAVE stars with external RV measurements contains 1265 stars. Their distributions in DENIS I magnitude and 2MASS $J-H$ versus $H-K$ color–color diagram are presented in Figure 32. Stars with $I < 9$ are mostly custom

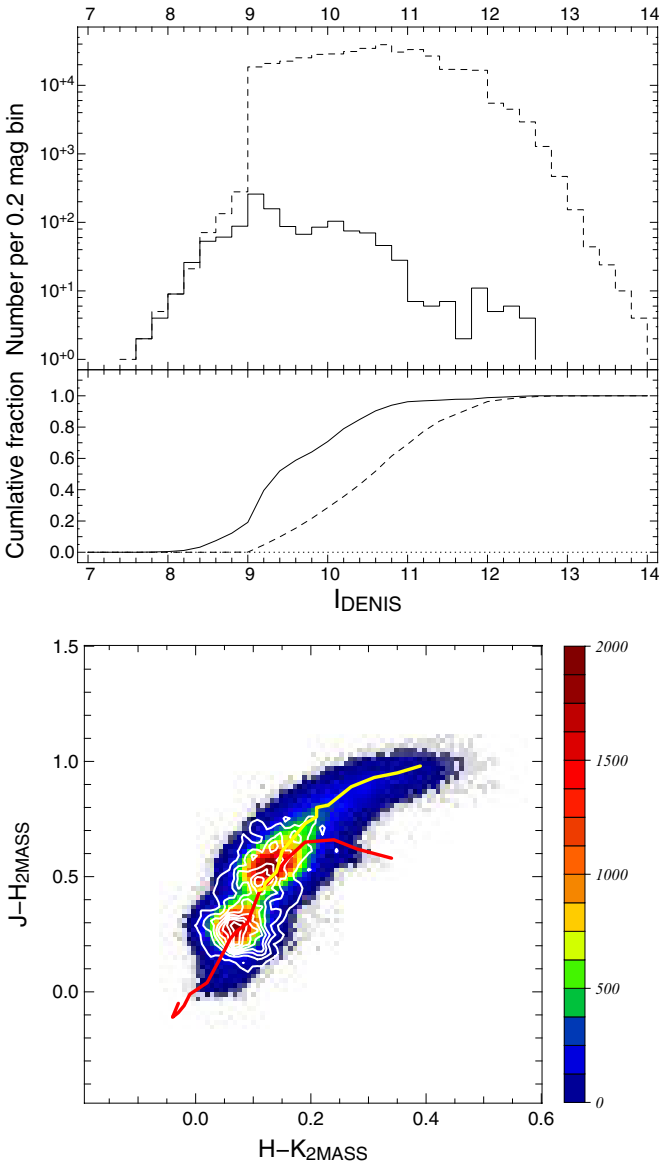

Figure 32. Top: DENIS I magnitude histogram of the sub-sample of RAVE stars with external radial velocity measurements (solid line) compared to the distribution of DENIS I magnitude for the full RAVE catalog (dashed line). Bottom: 2MASS $J-H$ vs. $H-K$ two-dimensional histogram of the RAVE DR4 catalog with a bin size of 0.02 mag on each axis. The contours show the location of the sub-sample with external HRV measurements. The thick yellow and red lines are fiducial colors from Table 2 of Wainscoat et al. (1992) for giant and dwarf stars, respectively.

(A color version of this figure is available in the online journal.)

RAVE observations of bright GCS stars. At fainter magnitudes the sample consists primarily of high-resolution re-observations of RAVE targets. In the 2MASS color–color diagram, we observe that this sample covers the two main peaks (representing dwarf and giant stars) present in the RAVE catalog. However, dwarfs are over-represented compared to the RAVE distribution due to the large number of GCS stars observed in this sample that are Hipparcos dwarfs.

The summary of the comparison to the control samples is given in Table 6. This table reports the number of objects in each sample, the total number of observations, the mean $\Delta RV = RV_{DR4} - RV_{ext}$, and the standard deviation. ΔRV is computed using an iterative σ-clipping technique to remove the contamination by spectroscopic binaries or problematic

Table 6
Summary of the Radial Velocity Comparison to External Samples

Sample	N_{stars}	N_{obs}	$\langle\Delta RV\rangle$	$\sigma_{\Delta RV}$ (σ_{clip}, n_{rej})
GCS	733	1024	0.28	1.72 (3,120)
Chubak	77	97	−0.07	1.28 (3,2)
Ruchti	314	445	0.78	1.78 (3,34)
Asiago	25	47	−0.22	2.95 (3,0)
ANU 2.3 m	73	203	−0.60	2.87 (3,18)
OHP Elodie	9	13	0.29	0.40 (2.5,3)
OHP Sophie	34	43	0.83	1.56 (3,4)
Full sample	1265	1872	0.20	1.52 (3,266)

Note. The mean difference in the radial velocities, ΔRV, has been computed as $\Delta RV = RV_{DR4} - RV_{ext}$.

measurements. No other quality cut was applied on the samples. The clipping parameter and the number of stars rejected for each sample are given in the last column of the table.

We note that the agreement between RAVE and the external sources is better than 1 km s^{-1} in all the cases. Figure 33 (top panel) presents the direct comparison of the DR4 radial velocities to the external source measurements. The blue circles are the known spectroscopic binaries and show a broader distribution than the remainder of the sample. Figure 33 (bottom panel) shows the histogram of the RV difference. This distribution can be adequately reproduced by the sum of two Gaussian functions, the peak representing the single stars being of zero mean with a dispersion of 1.5 km s^{-1}, consistent with our expectation for RAVE data.

As a final test, we check the dependence of the RV difference as a function of the Tonry–Davis correlation coefficient (R) and S/N of the RAVE data (Figure 34). Although an increase in the dispersion is observed for S/N < 30 pixel^{-1}, or R of 40, the absence of an apparent bias indicates that our RV measurements are reliable.

9. STELLAR DISTANCES, AGES, AND EXTINCTIONS

In the absence of parallaxes for the stars, the best way to obtain individual stellar distances is to project the atmospheric parameters on a set of theoretical isochrones and obtain the most likely value of the absolute magnitude of the stars. Up to now, the RAVE consortium has published a variety of studies using the distances inferred by red clump giants (e.g., Siebert et al. 2008; Veltz et al. 2008; Williams et al. 2013) and developed three different methods in order to obtain the individual stellar line-of-sight distances (Breddels et al. 2010; Zwitter et al. 2010; Burnett & Binney 2010). Previous RAVE catalogs published the derived distances for the first two of these methods.

Figure 35 presents for different regions of the T_{eff}–log g diagram the ratio between the distances obtained using the Zwitter et al. (2010) method with the DR3 parameters (Z10-DR3 hereafter) and with the DR4 ones (Z10-DR4 hereafter). It should be noted that Z10-DR3 distances have been obtained using only internal errors for the atmospheric parameters, whereas Z10-DR4 consider the quadratic sum of the external uncertainties (Table 5) and the internal ones (Table 1 or Table 2). One can see that the largest deviations in distances occur in parts of the H–R diagram that are (and should be) scarcely populated. As an overall mean, the Z10-DR3 distances are 6% larger than the Z10-DR4 ones, with the 1σ dispersion being at roughly 30%.

For the present DR4 catalog, we publish two sets of distances: one using the Z10 method with the DR4 parameters, as well

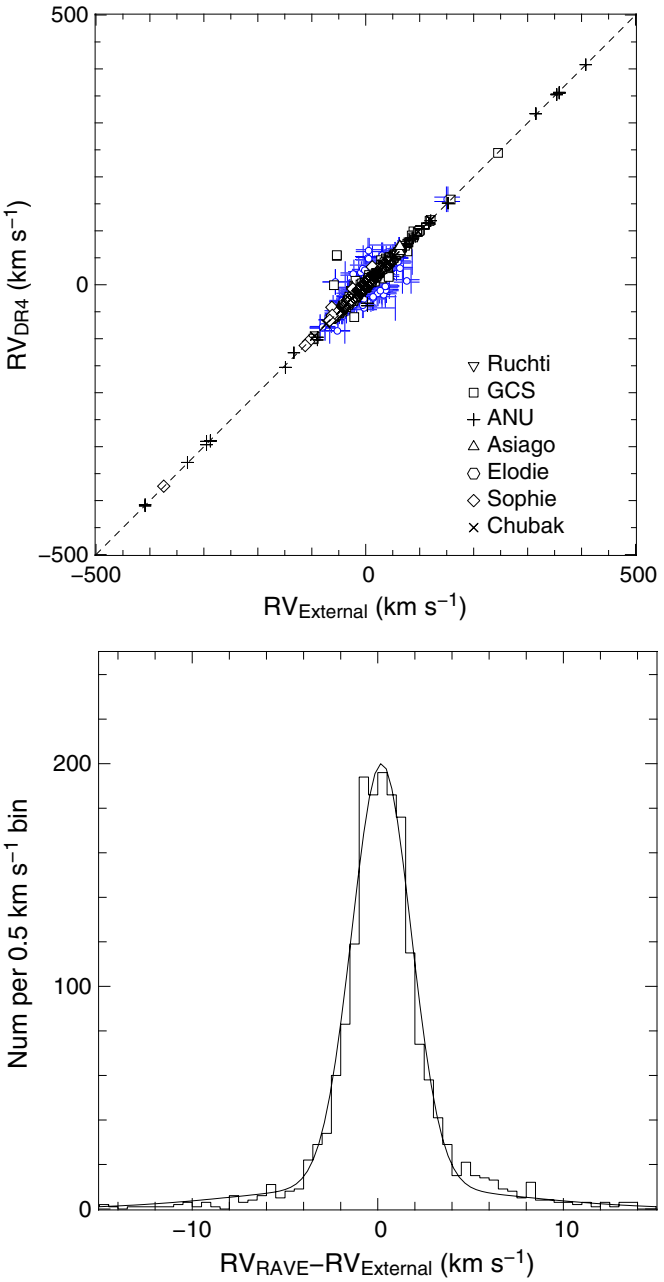

Figure 33. Top: comparison of RAVE radial velocities to external measurements. The blue circles are spectroscopic binaries detected in the high-resolution spectra. The dashed line marks the one-to-one relation. Bottom: histogram of the radial velocity difference. The histogram can be modeled using two Gaussian functions to account for normal stars and binaries/problematic spectra (black curve). The Gaussian function recovering the peak is at zero mean with a standard deviation of 1.5 km s^{-1}. The problematic spectra/binaries contribution to this sample is 5%.

(A color version of this figure is available in the online journal.)

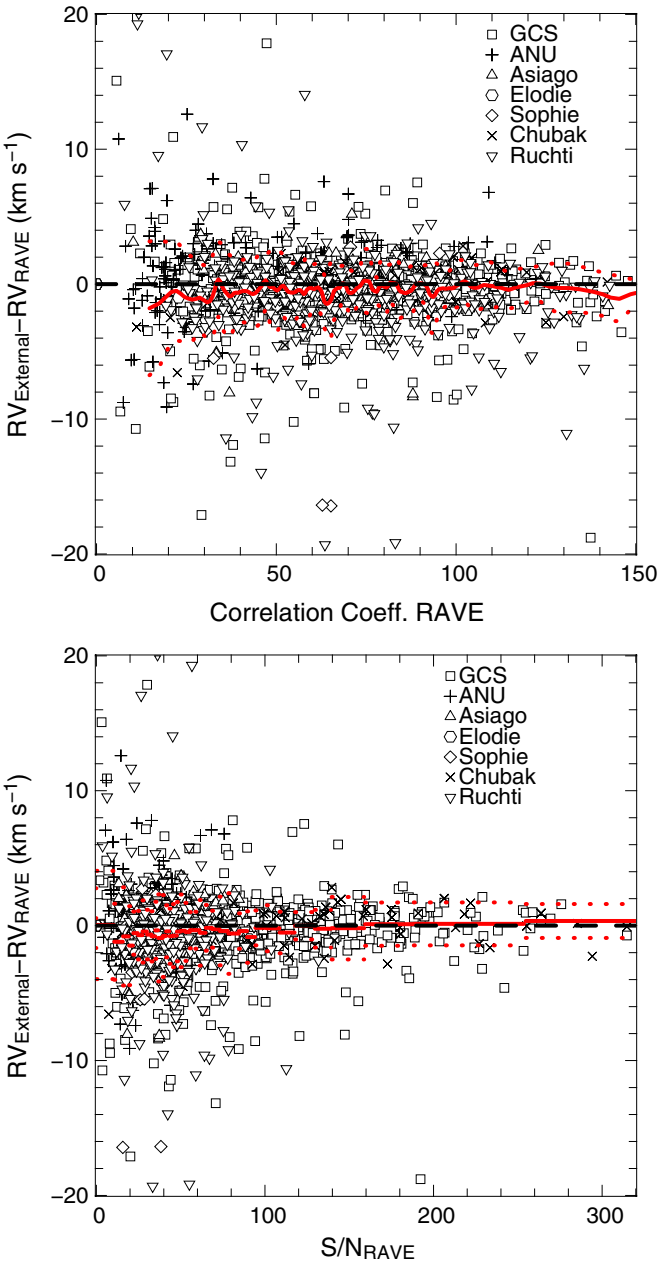

Figure 34. Radial velocity difference as a function of Tonry–Davis correlation coefficient (upper plot) and S/N (lower plot). The thick red line marks the mean relation, the red dotted line the dispersion. The symbols indicate the source of the external measurements.

(A color version of this figure is available in the online journal.)

as another set obtained using a more robust algorithm, based on the Bayesian distance-finding method of Burnett & Binney (2010). The improved algorithm is presented in Binney et al. (2013, B13 hereafter) and now takes into account the interstellar extinction, as well as kinematic correction factors obtained by the method of Schönrich et al. (2012). The pipeline determines the probability distribution function of each star in the space of initial mass, age, metallicity, distance, extinction, etc., and from this distribution an age, a distance, and an extinction are inferred from appropriate expectation values. The most reliable distance indicator turns out to be not the expectation value of the distance but the inverse of the expectation value of the parallax. Here we discuss briefly the results for only the distances, but we refer the reader to B13 for a full explanation of the method, as well as a detailed analysis of the reliability of the parameters.

The B13-DR4 spectrophotometric parallaxes have been computed for the stars that had spectra with S/N > 10 $pixel^{-1}$. For the targets that were observed several times, only the spectrum with the highest S/N has been used every time. The results have shown that the spectrophotometric parallaxes of Hipparcos stars are very satisfactory and are definitely improved by taking extinction into account. Nevertheless, an overestimation of less than 10% for the dwarfs and less than 20% for the giants is evident. The method has also been tested on the open

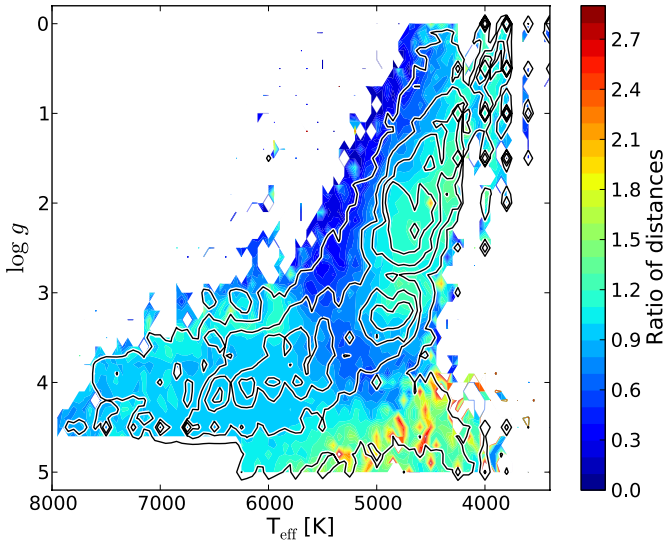

Figure 35. Comparison of the average ratio of distances in the $T_{\rm eff}$–log g plot for the stellar spectra with S/N > 20 pixel^{-1}. The ratio is the Zwitter et al. (2010) distance based on DR3 parameters divided by the Zwitter et al. (2010) distance based on DR4 parameters. The ratio is in filled contours, bin size is 50 K in temperature and 0.1 dex in gravity. Empty contours show the occurrence of $T_{\rm eff}$ and log g (expectation values) as calculated by DR4.

(A color version of this figure is available in the online journal.)

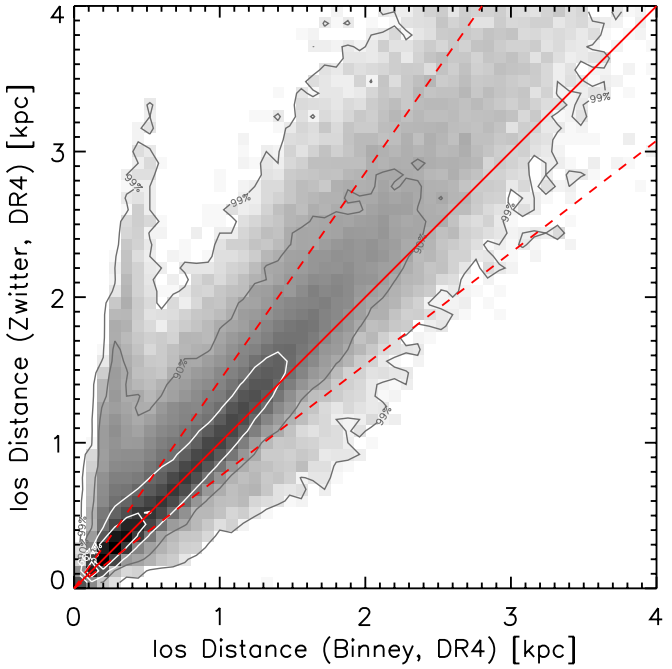

Figure 36. Comparison of the line-of-sight distance estimations obtained using the Binney et al. (2013) method (x-axis) and the ones obtained using the Zwitter et al. (2010) method combined with the Padova isochrones (y-axis). The red line is the 1:1 relation, and dashed lines show deviations of 30% from unity. Contour lines hold 33%, 66%, 90%, and 99% of the sample.

(A color version of this figure is available in the online journal.)

cluster spectra presented in Table 4, deriving very satisfactory distances, provided that a cluster-specific age prior is used. Indeed, our data barely constrain the ages of stars, so a star's adopted age is heavily influenced by the age prior used, and the prior that is appropriate for field stars leads to excessive ages being assigned to most cluster stars, which tend to be young.

Figure 36 compares the distance estimations obtained using the Padova isochrones and the Z10-DR4 or the B13-DR4 methods. From this figure one can see that for the bulk of the targets, the distances obtained with the two methods are quite similar. We find that the median of the distribution defined by Z10/B13 is equal to 1.02. However, for the most distant stars ($D \gtrsim 2$ kpc) Z10-DR4 predicts larger distances than B13-DR4. Finally, the targets for which B13-DR4 predicts $D \sim 0.5$ kpc and Z10-DR4 derives $D > 1.5$ kpc correspond to the most metal-poor giant stars of the sample, for which the atmospheric parameters have also the largest errors. This disagreement is mainly due to the fact that Z10 projects the atmospheric parameters on the isochrones, without having any a priori constraint on their expected output parameters, based on their position in the Galaxy, their RV, or proper motion. Hence, input atmospheric parameter values with large uncertainties, especially for metal-poor giant stars, naturally lead to erroneous distances and to the discrepancy shown in Figure 36.

We conclude that the B13-DR4 distances are more robust and hence should give better results if the priors are satisfied.

10. PHOTOMETRY FROM APASS

$BV\,g'r'i'$ photometric data of RAVE stars have been obtained as part of the ongoing APASS survey.[36] The APASS photometric survey covers the whole sky, from pole to pole, with ongoing observations from CTIO (Chile), for the southern hemisphere, and New Mexico for the northern counterpart. At both sites, a pair of twin remotely controlled, small telescopes obtain simultaneous CCD observations during dark- and gray-Moon time over five optical bands: B, V (tied to the equatorial standards of Landolt 2009) and g', r', i' bands (tied to the 158 primary standards given by Smith et al. 2002, which define the Sloan photometric system). The telescopes are 20 cm $f/3.6$ astrographs feeding Apogee U16m cameras (4096 × 4096 array, 9 μm pixels), which cover a field 2.9 deg wide with a 2.6 arcsec pixel^{-1} plate factor. The photometric filters are of the dielectric multi-layer type and are produced by Astrodon. Transmission curves and photometric performances of Astrodon filters used in the APASS survey are discussed and compared to more conventional types of photometric filters in Munari et al. (2012) and Munari & Moretti (2012). On average 80 fields are observed per night at each APASS location, 20 of them being standard fields (Landolt, Sloan).

The APASS observations are obtained with fixed exposure times (different and optimized for each photometric band), set to detect $V = 17$ stars at S/N = 5 on a single exposure. Stars brighter than $V = 10$ mag may saturate under optimal seeing conditions. At the time of writing, 90% of the whole sky has been covered, with 42 million stars measured on at least two distinct epochs. Differential photometry within a given field is accurate to better than 0.01 mag, and absolute photometry over the whole sky is currently accurate to better than 0.025 mag (closely similar to 2MASS accuracy). APASS astrometric positions are also highly accurate. Comparison with the positions given in the Carlsberg Meridian Catalog for the 118,940 RAVE stars in common shows a distribution peaked at a separation of 0.105 arcsec, with the median value at 0.177 arcsec. Although APASS DR7 is publicly available, its values are not published in RAVE DR4, because future APASS DR will provide better accuracy and coverage of RAVE DR4. Clearly APASS photometry will significantly enhance analysis of RAVE data. We recommend users to adopt APASS photometry as it becomes available.

[36] http://www.aavso.org./apass

Table 7
Catalog Description

Col	Format	Units	NULL	Label	Explanations
1	char(32)	...	N	RAVE_OBS_ID	Target designation
2	char(18)	...	N	RAVEID	RAVE target designation
3	double	deg	N	RAdeg	Right ascension
4	double	deg	N	DEdeg	Declination
5	double	deg	N	Glon	Galactic longitude
6	double	deg	N	Glat	Galactic latitude
7	float	km s^{-1}	N	HRV	Heliocentric radial velocity
8	float	km s^{-1}	N	eHRV	HRV error
9	float	(R+)	N	CorrelationCoeff	Tonry and Davis *R* correlation coefficient
10	float	...	N	PeakHeight	Height of correlation peak
11	float	...	N	PeakWidth	Width of correlation peak
12	float	km s^{-1}	Y	SkyRV	Measured HRV of sky
13	float	km s^{-1}	Y	eSkyRV	Error measured HRV of sky
14	float	(R+)	Y	SkyCorrelationCoeff	Tonry and Davis *R* sky correlation coefficient
15	float	km s^{-1}	Y	CorrectionRV	Zero-point correction applied radial velocity
16	char(5)	...	Y	ZeroPointFLAG	Quality flag for zero-point correction (Note 3)
17	float	...	Y	STN_SPARV	S/N value (preflux calibration) (Note 1)
18	char(16)	...	Y	ID_TYCHO2	TYCHO2 target designation
19	float	arcsec	Y	Dist_TYCHO2	Center distance to target catalog
20	char(2)	...	Y	XidQualityFLAG_TYCHO2	Crossmatch quality flag (Note 4)
21	float	mas yr^{-1}	Y	pmRA_TYCHO2	Proper-motion RA from TYCHO2
22	float	mas yr^{-1}	Y	epmRA_TYCHO2	Error proper-motion RA from TYCHO2
23	float	mas yr^{-1}	Y	pmDE_TYCHO2	Proper-motion DE from TYCHO2
24	float	mas yr^{-1}	Y	epmDE_TYCHO2	Error proper-motion DE from TYCHO2
25	char(16)	...	Y	ID_UCAC2	UCAC2 target designation
26	float	arcsec	Y	Dist_UCAC2	Center distance to target catalog
27	char(2)	...	Y	XidQualityFLAG_UCAC2	Crossmatch quality flag (Note 4)
28	float	mas yr^{-1}	Y	pmRA_UCAC2	Proper-motion RA from UCAC2
29	float	mas yr^{-1}	Y	epmRA_UCAC2	Error proper-motion RA from UCAC2
30	float	mas yr^{-1}	Y	pmDE_UCAC2	Proper-motion DE from UCAC2
31	float	mas yr^{-1}	Y	epmDE_UCAC2	Error proper-motion DE from UCAC2
32	char(16)	...	Y	ID_UCAC3	UCAC3 target designation
33	float	arcsec	Y	Dist_UCAC3	Center distance to target catalog
34	char(2)	...	Y	XidQualityFLAG_UCAC3	Crossmatch quality flag (Note 4)
35	float	mas yr^{-1}	Y	pmRA_UCAC3	Proper-motion RA from UCAC3
36	float	mas yr^{-1}	Y	epmRA_UCAC3	Error proper-motion RA from UCAC3
37	float	mas yr^{-1}	Y	pmDE_UCAC3	Proper-motion DE from UCAC3
38	float	mas yr^{-1}	Y	epmDE_UCAC3	error Proper-motion DE from UCAC3
39	char(16)	...	Y	ID_UCAC4	UCAC4 target designation
40	float	arcsec	Y	Dist_UCAC4	Center distance to target catalog
41	char(2)	...	Y	XidQualityFLAG_UCAC4	Crossmatch quality flag (Note 4)
42	float	mas yr^{-1}	Y	pmRA_UCAC4	Proper-motion RA from UCAC4
43	float	mas yr^{-1}	Y	epmRA_UCAC4	Error proper-motion RA from UCAC4
44	float	mas yr^{-1}	Y	pmDE_UCAC4	Proper-motion DE from UCAC4
45	float	mas yr^{-1}	Y	epmDE_UCAC4	Error proper-motion DE from UCAC4
46	char(16)	...	Y	ID_PPMXL	PPMXL target designation
47	float	arcsec	Y	Dist_PPMXL	Center distance to target catalog
48	char(2)	...	Y	XidQualityFLAG_PPMXL	Crossmatch quality flag (Note 4)
49	float	mas yr^{-1}	Y	pmRA_PPMXL	Proper-motion RA from PPMXL
50	float	mas yr^{-1}	Y	epmRA_PPMXL	Error proper-motion RA from PPMXL
51	float	mas yr^{-1}	Y	pmDE_PPMXL	Proper-motion DE from PPMXL
52	float	mas yr^{-1}	Y	epmDE_PPMXL	Error proper-motion DE from PPMXL
53	char(10)	...	N	Obsdate	Observation date yyyymmdd
54	char(14)	...	N	FieldName	Name of RAVE field (RA/DE)
55	int	...	N	PlateNumber	Number of field plate [1..3]
56	int	...	N	FiberNumber	Number of optical fiber [1,150]
57	float	K	Y	Teff_K	Effective temperature (Note 1)
58	float	K	Y	eTeff_K	Error effective temperature (Note 1)
59	float	dex	Y	logg_K	Log gravity (Note 1)
60	float	dex	Y	elogg_K	Error log gravity (Note 1)
61	float	dex	Y	Met_K	Metallicity [m/H] (Note 1)
62	float	dex	Y	Met_N_K	Metallicity [m/H] (Note 1)
63	float	dex	Y	eMet_K	Error/metallicity [m/H] (Note 1)
64	float	...	Y	SNR_K	S/N value (Note 1)
65	float	...	Y	Algo_Conv_K	Quality flag for stellar parameter pipeline [0...4] (Note 1, Note 5)
66	float	dex	Y	Al	Abundance of Al [Al/H]

Table 7
(Continued)

Col	Format	Units	NULL	Label	Explanations
67	int	...	Y	Al_N	Number of used spectral lines for calculation of abundance
68	float	dex	Y	Si	Abundance of Si [Si/H]
69	int	...	Y	Si_N	Number of used spectral lines for calculation of abundance
70	float	dex	Y	Fe	Abundance of Fe [Fe/H]
71	int	...	Y	Fe_N	Number of used spectral lines for calculation of abundance
72	float	dex	Y	Ti	Abundance of Ti [Ti/H]
73	int	...	Y	Ti_N	Number of used spectral lines for calculation of abundance
74	float	dex	Y	Ni	Abundance of Ni [Ni/H]
75	int	...	Y	Ni_N	Number of used spectral lines for calculation of abundance
76	float	dex	Y	Mg	Abundance of Mg [Mg/H]
77	int	...	Y	Mg_N	Number of used spectral lines for calculation of abundance
78	float	...	Y	CHISQ_c	χ^2 of the chemical pipeline (Note 1)
79	float	K	Y	Teff_SPARV	Effective temperature (Note 1)
80	float	dex	Y	logg_SPARV	Log gravity (Note 1)
81	float	dex	Y	alpha_SPARV	Metallicity (Note 1)
82	char(16)	...	Y	ID_2MASS	2MASS target designation
83	float	arcsec	Y	Dist_2MASS	Center distance to target catalog
84	char(2)	...	Y	XidQualityFLAG_2MASS	Crossmatch quality flag (Note 4)
85	double	mag	Y	Jmag_2MASS	*J* magnitude
86	double	mag	Y	eJmag_2MASS	Error *J* magnitude
87	double	mag	Y	Hmag_2MASS	*H* magnitude
88	double	mag	Y	eHmag_2MASS	Error *H* magnitude
89	double	mag	Y	Kmag_2MASS	*K* magnitude
90	double	mag	Y	eKmag_2MASS	Error *K* magnitude
91	char(16)	...	Y	ID_DENIS	DENIS target designation
92	double	arcsec	Y	Dist_DENIS	Center distance to target catalog
93	char(2)	...	Y	XidQualityFLAG_DENIS	Crossmatch quality flag (Note 4)
94	double	mag	Y	Imag_DENIS	*I* magnitude
95	double	mag	Y	eImag_DENIS	Error *I* magnitude
96	double	mag	Y	Jmag_DENIS	*J* magnitude
97	double	mag	Y	eJmag_DENIS	Error *J* magnitude
98	double	mag	Y	Kmag_DENIS	*K* magnitude
99	double	mag	Y	eKmag_DENIS	Error *K* magnitude
100	char(16)	...	Y	ID_USNOB1	USNOB1 target designation
101	double	arcsec	Y	Dist_USNOB1	Center distance to target catalog
102	char(2)	...	Y	XidQualityFLAG_USNOB1	Crossmatch quality flag (Note 4)
103	double	mag	Y	B1mag_USNOB1	B1 magnitude
104	double	mag	Y	R1mag_USNOB1	R1 magnitude
105	double	mag	Y	B2mag_USNOB1	B2 magnitude
106	double	mag	Y	R2mag_USNOB1	R2 magnitude
107	double	mag	Y	Imag_USNOB1	*I* magnitude
108	float	mas	Y	parallax	Parallax (Note 4)
109	float	mas	Y	e_parallax	Error parallax (Note 4)
110	float	kpc	Y	dist	Distance (Note 4)
111	float	kpc	Y	e_dist	Error distance (Note 4)
112	float	...	Y	DistanceModulus_Binney	Distance modulus (Note 4)
113	float	...	Y	eDistanceModulus_Binney	Distance modulus (Note 4)
114	float	...	Y	Av	Extinction (Note 4)
115	float	...	Y	e_Av	Error extinction (Note 4)
116	float	...	Y	age	Age (Note 4)
117	float	...	Y	e_age	Error age (Note 4)
118	float	MSun	Y	mass	Mass (Note 4)
119	float	MSun	Y	e_mass	Error mass (Note 4)
120	char(2)	...	Y	c1	n.th minimum distance (Note 6)
121	char(2)	...	Y	c2	n.th minimum distance (Note 6)
122	char(2)	...	Y	c3	n.th minimum distance (Note 6)
123	char(2)	...	Y	c4	n.th minimum distance (Note 6)
124	char(2)	...	Y	c5	n.th minimum distance (Note 6)
125	char(2)	...	Y	c6	n.th minimum distance (Note 6)
126	char(2)	...	Y	c7	n.th minimum distance (Note 6)
127	char(2)	...	Y	c8	n.th minimum distance (Note 6)
128	char(2)	...	Y	c9	n.th minimum distance (Note 6)
129	char(2)	...	Y	c10	n.th minimum distance (Note 6)
130	char(2)	...	Y	c11	n.th minimum distance (Note 6)
131	char(2)	...	Y	c12	n.th minimum distance (Note 6)

Table 7
(Continued)

Col	Format	Units	NULL	Label	Explanations
132	char(2)	...	Y	c13	n.th minimum distance (Note 6)
133	char(2)	...	Y	c14	n.th minimum distance (Note 6)
134	char(2)	...	Y	c15	n.th minimum distance (Note 6)
135	char(2)	...	Y	c16	n.th minimum distance (Note 6)
136	char(2)	...	Y	c17	n.th minimum distance (Note 6)
137	char(2)	...	Y	c18	n.th minimum distance (Note 6)
138	char(2)	...	Y	c19	n.th minimum distance (Note 6)
139	char(2)	...	Y	c20	n.th minimum distance (Note 6)

Notes. (1) Originating from: _K indicates values from stellar parameter pipeline, _N_K indicates a calibrated value, _c indicates values from chemical pipeline, _SPARV indicates values of radial velocity pipeline (used in DR3 also). (2) Cross-identification flag as follows: A = 1 association within 2 arcsec; B = 2 associations within 2 arcsec; C = more than 2 associations within 2 arcsec; D = nearest neighbor more than 2 arcsec away; X = no association found (within 10 arcsec limit). (3) Flag value of the form FGSH, F being for the entire plate, G for the 50 fiber group to which the fiber belongs. S flags the zero-point correction used: C for cubic and S for a constant shift. If H is set to * the fiber is close to a 15 fiber gap. For F and G the values can be A, B, C, D, or E: A = dispersion around correction lower than 1 km s^{-1}; B = dispersion between 1 and 2 km s^{-1}; C = dispersion between 2 and 3 km s^{-1}; D = dispersion larger than 3 km s^{-1}; E = less than 15 fibers available for the fit. (4) See Binney et al. (2013). (5) Flag of stellar parameter pipeline: 0 = pipeline converged; 1 = no convergence; 2 = MATISSE oscillates between two values and the mean has been performed; 3 = results of MATISSE at the boundaries or outside the grid and the DEGAS value has been adopted; 4 = the metal-poor giants with S/N < 20 have been re-run by DEGAS with a scale factor (i.e., internal parameter of DEGAS) of 0.40. (6) Morphological Flag n.th minimum distance to base spectrum given by one of the types *a, b, c, d, e, g, h, n, o, p, t, u, w* (see Matijevič et al. 2012).

11. CONCLUSIONS

The fourth public data release of the RAVE survey includes the stellar atmospheric parameters of 482,430 spectra obtained from 2004 April to 2012 December. Compared to the previous catalog of DR3, a new input catalog, based on DENIS DR3 and 2MASS, is used to select the observed targets. The new input catalog has the major new feature of extending to lower Galactic latitudes and providing more accurate astrometry, leading to fiber placement better matching stellar positions on the sky, which results in higher S/N spectra. In addition, the parameters have been revisited, thanks to a new pipeline, presented in Kordopatis et al. (2011a), and 809 reference spectra that allowed us to validate the effective temperatures and surface gravities and calibrate the metallicities. The RAVE stellar atmospheric parameters that are obtained with the new pipeline are free of any obvious systematics (no correlations between the derived parameters or as a function of S/N), in particular for the overall metallicities of the stars. The spectra with the lowest S/N have a distribution function of atmospheric parameter values that shows a well-understood pattern of discretization effects, but it has been shown that this discretization does not alter the accuracy of the derived parameters. We show that the MDFs of the observed stars shift toward lower metallicity values for the lower surface gravity bins, at the same time as the RV dispersion increases. This is in agreement with a change in the mixture of the probed Galactic populations as a function of the probed volume, passing from an old thin disk dominated population to the presence of more halo stars for the larger volume probed by the more luminous giant stars in low surface gravity bins. That is, at face value the distribution functions for derived stellar parameters are consistent with plausible astrophysical expectations.

In addition to the atmospheric parameters obtained with the new pipeline, those obtained with the DR3 pipeline are also published since they have been used in published analyses. However, they are of lower reliability than our DR4 data set, so situations demanding their re-analysis should be rather rare.

The abundances of six individual elements, namely, aluminum, silicon, titanium, iron, magnesium, and nickel, are published, using an improved version of the Boeche et al. (2011) chemical pipeline. The reliability of these elemental abundances varies according to the effective temperature, surface gravity, and metallicity of the star, the S/N of the spectrum, and of course the element itself.

The catalog also includes the line-of-sight distances computed using the methods presented in Binney et al. (2013) and Zwitter et al. (2010), as well as the ages and the interstellar extinctions that are a sub-product of the Binney et al. (2013) pipeline. Radial velocities, photometric information, proper motions, and stellar binarity flags complete the DR4 catalog entries.

We are most grateful to our referee, for his detailed and very relevant comments, which improved the quality of the presentation of the paper.

Funding for RAVE has been provided by the Australian Astronomical Observatory; the Leibniz-Institut für Astrophysik Potsdam (AIP); the Australian National University; the Australian Research Council; the French National Research Agency; the German Research Foundation (SPP 1177 and SFB 881); the European Research Council (ERC-StG 240271 Galactica); the Istituto Nazionale di Astrofisica at Padova; the Johns Hopkins University; the National Science Foundation of the USA (AST-0908326); the W. M. Keck Foundation; the Macquarie University; the Netherlands Research School for Astronomy; the Natural Sciences and Engineering Research Council of Canada; the Slovenian Research Agency; the Swiss National Science Foundation; the Science & Technology Facilities Council of the UK; Opticon; Strasbourg Observatory; and the Universities of Groningen, Heidelberg, and Sydney. The RAVE Web site is at http://www.rave-survey.org.

APPENDIX

Table 7 describes the contents of individual columns of the Fourth Data Release catalog. The catalog is accessible online at http://www.rave-survey.org and via the CDS VizieR service.

REFERENCES

Abadi, M. G., Navarro, J. F., Steinmetz, M., & Eke, V. R. 2003, ApJ, 591, 499
Allende Prieto, C., Barklem, P. S., Lambert, D. L., & Cunha, K. 2004, A&A, 420, 183

Alvarez, R., & Plez, B. 1998, A&A, 330, 1109
Antoja, T., Helmi, A., Bienayme, O., et al. 2012, MNRAS, 426, L1
Asplund, M., Grevesse, N., & Sauval, A. J. 2005, in ASP Conf. Ser. 336, Cosmic Abundances as Records of Stellar Evolution and Nucleosynthesis, ed. T. G. Barnes, III & F. N. Bash (San Francisco, CA: ASP), 25
Bijaoui, A., Recio-Blanco, A., de Laverny, P., & Ordenovic, C. 2012, StMet, 9, 55
Binney, J., Burnett, B., Kordopatis, G., et al. 2013, arXiv:1309.4270
Boeche, C., Siebert, A., Williams, M., et al. 2011, AJ, 142, 193
Brault, J., & Neckel, H. 1987, Spectral Atlas of Solar Absolute Disk-Averaged and Disk-Center Intensity from 3290 to 12510 Å, Available from ftp.hs.uni-hamburg.de/pub/outgoing/FTS-Atlas/
Breddels, M. A., Smith, M. C., Helmi, A., et al. 2010, A&A, 511, A90
Bruce, S. F., Higinbotham, J., Marshall, I., & Beswick, P. H. 2000, JMagR, 142, 57
Burnett, B., & Binney, J. 2010, MNRAS, 407, 339
Burnett, B., Binney, J., Sharma, S., et al. 2011, A&A, 532, A113
Carretta, E., Bragaglia, A., & Cacciari, C. 2004, ApJL, 610, L25
Casagrande, L., Ramírez, I., Meléndez, J., Bessell, M., & Asplund, M. 2010, A&A, 512, A54
Casagrande, L., Schönrich, R., Asplund, M., et al. 2011, A&A, 530, A138
Cayrel, R., Depagne, E., Spite, M., et al. 2004, A&A, 416, 1117
Chubak, C., Marcy, G., Fischer, D. A., et al. 2012, arXiv:1207.6212
DENIS Consortium. 2003, yCat, 1, 2002
DENIS Consortium. 2005, yCat, 1, 2002
Freeman, K., & Bland-Hawthorn, J. 2002, ARA&A, 40, 487
Fuhrmann, K. 1998a, A&A, 338, 161
Fuhrmann, K. 1998b, A&A, 330, 626
Fuhrmann, K. 2004, AN, 325, 3
Fuhrmann, K. 2008, MNRAS, 384, 173
Fulbright, J. P., Wyse, R. F. G., Ruchti, G. R., et al. 2010, ApJL, 724, L104
Girard, T. M., van Altena, W. F., Zacharias, N., et al. 2011, AJ, 142, 15
Gratton, R., Sneden, C., & Carretta, E. 2004, ARA&A, 42, 385
Gratton, R. G., Bonifacio, P., Bragaglia, A., et al. 2001, A&A, 369, 87
Gratton, R. G., Carretta, E., & Castelli, F. 1996, A&A, 314, 191
Gratton, R. G., Carretta, E., Claudi, R., Lucatello, S., & Barbieri, M. 2003, A&A, 404, 187
Grevesse, N. 2008, CoAst, 157, 156
Grevesse, N., & Sauval, A. J. 1998, SSRv, 85, 161
Gustafsson, B., Edvardsson, B., Eriksson, K., et al. 2008, A&A, 486, 951
Hambly, N. C., MacGillivray, H. T., Read, M. A., et al. 2001, MNRAS, 326, 1279
Hekker, S., & Meléndez, J. 2007, A&A, 475, 1003
Helmi, A., White, S. D. M., de Zeeuw, P. T., & Zhao, H. 1999, Natur, 402, 53
Hinkle, K., Wallace, L., Livingston, W., et al. 2003, in The Future of Cool-Star Astrophysics: 12th Cambridge Workshop on Cool Stars, Stellar Systems, and the Sun (2001 July 30–August 3), Vol. 12, ed. A. Brown, G. M. Harper, & T. R. Ayres (Boulder, CO: Univ. Colorado), 851
Høg, E., Fabricius, C., Makarov, V. V., et al. 2000, A&A, 355, L27
Kielkopf, J. F. 1973, JOSA, 63, 987
Kirby, E. N., Guhathakurta, P., Bolte, M., Sneden, C., & Geha, M. C. 2009, ApJ, 705, 328
Koch, A., & McWilliam, A. 2011, AJ, 142, 63
Kordopatis, G., Recio-Blanco, A., de Laverny, P., et al. 2011a, A&A, 535, A106
Kordopatis, G., Recio-Blanco, A., de Laverny, P., et al. 2011b, A&A, 535, A107
Landolt, A. U. 2009, AJ, 137, 4186
Luck, R. E., & Heiter, U. 2006, AJ, 131, 3069
Luck, R. E., & Heiter, U. 2007, AJ, 133, 2464
Matijevič, G., Zwitter, T., Bienaymé, O., et al. 2011, AJ, 141, 200
Matijevič, G., Zwitter, T., Bienaymé, O., et al. 2012, ApJS, 200, 14
Matijevič, G., Zwitter, T., Munari, U., et al. 2010, AJ, 140, 184
McWilliam, A. 1990, ApJS, 74, 1075
Mishenina, T. V., Bienaymé, O., Gorbaneva, T. I., et al. 2006, A&A, 456, 1109
Mishenina, T. V., & Kovtyukh, V. V. 2001, A&A, 370, 951
Mishenina, T. V., Soubiran, C., Bienaymé, O., et al. 2008, A&A, 489, 923
Mishenina, T. V., Soubiran, C., Kovtyukh, V. V., & Korotin, S. A. 2004, A&A, 418, 551
Munari, U., Bacci, S., Baldinelli, L., et al. 2012, BaltA, 21, 13
Munari, U., & Moretti, S. 2012, BaltA, 21, 22
Munari, U., Sordo, R., Castelli, F., & Zwitter, T. 2005, A&A, 442, 1127
Nordström, B., Mayor, M., Andersen, J., et al. 2004, A&A, 418, 989
Pace, G., Pasquini, L., & François, P. 2008, A&A, 489, 403
Pancino, E., Carrera, R., Rossetti, E., & Gallart, C. 2010, A&A, 511, A56
Pasetto, S., Grebel, E. K., Zwitter, T., et al. 2012a, A&A, 547, A70
Pasetto, S., Grebel, E. K., Zwitter, T., et al. 2012b, A&A, 547, A71
Pasquini, L., Randich, S., Zoccali, M., et al. 2004, A&A, 424, 951
Ramírez, I., Allende Prieto, C., & Lambert, D. L. 2007, A&A, 465, 271
Ramírez, S. V., & Cohen, J. G. 2003, AJ, 125, 224
Recio-Blanco, A., Bijaoui, A., & de Laverny, P. 2006, MNRAS, 370, 141
Robin, A. C., Reylé, C., Derrière, S., & Picaud, S. 2003, A&A, 409, 523
Roeser, S., Demleitner, M., & Schilbach, E. 2010, AJ, 139, 2440
Röser, S., Schilbach, E., Schwan, H., et al. 2008, A&A, 488, 401
Ruchti, G. R., Fulbright, J. P., Wyse, R. F. G., et al. 2011, ApJ, 737, 9
Salaris, M., Chieffi, A., & Straniero, O. 1993, ApJ, 414, 580
Sales, L. V., Helmi, A., Abadi, M. G., et al. 2009, MNRAS, 400, L61
Schönrich, R., Binney, J., & Asplund, M. 2012, MNRAS, 420, 1281
Seabroke, G. M., Gilmore, G., Siebert, A., et al. 2008, MNRAS, 384, 11
Sellwood, J. A., & Binney, J. J. 2002, MNRAS, 336, 785
Siebert, A., Bienaymé, O., Binney, J., et al. 2008, MNRAS, 391, 793
Siebert, A., Famaey, B., Binney, J., et al. 2012, MNRAS, 425, 2335
Siebert, A., Famaey, B., Minchev, I., et al. 2011a, MNRAS, 412, 2026
Siebert, A., Williams, M. E. K., Siviero, A., et al. 2011b, AJ, 141, 187
Smith, J. A., Tucker, D. L., Kent, S., et al. 2002, AJ, 123, 2121
Sneden, C. A. 1973, PhD thesis, Univ. Texas Austin
Soubiran, C., & Girard, P. 2005, A&A, 438, 139
Soubiran, C., Le Campion, J.-F., Cayrel de Strobel, G., & Caillo, A. 2010, A&A, 515, A111
Steinmetz, M., Zwitter, T., Siebert, A., et al. 2006, AJ, 132, 1645
Valdes, F., Gupta, R., Rose, J. A., Singh, H. P., & Bell, D. J. 2004, ApJS, 152, 251
Valenti, J. A., & Fischer, D. A. 2005, ApJS, 159, 141
van der Kruit, P. C., & Freeman, K. C. 2011, ARA&A, 49, 301
Veltz, L., Bienaymé, O., Freeman, K. C., et al. 2008, A&A, 480, 753
Wainscoat, R. J., Cohen, M., Volk, K., Walker, H. J., & Schwartz, D. E. 1992, ApJS, 83, 111
Williams, M. E. K., Steinmetz, M., Binney, J., et al. 2013, arXiv:1302.2468
Williams, M. E. K., Steinmetz, M., Sharma, S., et al. 2011, ApJ, 728, 102
Wilson, M. L., Helmi, A., Morrison, H. L., et al. 2011, MNRAS, 413, 2235
Zacharias, N., Finch, C., Girard, T., et al. 2010, AJ, 139, 2184
Zacharias, N., Finch, C. T., Girard, T. M., et al. 2013, AJ, 145, 44
Zacharias, N., Urban, S. E., Zacharias, M. I., et al. 2004, AJ, 127, 3043
Zwitter, T., Matijevič, G., Breddels, M. A., et al. 2010, A&A, 522, A54
Zwitter, T., Siebert, A., Munari, U., et al. 2008, AJ, 136, 421

Chapitre 3

Mouvements radiaux et verticaux causés par les bras spiraux

Dans ce chapitre, nous allons voir quels effets les bras spiraux peuvent avoir sur le mouvement des étoiles de la Voie Lactée. Jusqu'à présent, le modèle de la Galaxie est, en général supposé axisymétrique et stationnaire en première approximation. Dans ce type de modèle, les vitesses radiales et verticales moyennes sont nulles en tout point. Mais nous avons vu, avec des relevés spectroscopiques récents comme RAVE, que ces vitesses sont non-nulles et les gradients de vitesses ne sont pas négligeables.
Ceci peut être problématique car les modèles axisymétriques permettent de découpler les mouvements radiaux et verticaux, ce qui apparait ne plus être le cas. Ces mouvements sont de plus en plus considérés comme des éléments importants de la dynamique galactique. Pourtant, nous ne connaissons pas les biais que nous introduisons en tentant de modéliser les observations avec les modèles axisymétriques.
Dans le plan galactique, on sait depuis les années 60 que ce sont les composantes non-axisymétriques comme la barre centrale et/ou les bras spiraux qui sont à l'origine des vitesses radiales moyennes non-nulles mais elles sont généralement négligées dans les modèles. En ce qui concerne les vitesses verticales moyennes, ce sont des observations récentes et des travaux qui ont attribué des valeurs non-nulles à l'excitation du disque. Cela serait causé par l'interaction de galaxies satellites ou de sous-halos.
Nous nous sommes posés la question de savoir s'il y avait d'autres explications possibles qui ne font pas intervenir d'éléments extérieurs comme les bras spiraux ou la barre centrale de la Galaxie.

3.1 Mouvements radiaux : modèle analytique d'ondes de densité en 2D

Les résultats sont détaillés dans l'article ci-dessous intitulé "The properties of the local spiral arms from RAVE data : two-dimensional density wave approach" et publié dans le Monthly Notices of the Royal Astronomical Society.
Une analyse préliminaire de ce champ de vitesse dans un modèle analytique à deux dimensions a alors été entreprise (Siebert et al. 2012) dont je suis co-auteur. En supposant que le gradient était causé uniquement par les bras spiraux, et en se basant sur le modèle des ondes de densité de Lin & Shu (Binney & Tremaine 2008), une comparaison avec la vitesse radiale moyenne en fonction de la position dans le plan galactique a été effectuée. Cette analyse favorise une origine de ce gradient de vitesse radiale dans une perturbation spirale à deux bras plutôt que quatre (les χ^2 sont comparables mais l'angle d'enroulement des bras

est trop grand), avec une amplitude correspondant à 14% de la densité de la composante axisymétrique du disque, et avec une fréquence de rotation du pattern spiral de 18 $km.s^{-1}$ kpc^{-1} avec le Soleil proche de la résonance ultra-harmonique interne (200 pc en dehors). Ces résultats sont en accord avec les études sur l'emplacement des groupes mobiles abordés plus haut. La position des bras spiraux du meilleur modèle coïncide avec celle des bras de Persée et du Centaure obtenue par l'étude d'objets jeunes dont la dynamique se rapproche de celle du gaz.
Néanmoins, l'aspect problématique de ce modèle analytique est qu'il ne fait de prédiction que dans le plan galactique, alors que les données RAVE ont été obtenues en dehors de ce plan (le plan Galactique n'est pas observé par RAVE, l'extinction par la poussière empêchant de sonder les régions proches du plan).

Publication de "The properties of the local spiral arms from RAVE data : two-dimensional density wave approach"

Monthly Notices
of the
ROYAL ASTRONOMICAL SOCIETY

Mon. Not. R. Astron. Soc. **425,** 2335–2342 (2012) doi:10.1111/j.1365-2966.2012.21638.x

The properties of the local spiral arms from RAVE data: two-dimensional density wave approach

A. Siebert,[1⋆] B. Famaey,[1] J. Binney,[2] B. Burnett,[2] C. Faure,[1] I. Minchev,[3] M. E. K. Williams,[3] O. Bienaymé,[1] J. Bland-Hawthorn,[4] C. Boeche,[5] B. K. Gibson,[6,7] E. K. Grebel,[5] A. Helmi,[8] A. Just,[5] U. Munari,[9] J. F. Navarro,[10] Q. A. Parker,[11,12,13] W. A. Reid,[11,12] G. Seabroke,[14] A. Siviero,[3,15] M. Steinmetz[3] and T. Zwitter[16,17]

[1] *Observatoire Astronomique, Université de Strasbourg, CNRS, 11 rue de l'université, 67000 Strasbourg, France*
[2] *Rudolf Peierls Centre for Theoretical Physics, 1 Keble Road, Oxford OX1 3NP*
[3] *Leibniz-Institut für Astrophysik Potsdam (AIP), An der Sternwarte 16, D-14482 Potsdam, Germany*
[4] *Sydney Institute for Astronomy, University of Sydney, Sydney, NSW 2006, Australia*
[5] *Astronomisches Rechen-Institut, Zentrum für Astronomie der Universität Heidelberg, Mönchhofstr. 12-14, D-69120 Heidelberg, Germany*
[6] *Jeremiah Horrocks Institute, University of Central Lancashire, Preston PR1 2HE*
[7] *Department of Astronomy and Physics, Saint Mary's University, Halifax, Nova Scotia B3H 3C3, Canada*
[8] *Kapteyn Astronomical Institute, University of Groningen, PO Box 800, 9700 AV Groningen, the Netherlands*
[9] *INAF Astronomical Observatory of Padova, 36012 Asiago (VI), Italy*
[10] *Department of Physics and Astronomy, University of Victoria, Victoria, BC V8P 5C2, Canada*
[11] *Department of Physics and Astronomy, Faculty of Science, Macquary University, NSW 2109, Sydney, Australia*
[12] *Macquarie Research Centre for Astronomy, Astrophysics and Astrophotonics, NSW 2109, Sydney, Australia*
[13] *Australian Astronomical Observatory, PO Box 296, Epping, NSW 2121, Australia*
[14] *Mullard Space Science Laboratory, University College London, Holmbury St Mary, Dorking RH5 6NT*
[15] *Department of Physics and Astronomy 'G.Galilei', Padova University, Vicolo dellOsservatorio 2, Padova 35122, Italy*
[16] *Faculty of Mathematics and Physics, University of Ljubljana, Jadranska 19, SI-1000 Ljubljana, Slovenia*
[17] *Center of Excellence SPACE-SI, Askerceva cesta 12, SI-1000 Ljubljana, Slovenia*

Accepted 2012 July 2. Received 2012 July 2; in original form 2012 April 12

ABSTRACT

Using the Radial Velocity Experiment (RAVE) survey, we recently brought to light a gradient in the mean galactocentric radial velocity of stars in the extended solar neighbourhood. This gradient likely originates from non-axisymmetric perturbations of the potential, among which a perturbation by spiral arms is a possible explanation. Here, we apply the traditional density wave theory and analytically model the radial component of the two-dimensional velocity field. Provided that the radial velocity gradient is caused by relatively long-lived spiral arms that can affect stars substantially above the plane, this analytic model provides new independent estimates for the parameters of the Milky Way spiral structure. Our analysis favours a two-armed perturbation with the Sun close to the inner ultra-harmonic 4:1 resonance, with a pattern speed $\Omega_\mathrm{p} = 18.6^{+0.3}_{-0.2}\,\mathrm{km\,s^{-1}\,kpc^{-1}}$ and a small amplitude $A = 0.55^{+0.02}_{-0.02}$ per cent of the background potential (14 per cent of the background density). This model can serve as a basis for numerical simulations in three dimensions, additionally including a possible influence of the Galactic bar and/or other non-axisymmetric modes.

Key words: stars: kinematics and dynamics – Galaxy: fundamental parameters – Galaxy: kinematics and dynamics.

1 INTRODUCTION

It has long been recognized that internal secular evolution processes should play a major role in shaping galaxy discs. Among the main drivers of this secular evolution are the disc instabilities and associated non-axisymmetric perturbations, including the bar and spiral arms. Questions about their nature, transient or quasi-stationary (e.g. Sellwood 2010a; Quillen et al. 2011; Grand, Kawata & Cropper 2012a), about their detailed structure and dynamics such as their amplitude, pattern speed, pitch angle or number of arms, as well as questions about their detailed influence on secular

⋆E-mail: arnaud.siebert@astro.unistra.fr

processes like stellar migration (Sellwood & Binney 2002; Minchev & Famaey 2010), are all essential elements for a better understanding of galactic evolution. The Milky Way provides a unique laboratory in which a snapshot of the dynamical effect of present-day disc non-axisymmetries can be studied in great detail, and help answering the above questions.

Current knowledge of the structure and dynamics of the bar and the spiral arms of the Milky Way relies both on the gas and, notably, on its observed longitude–velocity diagram (Binney et al. 1991; Bissantz, Englmaier & Gerhard 2003; Englmaier, Pohl & Bissantz 2011) or masers in high-mass star-forming regions (Reid et al. 2009, and references therein), and on the stars (e.g. Georgelin & Georgelin 1976; Binney, Gerhard & Spergel 1997; Stanek et al. 1997; Benjamin et al. 2005; Lépine et al. 2011b). For the spiral arms, both types of constraints are combined in a recent study by Vallée (2008), whose model predicts the location in space and velocity for the spiral arms.

With the advent of new spectroscopic and astrometric surveys, six-dimensional phase-space information for stars in an increasingly large volume around the Sun allows us to set new dynamical constraints on the non-axisymmetric perturbations of the Galactic potential. An example of such new detailed kinematical information on stellar motions in the extended solar neighbourhood is the recently detected (galactocentric) radial velocity gradient of $\sim$4 km s^{-1} kpc^{-1} by Siebert et al. (2011a), making use of more than 200 thousand stars from the Radial Velocity Experiment (RAVE) survey. If this result is not owing to systematic distance errors (which the geometry of the radial velocity flow seems to exclude by not depending on distance and longitude in any systematically biased way), and more importantly, if one assumes that, at first order, what is seen above the plane is a reflection of what would happen in a razor-thin disc, and that the spiral arms are long-lived, one can apply the analytic density wave description of spiral arms proposed by Lin & Shu (1964) to constrain the shape, amplitude and dynamics of spiral arms.

Whether long-lived density waves are the correct description of spiral patterns in galaxies remains heavily debated. From a theoretical point of view, while it seems that the radial velocity dispersion profile needed to support long-lived spiral waves in barless discs (e.g. Bertin & Lin 1996) would be heavily unstable (Sellwood 2010a), the situation is much less clear in the presence of a central bar, where non-linear mode coupling between the bar and spiral could sustain a long-lived spiral pattern (Voglis, Stavropoulos & Kalapotharakos 2006; Salo et al. 2010; Quillen et al. 2011; Minchev et al. 2012), while Grand, Kawata & Cropper (2012b), however, find that spiral arms are transient even in the presence of a central bar. On the other hand, D'Onghia et al. (2012) find locally long-lived self-perpetuating spiral arms which could be locally consistent with density waves, but fluctuating in amplitude with time. Furthermore, long-lived spirals can also develop as being sustained by coherent oscillations due to a flyby galaxy encounter (Struck, Dobbs & Hwang 2011), a process we know to be ongoing for the Milky Way, and cosmologically simulated disc galaxies exhibit a distribution of young stars consistent with the predictions of classical density wave theory for long-lived spirals (Pilkington, Gibson & Jones 2012). Finally, let us note that both long-lived and transient spirals can coexist in a galaxy, which adds complexity to the picture.

On the observational side the situation is also unclear. Evidence seems to exist for both transient and long-lived spiral arms: e.g. M81 apparently contains long-lived spiral arms consistent with the classical density wave theory (Lowe et al. 1994; Adler & Wefstpfahl 1996; Kendall et al. 2008) while in M51, even if its disc streaming motion appears consistent with the density wave description, the mass fluxes are inconsistent with a steady flow (Shetty 2007). Studying observational tracers for different stages of the star formation sequence in 12 nearby spiral galaxies, Foyle et al. (2011) also found that they do not show the expected spatial ordering for long-lived spiral arms, from upstream to downstream in the corotating frame. In the Milky Way, many of the dynamical constraints on spiral arms currently come from local constraints provided by velocity space substructures also known as moving groups (Dehnen 1998; Famaey et al. 2005). For instance, examining the local stellar distribution in action space, Sellwood (2010b) found that stars from the Hyades moving group were concentrated along a resonance line in action space, which was interpreted as a signature of scattering at the inner Lindblad resonance of a transient spiral pattern (see also McMillan 2011, who found that this feature could also be associated with an outer Lindblad resonance). However, in this picture, only the Hyades moving group is accounted for, and the remaining substructures observed in the local phase space distribution must be explained by invoking other origins. Models based only on transient spiral arms (e.g. De Simone, Wu & Tremaine 2004) were actually unable to reproduce the precise location of the various other prominent moving groups, such as Sirius. On the other hand, models based on long-lived spiral arms, locating the 4:1 inner resonance close to the Sun, were able to reproduce both the position of the Hyades and Sirius moving groups at the same time (Quillen & Minchev 2005; Pompéia et al. 2011) as well as other moving groups (Antoja et al. 2011). Other observational arguments based on the step-like metallicity gradient in the Galactic disc also argue in favour of long-lived spirals (Lépine et al. 2011a).

Given this theoretical and observational situation, we here make the conservative assumption that interesting information can be retrieved from the classical analytic treatment of spiral arms as long-lived density waves. This analytic model could then serve as a basis for numerical simulations in a three-dimensional disc. This paper is structured as follows. In Section 2, we review the data, as well as the analytic density wave model we are using. We present and discuss our results in Section 3, and conclude in Section 4.

2 DATA AND METHOD

2.1 Two-dimensional velocity field

Our analysis is based on data from the RAVE survey (Steinmetz et al. 2006; Zwitter et al. 2008; Siebert et al. 2011b) which provides line-of-sight velocities with a precision of 2 km s^{-1} for a large number of bright stars in the Southern hemisphere with $9 < I < 12$. RAVE selects its targets randomly in the I-band interval, and so its properties are similar to a magnitude limited survey. The RAVE catalogue is cross-matched with astrometric (PPMX, UCAC2, Tycho-2) and photometric catalogues (2MASS, DENIS) to provide additional proper motions and magnitudes. In this study, we use the internal version of the catalogue which contains data for 434 807 spectra (393 903 stars). To compute the galactocentric velocities, knowledge of the distance to the star is required. For RAVE stars, distances to 30 per cent are available in three studies: Breddels et al. (2010), Zwitter et al. (2010) and Burnett et al. (2011). All catalogues provide compatible distance estimators and the velocity maps generated using the different catalogues are similar.

Our final sample consists of 213 713 stars from this survey limited to a distance of 2 kpc from the Sun and to a height of 1 kpc above and below the plane. We demonstrated the existence of a velocity

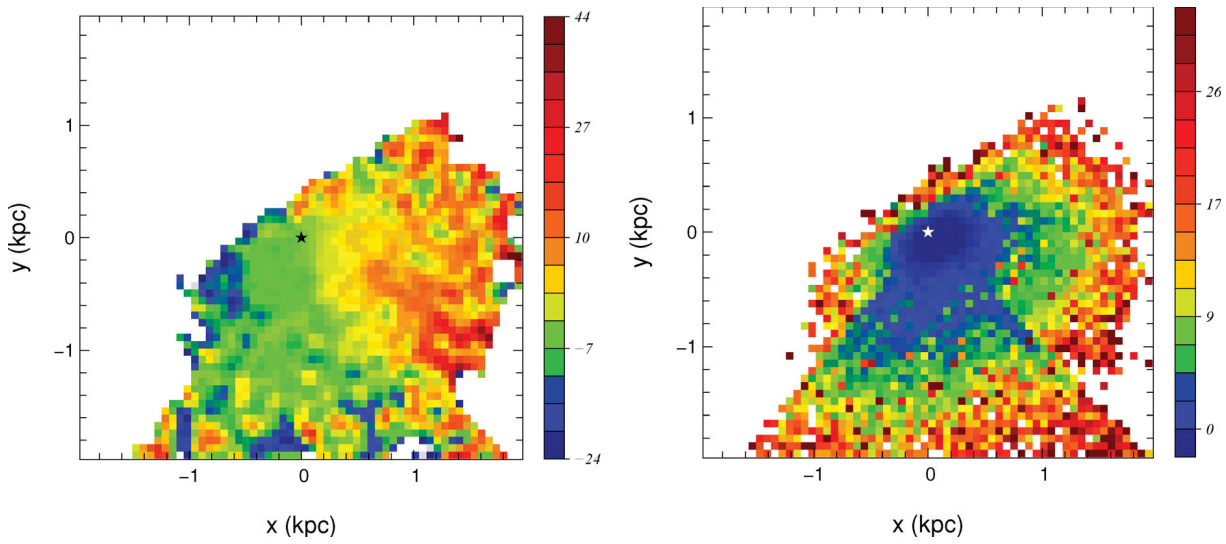

Figure 1. Left: velocity field for the radial component of the velocity vector $\langle V_R \rangle$ as a function of location in the Galactic plane. Right: associated random error on the mean velocity. In both panels, the location of the Sun is marked by a star; the Galactic Centre is towards positive x and the y-axis is oriented towards the Galactic rotation. The colour coding follows the mean velocity and mean velocity error in km s^{-1}.

gradient of disc stars in the fourth quadrant, directed radially from the Galactic Centre (Siebert et al. 2011a). The two-dimensional mean galactocentric radial velocity field in the Galactic plane is presented in Fig. 1 where we use a box 4×4 kpc in size, centred on the Sun, sampled using 60 bins in each direction. For this analysis, we restrict ourselves to bins containing more than five stars and the mean velocity is computed using a median function. Note that converting velocities in the heliocentric reference frame into the (V_R, V_θ) galactocentric coordinates requires the galactocentric radius of the Sun R_0, the Sun's peculiar velocity $\boldsymbol{v}_\odot$ with respect to the Local Standard of Rest (LSR) and the motion of the LSR with respect to the Galactic Centre v_{LSR}. We assume $R_0 = 8$ kpc for the distance of the Sun to the Galactic Centre and $V_{LSR} = 220\,\mathrm{km\,s^{-1}}$ to match the values used for the mass model (see Section 2.2). We use the latest determination of the value of the solar motion by Schönrich, Binney & Dehnen (2010): $(U_\odot, V_\odot) = (11.1, 12.24)\,\mathrm{km\,s^{-1}}$.

The gradient affects a sample dominated at large distances by red giants, with a typical velocity dispersion $\sigma_R \sim 30$–$40\mathrm{km\,s^{-1}}$, and affects stars substantially above the plane, keeping in mind that RAVE lines of sight are typically at $|b| > \sim 20^\circ$. The zone where the gradient is the steepest is populated with stars with typically $|z| \sim 500$ pc. However, if U_{LSR} is positive (a local mean motion towards the inner Galaxy), then $\langle V_R \rangle$ would be by construction negative in the Sun's neighbourhood and reach 0 at larger distances and larger heights. In the modelling procedure hereafter, we let $\langle V_R \rangle_{R_0} \equiv -U_{LSR}$ be a parameter of the model to allow us to account for uncertainties on this quantity.

Ideally, one would also use the tangential velocity field $\langle V_\theta \rangle$ in combination with the $\langle V_R \rangle$ field. However, as stated above, our sample reaches distances to the Galactic plane of 1 kpc, avoiding the regions close to the plane. The RAVE survey mimicking a magnitude limited survey in fields 6° in diameter on the sky, each field containing a different number of stars, the stellar population mixture varies from point to point on the maps. Therefore, the contribution of the asymmetric drift is difficult to estimate while it enters the calculation of the V_θ component. Hence, we chose to restrict our analysis to the $\langle V_R \rangle$ field, although we give the full set of equations, including this component, in the next section.

2.2 Density wave model

To model the velocity field, we use the density wave description of spiral arms proposed by Lin & Shu (1964) and further developed in Lin, Yuan & Shu (1969) and Shu, Stachnik & Yost (1971). This model is based on an asymptotic analysis of the WKBJ type of the Euler/Boltzmann equations, valid only in the regime of weak, long-lived and tightly wound spirals (small pitch angle). This model being well known and documented (see e.g. Binney & Tremaine 2008), we restrict its description to the main results used in this study.

The perturbation to the potential considered is of the form

$$\Phi_1 = A(R) \exp[i(\omega t - m\theta + \Phi(R))]\,, \tag{1}$$

where $A(R)$ is the amplitude of the perturbation, m is the number of arms and $\Phi(R)$ is a monotonic function. The perturbation rotates at an angular frequency given by

$$\Omega_p = \omega/m\,. \tag{2}$$

The perturbations in the components of the mean velocities $\langle V_R \rangle$ and $\langle V_\theta \rangle$, where (R, θ) are the coordinates in the cylindrical coordinate system centred on the Galaxy, are given by

$$\begin{aligned} \langle V_R \rangle &= \frac{kA}{\kappa} \frac{\nu}{1-\nu^2} \mathcal{F}_\nu^{(1)}(x) \cos(\chi) \\ \langle V_\theta \rangle &= -\frac{1}{2} \frac{kA}{\Omega} \frac{1}{1-\nu^2} \mathcal{F}_\nu^{(2)}(x) \sin(\chi) \end{aligned} \tag{3}$$

where

$$x = \frac{k^2 \sigma_R^2}{\kappa^2}\,, \tag{4}$$

k being the radial wavenumber, σ_R is the velocity dispersion, κ is the epicyclic frequency and ν is defined by $\nu = m(\Omega_p - \Omega)/\kappa$.

The functions $\mathcal{F}_\nu^{(1)}$ and $\mathcal{F}_\nu^{(2)}$ are the 'reduction factors' that correct the mean velocities for the effect of velocity dispersion, lowering the effect of the spiral perturbation on the velocity field as the velocity dispersion increases. In the limit of a zero velocity dispersion ($\mathcal{F}_\nu^{(1)} = \mathcal{F}_\nu^{(2)} = 1$) we recover the velocity field of the gas while if σ_R becomes large, $\mathcal{F}_\nu^{(1)} = \mathcal{F}_\nu^{(2)} \to 0$ and the velocity field becomes

unaffected by the spiral perturbation. The two functions are given in appendix B of Lin et al. (1969).

The phase of the spiral pattern χ is defined by

$$\chi = \omega t - m\theta + \Phi(R) \tag{5}$$

which, in the case of logarithmic spirals with $\Phi(R) = m \cot g\, i \ln R$ in equation (1) (i being the pitch angle), can be written in a more convenient form as

$$\chi = \chi_0 + m(\cot g\, i\ \ln(R/R_0) - (\theta - \theta_0))\,. \tag{6}$$

The subscripts 0 in the previous equation refer to the value at the Sun's location. The radial wavenumber k is then given by

$$k(R) = \Phi'(R) = m \cot g\, i / R\,, \tag{7}$$

with $k(R) < 0$ for trailing waves and $k(R) > 0$ for leading waves.

The mean velocities of equation (3) vary in the Galactic plane as a function of R and θ, the modulation depending on the mass model via Ω and κ, the velocity dispersion in the radial direction $\sigma_{\rm R}$ via the reduction factors and on the parameters of the spiral perturbation. These parameters are the number of arms m, the amplitude of the perturbation A, its pattern speed $\Omega_{\rm p}$, the pitch angle i and the phase χ_0. In addition we chose to include $\langle V_{\rm R}\rangle_{R_0}$ as a free parameter while computing the model to account for possible uncertainties on $U_{\rm LSR}$. While this parameter is usually taken into account while computing the velocities ($V_{\rm R}$, V_θ) of the observations, here we include it as a correction to the predicted $\langle V_{\rm R}\rangle$ and $\langle V_\theta\rangle$ in the model to avoid the computation of the velocity field at each step which is time consuming. In the remainder of the paper, we will denote $\boldsymbol{P}$ as the vector of model parameters $\boldsymbol{P} = (m, A, \Omega_{\rm p}, i, \chi_0, \sigma_{\rm R}, \langle V_{\rm R}\rangle_{R_0})$.

For the rotation curve of the Milky Way, we use the models I and II of Binney & Tremaine (2008), table 2.3, based on the mass models of Dehnen & Binney (1998). These models reproduce equally well the circular-speed curve and other observationally constrained quantities such as the Oort constants, the surface mass density within 1.1 kpc or the total mass within 100 kpc of the Milky Way. The two models correspond to two limiting cases where either the disc or the halo dominates the rotation curve (model I and II, respectively). The models being computed for $R_0 = 8$ kpc and $V_{\rm co} \sim 220\,{\rm km\,s^{-1}}$, we use the same values for these two parameters when computing the galactocentric velocities in Fig. 1.

In practice, our tests showed that all our solutions converged on approximately the same value for $\sigma_{\rm R}$. This is due to our sample being dominated by the old thin disc population, and we chose to fix $\sigma_{\rm R}$ to the best-fitting value, $\sigma_{\rm R} = 34.2\,{\rm km\,s^{-1}}$, to reduce the dimension of our parameter space. This value of the dispersion fits very well the observed dispersion from the RAVE sample, excluding the tails representative of the thick disc population and of large proper motion errors. Hence, the model parameters we consider in the remainder of the paper is $\boldsymbol{P} = (m, A, \Omega_{\rm p}, i, \chi_0, \langle V_{\rm R}\rangle_{R_0})$.

The mean velocities of equation (3) are compared to the two-dimensional velocity field of Section 2.1. The comparison is done using a chi-square estimator

$$\chi^2 = \sum_i \frac{(\langle V_{\rm R}\rangle_{i,\rm obs} - \langle V_{\rm R}\rangle_{i,\rm model})^2}{\sigma^2_{i,\rm obs}}\,, \tag{8}$$

where the sum is on all bins containing at least five stars and $\sigma_{i,\rm obs}$ is the error on the mean velocity shown in Fig. 1 (right-hand panel). We restrict the analysis to the mean velocity in the radial direction, the tangential velocities being affected by the asymmetric drift which cannot be properly taken into account in the model, our sample being a mixture of stellar populations of different ages, even though it is dominated by the old thin disc (see Section 2.1).

We note also that systematic distance errors would affect the results presented below. As shown in the first paper (Siebert et al. 2011a), a systematic error in the distances affects the measured gradient in $\langle V_{\rm R}\rangle$ by approximately the same factor: a 20 per cent overestimate/underestimate of the distances induces a ∼20 per cent overestimate/underestimate of the amplitude of the velocity gradient in $\langle V_{\rm R}\rangle$, which to the first order results in a higher/lower amplitude A of the spiral perturbation by the same amount. However, as shown in the same paper, an independent estimate of the velocity field using red clump stars, for which an unbiased distance estimate can be obtained, shows a good agreement of the velocity fields, giving us confidence that our distances cannot be strongly affected by an unknown bias and we will not consider this possibility in the remainder in this paper.

3 RESULTS AND DISCUSSION

3.1 Parameter space sampling

The number of arms in the Milky Way is not known with certainty. Both two-armed and four-armed spiral pattern are considered in the literature although an $m = 2$ mode in the stars seems to be favoured. In the analysis, we will consider both cases and look for the best matching solution for either number of spiral arms.

Also, some recent works have suggested that the LSR is not on a circular orbit; e.g. $U_{\rm LSR}$ might not be 0 $\rm km\,s^{-1}$(Smith et al. 2009; Smith, Whiteoak & Evans 2012; Moni-Bidin, Carraro & Mendez 2012). Therefore, we include the possibility for a non-null U component of the LSR in the model.

For the minimization, we considered the standard value of $U_{\rm LSR} = 0\,{\rm km\,s^{-1}}$ [1] as well as values of $\pm 5\,{\rm km\,s^{-1}}$ whose amplitude corresponds to the finding of Smith et al. (2012). Finally, we left $\langle V_{\rm R}\rangle_{R_0}$ as a free parameter in the fit. However, we note that our sample reaches only 2 kpc away from the Sun, not deep enough in the plane to disentangle the effect of a radial motion of the LSR from uncertainties in the U component of the solar motion with respect to the LSR. Therefore we should keep in mind that a non-null best-fitting value of the $\langle V_{\rm R}\rangle_{R_0}$ parameter does not necessarily imply a radial motion of the LSR.

The summary of the chi-square analysis is presented in Table 1 and the chi-square contours for the best models are presented in Fig. 2. In this figure, the two panels show the 1σ, 2σ and 3σ contours, fixing all the other parameters to the best-fitting solution, in the $\Omega_{\rm p}$ versus amplitude plane (left-hand panel) and pitch angle i versus phase χ_0 (right-hand panel). The plain lines are for the mass model I, and the red dashed lines are for model II.

The best-fitting model is obtained for a two-armed spiral mode with the mass model II. The best-fitting solution for model I is equally good with a chi-square difference of 0.5. Generally, the difference between the two mass models is low. This is expected as within the region sampled by the RAVE data, the models are comparable with $\Omega_{\rm mI} - \Omega_{\rm mII} \approx 0.35\,{\rm km\,s^{-1}\,kpc^{-1}}$. The density wave model being not sensitive to the details of the mass model – the latter entering the equations only through $\Omega(R)$ and κ – the two models can only be distinguished in regions where they are significantly different (e.g. closer to the Galactic Centre).

[1] Recall that $U_{\rm LSR} \equiv -\langle V_{\rm R}\rangle_{R_0}$.

Table 1. Chi-square results. Parameters with error bars were kept free in the minimization. The error bars correspond to the 1σ internal errors obtained from the chi-square contour. Models marked with an asterisk (*) have a large pitch angle (open arms) and do not satisfy the tight-winding approximation. The number of pixels used in the minimization procedure is 1595.

Mass model	m	$\langle V_R \rangle_{R_0}$ km s^{-1}	Ω_p km s^{-1} kpc^{-1}	A per cent (total, disc)	i (○)	χ_0 (○)	χ^2	
I	2	$0.9^{+0.1}_{-0.1}$	$18.9^{+0.3}_{-0.2}$	$(0.50^{+0.02}_{-0.02}, 2.27^{+0.08}_{-0.07})$	$-10.0^{+0.4}_{-0.4}$	$76.9^{+1.1}_{-1.2}$	1829.00	
I	2	-5	$16.1^{+0.1}_{-0.1}$	$(0.78^{+0.01}_{-0.01}, 3.50^{+0.07}_{-0.06})$	$-23.2^{+0.3}_{-0.5}$	$57.3^{+0.6}_{-0.5}$	1943.14	(*)
I	2	0	$18.8^{+0.2}_{-0.3}$	$(0.49^{+0.02}_{-0.02}, 2.21^{+0.08}_{-0.09})$	$-9.1^{+0.3}_{-0.4}$	$65.8^{+1.5}_{-1.0}$	1831.99	
I	2	5	$19.3^{+0.1}_{-0.2}$	$(0.69^{+0.02}_{-0.01}, 3.12^{+0.09}_{-0.05})$	$-15.6^{+0.7}_{-0.6}$	$112.1^{+1.0}_{-0.9}$	1853.04	
II	2	$0.9^{+0.3}_{-0.2}$	$18.6^{+0.3}_{-0.2}$	$(0.55^{+0.02}_{-0.02}, 3.09^{+0.10}_{-0.13})$	$-10.0^{+0.4}_{-0.4}$	$76.0^{+1.3}_{-1.0}$	1828.46	
II	2	-5	$15.1^{+0.1}_{-0.1}$	$(0.71^{+0.01}_{-0.01}, 3.93^{+0.06}_{-0.07})$	$-22.3^{+0.3}_{-0.6}$	$55.7^{+0.7}_{-0.4}$	1940.75	(*)
II	2	0	$18.5^{+0.3}_{-0.2}$	$(0.54^{+0.02}_{-0.03}, 3.03^{+0.09}_{-0.15})$	$-9.3^{+0.4}_{-0.3}$	$66.6^{+1.3}_{-1.1}$	1830.17	
II	2	5	$16.2^{+0.1}_{-0.1}$	$(0.51^{+0.01}_{-0.01}, 2.84^{+0.07}_{-0.05})$	$-16.3^{+0.7}_{-0.6}$	$111.3^{+0.9}_{-0.8}$	1859.98	
I	4	$4.9^{+0.1}_{-0.1}$	$25.8^{+0.1}_{-0.1}$	$(0.71^{+0.02}_{-0.01}, 3.22^{+0.08}_{-0.06})$	$-26.0^{+0.6}_{-0.5}$	$132.8^{+1.8}_{-1.7}$	1833.52	(*)
II	4	$4.9^{+0.1}_{-0.1}$	$25.9^{+0.1}_{-0.1}$	$(0.91^{+0.03}_{-0.02}, 5.09^{+0.16}_{-0.09})$	$-26.7^{+1.0}_{-0.4}$	$135.0^{+2.3}_{-1.7}$	1829.55	(*)

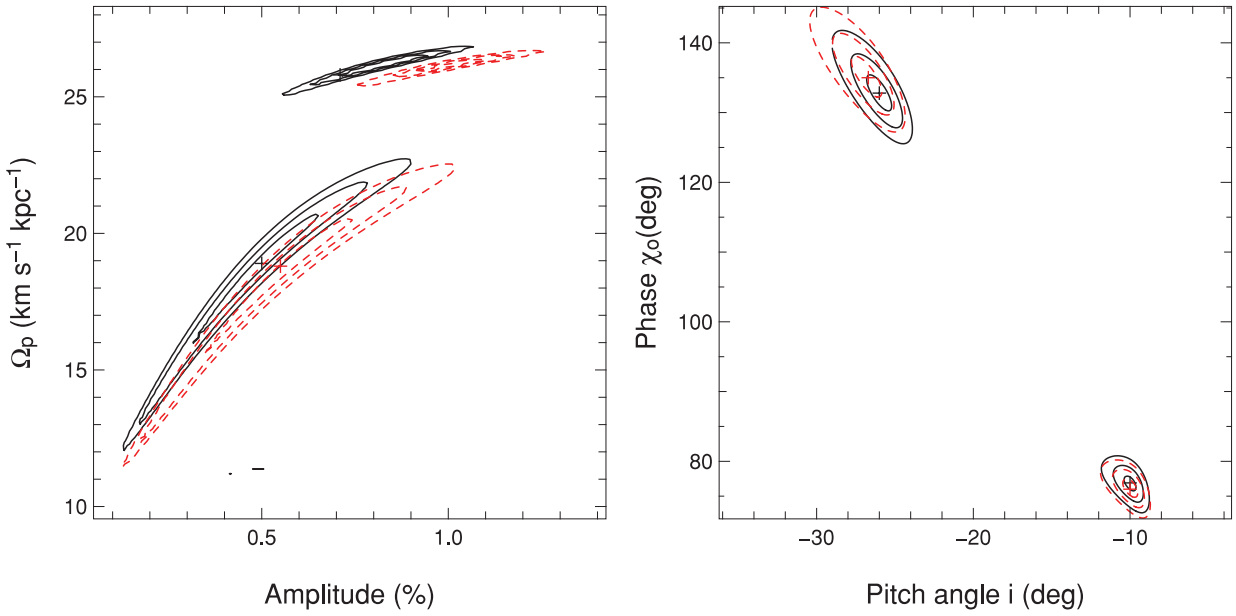

Figure 2. Cuts through the chi-square space around the best-fitting models in the amplitude versus pattern speed plane (left-hand panel) and phase versus pitch angle plane (right-hand panel). The crosses mark the location of the best fit while the contours are the 1σ, 2σ and 3σ limits. The amplitude in the left-hand panel is given as a percentage of the background potential at the Sun's location. The plain lines are for the mass model I and the dashed lines for the mass model II. In both panels the top contours are for $m = 4$, and the bottom contours for $m = 2$.

The chi-square value of the best $m = 4$ solution is also close to the best $m = 2$ solution. However, for $m = 4$ the pitch angle i is found to be $\approx -26^\circ$, out of the bounds of the tight-winding approximation upon which the density wave model relies ($\max(|i|) \approx 15^\circ$–$20^\circ$; Lin et al. 1969). Hence, for a four-armed pattern, we conclude that no satisfactory solution is found and we will discard four-armed patterns in the following discussion.

Focusing on the $m = 2$ mode, a strong correlation is observed between the amplitude and the pattern speed while the correlation is weaker between the pitch angle and the phase (Fig. 2). If the phase and pitch angle are well determined, the shape of the contours in amplitude versus Ω_p indicates a large range in possible solutions at the 3σ level: Ω_p varies from 12 to 22 km s^{-1} kpc^{-1} and the amplitude from 0.1 to 0.9 per cent of the background potential. The amplitude of the best-fitting model is $A = 0.55$ per cent of the background potential. This value translates to 14 per cent of the background density which is close to the value proposed by Minchev & Famaey (2010) and consistent with earlier determinations summarized in Antoja et al. (2011) for the local spiral amplitude. We also note that corotating waves ($\Omega_p \sim 27.5$ km s^{-1} kpc^{-1}) seem to be excluded.

Finally, among the $m = 2$ solutions, a low radial component of the LSR velocity is preferred. The best-fitting model converges to $\langle V_R \rangle_{R_0} = 0.9$ km s^{-1} while a zero radial component cannot be ruled out when comparing the chi-square values. On the other hand, a more pronounced outwards motion of the LSR ($\langle V_R \rangle_{R_0} = 5$ km s^{-1}) shows significantly larger chi-square values while an inwards motion of -5 km s^{-1} as suggested by Smith et al. (2012) is even less consistent. However in the latter case, the model converges outside of the range of allowed values for the pitch angle which limits the conclusions one can draw from this result. We note that our

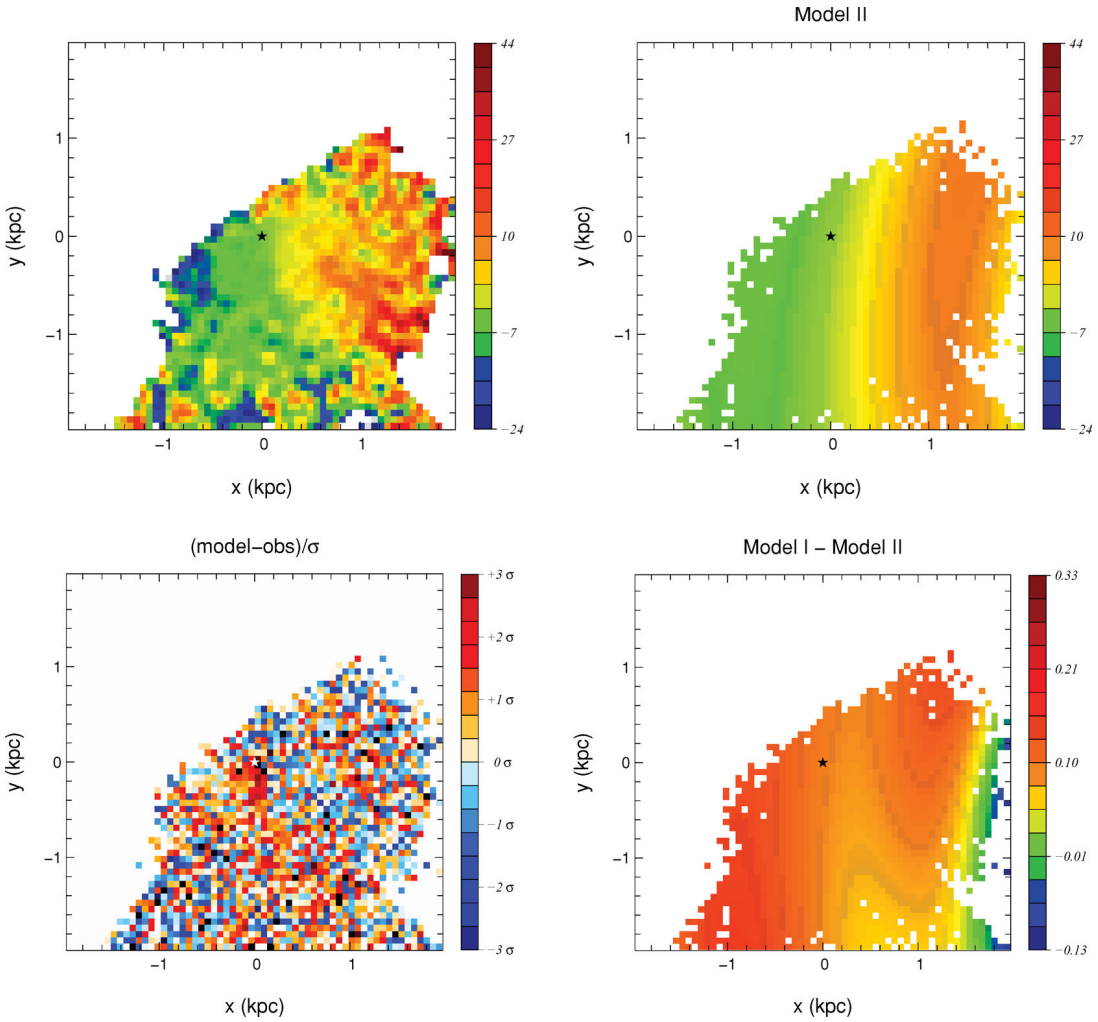

Figure 3. Top panels: observed velocity field (left) and model velocity field for the best-fitting solution using the mass model II (right). Bottom right: velocity field difference between the best-fitting solutions using the mass model I and II. The colour coding follows the median galactocentric radial velocity in km s^{-1} in the three panels. Bottom left: difference $\langle V_{\rm R,mII}\rangle - \langle V_{\rm R,observed}\rangle$ normalized by the observational errors showing that all velocities on the two-dimensional map are well recovered within the observational uncertainties. On all panels, the Sun's location is at (0,0) and is marked by the black or white star.

best-fitting value is consistent with the Schönrich et al. (2010) errors at the 2σ level when considering the error bars on the determination of U (e.g. $U = 11.1^{0.69}_{-0.75}$ km s^{-1}). In the next section, we will concentrate on the best $m = 2$ models and their implications for the structure of the Galactic disc.

3.2 Resonances and spiral structure

The best-fitting $\langle V_{\rm R}\rangle$ velocity fields for the $m = 2$ solutions using the mass models II is presented in Fig. 3. Although both reproduce equally well the structure of the velocity field between $y = \pm 1$ kpc, a small difference between the two solutions exists, model I predicting larger velocities in the top right and lower left corners of our sample (bottom-right panel). However the velocity difference reaches only 0.2 km s^{-1}, a level that lies below the capabilities of our data. The region below $y = -1$ kpc and at $0 < x < 1$ kpc is apparently poorly reproduced; however the lower-left panel of Fig. 3 indicates that our solution stays well within the observational errors. The right-hand panel of Fig. 1 indicates that this region suffers from large velocity errors and has therefore a lower weight in the solution. In the regions where our data are of the best quality (mostly $|y| <$ 1 kpc), our models reproduce adequately the observed velocity field.

Focusing on the pattern speed, our best models suggest that the Sun is located ∼200 pc inside the inner 4:1 resonance (ultra-harmonic resonance or UHR) of the spiral pattern (Fig. 4). Our finding for the pattern speed $\Omega_{\rm p} = 18$–19 km s^{-1} kpc^{-1} is in agreement with recent studies that also place the Sun close to the UHR: $\Omega_{\rm p} = 17$ km s^{-1} kpc^{-1} by Antoja et al. (2011), $\Omega_{\rm p} = 18$ km s^{-1} kpc^{-1} by Quillen & Minchev (2005) or $\Omega_{\rm p}/\Omega_0 = 0.65$ by Pompéia et al. (2011) to be compared to $\Omega_{\rm p}/\Omega_0 \sim 0.68$ in our study. However, as shown by Gerhard (2011), determinations of the spiral arms' pattern speed range from 17 to 28 km s^{-1} kpc^{-1}, the higher values being preferred by open cluster birthplaces while hydrodynamical simulations and phase space substructures favour slower pattern speeds. It is interesting to note that the pattern speeds found from velocity space substructures (Quillen & Minchev 2005; Antoja et al. 2011; Pompéia et al. 2011) are close to our value. This would indicate a similar origin for the velocity gradient and the velocity substructures, reinforcing our assumption that the velocity gradient we observed is due to spiral arms. However this statement must be put in perspective as both types of study rely on the same assumptions that the spiral pattern is long-lived and tightly wound.

Comparing the predicted density pattern to the location of the spiral arms obtained by Englmaier et al. (2011) in the gas,

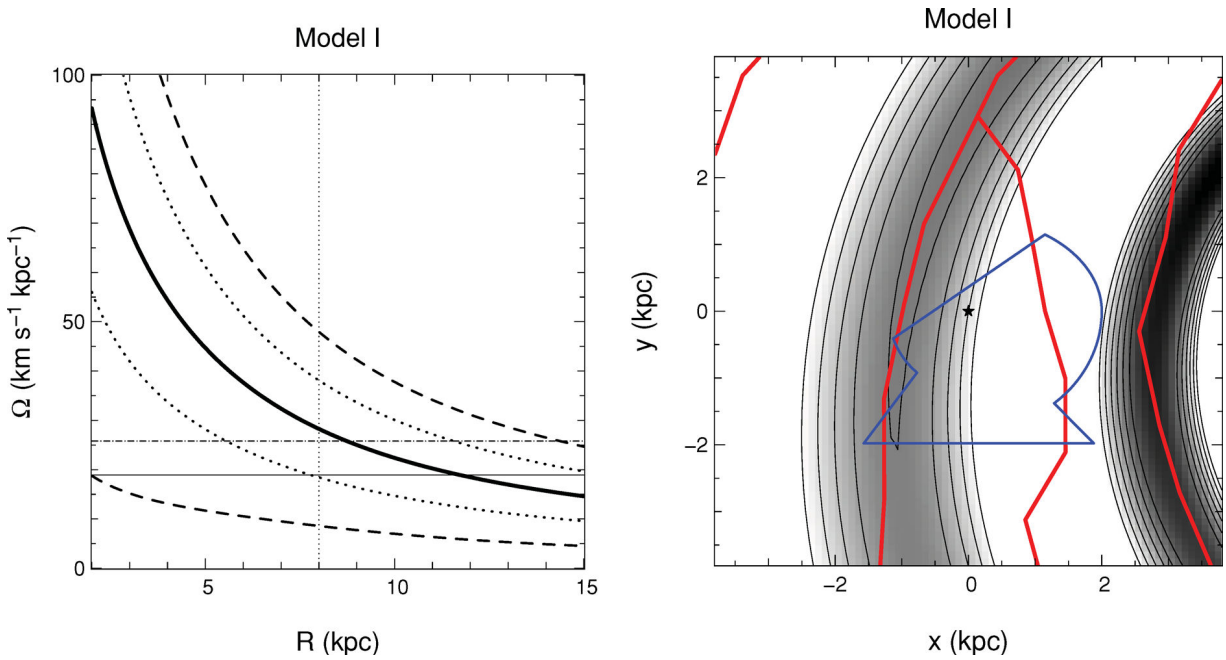

Figure 4. Left: circular frequency as a function of galactocentric distance for the mass model I of Binney & Tremaine (thick lines). The dotted and dashed lines are, respectively, the relations $\Omega \pm \kappa/4$ and $\Omega \pm \kappa/2$ versus R. The location of the Sun is marked by the vertical dotted line at $R_0 = 8$ kpc . The horizontal lines are the pattern speed corresponding to the best-fitting models for $m = 2$ (plain lines) and $m = 4$ (dash–dotted lines). Right: density associated with the best model. The grey shading and contours represent the overdensity associated with the spiral perturbation. The contours are evenly spaced by $0.1\Sigma_0$, the background column density, from 0.1 to $0.5\Sigma_0$. The blue contour depicts the footprint of the RAVE data. The red lines mark the location of the spiral arms in the gas from Englmaier et al. (2011). From left to right we have Cygnus arm (top-left corner), the Perseus arm, the Sagittarius–Carina arm and the Scutum–Centaurus arm. The results for the mass model II are almost identical and are therefore not presented.

we find a good agreement (Fig. 4, right-hand panel). Both the Perseus arm and the Centaurus arm are recovered at the proper location. The Sagittarius–Carina arm is not recovered in our models. This indicates that this feature is not a dominant feature in the Solar neighbourhood, reinforcing the view that the Milky Way spiral arm pattern is dominated by two main arms, Perseus and Centaurus (Drimmel 2000; Drimmel & Spergel 2001; Benjamin et al. 2005; Churchwell et al. 2009). Contrary to the $m = 2$ models, our best-fitting $m = 4$ solution does not reproduce any of the known spiral arms, in addition to being invalidated by its large pitch angle, hence an $m = 2$ mode for the spiral pattern in the Milky Way is preferred within the Lin–Shu regime.

4 CONCLUSION

We have analysed the velocity gradient detected by Siebert et al. (2011a) using the RAVE data in the framework of the density wave model of Lin & Shu (1964), assuming that the velocity gradient we detected is due only to spiral arms and that the spiral arms in the Milky Way are long-lived.

Our model converges properly for an $m = 2$ pattern, while if the chi-square of the $m = 4$ solutions are comparable, the predicted pitch angle is too large, invalidating the solution.

The best-fitting solutions for $m = 2$ adequately reproduce the observed velocity field for $\langle V_R \rangle$ in the region $|y| < 1$ kpc where our data are the most reliable. Outside of this region, the difference between the model and the observations is still within the observational errors although the agreement is less clear.

The predicted pattern speed places the Sun about 200 pc outside the inner UHR of the spiral arms. Such a location of the Sun is consistent with previous works based on velocity space substructures, suggesting a similar origin for the velocity space substructures and the $\langle V_R \rangle$ gradient. Our best-fitting value for the amplitude of the spiral perturbation, $A = 0.55^{+0.02}_{-0.02}$ per cent of the background potential or 14 per cent of the background density, is consistent with the value proposed by e.g. Minchev & Famaey (2010) and is also in the range of earlier measurements as summarized in Antoja et al. (2011).

Comparing our model to the location of spiral arms in the gas, we find a good agreement with the location of the major spiral arms given by Englmaier et al. (2011). The density enhancement predicted by our best model matches the location of the Perseus and Centaurus arms. The Sagittarius arm is not reproduced by our solution which tends to reinforce previous studies concluding that the Milky Way spiral potential is dominated by a two-armed mode, the Sagittarius–Carina arm being a minor feature for the dynamics of the disc.

Our study relies on the density wave model of Lin & Shu (1964) and we assumed no vertical variation of the $\langle V_R \rangle$ field within the limit of our data. RAVE data do contain the three-dimensional spatial information which we will use in further studies. However, going from 2D to 3D requires an upgrade of our modelling technique taking properly into account the asymmetric drift and the vertical variation of the spiral potential. Moreover, vertical perturbations leading to possible variations of $\langle V_z \rangle(R, z)$ (Smith et al. 2012; Widrow et al. 2012; Williams et al., in preparation) are intrinsically not taken into account in our analysis. Future 3D simulations of such perturbations and their possible influence on the $\langle V_R \rangle$ field will be necessary to disentangle their possible effects from the velocity gradient modelled here. Finally we note that our model is local as a result of the tight-winding approximation (see e.g. discussion in Binney 2012, section 1.4.2). Ongoing surveys like *Gaia*-ESO

(GES) or SDSS/SEGUE will provide data in the Galactic plane that can be used to test our models further in towards the Galactic Centre (GES) or further out (SDSS/SEGUE). It will be interesting to test whether these two surveys predict the same pattern speed for the spiral arms.

ACKNOWLEDGMENTS

Funding for RAVE has been provided by: the Australian Astronomical Observatory; the Leibniz-Institut fuer Astrophysik Potsdam (AIP); the Australian National University; the Australian Research Council; the French National Research Agency; the German Research Foundation (SPP 1177 and SFB 881); the European Research Council (ERC-StG 240271 Galactica); the Istituto Nazionale di Astrofisica at Padova; The Johns Hopkins University; the National Science Foundation of the USA (AST-0908326); the W. M. Keck foundation; the Macquarie University; the Netherlands Research School for Astronomy; the Natural Sciences and Engineering Research Council of Canada; the Slovenian Research Agency; the Swiss National Science Foundation; the Science & Technology Facilities Council of the UK; Opticon; Strasbourg Observatory; and the Universities of Groningen, Heidelberg and Sydney. The RAVE web site is: http://www.rave-survey.org.

REFERENCES

Adler D., Wefstpfahl D., 1996, AJ, 111, 735
Antoja T., Figueras F., Romero-Gómez M., Pichardo B., Valenzuela O., Moreno E., 2011, MNRAS, 418, 1423
Benjamin R. A. et al., 2005, ApJ, 630, 149
Bertin G., Lin C. C., 1996, Spiral Structure in Galaxies. The MIT Press, Cambridge, MA
Binney J., 2012, in Falcon-Barroso J., Knapen J. H., eds, Secular Evolution of Galaxies, to appear (arXiv:1202.3403)
Binney J., Tremaine S., 2008, Galactic Dynamics. Princeton Univ. Press, Princeton, NJ
Binney J., Gerhard O., Stark A. A., Bally J., Uchida K. I., 1991, MNRAS, 252, 210
Binney J., Gerhard O., Spergel D., 1997, MNRAS, 288, 365
Bissantz N., Englmaier P., Gerhard O., 2003, MNRAS, 340, 949
Breddels M. A. et al., 2010, A&A, 511, A90
Burnett B. et al., 2011, A&A, 532, A113
Churchwell E. et al., 2009, PASP, 121, 213
D'Onghia E., Vogelsberger M., Hernquist L., 2012, preprint (arXiv:1204.0513)
De Simone R., Wu X., Tremaine S., 2004, MNRAS, 350, 627
Dehnen W., 1998, AJ, 115, 2384
Dehnen W., Binney J., 1998, MNRAS, 294, 429
Drimmel R., 2000, A&A, 358L, 13
Drimmel R., Spergel D. N., 2001, ApJ, 556, 181
Englmaier P., Pohl M., Bissantz N., 2011, Memorie della Societa Astronomica Italiana Suppl., 18, 199
Famaey B., Jorissen A., Luri X., Mayor M., Udry S., Dejonghe H., Turon C., 2005, A&A, 430, 165
Foyle K., Rix H. W., Dobbs C. L., Leroy A. K., Walter F., 2011, ApJ, 735, 101
Georgelin Y. M., Georgelin Y. P., 1976, A&A, 49, 57
Gerhard O., 2011, Memorie della Societa Astronomica Italiana Suppl., 18, 185
Grand R. J. J., Kawata D., Cropper M., 2012a, MNRAS, 421, 1529
Grand R. J. J., Kawata D., Cropper M., 2012b, MNRAS, preprint (arXiv:1202.6387)
Kendall S., Kennicutt R. C., Clarke C., Thornley M. D., 2008, MNRAS, 387, 1007
Lépine J. R. D. et al., 2011a, MNRAS, 417, 698
Lépine J. R. D., Roman-Lopes A., Abraham Z., Junqueira T. C., Mishurov Y. N., 2011b, MNRAS, 414, 1607
Lin C. C., Shu F. H., 1964, ApJ, 140, 646
Lin C. C., Yuan C., Shu F. H., 1969, ApJ, 155, 721
Lowe S. A., Roberts W. W., Yang J., Bertin G., Lin C. C., 1994, ApJ, 427, 184
McMillan P. J., 2011, MNRAS, 418, 1565
Minchev I., Famaey B., 2010, ApJ, 722, 112
Minchev I., Famaey B., Quillen A. C., Di Matteo P., Combes F., Vlajic M., Erwin P., Bland-Hawthorn J., 2012, preprint (arXiv:1203.2621)
Moni-Bidin C., Carraro G., Mendez R. A., 2012, ApJ, 747, 101
Pilkington K., Gibson B. K., Jones D. H., 2012, preprint (arXiv1203.1996)
Pompéia L. et al., 2011, MNRAS, 415, 1138
Quillen A. C., Minchev I., 2005, AJ, 130, 576
Quillen A. C., Dougherty J., Bagley M. B., Minchev I., Comparetta J., 2011, MNRAS, 417, 762
Reid M. J. et al., 2009, ApJ, 700, 137
Salo H., Laurikainen E., Buta R., Knapen J. H., 2010, ApJ, 715, 56
Schönrich R., Binney J., Dehnen W., 2010, MNRAS, 403, 1829
Sellwood J., 2010a, MNRAS, 410, 1637
Sellwood J., 2010b, MNRAS, 409, 145
Sellwood J., Binney J., 2002, MNRAS, 336, 785
Shetty R., Vogel S. N., Ostriker E. C., Teuben P. J., 2007, ApJ, 665, 1138
Shu F. H., Stachnik R. V., Yost J. C., 1971, ApJ, 166, 465
Siebert A. et al., 2011a, MNRAS, 412, 2026
Siebert A. et al., 2011b, AJ, 141, 187
Smith M. C. et al., 2009, MNRAS, 399, 1223
Smith M. C., Whiteoak S. H., Evans N. W., 2012, ApJ, 746, 181
Stanek K. Z., Udalski A., Szymanski M., Kaluzny J., Kubiak Z. M., Mateo M., Krzemiński W., 1997, ApJ, 477, 163
Steinmetz M. et al., 2006, AJ, 132, 1645
Struck C., Dobbs C. L., Hwang J.-S., 2011, MNRAS, 414, 2498
Vallée J. P., 2008, AJ, 135, 1301
Voglis N., Stavropoulos I., Kalapotharakos C., 2006, MNRAS, 372, 901
Widrow L. M., Gardner S., Yanni B., Dodelson S., Chen H. Y., 2012, ApJ, 750, L41
Zwitter T. et al., 2008, AJ, 136, 421
Zwitter T. et al., 2010, A&A, 522A, 54

This paper has been typeset from a TEX/LATEX file prepared by the author.

3.2 Mouvements verticaux : quelques pistes

Si en deux dimensions, la comparaison observations-modèle est en accord avec une action des bras spiraux, en trois dimensions, nous ne savons pas à quoi nous attendre.
Les observations de Widrow et al. (2012), sur un échantillon de 11,000 étoiles appartenant à la séquence principale du relevé SEGUE (Sloan Extension for Galactic Understanding and Evolution) ont révélé un gradient de vitesse d'environ $3-5$ km.s^{-1} kpc^{-1} en traçant la vitesse verticale moyenne en fonction de la distance absolue du plan galactique. Ils ont constaté que ces vitesses vont jusqu'à 10 km.s^{-1} à des hauteurs de 1.5 kpc de part et d'autre du plan galactique avec une asymétrie nord-sud dans le nombre. Ils ont pensé qu'un satellite ou qu'un sous-halo de matière noire aurait pu faire osciller le disque en transférant une partie de son énergie. Le disque serait ensuite retourné à l'équilibre mais avec une plus grande dispersion de vitesse verticale due à un chauffage de ce dernier. Comme nous l'avons vu plus tôt, Williams et al. (2013) ont montré que la vitesse verticale moyenne était non-nulle et qu'elle présentait une structure ondulatoire. Avec LAMOST (pour Large Sky Area Multi-Object Fibre Spectroscopic Telescope ou Guo Shoujing Telescope), Carlin et al. (2013) observent que les étoiles au-dessus du plan ont des mouvements radiaux vers l'extérieur avec des vitesses verticales vers le bas alors qu'en-dessous du plan, ils observent le contraire.
Nous allons donc rechercher la cause de ces gradients de vitesses.

3.2.1 Interaction avec un satellite

À la suite de leurs précédentes découvertes, Widrow et al. (2014) ont fait l'hypothèse que l'asymétrie Nord-Sud pouvait être causée par les débris d'un satellite qui se seraient mélangés avec les étoiles du disque. Ils ont démontré à l'aide d'un *toy modèle* construit avec des modèles réalistes de la Voie Lactée (Kuijken & Gilmore (1989) ; modèle de Besançon Robin et al. (2003) + le meilleur modèle de Widrow et al. (2008)) que cet effet pouvait être à l'origine des observations. Ils ont également établi que les perturbations des vitesses n'étaient pas seulement dues à une excitation du *breathing mode*, comme on peut le voir avec Williams et al. (2013), mais aussi, à celui du *bending mode* lorsque la vitesse verticale du satellite est plus faible que celle des étoiles du disque.
Dans le cas où un seul satellite engendre les perturbations, Widrow et al. (2014) ont linéarisé les vitesses verticales moyennes en fonction de z par une droite affine. La pente est le paramètre A(x,y) pour le *breathing mode* et la constante de z est le paramètre B(x,y) pour le *bending mode*. La figure 3.1 représente la densité et les paramètres A et B de la galaxie dans le repère galactocentrique à 2 époques différentes : au moment où le satellite passe dans le plan du disque et 250 Myr plus tard. À 250 Myr, on peut voir que la structure spirale est plutôt grossière en densité et on peut deviner une structure pour les paramètres A et B. En tous cas, la perturbation causée par le satellite se voit à grande échelle et elle n'est pas uniforme. Néanmoins, localement, la simulation peut être comparable avec les observations.
Dans le cas où c'est un ensemble de satellites, Widrow et al. (2014) se sont servis de 100 sous-halos de Gauthier et al. (2006) dans lesquels les simulations du disque perturbé ont mené à la formation d'une barre à partir de 5 Gyr. Les simulations de Widrow et al. (2014) ont montré qu'une structure spirale pour la densité, le *bending mode* et le *breathing mode* se

formait avant la barre, vers 2.5 Gyr. Mais après 10 Gyr, on ne peut plus rien distinguer à part une longue barre de 20 kpc en densité.
Il est donc possible que les effets soient causés par excitation extérieure mais on a besoin du bon satellite.

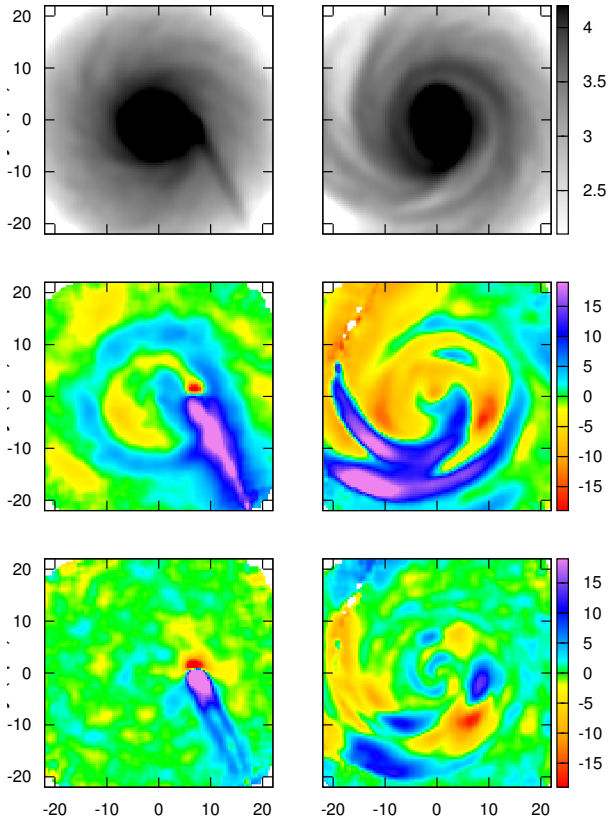

FIGURE 3.1 – Perturbations par un satellite. En haut : carte de densité, au milieu : paramètre B, en bas : paramètre A. Colonne de gauche : instant où le satellite traverse le disque, colonne de droite : le disque 250 Myr plus tard. Crédit : Widrow et al. (2014)

3.2.2 Effets de la barre centrale

Monari et al. (2013), à l'aide d'un modèle de particules tests dans un potentiel galactique en 3 dimensions comprenant un bulbe (Hernquist 1990), des disques mince et épais (Miyamoto & Nagai 1975), un halo (Navarro et al. 1997) et une barre de Ferrers (1870), ont mis en évidence que la barre a un effet sur la distribution des vitesses radiales et azimutales des étoiles du disque mince ainsi que, plus faiblement, sur celles du disque épais et ce, même jusqu'à 1 kpc (fig.3.2).

Monari et al. (2014) ont alors tenté de déterminer si la barre est à l'origine des effets sur les vitesses verticales. La figure montre les résultats obtenus. Au niveau des vitesses radiales

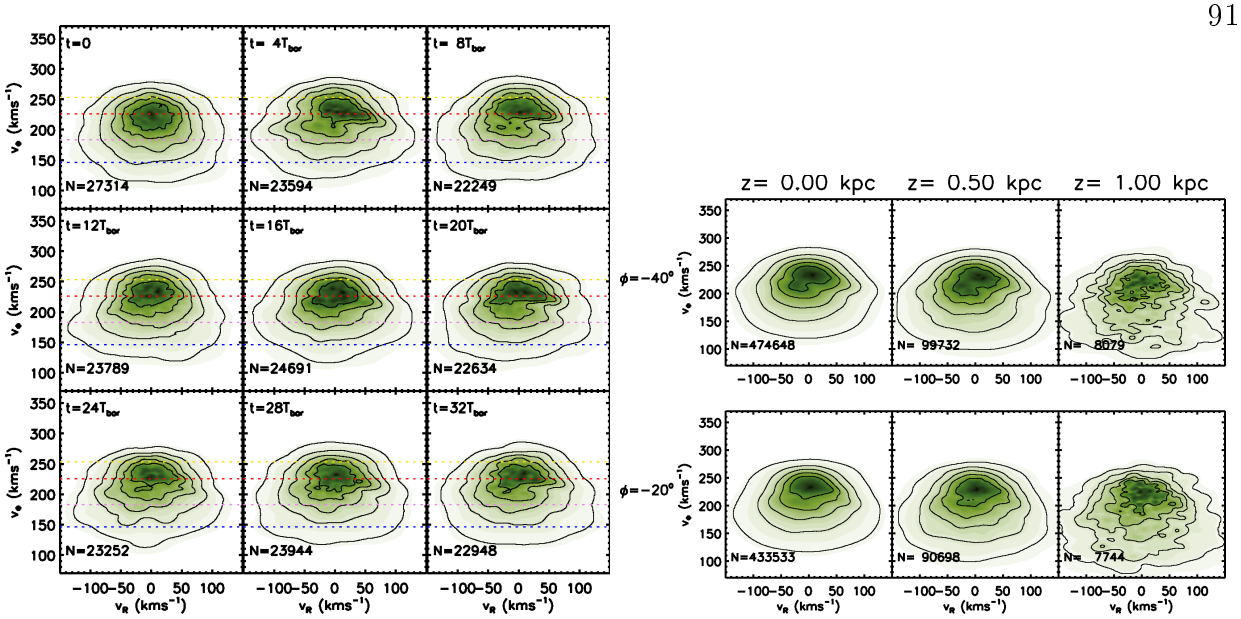

FIGURE 3.2 – À gauche : évolution des vitesses radiales en fonction des vitesses azimutales pour le disque mince. À droite : cinématique pour des sélections à différentes positions angulaire et verticale pour le disque mince, crédit : Monari et al. (2013)

moyennes (fig.3.3 à gauche), on retrouve bien un gradient qui augmente en s'éloignant du plan mais celui-ci reste faible. Quant aux vitesses verticales moyennes (fig.3.3 à droite), aucun gradient ne se dégage. On peut donc exclure la barre centrale comme facteur des mouvements verticaux moyens non-nuls.

3.3 Mouvements radiaux et verticaux causés par les bras spiraux

Avec les indices que nous avons trouvé grâce au relevé RAVE, nos recherches ont donc porté sur la réponse d'une population d'étoiles vieilles du disque mince à une perturbation des bras spiraux, sans prendre en compte de perturbation extérieure. Nous savons par ailleurs qu'une telle perturbation spirale peut se développer naturellement dans des simulations auto-cohérentes de disques isolés sans l'aide d'aucun perturbateur externe (Minchev et al. 2012). Pour atteindre notre objectif, nous avons utilisé une méthode de particules tests dans laquelle, des orbites de particules sans masse sont intégrées dans un potentiel axisymétrique auquel on a ajouté une perturbation spirale que nous avons fait grandir adiabatiquement sur environ 3.5 Gyr.

3.3.1 Le modèle développé durant cette thèse

J'ai commencé par développer un premier programme pour générer des conditions initiales réalistes et représentatives de la population que nous souhaitons tester. Nous avons choisi le modèle I de Binney & Tremaine (2008) décrit dans l'introduction comme potentiel

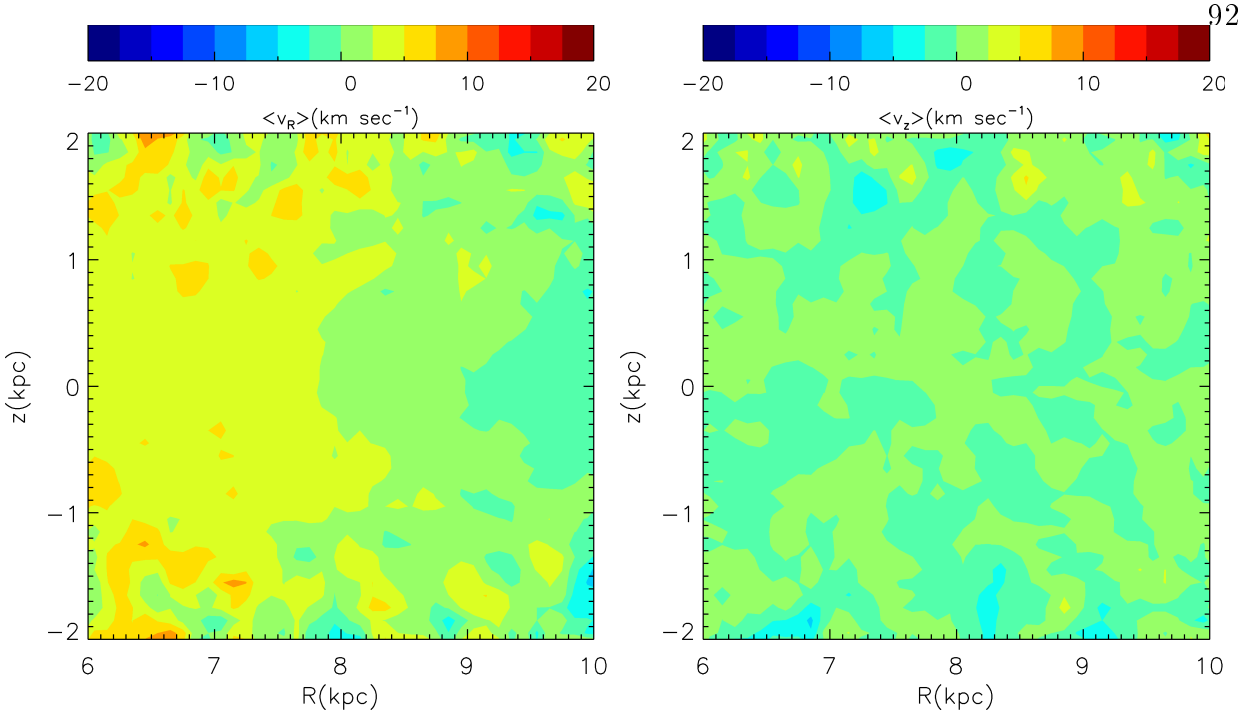

FIGURE 3.3 – Vitesses radiales moyenne (à gauche) et vitesses verticales moyennes (à droite) dans le plan méridien, crédit Monari et al. (2014)

axisymétrique réaliste pour représenter la Voie Lactée. Nous nous sommes servi de la fonction de distribution de Bienayme & Séchaud (1997) tridimensionnelle, basée sur la fonction de Shu. Ensuite, dans un second programme, j'ai intégré ces conditions initiales dans un potentiel spiral logarithmique auquel on a ajouté une dépendance verticale en sécante hyperbolique au carré.
Pour le calcul du potentiel, j'ai eu à disposition une version en langage C d'une adaptation du code GALPOT écrit par Dehnen que j'ai ensuite adapté en langage CUDA. Un des objectifs de cette thèse était le développement de simulations numériques en utilisant des processeurs graphiques (GPU) en parallèles du CPU nous octroyant une plus grande capacité de calcul. Le GPU, avec 256 cœurs, accélère les portions de code les plus lourdes en calcul, le reste de l'application restant affecté au CPU.

3.3.1.1 Les conditions initiales

Le calcul des conditions initiales se fait en deux étapes. Tout d'abord, la fonction de distribution de Bienayme & Séchaud (1997) à 2 dimensions (on se place dans le plan) permet de déterminer un rayon, une vitesse radiale puis une vitesse azimutale d'une particule test. Enfin, il ne reste plus qu'à déterminer sa position en hauteur puis sa vitesse verticale avec la fonction de distribution de Bienayme & Séchaud (1997) à 3 dimensions. Comme le disque est axisymétrique, l'angle θ est choisi aléatoirement à la fin.
On commence par établir la densité de surface (donnée par GALPOT) sur l'intervalle de rayon qui nous intéresse. On en calcule ensuite sa distribution cumulée. On prend un nom-

bre tiré aléatoirement puis on regarde à quelle valeur il correspond sur la courbe interpolée de la densité de surface cumulée en fonction de notre intervalle de rayon. On a donc trouvé une valeur pour le rayon de notre particule test. On s'y prend de la même façon pour calculer les autres valeurs sauf que l'équivalent de la densité de surface doit être calculé à partir de la fonction de distribution de Bienayme & Séchaud (1997) intégrée.
Pour déterminer cette fonction de distribution, je calcule au préalable à l'aide de GALPOT les moments angulaires circulaires et les densités de surface du disque sur un autre intervalle en rayon. On calcule le moment angulaire $L_z = Rv_\theta$ de la position où l'on se trouve sur la grille. Si L_z est positif, on regarde quelle est la valeur du rayon circulaire R_c associée sur la courbe interpolée du moment angulaire en fonction du nouvel intervalle en rayon. Ensuite, pour le cas 2D, on obtient ρ_d en interpolant l'image de R_c avec les densités de surface du disque et pour le cas 3D, une fonction de GALPOT nous permet de l'obtenir. Ainsi on peut calculer l'énergie circulaire ce qui nous permet de trouver la valeur de la fonction de distribution au point où l'on se trouve.

Par cette méthode, 4×10^7 conditions initiales sont calculées avec une grille polaire en 3 dimensions pour des rayons compris entre $R = 4$ et 15 kpc, des z compris entre 0 et 1.5 kpc. Dans ce cas-là un pas logarithmique est adapté pour avoir des pas petits pour les valeurs proches du plan galactique puis plus espacés en s'éloignant (pour les z négatifs, j'ai aléatoirement pris l'opposé). Pour les vitesses, les intervalles sont choisis de façon à optimiser au mieux le temps de calcul très long.

3.3.1.2 L'intégrateur d'orbite

Les bras spiraux sont décrits par le potentiel spiral logarithmique auquel on a ajouté une dépendance verticale en sécante hyperbolique au carré (Patsis & Grosbol 1996) de petite échelle de hauteur (100 pc).

$$\Phi_s(R, \theta, z) = -A \cos\left[m\left(\Omega_P t - \theta + \frac{\ln(R)}{\tan p}\right)\right] \operatorname{sech}^2\left(\frac{z}{z_0}\right) \tag{3.1}$$

où A est l'amplitude de la perturbation, m est le mode de la spirale ($m = 2$ pour une spirale à 2 bras), Ω_P est sa vitesse angulaire, p son angle d'enroulement, et z_0 la hauteur d'échelle de la spirale.

Les paramètres du potentiel spiral utilisé dans notre simulation sont inspirés par la solution analytique trouvée dans Siebert et al. (2012). Pour cela, le formalisme 2D classique de Lin & Shu qui satisfait le gradient de vitesse radiale observé avec RAVE (Siebert et al. 2011a) est choisi. Les paramètres utilisés sont listés dans la Table 3.1. L'amplitude A utilisée correspond à 1% du potentiel axisymétrique au rayon solaire (3% du potentiel du disque).

Comme il est impossible d'ajouter la perturbation spirale trop brutalement, nous nous assurons de faire grandir la perturbation de manière adiabatique en multipliant la perturbation du potentiel du facteur de croissance. De plus avant de commencer à faire croître la spirale, la simulation est exécutée dans le potentiel axisymétrique pendant deux rotations

TABLE 3.1 – Paramètres du potentiel spiral et emplacement des résonances principales

Paramètre	Potentiel spiral
m	2
A (km^2 s^{-2})	1000
p (deg)	-9.9
z_0(kpc)	0.1
Ω_P(kms^{-1} kpc^{-1})	18.6
$R_{\rm ILR}$(kpc)	1.94
$R_{\rm IUHR}$(kpc)	7.92
$R_{\rm CR}$(kpc)	11.97

($\sim$ 0.5 Gyr). Donc à partir de $t \approx 0.5$ Gyr et jusqu'à $t \approx 3.5$ Gyr, j'ai appliqué le facteur $\epsilon(t) = \frac{1}{2}(\tanh(1.7 \times t - 3.4) + 1)$.
Cette croissance adiabatique n'est pas réaliste mais c'est la réponse stationnaire des étoiles une fois que le disque est stable qui nous intéresse.
L'intégration d'orbite est réalisée pendant un temps représentant 6.5 Gry en utilisant un algorithme de Runge-Kutta d'ordre 4 exécuté sur des processeurs graphiques (GPUs). Les algorithmes de Runge-Kutta sont des méthodes d'analyse numérique d'approximation de solutions d'équations différentielles. Elles dérivent de la méthode d'Euler, sont simples à utiliser et stables mais demandent, en général, plus de temps de calcul.

3.3.2 Les résultats

Les résultats sont détaillés dans l'article ci-dessous intitulé "Radial and vertical flows induced by galactic spiral arms : likely contributors to our 'wobbly Galaxy"' et publié dans le Monthly Notices of the Royal Astronomical Society.
Il montre que la réponse à une perturbation spirale est pratiquement stable, seul un léger chauffage persiste, et stationnaire.
Dans le plan du disque, on retrouve les résultats du modèle 2D des ondes de densité de Lin & Shu. On retrouve qualitativement et quantitativement les observations de Siebert et al. (2011a) avec un facteur 2 près dû à l'intégration de la sécante hyperbolique au carrée.
On a montré que dans le plan méridien, le champ de vitesse des particules tests était affectés bien au-delà du plan du disque.
Nos plus importants résultats sont ceux des vitesses verticales dans le plan méridien. On voit clairement une asymétrie Nord-Sud comme dans Williams et al. (2013). À l'entrée des bras spiraux, au-dessus du plan galactique, les vitesses sont négatives et positives en dessous du plan. On a donc une compression. À la sortie des bras, les vitesses sont positives au-dessus et négatives en dessous. On a une expansion. On a aussi remarqué qu'une fois la corotation passée, les zones de compressions et d'expansions s'inversent.
Si l'on regarde le champ de vitesse total, on voit qu'il s'agit de *sink points* et de *source points*.
Nous avons linéarisé l'équation d'Euler pour un fluide froid dans *un toy model* en 3 dimensions

en suivant le même raisonnement que dans la section 1.5.1.1, et nous avons retrouvé nos résultats de façon qualitative (voir section 3.3 de l'article de Faure et al. 2014 inclus à la fin de ce chapitre). Les résultats de nos simulations à particules tests sont quant à elles un bon indicateur de la valeur du facteur de réduction (voir section 1.5.1.2) dans le cas stellaire, pour une population typique du disque de la Voie Lactée et nous avons retrouvé nos résultats.

3.3.3 Simulation N-corps

Quelques mois après la sortie de notre publication, Debattista (2014) a confirmé que l'on retrouvait les mêmes effets avec les simulations N-corps pour les spirales à *Grand Design*.

Publication de "Radial and vertical flows induced by galactic spiral arms : likely contributors to our 'wobbly Galaxy"'

Monthly Notices
of the
ROYAL ASTRONOMICAL SOCIETY
MNRAS **440,** 2564–2575 (2014) doi:10.1093/mnras/stu428

Radial and vertical flows induced by galactic spiral arms: likely contributors to our 'wobbly Galaxy'

Carole Faure,* Arnaud Siebert and Benoit Famaey
Observatoire Astronomique de Strasbourg, Université de Strasbourg, CNRS, UMR 7550, 11 rue de l'Université, F-67000 Strasbourg, France

Accepted 2014 March 3. Received 2014 March 3; in original form 2014 February 3

ABSTRACT

In an equilibrium axisymmetric galactic disc, the mean Galactocentric radial and vertical velocities are expected to be zero everywhere. In recent years, various large spectroscopic surveys have however shown that stars of the Milky Way disc exhibit non-zero mean velocities outside of the Galactic plane in both the Galactocentric radial and vertical velocity components. While radial velocity structures are commonly assumed to be associated with non-axisymmetric components of the potential such as spiral arms or bars, non-zero vertical velocity structures are usually attributed to excitations by external sources such as a passing satellite galaxy or a small dark matter substructure crossing the Galactic disc. Here, we use a three-dimensional test-particle simulation to show that the global stellar response to a spiral perturbation induces both a radial velocity flow and non-zero vertical motions. The resulting structure of the mean velocity field is qualitatively similar to what is observed across the Milky Way disc. We show that such a pattern also naturally emerges from an analytic toy model based on linearized Euler equations. We conclude that an external perturbation of the disc might not be a requirement to explain all of the observed structures in the vertical velocity of stars across the Galactic disc. Non-axisymmetric internal perturbations can also be the source of the observed mean velocity patterns.

Key words: stars: kinematics and dynamics – Galaxy: disc – Galaxy: kinematics and dynamics – galaxies: spiral.

1 INTRODUCTION

The Milky Way has long been known to possess spiral structure, but studying the nature and the dynamical effects of this structure has proven to be elusive for decades. Even though its fundamental nature is still under debate today, it has nevertheless started to be recently considered as a key player in galactic dynamics and evolution (e.g. Antoja et al. 2009; Lépine et al. 2011; Quillen et al. 2011; Minchev et al. 2012; Roskar et al. 2012, for recent works, or Sellwood 2014 for a review). However, zeroth-order dynamical models of the Galaxy still mostly rely on the assumptions of a smooth time-independent and axisymmetric gravitational potential. For instance, recent determinations of the circular velocity at the Sun's position and of the peculiar motion of the Sun itself all rely on the assumption of axisymmetry and on minimizing the non-axisymmetric residuals in the velocity field (Reid et al. 2009; McMillan & Binney 2010; Bovy et al. 2012; Schönrich 2012). Such zeroth-order assumptions are handy since they allow us to develop dynamical models based on a phase-space distribution function depending only on three isolating integrals of motion, such as the action integrals (e.g. Binney 2013; Bovy & Rix 2013). Actually, an action-based approach does not necessarily have to rely on the axisymmetric assumption, as it is also possible to take into account the main non-axisymmetric component (e.g. the bar, see Kaasalainen & Binney 1994) by modelling the system in its rotating frame (e.g. Kaasalainen 1995). However, the other non-axisymmetric components such as spiral arms rotating with a different pattern speed should then nevertheless be treated through perturbations (e.g. Kaasalainen 1994; McMillan 2013).

The main problem with such current determinations of Galactic parameters, through zeroth-order axisymmetric models, is that it is not clear that assuming axisymmetry and dynamical equilibrium to fit a benchmark model does not bias the results, by e.g. forcing this benchmark model to fit non-axisymmetric features in the observations that are not present in the axisymmetric model itself. This means that the residuals from the fitted model are not necessarily representative of the true amplitude of non-axisymmetric motions. In this respect, it is thus extremely useful to explore the full range of possible effects of non-axisymmetric features such as spiral arms in both fully controlled test-particle simulations as well as self-consistent simulations, and to compare these with observations.

* E-mail: carole.faure@astro.unistra.fr

With the advent of spectroscopic and astrometric surveys, observational phase-space information for stars in an increasingly large volume around the Sun have allowed us to see more and more of these dynamical effect of non-axisymmetric components emerge in the data. Until recently, the most striking features were found in the solar neighbourhood in the form of moving groups, i.e. local velocity-space substructures shown to be made of stars of very different ages and chemical compositions (e.g. Chereul, Crézé & Bienaymé 1998, 1999; Dehnen 1998; Famaey et al. 2005, 2007; Famaey, Siebert & Jorissen 2008; Pompéia et al. 2011). Various non-axisymmetric models have been argued to be able to represent these velocity structures equally well, using transient (e.g. De Simone, Wu & Tremaine 2004) or quasi-static spirals (e.g. Quillen & Minchev 2005; Antoja et al. 2011), with or without the help of the outer Lindblad resonance from the central bar (e.g. Dehnen 2000; Antoja et al. 2009; Minchev et al. 2010; McMillan 2013; Monari, Antoja & Helmi 2013). The effects of non-axisymmetric components have also been analysed a bit less locally by Taylor expanding to first order the planar velocity field in the Cartesian frame of the Local Standard of Rest, i.e. measuring the Oort constants A, B, C and K (Kuijken & Tremaine 1994; Olling & Dehnen 2003), a procedure valid up to distances of less than 2 kpc. While old data were compatible with the axisymmetric values $C = K = 0$ (Kuijken & Tremaine 1994), a more recent analysis of ACT/Tycho2 proper motions of red giants yielded $C = -10\,\mathrm{km\,s^{-1}\,kpc^{-1}}$ (Olling & Dehnen 2003). Using line-of-sight (l.o.s.) velocities of 213 713 stars from the RAVE survey (Steinmetz et al. 2006; Zwitter et al. 2008; Siebert et al. 2011a; Kordopatis et al. 2013), with distances $d < 2\,\mathrm{kpc}$ in the longitude interval $-140^\circ < l < 10^\circ$, Siebert et al. (2011b) confirmed this value of C, and estimated a value of $K = +6\,\mathrm{km\,s^{-1}\,kpc^{-1}}$, implying a Galactocentric radial velocity[1] gradient of $C + K = \partial V_\mathrm{R}/\partial R \simeq -4\,\mathrm{km\,s^{-1}\,kpc^{-1}}$ in the solar suburb (extended solar neighbourhood, see also Williams et al. 2013). The projection on to the plane of the mean l.o.s. velocity as a function of distance towards the Galactic Centre ($|l| < 5^\circ$) was also examined by Siebert et al. (2011b) both for the full RAVE sample and for red clump candidates (with an independent method of distance estimation), and clearly confirmed that the RAVE data are not compatible with a purely axisymmetric rotating disc. This result is not owing to systematic distance errors as considered in Binney et al. (2014), because the *geometry* of the radial velocity flow cannot be reproduced by systematic distance errors alone (Siebert et al. 2011b; Binney et al. 2014). Assuming, to first order, that the observed radial velocity map in the solar suburb is representative of what would happen in a razor-thin disc, and that the spiral arms are long-lived, Siebert et al. (2012) applied the classical density wave description of spiral arms (Lin & Shu 1964; Binney & Tremaine 2008) to constrain their parameters in the Milky Way. They found that the best fit was obtained for a two-armed perturbation with an amplitude corresponding to ∼15 per cent of the background density and a pattern speed $\Omega_\mathrm{P} \simeq 19\,\mathrm{Gyr^{-1}}$, with the Sun close to the 4:1 inner ultraharmonic resonance (IUHR). This result is in agreement with studies based on the location of moving groups in local velocity space (Quillen & Minchev 2005; Antoja et al. 2011; Pompéia et al. 2011). This study was advocated to be a useful first-order benchmark model to then study the effect of spirals in three dimensions.

In three dimensions, observations of the solar suburb from recent spectroscopic surveys actually look even more complicated. Using the same red clump giants from RAVE, it was shown that the mean *vertical* velocity was also non-zero and showed clear structure suggestive of a wave-like behaviour (Williams et al. 2013). Measurements of l.o.s. velocities for 11 000 stars with SEGUE also revealed that the mean vertical motion of stars reaches up to 10 km s^{-1} at heights of 1.5 kpc (Widrow et al. 2012), echoing previous similar results by Smith, Whiteoak & Evans (2012). This is accompanied by a significant wave-like north–south asymmetry in SDSS (Widrow et al. 2012; Yanny & Gardner 2013). Observations from LAMOST in the outer Galactic disc (within 2 kpc outside the solar radius and 2 kpc above and below the Galactic plane) also recently revealed (Carlin et al. 2013) that stars above the plane exhibit a net outward motion with downward mean vertical velocities, whilst stars below the plane exhibit the opposite behaviour in terms of vertical velocities (moving upwards, i.e. towards the plane too), but not so much in terms of radial velocities, although slight differences are also noted. There is thus a growing body of evidence that Milky Way disc stars exhibit velocity structures across the Galactic plane in *both* the Galactocentric radial and vertical components. While a global radial velocity gradient such as that found in Siebert et al. (2011b) can naturally be explained with non-axisymmetric components of the potential such as spiral arms, such an explanation is a priori less self-evident for vertical velocity structures. For instance, it was recently shown that the central bar cannot produce such vertical features in the solar suburb (Monari et al. 2014). For this reason, such non-zero vertical motions are generally attributed to vertical excitations of the disc by external means such as a passing satellite galaxy (Widrow et al. 2012). The Sagittarius dwarf has been pinpointed as a likely culprit for creating these vertical density waves as it plunged through the Galactic disc (Gomez et al. 2013), while other authors have argued that these could be due to interaction of the disc with small starless dark matter subhaloes (Feldmann & Spolyar 2013).

Here, we rather investigate whether such vertical velocity structures can be expected as the response to disc non-axisymmetries, especially spiral arms, in the absence of external perturbations. As a first step in this direction, we propose to qualitatively investigate the response of a typical old thin-disc stellar population to a spiral perturbation in controlled test-particle orbit integrations. Such test-particle simulations have revealed useful in 2D to understand the effects of non-axisymmetries and their resonances on the disc stellar velocity field, including moving groups (e.g. Antoja et al. 2009, 2011; Pompéia et al. 2011), Oort constants (e.g. Minchev, Nordhaus & Quillen 2007), radial migrations (e.g. Minchev & Famaey 2010), or the dip of stellar density around corotation (e.g. Barros, Lépine & Junqueira 2013). Recent test-particle simulations in 3D have rather concentrated on the effects of the central bar (Monari et al. 2013, 2014), while we concentrate here on the effect of spiral arms, with special attention to mean vertical motions. In Section 2, we give details on the model potential, the initial conditions and the simulation technique, while results are presented in Section 3, and discussed in comparison with solutions of linearized Euler equations. Conclusions are drawn in Section 4.

2 MODEL

To pursue our goal, we use a standard test-particle method where orbits of massless particles are integrated in a time-varying potential. We start with an axisymmetric background potential representative of the Milky Way (Section 2.1), and we adiabatically grow a spiral perturbation on it within ∼3.5 Gyr. Once settled, the spiral perturbation is kept at its full amplitude. This is not supposed to be

[1] In this paper, *'radial velocity'* refers to the Galactocentric radial velocity, not to be confused with the l.o.s. velocity.

representative of the actual complexity of spiral structure in real galaxies, where self-consistent simulations indicate that it is often coupled to a central bar and/or a transient nature with a lifetime of the order of only a few rotations. Nevertheless, it allows us to investigate the stable response to an old enough spiral perturbation (∼600 Myr to 1 Gyr in the self-consistent simulations of Minchev et al. 2012). The adiabatic growth of this spiral structure is not meant to be realistic, as we are only interested in the orbital structure of the old thin-disc test population once the perturbation is stable.

We generate initial conditions for our test stellar population from a discrete realization of a realistic phase-space distribution function for the thin disc defined in integral-space (Section 2.2), and integrate these initial conditions forward in time within a given time-evolving background + spiral potential (Section 2.3). We then analyse the mean velocity patterns seen in configuration space, both radially and vertically, and check whether such patterns are stable within the rotating frame of the spiral.

2.1 Axisymmetric background potential

The axisymmetric part of the Galactic potential is taken to be Model I of Binney & Tremaine (2008). Its main parameters are summarized in Table 1 for convenience. The central bulge has a truncated power-law density of the form

$$\rho_{\rm b}(R,z) = \rho_{\rm b0} \times \left(\frac{\sqrt{R^2+(z/q_{\rm b})^2}}{a_{\rm b}}\right)^{-\alpha_{\rm b}} \exp\left(-\frac{R^2+(z/q_{\rm b})^2}{r_{\rm b}^2}\right), \quad (1)$$

where R is the Galactocentric radius within the mid-plane, z the height above the plane, $\rho_{\rm b0}$ the central density, $r_{\rm b}$ the truncation radius and $q_{\rm b}$ the flattening. The total mass of the bulge is $M_{\rm b} = 5.18 \times 10^9\,{\rm M}_\odot$.

Table 1. Parameters of the axisymmetric background model potential (Binney & Tremaine 2008).

Parameter	Axisymmetric potential
$M_{\rm b}({\rm M}_\odot)$	5.18×10^9
$M_{\rm d}({\rm M}_\odot)$	5.13×10^{10}
$M_{\rm h,<100\ kpc}({\rm M}_\odot)$	$6. \times 10^{11}$
$\rho_{\rm b0}({\rm M}_\odot\,{\rm pc}^{-3})$	0.427
$a_{\rm b}$(kpc)	1.0
$r_{\rm b}$(kpc)	1.9
$\alpha_{\rm b}$	1.8
$q_{\rm b}$	0.6
$\Sigma_{\rm d0} + \Sigma_{\rm g}({\rm M}_\odot\,{\rm pc}^{-2})$	1905.0
$R_{\rm d}$(kpc)	2.0
$R_{\rm g}$(kpc)	4.0
$R_{\rm m}$(kpc)	4.0
$\alpha_{\rm d,1}$	14/15
$\alpha_{\rm d,2}$	1/15
$z_{\rm d,1}$(kpc)	0.3
$z_{\rm d,2}$(kpc)	1.0
$z_{\rm g}$(kpc)	0.08
$\rho_{\rm h0}({\rm M}_\odot\,{\rm pc}^{-3})$	0.711
$a_{\rm h}$(kpc)	3.83
$\alpha_{\rm h}$	−2.0
$\beta_{\rm h}$	2.96
$q_{\rm h}$	0.8

The stellar disc is a sum of two exponential profiles (for the thin and thick discs):

$$\rho_{\rm d}(R,z) = \Sigma_{\rm d0} \times \left(\sum_{i=1}^{i=2} \frac{\alpha_{{\rm d},i}}{2z_{{\rm d},i}} \exp\left(-\frac{|z|}{z_{{\rm d},i}}\right)\right) \exp\left(-\frac{R}{R_{\rm d}}\right), \quad (2)$$

where $\Sigma_{\rm d0}$ is the central surface density, $\alpha_{\rm d,1}$ and $\alpha_{\rm d,2}$ the relative contributions of the thin and thick discs, $z_{\rm d,1}$ and $z_{\rm d,2}$ their respective scaleheights and $R_{\rm d}$ the scalelength. The total mass of the disc is $M_{\rm d} = 5.13 \times 10^{10}\,{\rm M}_\odot$. The disc potential also includes a contribution from the interstellar medium of the form

$$\rho_{\rm g}(R,z) = \frac{\Sigma_{\rm g}}{2z_{\rm g}} \times \exp\left(-\frac{R}{R_{\rm g}} - \frac{R_{\rm m}}{R} - \frac{|z|}{z_{\rm g}}\right), \quad (3)$$

where $R_{\rm m}$ is the radius within which there is a hole close to the bulge region, $R_{\rm g}$ is the scalelength, $z_{\rm g}$ the scaleheight and $\Sigma_{\rm g}$ is such that it contributes to 25 per cent of the disc surface density at the Galactocentric radius of the Sun.

Finally, the dark halo is represented by an oblate two-power-law model with flattening $q_{\rm h}$, of the form

$$\rho_{\rm h}(R,z) = \rho_{\rm h0} \times \left(\frac{\sqrt{R^2+(z/q_{\rm h})^2}}{a_{\rm h}}\right)^{-\alpha_{\rm h}} \times \left(1+\frac{\sqrt{R^2+(z/q_{\rm h})^2}}{a_{\rm h}}\right)^{\alpha_{\rm h}-\beta_{\rm h}}. \quad (4)$$

The potential is calculated using the GALPOT routine (Dehnen & Binney 1998). The rotation curve corresponding to this background axisymmetric potential is displayed in Fig. 1. For radii smaller than 11 kpc, the total rotation curve (black line) is mostly influenced by the disc (blue-dashed line) and above by the halo (red-dotted line).

2.2 Initial conditions

The initial conditions for the test stellar population are set from a discrete realization of a phase-space distribution function (Shu 1969; Bienaymé & Séchaud 1997) which can be written in integral space as

$$f(E_{\rm R}, L_z, E_z) = \frac{\Omega\,\rho_{\rm d}}{\sqrt{2}\kappa\pi^{3/2}\sigma_{\rm R}^2\sigma_z} \exp\left(\frac{-(E_{\rm R}-E_{\rm c})}{\sigma_{\rm R}^2} - \frac{E_z}{\sigma_z^2}\right), \quad (5)$$

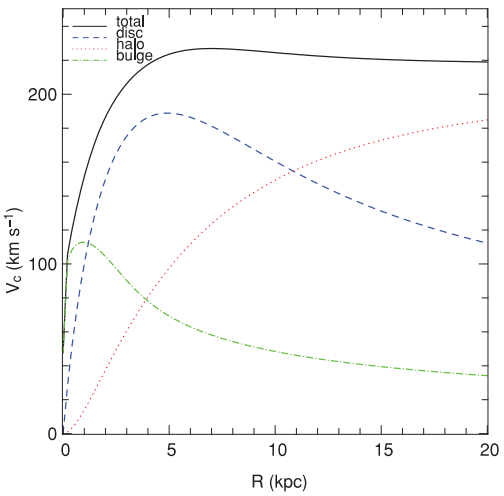

Figure 1. Rotation curve corresponding to the background axisymmetric potential.

in which the angular velocity Ω, the radial epicyclic frequency κ and the disc density in the plane $\rho_{\rm d}$ are all functions of L_z, being taken at the radius $R_{\rm c}(L_z)$ of a circular orbit of angular momentum L_z. The scalelength of the disc is taken to be 2 kpc as for the background potential. The energy $E_{\rm c}(L_z)$ is the energy of the circular orbit of angular momentum L_z at the radius $R_{\rm c}$. Finally, the radial and vertical dispersions $\sigma_{\rm R}^2$ and σ_z^2 are also function of L_z and are expressed as:

$$\sigma_{\rm R}^2 = \sigma_{\rm R_\odot}^2 \exp\left(\frac{2\,{\rm R}_\odot - 2R_{\rm c}}{R_{\sigma_{\rm R}}}\right), \quad (6)$$

$$\sigma_z^2 = \sigma_{z_\odot}^2 \exp\left(\frac{2\,{\rm R}_\odot - 2R_{\rm c}}{R_{\sigma_z}}\right) \quad (7)$$

where $R_{\sigma_{\rm R}}/R_{\rm d} = R_{\sigma_z}/R_{\rm d} = 5$ (Bienaymé & Séchaud 1997). The initial velocity dispersions thus decline exponentially with radius but at each radius, it is isothermal as a function of height. These initial values are set in such a way as to be representative of the old thin disc of the Milky Way after the response to the spiral perturbation. Indeed, the old thin disc is the test population we want to investigate the response of.

From this distribution function, 4×10^7 test-particle initial conditions are generated in a 3D polar grid between $R = 4$ and 15 kpc (see Fig. 2). This allows a good resolution in the solar suburb. Before adding the spiral perturbation, the simulation is run in the axisymmetric potential for two rotations (∼500 Myr), and is indeed stable.

2.3 Spiral perturbation and orbit integration

In 3D, we consider a spiral arm perturbation of the Lin–Shu type (Lin & Shu 1964; see also Siebert et al. 2012) with a sech^2 vertical profile (a pattern that can be supported by three-dimensional periodic orbits, see e.g. Patsis & Grosbøl 1996) and a small (∼100 pc) scaleheight

$$\Phi_s(R,\theta,z) = -A\cos\left[m\left(\Omega_{\rm P}t - \theta + \frac{\ln(R)}{\tan p}\right)\right]{\rm sech}^2\left(\frac{z}{z_0}\right) \quad (8)$$

in which A is the amplitude of the perturbation, m is the spiral pattern mode ($m = 2$ for a two-armed spiral), $\Omega_{\rm P}$ is the pattern speed, p the pitch angle and z_0 is the spiral scaleheight. The edge-on shapes of orbits of these thick spirals are determined by the vertical resonances existing in the potential.

The parameters of the spiral potential used in our simulation are inspired by the analytic solution found in Siebert et al. (2012) using the classical 2D Lin–Shu formalism to fit the radial velocity gradient observed with RAVE (Siebert et al. 2011b). The parameters used

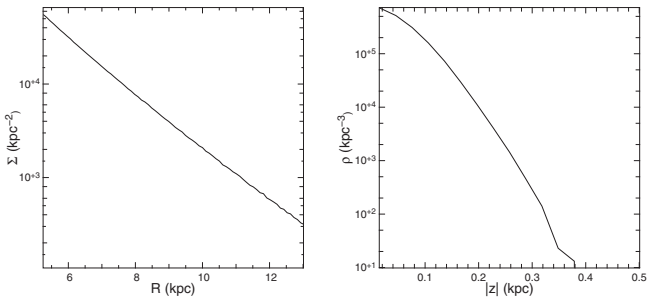

Figure 2. Initial conditions. Left-hand panel: number of stars per kpc^2 (surface density) within the Galactic plane as a function of R. Right-hand panel: stellar density as a function of z at $R = 8$ kpc.

Table 2. Parameters of the spiral potential and location of the main resonances.

Parameter	Spiral potential
m	2
A (km^2 s^{-2})	1000
p (deg)	–9.9
z_0(kpc)	0.1
$\Omega_{\rm P}$(km s^{-1} kpc^{-1})	18.6
$R_{\rm ILR}$(kpc)	1.94
$R_{\rm IUHR}$(kpc)	7.92
$R_{\rm CR}$(kpc)	11.97

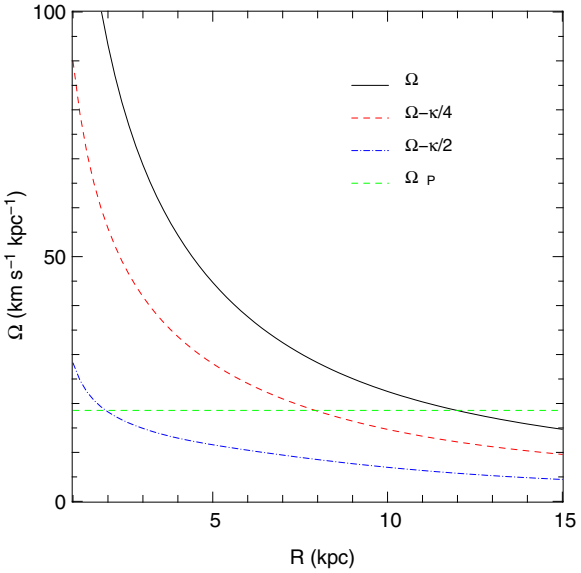

Figure 3. Positions of the main radial resonances of the spiral potential. $\Omega(R) = v_{\rm c}(R)/r$ is the local circular frequency, and $v_{\rm c}(R)$ is the circular velocity. The 2: 1 ILR occurs along the curve $\Omega(R) - \kappa/2$, where κ is the local radial epicyclic frequency. The inner 4: 1 IUHR occurs along the curve $\Omega(R) - \kappa/4$.

here are summarized in Table 2. The amplitude A which we use corresponds to 1 per cent of the background axisymmetric potential at the solar radius (3 per cent of the disc potential). The positions of the main radial resonances, i.e. the 2:1 inner Lindblad resonance (ILR) and 4:1 IUHR, are illustrated in Fig. 3. The presence of the 4:1 IUHR close to the Sun is responsible for the presence of the Hyades and Sirius moving groups in the local velocity space at the solar radius (see Pompéia et al. 2011), associated with square-shaped resonant orbital families in the rotating spiral frame. Vertical resonances are also displayed in Fig. 4.

Such a spiral perturbation can grow naturally in self-consistent simulations of isolated discs without the help of any external perturber (e.g. Minchev et al. 2012). As we are interested hereafter in the global response of the thin-disc stellar population to a quasi-static spiral perturbation, we make sure to grow the perturbation adiabatically by multiplying the above potential perturbation by a growth factor starting at $t \approx 0.5$ Gyr and finishing at $t \approx 3.5$ Gyr: $\epsilon(t) = \frac{1}{2}(\tanh(1.7 \times t - 3.4) + 1)$. The integration of orbits is performed using a fourth-order Runge–Kutta algorithm run on Graphics Processing Units. The growth of this spiral is not meant to be realistic, as we are only interested in the orbital structure of the old thin disc once the perturbation is stable.

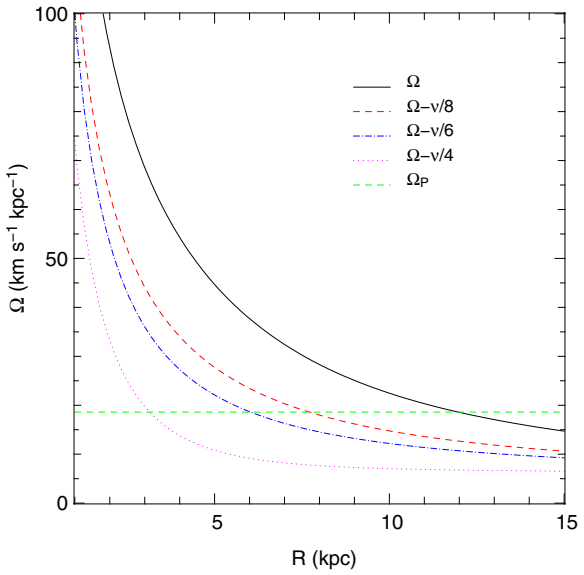

Figure 4. Positions of the 4:1, 6:1 and 8:1 vertical resonances. When $\Omega - \Omega_P = \nu/n$, where ν is the vertical epicyclic frequency, the star makes precisely n vertical oscillations along one rotation within the rotating frame of the spiral.

3 RESULTS

3.1 Radial velocity flow

The histogram of individual Galactocentric radial velocities, v_R, as well as the time-evolution of the radial velocity dispersion profile starting from $t = 3.5$ Gyr (once the steady spiral pattern is settled) are plotted on Fig. 5. It can be seen that these are reasonably stable, and that the mean radial motion of stars is very close to zero (albeit slightly positive). Our test population is thus almost in perfect equilibrium.

However, due to the presence of spiral arms, the mean Galactocentric radial velocity $\langle v_R \rangle$ of our test population is non-zero at given positions within the frame of the spiral arms. The map of $\langle v_R \rangle$ as a function of position in the plane is plotted on Fig. 6, for different time-steps (4, 5, 6 and 6.5 Gyr). Within the rotating frame of the spiral pattern, the locations of these non-zero mean radial velocities are stable over time: this means that the response to the spiral perturbation is stable, even though the amplitude of the non-zero velocities might slightly decrease with time. Within corotation, the mean $\langle v_R \rangle$ is negative within the arms (mean radial motion towards the Galactic Centre) and positive (radial motion towards the anticentre) between the arms. Outside corotation, the pattern is reversed. This is exactly what is expected from the Lin–Shu density wave theory (see, e.g. equation 3 in Siebert et al. 2012).

If we place the Sun at $(R, \theta) = (8\,\mathrm{kpc}, 26^\circ)$ in the frame of the spiral, we can plot the expected radial velocity field in the solar suburb (Fig. 7). We see that the Galactocentric radial velocity is positive in the inner Galaxy, as observed by Siebert et al. (2011b), because the inner Galaxy in the local suburb corresponds to an interarm region located within the corotation of the spiral. Observations towards the outer arm (which should correspond to the Perseus arm in the Milky Way) should reveal negative Galactocentric radial velocities.

An important aspect of the present study is the behaviour of the response to a spiral perturbation away from the Galactic plane. The spiral perturbation of the potential is very thin in our model ($z_0 = 100$ pc) but as we can see on Figs 8 and 9, the radial velocity flow is not varying much as a function of z up to five times the scaleheight of the spiral perturber. This justifies the assumption made in Siebert et al. (2012) that the flow observed at ∼500 pc above the plane was representative of what was happening in the plane. Nevertheless, above these heights, the trend seems to be reversed, probably due to the higher eccentrities of stars, corresponding to different guiding radii. This could potentially provide a useful observational constraint on the scaleheight of the spiral potential, a test that could be conducted with the forthcoming surveys.

3.2 Non-zero mean vertical motions

If we now turn our attention to the vertical motion of stars, we see on Fig. 10 that the total mean vertical motion of stars remains zero at all times, but that there is still a slight, but reasonable, vertical heating going on in the inner Galaxy.

What is most interesting is to concentrate on the mean vertical motion $\langle v_z \rangle$ as a function of position above or below the Galactic disc. As can be seen on Figs 11 and 12, while the vertical velocities are generally close to zero right within the plane, they are non-zero outside of it. At a given azimuth within the frame of the spiral, these non-zero vertical velocity patterns are extremely stable over time (Fig. 11). Within corotation the mean vertical motion is directed away from the plane at the outer edge of the arm and towards the plane at the inner edge of the arm. The pattern of $\langle v_z \rangle$ above and below the plane are thus mirror-images, and the direction of the mean motion changes roughly in the middle of the interarm

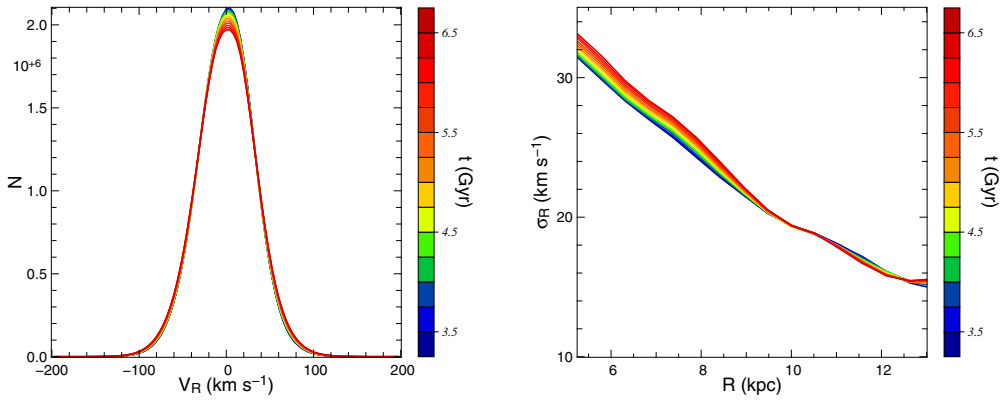

Figure 5. Left-hand panel: histogram of Galactocentric radial velocities as a function of time. Right-hand panel: time evolution of the $\sigma_R(R)$ profile averaged over all azimuths. The colour-scale indicates the time-steps in Gyr.

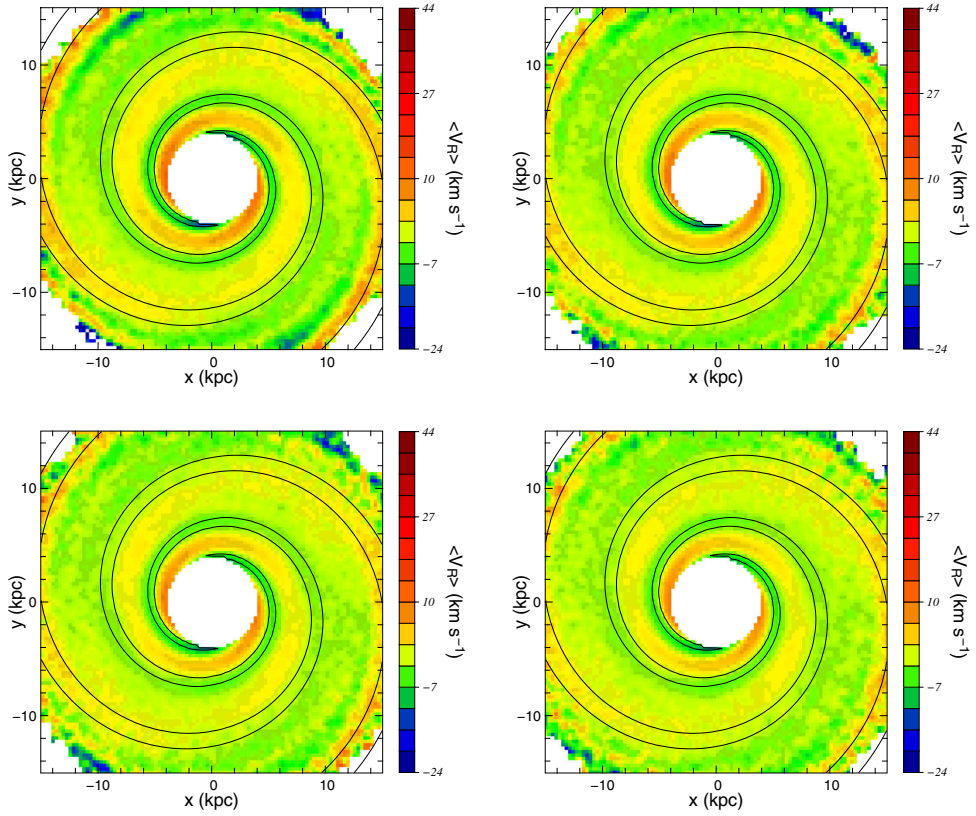

Figure 6. Top-left panel: mean Galactocentric radial velocity $\langle v_R \rangle$ as a function of position in the Galactic plane soon after the adiabatic growth of the spiral ($t = 4$ Gyr). Isocontours of the spiral potential are overplotted, corresponding to 80 per cent of the minimum of the perturber potential, and thus delimiting the region where the spiral potential is between 80 and 100 per cent of its minimum (or maximum in absolute value). Top right: same at $t = 5$ Gyr. Everything is plotted here within the rotating frame of the spiral, so that the spiral does not move from one snapshot to the other. Bottom-left panel: same at $t = 6$ Gyr. Bottom right: same at the final time-step $t = 6.5$ Gyr.

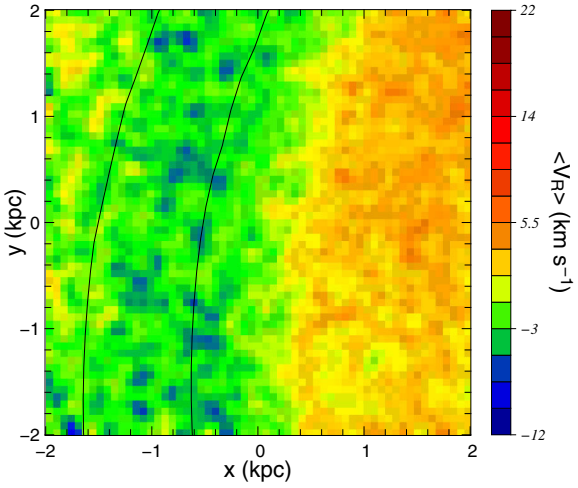

Figure 7. Galactocentric radial velocities in the solar suburb, centred at $(R, \theta) = (8\,\mathrm{kpc}, 26^\circ)$ at $t = 4$ Gyr. On this plot, the Sun is centred on $(x, y) = (0, 0)$, positive x indicates the direction of the Galactic Centre, and positive y the direction of Galactic rotation (as well as the sense of rotation of the spiral pattern). The spiral potential contours overplotted (same as on Fig. 6, delimiting the region where the spiral potential is between 80 and 100 per cent of its absolute maximum) would correspond to the location of the Perseus spiral arm in the outer Galaxy. This figure can be qualitatively compared to fig. 4 of Siebert et al. (2011b) and fig. 3 of Siebert et al. (2012).

region. This produces diagonal features in terms of isocontours of a given $\langle v_z \rangle$, corresponding precisely to the observation using RAVE by Williams et al. (2013, see especially their fig. 13), where the change of sign of $\langle v_z \rangle$ precisely occurs in between the Perseus and Scutum main arms.

Our simulation predicts that the $\langle v_z \rangle$ pattern is reversed outside of corotation (beyond 12 kpc), where stars move towards the plane on the outer edge of the arm (rather than moving away from the plane): this can indeed be seen, e.g. on the right-hand panel of the second row of our Fig. 12. If we now combine the information on $\langle v_R \rangle$ and $\langle v_z \rangle$, we can plot the global meridional velocity flow $\langle \boldsymbol{v} \rangle = \langle v_R \rangle \mathbf{1}_R + \langle v_z \rangle \mathbf{1}_z$ on Figs 13 and 14. The picture that emerges is the following: in the interarm regions located within corotation, stars move on average from the innerarm to the outer arm by going outside of the plane, and then coming back towards the plane at mid-distance between the two arms, to finally arrive back on the inner edge of the outer arm. For each azimuth, there are thus 'source' points, preferentially on the outer edge of the arms (inside corotation, whilst on the inner edge outside corotation), out of which the mean velocity vector flows, while there are 'sink' points, preferentially on the inner edge of the arms (inside corotation), towards which the mean velocity flows. This supports the interpretation of the observed RAVE velocity field of Williams et al. (2013) as 'compression/rarefaction' waves.

3.3 Interpretation from linearized Euler equations

In order to understand these features found in the meridional velocity flow of our test-particle simulation, we now turn to the fluid

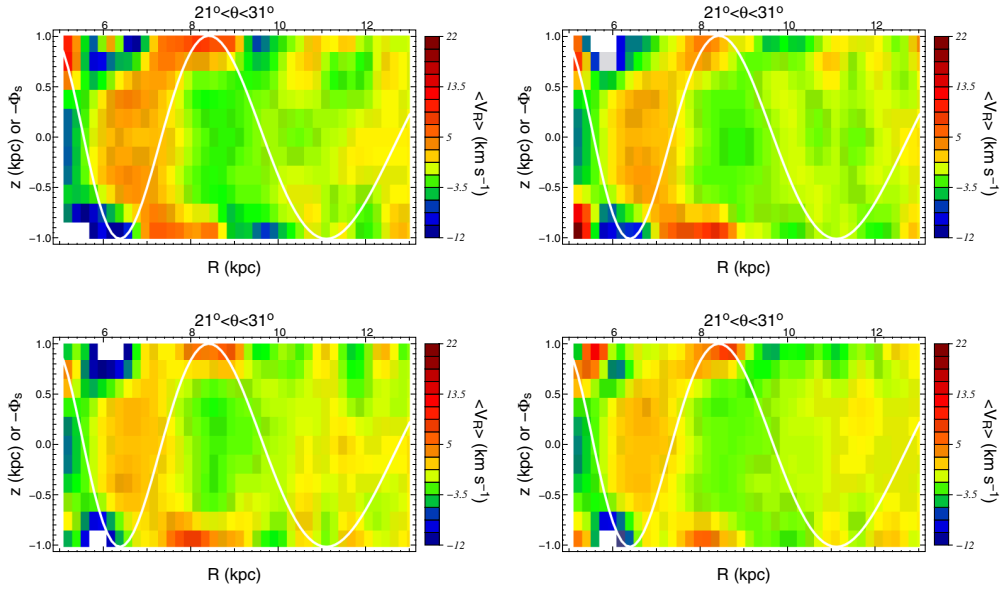

Figure 8. Top-left panel: mean Galactocentric radial velocity at $t = 4$ Gyr in the meridional (R, z)-plane for $21^\circ < \theta < 31^\circ$ (within the frame of the spiral). The white line indicates the location of spiral arms, in terms of overdensities and underdensities generating the spiral potential (normalized $-\Phi_s$, i.e. spiral arms are located at the peaks). Top right: same at $t = 5$ Gyr. Bottom left: same at $t = 6$ Gyr. Bottom right: same at the final time-step $t = 6.5$ Gyr.

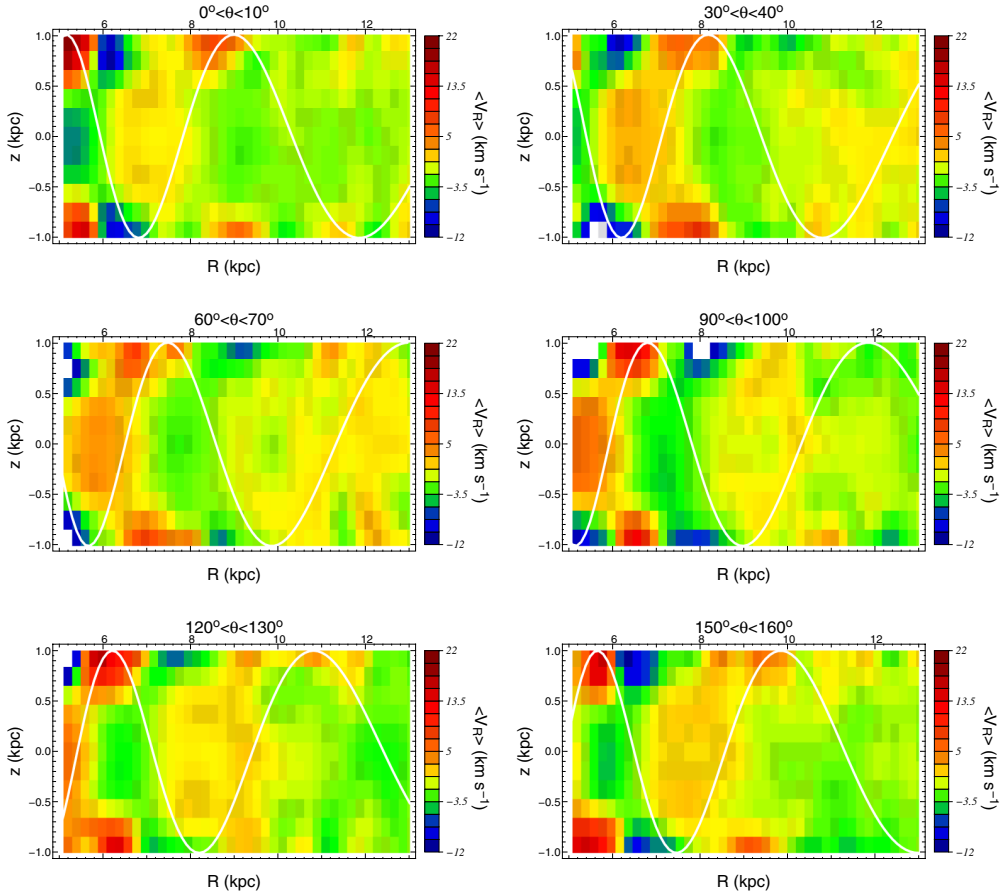

Figure 9. Same as Fig. 8, but for six different azimuths at a fixed time ($t = 6$ Gyr).

approximation based on linearized Euler equations, developed, e.g. in Binney & Tremaine (2008, Section 6.2). A rigorous analytical treatment of a quasi-static spiral perturbation in a three-dimensional stellar disc should rely on the linearized Boltzmann equations, which we plan to do in full in a forthcoming paper, but the fluid approximation can already give important insights on the shape of the velocity flow expected in the meridional plane. In the full Boltzmann-based treatment, the velocity flow will be tempered by

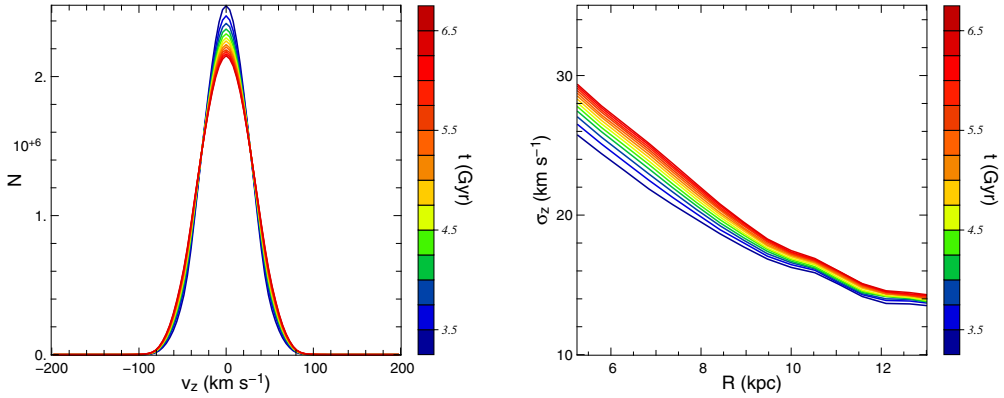

Figure 10. Left-hand panel: histogram of vertical velocities as a function of time. Right-hand panel: time evolution of the $\sigma_z(R)$ profile averaged over all azimuths.

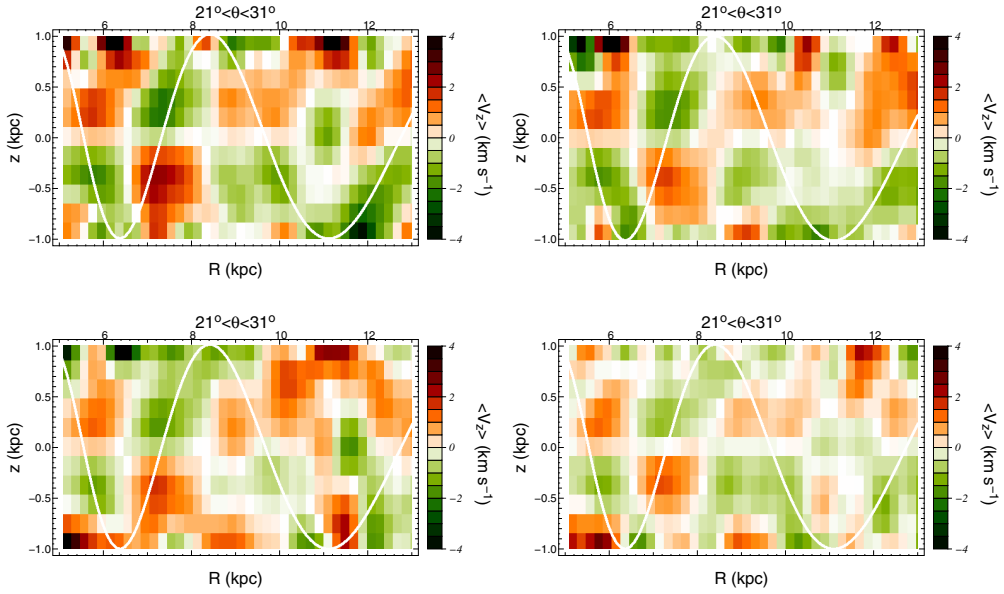

Figure 11. Top-left panel: mean vertical velocity $\langle v_z \rangle$ at $t = 4$ Gyr in the meridional (R, z)-plane for $21^\circ < \theta < 31^\circ$ (within the frame of the spiral). Top right: same at $t = 5$ Gyr. Bottom left: same at $t = 6$ Gyr. Bottom right: same at the final time-step $t = 6.5$ Gyr. This figure can be compared at the qualitative level to fig. 13 of Williams et al. (2013).

reduction factors both in the radial (see e.g. Binney & Tremaine 2008, appendix K) and vertical directions.

Let us rewrite our perturber potential of equation (8) as

$$\Phi_{\rm s} = \boldsymbol{Re}\{\Phi_a(R, z) \exp[{\rm i}\, m(\Omega_{\rm P} t - \theta)]\} \tag{9}$$

with

$$\Phi_{\rm a} = -A\, {\rm sech}^2\left(\frac{z}{z_0}\right) \exp\left({\rm i}\frac{m \ln(R)}{\tan p}\right). \tag{10}$$

Then, if we write solutions to the linearized Euler equations for the response of a cold fluid as

$$\begin{cases} v_{\rm Rs} = \boldsymbol{Re}\{v_{\rm Ra}(R, z) \exp[{\rm i}\, m(\Omega_{\rm P} t - \theta)]\} \\ v_{z{\rm s}} = \boldsymbol{Re}\{v_{z{\rm a}}(R, z)) \exp[{\rm i}\, m(\Omega_{\rm P} t - \theta)]\} \end{cases}, \tag{11}$$

we find, following the same steps as in Binney & Tremaine (2008, section 6.2)

$$\begin{cases} v_{\rm Ra} = -\frac{m(\Omega - \Omega_{\rm P})}{\Delta} k \Phi_a + {\rm i}\frac{2\Phi_a}{\Delta}\left(\frac{2\Omega \tanh(z/z_0)}{m(\Omega - \Omega_{\rm P}) z_0} + \frac{m\Omega}{R}\right) \\ v_{z{\rm a}} = -\frac{2{\rm i}}{m(\Omega - \Omega_{\rm P}) z_0} \tanh\left(\frac{z}{z_0}\right) \Phi_a \end{cases}, \tag{12}$$

where $k = m/(R \tan p)$ is the radial wavenumber and $\Delta = \kappa^2 - m^2(\Omega - \Omega_{\rm P})^2$.

If we plot these solutions for $v_{\rm Rs}$ and $v_{z{\rm s}}$ at a given angle (for instance $\theta = 30^\circ$), we get the same pattern as in the simulation (Fig. 15). Of course, the velocity flow plotted on Fig. 15 would in fact be damped by a reduction factor depending on both radial and vertical velocity dispersions when treating the full linearized Boltzmann equation, which will be the topic of a forthcoming paper. Nevertheless, this qualitative consistency between analytical results and our simulations is an indication that the velocity pattern observed by Williams et al. (2013) is likely linked to the

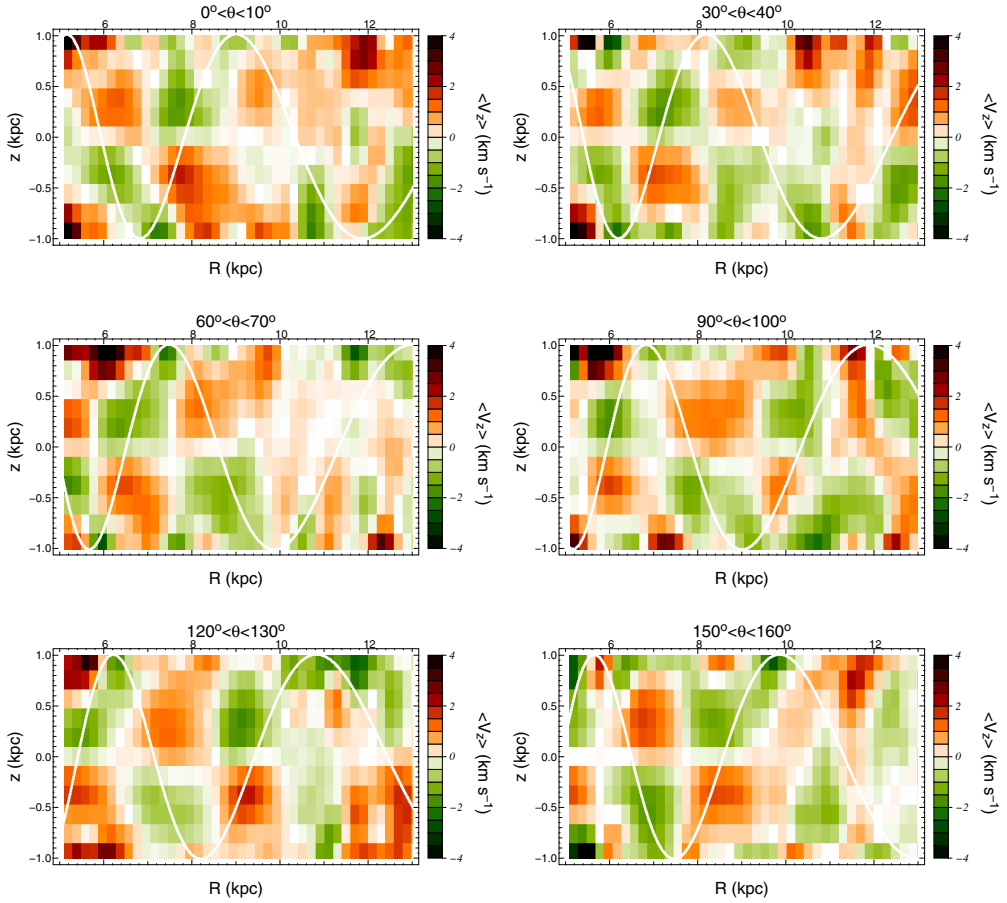

Figure 12. Same as Fig. 11, but for six different azimuths at a fixed time ($t = 6$ Gyr).

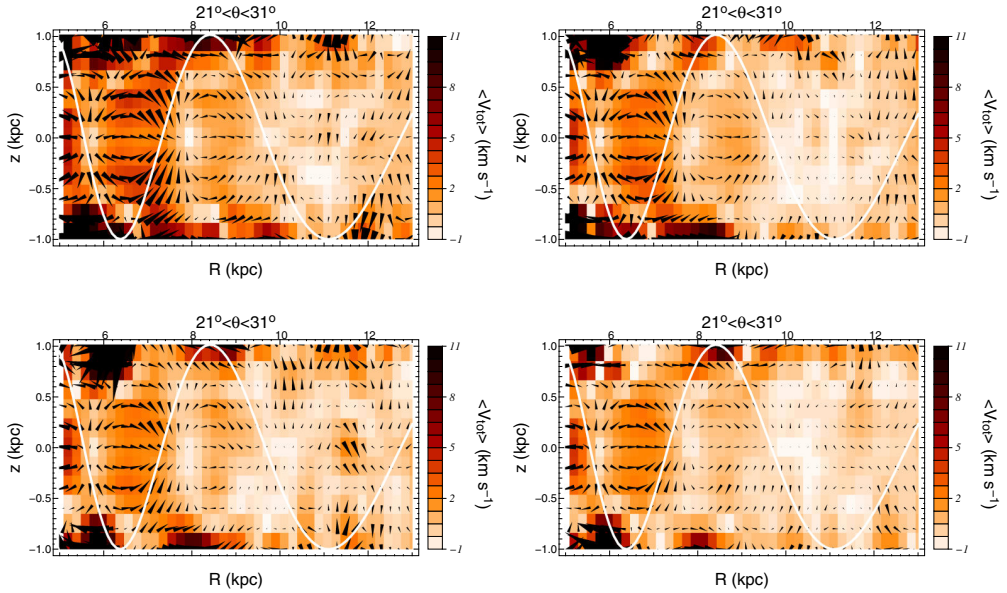

Figure 13. Top-left panel: 'total' velocity flow in the meridional (R, z)-plane $\sqrt{\langle v_R\rangle^2 + \langle v_z\rangle^2}$ at $t = 4$ Gyr for $21^\circ < \theta < 31^\circ$. Arrows indicate the direction of the velocity flow $\langle \boldsymbol{v}\rangle = \langle v_R\rangle \mathbf{1}_R + \langle v_z\rangle \mathbf{1}_z$. Top right: same at $t = 5$ Gyr. Bottom left: same at $t = 6$ Gyr. Bottom right: same at the final time-step $t = 6.5$ Gyr.

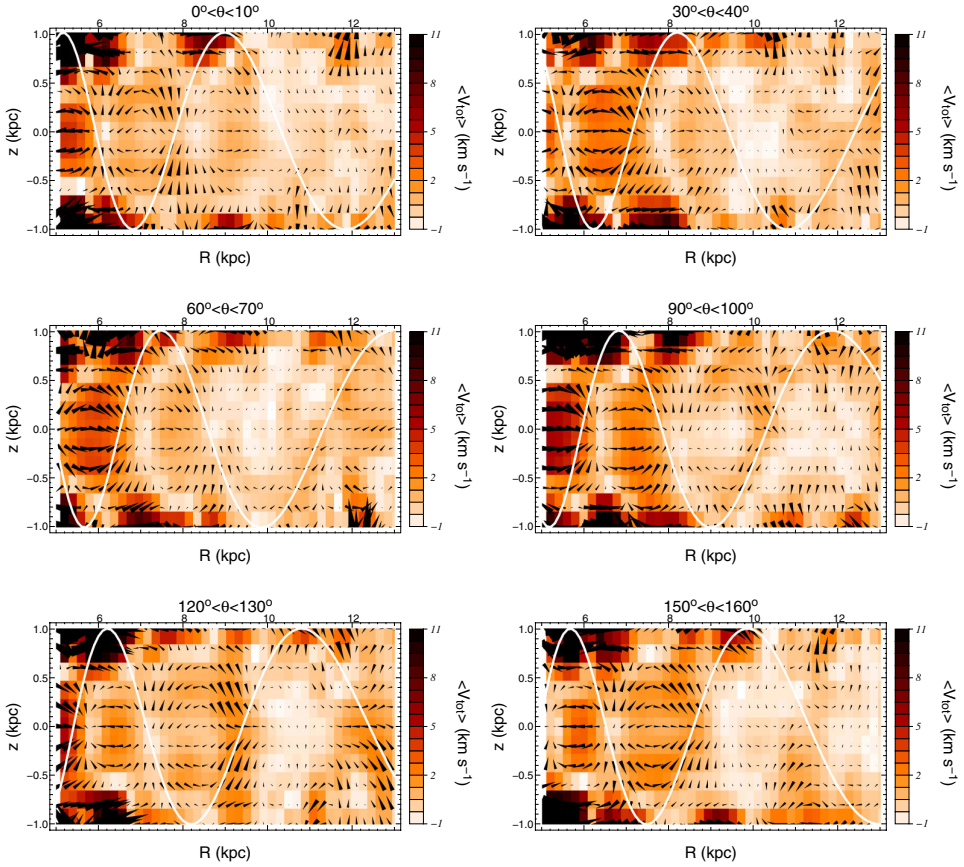

Figure 14. Same as Fig. 13, but for six different azimuths at a fixed time ($t = 6$ Gyr).

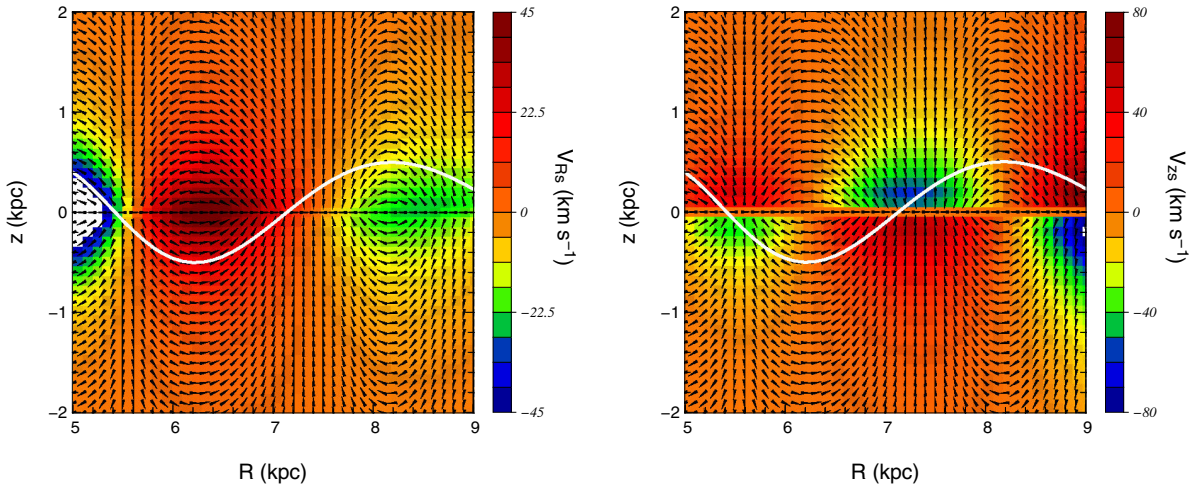

Figure 15. Analytical calculation of the response of a cold fluid to a spiral perturbation (equation 9) in terms of radial velocity $v_{\rm Rs}$ (left-hand panel) and vertical velocity $v_{\rm zs}$ (right-hand panel). This velocity flow is computed at $\theta = 30^\circ$ and $t = 0$ from the solution of linearized Euler equations in equations (11) and (12). Arrows indicate the direction of the fluid velocity vector in the meridional plane. The white line indicates the absolute value of the spiral potential. The shape of the pattern is the same as in the simulation, and similar to fig. 13 of Williams et al. (2013).

potential perturbation by spiral arms. Interestingly, this analytical model also predicts that the radial velocity gradient should become noticeably north/south asymmetric close to corotation.

4 DISCUSSION AND CONCLUSIONS

In recent years, various large spectroscopic surveys have shown that stars of the Milky Way disc exhibit non-zero mean velocities outside of the Galactic plane in both the Galactocentric radial component and vertical component of the mean velocity field (e.g. Siebert et al. 2011b; Carlin et al. 2013; Williams et al. 2013). While it is clear that such a behaviour could be due to a large combination of factors, we investigated here whether spiral arms are able to play a role in these observed patterns. For this purpose, we investigated the orbital response of a test population of stars representative of the old thin disc to a stable spiral perturbation. This is done using a test-particle

simulation with a background potential representative of the Milky Way.

We found non-zero velocities both in the Galactocentric radial and vertical velocity components. Within the rotating frame of the spiral pattern, the location of these non-zero mean velocities in both components are stable over time, meaning that the response to the spiral perturbation is stable. Within corotation, the mean $\langle v_R \rangle$ is negative within the arms (mean radial motion towards the Galactic Centre) and positive (radial motion towards the anticentre) between the arms. Outside corotation, the pattern is reversed, as expected from the Lin–Shu density wave theory (Lin & Shu 1964). On the other hand, even though the spiral perturbation of the potential is very thin, the radial velocity flow is still strongly affected above the Galactic plane. Up to five times the scaleheight of the spiral potential, there are no strong asymmetries in terms of radial velocity, but above these heights, the trend in the radial velocity flow is reversed. This means that asymmetries could be observed in surveys covering different volumes above and below the Galactic plane. Also, forthcoming surveys like *Gaia*, 4MOST, WEAVE will be able to map this region of the disc of the Milky Way and measure the height at which the reversal occurs. Provided this measurement is successful, it would give a measurement of the scaleheight of the spiral potential.

In terms of vertical velocities, within corotation, the mean vertical motion is directed away from the plane at the outer edge of the arms and towards the plane at the inner edge of the arms. The patterns of $\langle v_z \rangle$ above and below the plane are thus mirror-images (see e.g. Carlin et al. 2013). The direction of the mean vertical motion changes roughly in the middle of the interarm region. This produces diagonal features in terms of isocontours of a given $\langle v_z \rangle$, as observed by Williams et al. (2013). The picture that emerges from our simulation is one of 'source' points of the velocity flow in the meridional plane, preferentially on the outer edge of the arms (inside corotation, whilst on the inner edge outside corotation), and of 'sink' points, preferentially on the inner edge of the arms (inside corotation), towards which the mean velocity flows.

We have then shown that this qualitative structure of the mean velocity field is also the behaviour of the analytic solution to linearized Euler equations for a toy model of a cold fluid in response to a spiral perturbation. In a more realistic analytic model, this fluid velocity would in fact be damped by a reduction factor depending on both radial and vertical velocity dispersions when treating the full linearized Boltzmann equation.

In a next step, the features found in the present test-particle simulations will also be checked for in fully self-consistent simulations with transient spiral arms, to check whether non-zero mean vertical motions as found here are indeed generic. The response of the gravitational potential itself to these non-zero motions should also have an influence on the long-term evolution of the velocity patterns found here, in the form of e.g. bending and corrugation waves. The effects of multiple spiral patterns (e.g. Quillen et al. 2011) and of the bar (e.g. Monari et al. 2013, 2014) should also have an influence on the global velocity field and on its amplitude. Once all these different dynamical effects and their combination will be fully understood, a full quantitative comparison with present and future data sets in 3D will be the next step.

This work on the orbital response of the thin disc to a small spiral perturbation by no means implies that no external perturbation of the Milky Way disc happened in the recent past, by e.g. the Sagittarius dwarf (e.g. Gomez et al. 2013). Such a perturbation could of course be responsible for parts of the velocity structures observed in various recent large spectrosocpic surveys. For instance, concerning the important north–south asymmetry spotted in stellar densities at relatively large heights above the disc, spiral arms are less likely to play an important role. Nevertheless, any external perturbation will also excite a spiral wave, so that understanding the dynamics of spirals is also fundamental to understanding the effects of an external perturber. The qualitative similarity between our simulation (e.g. Fig. 11), as well as our analytical estimates for the fluid approximation (Fig. 15), and the velocity pattern observed by Williams et al. (2013, their fig. 13) indicates that spiral arms are likely to play a non-negligible role in the observed velocity pattern of our 'wobbly Galaxy'.

ACKNOWLEDGEMENTS

We thank the referee for insightful and constructive comments.

REFERENCES

Antoja T., Valenzuela O., Pichardo B., Moreno E., Figueras F., Fernández D., 2009, ApJ, 700, L78
Antoja T., Figueras F., Romero-Gómez M., Pichardo B., Valenzuela O., Moreno E., 2011, MNRAS, 418, 1423
Barros D., Lépine J., Junqueira T., 2013, MNRAS, 435, 2299
Bienaymé O., Séchaud N., 1997, A&A, 323, 781
Binney J., 2013, New Astron. Rev., 57, 29
Binney J., Tremaine S., 2008, Galactic Dynamics. Princeton Univ. Press, Princeton, NJ
Binney J. et al., 2014, MNRAS, 439, 1231
Bovy J., Rix H.-W., 2013, ApJ, 779, 115
Bovy J. et al., 2012, ApJ, 759, 131
Carlin J. L. et al., 2013, ApJ, 777, L5
Chereul E., Crézé M., Bienaymé O., 1998, A&A, 340, 384
Chereul E., Crézé M., Bienaymé O., 1999, A&AS, 135, 5
De Simone R., Wu X., Tremaine S., 2004, MNRAS, 350, 627
Dehnen W., 1998, AJ, 115, 2384
Dehnen W., 2000, AJ, 119, 800
Dehnen W., Binney J., 1998, MNRAS, 294, 429
Famaey B., Jorissen A., Luri X., Mayor M., Udry S., Dejonghe H., Turon C., 2005, A&A, 430, 165
Famaey B., Pont F., Luri X., Udry S., Mayor M., Jorissen A., 2007, A&A, 461, 957
Famaey B., Siebert A., Jorissen A., 2008, A&A, 483, 453
Feldmann R., Spolyar D., 2013, preprint (arXiv:1310.2243)
Gomez F., Minchev I., O'Shea B., Beers T. C., Bullock J. S., Purcell C. W., 2013, MNRAS, 429, 159
Kaasalainen M., 1994, MNRAS, 268, 1041
Kaasalainen M., 1995, Phys. Rev. E, 52, 1193
Kaasalainen M., Binney J., 1994, MNRAS, 268, 1033
Kordopatis G. et al., 2013, AJ 146, 134
Kuijken K., Tremaine S., 1994, ApJ, 421, 178
Lépine J. et al., 2011, MNRAS, 417, 698
Lin C. C., Shu F. H., 1964, ApJ, 140, 646
McMillan P. J., 2013, MNRAS, 430, 3276
McMillan P. J., Binney J., 2010, MNRAS, 402, 934
Minchev I., Famaey B., 2010, ApJ, 722, 112
Minchev I., Nordhaus J., Quillen A., 2007, ApJ, 664, L31
Minchev I., Boily C., Siebert A., Bienaymé O., 2010, MNRAS, 407, 2122
Minchev I., Famaey B., Quillen A., Di Matteo P., Combes F., Vlajić M., Erwin P., Bland-Hawthorn J., 2012, A&A, 548, A126
Monari G., Antoja T., Helmi A., 2013, preprint (arXiv:1306.2632)
Monari G., Helmi A., Antoja T., Steinmetz M., 2014, preprint (arXiv:1402.4479)
Olling R., Dehnen W., 2003, ApJ, 599, 275
Patsis P. A., Grosbøl P., 1996, A&A, 315, 371
Pompéia L. et al., 2011, MNRAS, 415, 1138
Quillen A., Minchev I., 2005, AJ, 130, 576

Quillen A., Dougherty J., Bagley M., Minchev I., Comparetta J., 2011, MNRAS, 417, 762
Reid M. et al., 2009, ApJ, 700, 137
Roskar R., Debattista V., Quinn T., Wadsley J., 2012, MNRAS, 426, 2089
Schönrich R., 2012, MNRAS, 427, 274
Sellwood J., 2014, Rev. Mod. Phys., 86, 1
Shu F. H., 1969, ApJ, 158, 505
Siebert A. et al., 2011a, AJ, 141, 187
Siebert A. et al., 2011b, MNRAS, 412, 2026
Siebert A. et al., 2012, MNRAS, 425, 2335
Smith M., Whiteoak S. H., Evans N. W., 2012, ApJ, 746, 181
Steinmetz M. et al., 2006, AJ, 132, 1645
Widrow L., Gardner S., Yanny B., Dodelson S., Chen H.-Y., 2012, ApJ, 750, L41
Williams M. et al., 2013, MNRAS, 436, 101
Yanny B., Gardner S., 2013, ApJ, 777, 91
Zwitter T. et al., 2008, AJ, 136, 421

This paper has been typeset from a TEX/LATEX file prepared by the author.

Chapitre 4

Conclusion

Nous avons réalisé ce travail pour montrer que les bras spiraux pouvaient jouer un rôle important sur la structure du champ de vitesse du disque. Malgré des signes encourageants, nous ne savions pas jusqu'à quelles mesures nos recherches allaient être concluantes et les résultats obtenus sont très positifs, nous sommes allés à des temps jusqu'à 6,5 milliards d'années pour l'intégration, temps où notre population test est presque en équilibre parfait. Dans le référentiel tournant de la spirale, la réponse est plutôt stable.
Comme attendu, nous avons obtenu des vitesses moyennes radiales non-nulles, et de manière plus novatrice également des vitesses verticales non-nulles. Pour la vitesse radiale, on retrouve la configuration attendue par la théorie des ondes de densité de Lin & Shu ainsi que celle observée par Siebert et al. (2011a) au voisinage solaire.
On a aussi constaté que bien que la perturbation spirale est fine, les vitesses radiales en ressentent ses effets plus loin de part en part du plan Galactique jusqu'à 5 fois l'échelle de hauteur de la perturbation spirale. En outre, la configuration des vitesses verticales est similaire à celle observée par Williams et al. (2013). On retrouve bien la configuration diagonale des isocontours de la vitesse verticale moyenne.
En combinant ces deux champs de vitesse, on a remarqué qu'avant la corotation, dans les bras, le mouvement moyen des étoiles se fait de l'intérieur vers l'extérieur en sortant du plan puis reviennent dans le plan à mi-distance entre les deux bras pour finalement arriver au niveau interne du bras suivant.

Enfin, afin de comprendre l'origine physique de cette structure du champ de vitesse, nous avons linéarisé les équations d'Euler pour un fluide froid soumis à une perturbation spirale. La structure en 3 dimensions du champ de vitesse obtenue est similaire à celle des simulations. Ceci m'a permis de montrer que le champ de vitesse se compose de *source point* dans la partie externe et de *sink point* dans la partie interne des bras et inversement après la corotation.

Cette thèse a pu démontrer que les structures verticales de l'espace des vitesses, que la plupart des auteurs attribuent à une perturbation externe, peuvent être expliquées par l'action des bras spiraux. Néanmoins, il est pour l'instant prématuré d'exclure une participation de perturbations externes aux effets observés. En effet, l'origine des bras spiraux est encore incertaine et, s'ils se développent comme des modes propres des disques galactiques, ils sont également induits par l'effet de perturbateurs externes. Aussi, comme montré par les études

sur l'action de satellites sur le disque, ils peuvent également créer des vitesses non nulles dans le disque.

Pour différencier ces deux modèles, des données à plus grande échelle dans le disque galactique sont nécessaires, la géométrie prédite de la réponse étant très différente entre ces deux théories. Le satellite Gaia de l'ESA qui a été lancé en décembre 2013 devrait nous permettre de construire les cartes de champs de vitesse pour une grande partie du disque Galactique avec une grande précision. Le catalogue sera disponible en 2020. Ces cartes nous permettront de discriminer entre les 2 modèles possibles. Comme souvent, il est probable qu'un mélange des deux effets soit à l'oeuvre, et c'est l'importance de chaque phénomène respectif qu'il faudra quantifier. Quoi qu'il en soit, l'apport essentiel de mon travail aura été de montrer qu'on ne peut pas négliger les perturbations non-axisymetriques internes de la Galaxie comme facteur engendrant des mouvements globaux verticaux des étoiles de part et d'autre du disque galactique, ce qui devra donc être pris en compte dans les futurs modèles de la Galaxie.

Bibliographie

Adibekyan, V. Z., Figueira, P., Santos, N. C., et al. 2013, A&A, 554, A44

Antoja, T., Figueras, F., Fernández, D., & Torra, J. 2008, A&A, 490, 135

Antoja, T., Figueras, F., Romero-Gómez, M., et al. 2011, MNRAS, 418, 1423

Antoja, T., Valenzuela, O., Pichardo, B., et al. 2009, ApJ, 700, L78

Baade, W. 1944, Contributions from the Mount Wilson Observatory / Carnegie Institution of Washington, 696, 1

Bensby, T., Alves-Brito, A., Oey, M. S., Yong, D., & Meléndez, J. 2011, ApJ, 735, L46

Bienayme, O. & Séchaud, N. 1997, A&A, 323, 781

Bijaoui, A., Recio-Blanco, A., de Laverny, P., & Ordenovic, C. 2012, Statistical Methodology, 9, 55

Binney, J., Burnett, B., Kordopatis, G., et al. 2014, MNRAS, 439, 1231

Binney, J., Gerhard, O. E., Stark, A. A., Bally, J., & Uchida, K. I. 1991, MNRAS, 252, 210

Binney, J. & Tremaine, S. 2008, Galactic Dynamics : Second Edition

Blitz, L. & Spergel, D. N. 1991, ApJ, 379, 631

Burnett, B. & Binney, J. 2010, MNRAS, 407, 339

Carlin, J. L., DeLaunay, J., Newberg, H. J., et al. 2013, ApJ, 777, L5

Carollo, D., Beers, T. C., Chiba, M., et al. 2010, ApJ, 712, 692

Christlieb, N., Bessell, M. S., Beers, T. C., et al. 2002, Nature, 419, 904

Cohen, R. J. & Few, R. W. 1976, MNRAS, 176, 495

Combes, F. 1991, ARA&A, 29, 195

Corbelli, E. & Salpeter, E. E. 1988, ApJ, 326, 551

De Simone, R., Wu, X., & Tremaine, S. 2004, MNRAS, 350, 627

Debattista, V. P. 2014, MNRAS, 443, L1

D'Onghia, E., Vogelsberger, M., & Hernquist, L. 2013, ApJ, 766, 34

Famaey, B., Siebert, A., & Jorissen, A. 2008, A&A, 483, 453

Ferrers, N. M. 1870, Royal Society of London Philosophical Transactions Series I, 160, 1

Fujii, M. S., Baba, J., Saitoh, T. R., et al. 2011, ApJ, 730, 109

Gauthier, J.-R., Dubinski, J., & Widrow, L. M. 2006, ApJ, 653, 1180

Georgelin, Y. M. & Georgelin, Y. P. 1976, A&A, 49, 57

Gilmore, G. & Reid, N. 1983, MNRAS, 202, 1025

Gilmore, G., Seabroke, G., & RAVE Collaboration. 2004, in Bulletin of the American Astronomical Society, Vol. 36, American Astronomical Society Meeting Abstracts, 142.09

Goldreich, P. & Lynden-Bell, D. 1965, MNRAS, 130, 125

Gonzalez, O. A., Rejkuba, M., Zoccali, M., et al. 2013, A&A, 552, A110

Hambly, N. C., MacGillivray, H. T., Read, M. A., et al. 2001, MNRAS, 326, 1279

Haywood, M., Di Matteo, P., Lehnert, M. D., Katz, D., & Gómez, A. 2013, A&A, 560, A109

Hernquist, L. 1990, ApJ, 356, 359

Høg, E., Fabricius, C., Makarov, V. V., et al. 2000, A&A, 355, L27

Hubble, E. P. 1926a, ApJ, 63, 236

Hubble, E. P. 1926b, ApJ, 64, 321

Kuijken, K. & Gilmore, G. 1989, MNRAS, 239, 571

Levine, E. S., Blitz, L., & Heiles, C. 2006, Science, 312, 1773

Levine, E. S., Blitz, L., Heiles, C., & Weinberg, M. 2005, in Bulletin of the American Astronomical Society, Vol. 37, American Astronomical Society Meeting Abstracts, 1225

Lin, C. C. & Shu, F. H. 1964, ApJ, 140, 646

López-Corredoira, M., Cabrera-Lavers, A., Garzón, F., & Hammersley, P. L. 2002, A&A, 394, 883

Lynden-Bell, D. & Kalnajs, A. J. 1972, MNRAS, 157, 1

Lynden-Bell, D. & Ostriker, J. P. 1967, MNRAS, 136, 293

Marinacci, F., Binney, J., Fraternali, F., et al. 2010, in American Institute of Physics Conference Series, Vol. 1240, American Institute of Physics Conference Series, ed. V. P. Debattista & C. C. Popescu, 166–168

Martinez-Valpuesta, I. & Gerhard, O. 2013, ApJ, 766, L3

Minchev, I., Famaey, B., Quillen, A. C., et al. 2012, A&A, 548, A127

Minchev, I., Quillen, A. C., Williams, M., et al. 2009, MNRAS, 396, L56

Miyamoto, M. & Nagai, R. 1975, PASJ, 27, 533

Monari, G., Antoja, T., & Helmi, A. 2013, ArXiv e-prints

Monari, G., Helmi, A., Antoja, T., & Steinmetz, M. 2014, ArXiv e-prints

Munari, U., Siviero, A., Bienaymé, O., et al. 2009, A&A, 503, 511

Nakada, Y., Onaka, T., Yamamura, I., et al. 1991, Nature, 353, 140

Navarro, J. F., Frenk, C. S., & White, S. D. M. 1997, ApJ, 490, 493

Olling, R. P. & Dehnen, W. 2003, ApJ, 599, 275

Oort, J. H., Kerr, F. J., & Westerhout, G. 1958, MNRAS, 118, 379

Patsis, P. A. & Grosbol, P. 1996, A&A, 315, 371

Peters, I. W. L. 1975, ApJ, 195, 617

Pompéia, L., Masseron, T., Famaey, B., et al. 2011, MNRAS, 415, 1138

Quillen, A. C. & Minchev, I. 2005, AJ, 130, 576

Recio-Blanco, A., Bijaoui, A., & de Laverny, P. 2006, MNRAS, 370, 141

Recio-Blanco, A., de Laverny, P., Kordopatis, G., et al. 2014, A&A, 567, A5

Reylé, C., Marshall, D. J., Robin, A. C., & Schultheis, M. 2009, A&A, 495, 819

Robin, A. C., Reylé, C., Derrière, S., & Picaud, S. 2003, A&A, 409, 523

Robin, A. C., Reylé, C., Fliri, J., et al. 2014, A&A, 569, A13

Roeser, S., Demleitner, M., & Schilbach, E. 2010, AJ, 139, 2440

Rosse, T. E. O. 1850, Royal Society of London Philosophical Transactions Series I, 140, 499

Ryan, S. G., Norris, J. E., & Beers, T. C. 1996, ApJ, 471, 254

Schödel, R., Ott, T., Genzel, R., et al. 2002, Nature, 419, 694

Schultheis, M., Chen, B. Q., Jiang, B. W., et al. 2014, A&A, 566, A120

Seabroke, G. M. & Gilmore, G. 2007, MNRAS, 380, 1348

Sellwood, J. A. & Binney, J. J. 2002, MNRAS, 336, 785

Sellwood, J. A. & Carlberg, R. G. 1984, ApJ, 282, 61

Sellwood, J. A. & Carlberg, R. G. 2014, ApJ, 785, 137

Sevenster, M. N. 1999, MNRAS, 310, 629

Shu, F. H. 1969, ApJ, 158, 505

Siebert, A., Famaey, B., Binney, J., et al. 2012, MNRAS, 425, 2335

Siebert, A., Famaey, B., Minchev, I., et al. 2011a, MNRAS, 412, 2026

Siebert, A., Williams, M. E. K., Siviero, A., et al. 2011b, AJ, 141, 187

Steinmetz, M., Zwitter, T., & Siebert, A. 2006, AJ, 132, 1645

Toomre, A. 1969, ApJ, 158, 899

Toomre, A. 1981, 111

Urquhart, J. S., Figura, C. C., Moore, T. J. T., et al. 2014, MNRAS, 437, 1791

Wegg, C. & Gerhard, O. 2013, MNRAS, 435, 1874

Widrow, L. M., Barber, J., Chequers, M. H., & Cheng, E. 2014, MNRAS, 440, 1971

Widrow, L. M., Gardner, S., Yanny, B., Dodelson, S., & Chen, H.-Y. 2012, ApJ, 750, L41

Widrow, L. M., Pym, B., & Dubinski, J. 2008, ApJ, 679, 1239

Williams, M. E. K., Steinmetz, M., Binney, J., et al. 2013, MNRAS, 436, 101

Zacharias, N., Finch, C., Girard, T., et al. 2010, AJ, 139, 2184

Zacharias, N., Finch, C. T., Girard, T. M., et al. 2013, AJ, 145, 44

Zacharias, N., Urban, S. E., Zacharias, M. I., et al. 2004, AJ, 127, 3043

Zolotov, A., Willman, B., Brooks, A. M., et al. 2009, ApJ, 702, 1058

Zwitter, T., Matijevič, G., Breddels, M. A., et al. 2010, A&A, 522, A54

Carole FAURE

Simulation des effets des bras spiraux sur la dynamique stellaire dans la Voie Lactée

Observatoire astronomique de Strasbourg

Résumé

Dans un disque axisymétrique en équilibre, les vitesses galactocentriques radiales et verticales sont théoriquement nulles. Pourtant, de grands relevés spectroscopiques ont révélé que les étoiles du disque de la Voie Lactée sont animées de vitesses non nulles dans les directions radiale et verticale. Les structures en vitesse radiale sont généralement associées aux composantes non-axisymétriques du potentiel. Celles en vitesse verticale non nulle sont souvent associées à des excitations externes.

Nous avons montré que la réponse stellaire à une perturbation spirale produit un déplacement radial et des mouvements verticaux non nuls. La structure du champ moyen de vitesse obtenue est cohérente avec les observations. De plus un modèle simple reposant sur une linéarisation des équations d'Euler reproduit naturellement ce résultat. Nous concluons que ces structures observées pourraient aussi être engendrées par des perturbations internes non-axisymétriques.

Mots-clés : dynamique et cinématique galactique – structure de la Galaxie – méthodes numériques : particules test

Résumé en anglais

In an equilibrium axisymmetric galactic disc, the mean galactocentric radial and vertical velocities are expected to be zero everywhere. Recent spectroscopic surveys have however shown that stars of the Milky Way disc exhibit non-zero mean velocities outside of the Galactic plane in both the radial and vertical velocity components. While radial velocity structures have already often been assumed to be linked with non-axisymmetric components of the potential, non-zero vertical velocity structures are usually rather attributed to excitations by external sources. We show that the stellar response to a spiral perturbation induces both a radial velocity flow and non-zero vertical motions. The resulting structure of the mean velocity field is qualitatively similar to the observations. Such a pattern also emerges from an analytic toy model based on linearized Euler equations. In conclusion, non-axisymmetric internal perturbations can also be the source of the observed mean velocity patterns.

Key words: galactic dynamics and kinematics – structure of the Galaxy – numerical methods: test particles